Rotary Micro-Electro-Mechanical Scanner for Chip-level Beam Steering Application

by

Amit GOUR

MANUSCRIPT BASED THESIS PRESENTED TO ÉCOLE DE TECHNOLOGIE SUPÉRIEURE IN PARTIAL FULFILLMENT FOR THE DEGREE OF DOCTOR OF PHILOSOPHY
Ph.D.

MONTREAL, DECEMBER 1, 2021

ÉCOLE DE TECHNOLOGIE SUPÉRIEURE
UNIVERSITÉ DU QUÉBEC

BOARD OF EXAMINERS

THIS THESIS HAS BEEN EVALUATED

BY THE FOLLOWING BOARD OF EXAMINERS

Mr. Frédéric Nabki, Thesis supervisor
Department of Electrical Engineering, École de Technologie Supérieure

Mr. Michaël Ménard, co-Supervisor
Department of Electrical Engineering, École de Technologie Supérieure

Mr. Ricardo J. Zednik, President of the board of examiners
Department of Mechanical Engineering, École de Technologie Supérieure

Mr. Vahé Nerguizian, Member of the jury
Department of Electrical Engineering, École de Technologie Supérieure

Mr. Yves-Alain Peter, External examiner
Department of Engineering Physics, École Polytechnique de Montréal

THIS THESIS WAS PRESENTED AND DEFENDED

IN THE PRESENCE OF A BOARD OF EXAMINERS AND THE PUBLIC

ON NOVEMBER 17, 2021

AT ÉCOLE DE TECHNOLOGIE SUPÉRIEURE

ACKNOWLEDGEMENTS

First and foremost, I would like to express my sincere gratitude to my supervisors, Professor Fredric Nabki and Professor Michaël Ménard for the immeasurable amount of support, patience, and the true guidance throughout my doctoral journey. I would also express my deep gratitude to them for providing me a lot of opportunities with open mind in both research work and industry experience. I am grateful for their foresight, financial support and technical guidance.

Professor Nabki's profound knowledge in MEMS and his enthusiasm towards scientific research has been inspirational. He has been a great mentor, who always encouraged me to believe in my potential to pursue and accomplish multiple challenges. I have learned so much from his incredible potential to focus on the essence of a problem, cutting right through all the noise around it. Its been amazing experience and inspiring to witness his uncompromising tenacity in pursuing what he believes in, with regards to handling technical and non-technical issues.

Professor Menard's expertise in optical systems and attention to fundamentals served as the great guidance to my research activity and was instrumental to the success of this work. His persistent encouragement and insightful feedback helped me on solving multiple obstacles occurred during my research work. I would also like to thank him for introducing me to the world of photonic integrated circuits back in 2016 and guiding me to explore this area. I am grateful for the opportunity to witness his commitment and be inspired.

I extend my sincere gratitude to the members of the thesis committee, Prof. Yves-Alain Peter from the École Polytechnique de Montréal, Prof. Ricardo J. Zednik and Prof. Vahé Nerguizian both from the École de Technologie Supérieure for their time, encouragement and critical feedback.

I wish to thank Ali Lashari for his initial hands-on training on micromotor testing and developing the robust function generator kit for the micromotor actuation that have been a key component for the testing all the MEMS chips. I wish to thank Alexandre Robichaud who has assisted and trained me on fabrication and characterization equipments, that helped me to develop first

iteration of adhesive bonding. He has been very resourceful for arranging test setups for MEMS chip characterization. Later, Mathieu Gratuze assisted and trained me with the vibrometer that became a very important for the optical characterization of the micro-scanner. I wish them success in all their future endeavours.

I would also like to thank past and future students of our research group for their help and all the exhilarating discussions. Thank you Devika, Suraj, Shiva, Abdul, Nakisa, Amin, and many others for all the support and inspiration.

I extend my acknowledgments and gratitude to the technicians, colleagues at the LACIME research center and my fellow engineering students at ÉTS for there assistance and collaboration during my research work.

I would also like to thank the Natural Sciences and Engineering Research Council (NSERC) and the Microsystems Strategic Alliance of Quebec (ReSMiQ), for the financial support of this work. Thanks to CMC for the support, chip fabrication, training courses, and EDA workshops they provided throughout my doctoral study.

Finally, I would like to thank my family and parents for their unconditional support, love and sacrifices.

Scanner micro-électromécanique rotatif sur puce pour le contrôle de faisceau lumineux

Amit GOUR

RÉSUMÉ

Plusieurs systèmes avancés, tels que la tomographie par cohérence optique (OCT), la détection et la télémétrie de la lumière (LIDAR) et les systèmes avancés d'aide à la conduite (ADAS), se composent de divers modules conçus pour répondre à des spécifications strictes. Ces modules comprennent des composants électroniques, mécaniques et optiques, ce qui peut rendre le système volumineux, encombrant, gourmand en énergie et coûteux. Avec l'utilisation de technologies micro et nano, ces modules peuvent être miniaturisés sans compromettre les performances du système. En conséquence, la vision de ce travail est de développer des composants compacts et abordables pouvant être utilisés dans des systèmes avancés en tirant parti des avantages de la technologie des micro-systèmes électromécaniques (MEMS) et de la fabrication par lots. Elle peut non seulement permettre la miniaturisation du système, mais également en améliorer les performances en termes de consommation d'énergie. Les scanners polygonaux sont des dispositifs essentiels pour les systèmes tels que l'OCT et le LIDAR qui sont largement utilisés dans l'imagerie biomédicale et la détection de l'environnement, respectivement. En règle générale, ces scanners se composent d'un miroir polygonal métallique monté sur un moteur à courant continu, offrant une plage de fonctionnement à grande vitesse en fonction de l'application. Les scanners polygonaux actuels ont une grande taille, consomment une grande quantité d'énergie et sont lourds. De plus, ces caractéristiques des scanners polygonaux deviennent de sérieux obstacles lorsqu'ils sont utilisées dans des systèmes aux ressources limitées, tels que le LIDAR pour les systèmes de navigation dans les drones ou les véhicules aériens sans pilote. Par conséquent, il existe un besoin pour des scanners polygonaux miniaturisés qui peuvent accomplir des fonctionnalités similaires à celles des scanners conventionnels mais qui nécessitent moins d'énergie et occupent un espace plus petit. Ce travail de recherche est axé sur l'exploitation des technologies MEMS afin de réaliser des versions à l'échelle de puces de scanners polygonaux rotatifs grâce à l'innovation dans l'intégration de micro-dispositifs basés sur MEMS. Un scanner polygonal miniaturisé nécessite un micromiroir vertical monté sur une plate-forme rotative à haute vitesse au niveau de la puce. De nouvelles techniques pour surmonter les défis de la miniaturisation des scanners polygonaux à l'aide des technologies MEMS et de micro-assemblage sont présentées. Un micromoteur basé sur l'actionnement électrostatique a été conçu et fabriqué en utilisant le procédé PolyMUMPS pour mettre en œuvre la plate-forme rotative. Divers micro-polyèdres de différentes tailles pour le contrôle du faisceau ont été conçus et fabriqués en utilisant le procédé PiezoMUMPS et une technique d'intégration simple a été développée pour monter ces micro-polyèdres sur le micromoteur. Le micro-scanner réalisé a une taille globale de 1 mm^3 et consomme une puissance inférieure à 1 milliwatt.

Mots-clés: Scanner polygonal, LIDAR, OCT, micromoteur électrostatique, micro-scanner, micro-polyèdre, micro-assemblage, procédé PolyMUMPS

Rotary Micro-Electro-Mechanical Scanner for Chip-level Beam Steering Application

Amit GOUR

ABSTRACT

Advanced systems, such as optical coherence tomography (OCT), light detection and ranging (LIDAR) and advanced driving assisting systems (ADAS), consist of various modules that are designed to meet stringent specifications. These modules require electronic, mechanical and optical components, which can make the system large, bulky, power hungry and expensive. With the use of micro-and-nano technologies, such modules can be miniaturized without compromising the system performance. Accordingly, the vision of this work is to develop compact and affordable components that can be used in advanced systems by leveraging the benefits of micro-electro-mechanical system (MEMS) technology and batch manufacturing. It can not only enable system miniaturization but also improve system performance in terms of power consumption. Polygon scanners are crucial devices for systems such as OCT and LIDAR that are widely used in biomedical imaging and environment sensing, respectively. Typically, these scanners consist of a metallic polygon mirror mounted on a DC micromotor, providing a range of high-speed operation depending upon the application. Current polygon scanners have a large footprint, consume a large amount of power and are heavy. Moreover, these features of polygon scanners become serious impediments when they are used in resource limited systems, such as LIDAR for navigation systems in drones or unmanned aerial vehicles. Consequently, there is a need for miniaturized polygon scanners that can accomplish similar functionality as conventional polygon scanners but that require less power and occupy a smaller real-estate. This research work is focused on exploiting MEMS technologies in order to realize chip scale versions of rotary polygon scanners through innovation in the integration of MEMS based micro-devices. A miniaturized polygon scanner requires a vertical micromirror mounted on a chip-level high speed rotary platform. Novel techniques to overcome the challenges of polygon scanner miniaturization using MEMS and micro-assembly technologies are presented. A micromotor based on electrostatic actuation was designed and fabricated using the PolyMUMPS process to implement the rotary platform. Various micro-polyhedron of different size for beam deflection were designed and fabricated using the PiezoMUMPS process and a simple integration technique was developed to mount these micro-polyhedrons onto the micromotor. The realized micro-scanner has an overall size of 1 mm^3 and consumes power less than 1 milliwatts.

Keywords: Polygon scanner, LIDAR, OCT, Electrostatic micromotor, micro-scanner, micro-polyhedron, micro-assembly,PolyMUMPS Process

TABLE OF CONTENTS

LIST OF TABLES

LIST OF FIGURES

Page

LIST OF ABBREVIATIONS

CMOS	Complementary Metal Oxide Semiconductor
CPB	Central Pin Bearing
CTE	Cofficient of Thermal Expansion
DFB	Distributed Feedback
DLP	Digital Lightight Processor
DRIE	Deep Reactive Ion Etching
EWD	Electrowetting Droplets
FEA	Finite Element Analyses
IC	Integrated Circuit
IoT	Internet of Things
LIDAR	Light Detection and Ranging
LMD	Liquid Metal Drops
MEMS	Micro-electro-mechanical systems
MOEMS	Micro-opto-electro-mechanical systems
MRMI	Micro Ranging and Micro Imaging
OCT	Optical Coherence Tomography
PCB	Printed Circuit Board
PZT	Piezoelectric
SEM	Scanning Electron Microscopy

SOI	Silicon on Insulator
VCM	Variable capacitance micromotor
VCSEL	Vertical Cavity Surface Emitting Laser

INTRODUCTION

Preface

The miniaturization of technological devices has led to the development of numerous products in many application areas. Portable personal computers, smartphones, smartwatches, fitness tracking devices and augmented reality devices are a few examples of consumer devices that are now possible thanks to the miniaturization and assembly of electronic circuits and sensor systems. In addition, niche systems such as unmanned aerial vehicles, drones, autonomous marine vehicles, micro-robots, home-automation-sensors, service robots are becoming popular for various applications and their demand is on the rise (Barbedo, 2019; Kim et al., 2019; Bao et al., 2020; Breguet et al., 2006; Risteska Stojkoska & Trivodaliev, 2017; Nikitenko et al., 2014).

The development of these systems is possible because sub-systems that are capable of providing the required functionalities in smaller form factors and low-cost are becoming readily available. Integrated circuit (IC) technology and its spin-off micro-electro-mechanical-systems (MEMS) are the two main technologies that played a major role in achieving this feat of system-scaling, meeting end user market demand with innovative products.

The first pioneering demonstration of a MEMS sensor as an accelerometer was performed in the early 1980's at Stanford University (USA) (Roylance & Angell, 1979). Today, MEMS sensors are used in a multitude of fields. Large-scale and large-volume production of MEMS sensors is possible through batch fabrication, which makes them affordable. MEMS capabilities will likely improve in the future resulting in more sophisticated miniaturized systems for applications such as the internet of things (IoT), light-detection and ranging (LIDAR), biomedical non-invasive imaging, 5G telecommunication, bio-sensors and many more (Zhu et al., 2020).

The multidisciplinary and multiphysics nature of MEMS devices and their fabrication processes is a design challenge, requiring expertise and specific knowledge in several domains simultaneously. Micro-Opto-Electro-Mechanical-Systems (MOEMS), is one of the application areas that emerged due to the intensive study and progress made by various research groups around the world in developing miniaturized optical systems using MEMS and micro-optics. Small size, reliability, multi-functionality and cost-effectiveness are key benefits of MOEMS over conventional optical systems, providing a better solution to various challenges in developing optical systems.

Optical scanning micro-devices are one of the key parts of MOEMS research, enabling portable and truly miniaturized systems (Motamedi, Wu & Pister, 1997). The first light scanning micro-mirror was published in 1980 (Petersen, 1980). Micro-mirrors are among the most-sought and intensively researched MOEMS devices for scanning applications. Scanners based on MEMS micromirrors are the leading technology for many application fields such as confocal-microscopy, pico-projectors, heads-up displays, finger-print sensors, optical switches, laser displays, digital light processsors (DLP), optical coherence tomography (OCT), LIDAR, and barcode readers (Choi et al., 2014; Freeman, Champion & Madhavan, 2009; Chellappan, Erden & Urey, 2010; Shin et al., 2012; Xie, Pan & Fedder, 2003; Hedili, Freeman & Urey, 2012; Kim et al., 2008b; Lee, 2004; Ye et al., 2017b; Kiang et al., 1996). MOEMS devices play an important role in setting the performance and limitations of a miniaturised scanning system.

The capability of MOEMS technology to integrate optical, mechanical and electronic components shows great potential to produce reliable compact next-generation devices. Lately, there has been growing interest in developing a micro-beam-steering system for high-speed scanning applications such as LIDAR, optical switches and optical coherence tomography or confocal microscopy. This is in the hopes of enabling miniaturization and high-degree of system integration, and achieving cost-effective, low-footprint and low-power on-chip optical systems.

A notable challenge in the development of optical scanning MOEMS devices is the limited rotary motion of scanning mirrors, or scan angle. In this work, a miniaturized chip-level full-rotary beam steering system was developed to extend the integration potential of MOEMS technology in optical scanning applications. Using the methodology presented in this work, it is expected that the micro-optical elements and the rotary MEMS will be integrated to produce hybrid systems with increased beam steering capabilities.

Motivation

Micro-ranging and micro-imaging (MRMI) are important measurement techniques used for environment sensing in industrial applications. Laser scanning technology is used to implement these techniques in-order to detect the surrounding objects and derive their characteristics. Beam steering devices are used to reflect the laser beam in order to scan a wide observation field, thereby analyzing real-world objects or surfaces and collecting data for constructing three-dimensional images and measuring range.

Currently, MRMI techniques are widely used in manufacturing industries but have limited application in other fields due to the high cost and large form factor of the instruments. For instance, OCT provides high-resolution micro-imaging and has emerged as a powerful non-invasive medical imaging diagnostic technique. Particularly, OCT has revolutionized the clinical practice of ophthalmology owing to its superior performance in providing ultra-high resolutions cross-sectional subsurface images of samples. Now a multitude of other non-medical applications of OCT are emerging, such as the measurement of thicknesses in multi-layered foils or pharmaceutical tablets, thin films in organic solar cells, damages in paper or printed electronics products, characterization of laser-drilled holes, degradation of food and polymers, and the conservation analysis of artwork (Nemeth et al., 2013; Koller et al., 2011; Webster et al., 2010; Thrane et al., 2012; Alarousu et al., 2005; Czajkowski et al., 2010; Stifter et al., 2010; Targowski & Iwanicka, 2012; Jeught, Bradu & Podoleanu, 2010).

In its first 25 years, the OCT industry grew dramatically, steered by the need for new low-cost, high-resolution, non-invasive imaging solutions for various therapeutic and diagnostic applications. In 2015, the OCT system market was $750 million/year and over the past 25 years cumulative revenue has surpassed $5 billion. However, a typical FDA approved OCT system costs about $70,000, limiting its application in small clinical centers and developing countries.

A commercial table-top OCT system with swept source laser is shown in figure 0.1. The typical configuration of an OCT system consists of a laser source, a sample arm for scanning the test area, a reference arm for time delay and a data-acquisition system. Polygon optical scanners are used to implement an optical filter in a swept source OCT for wavelength tuning and are used in time-domain OCT to implement a delay line in the reference arm.

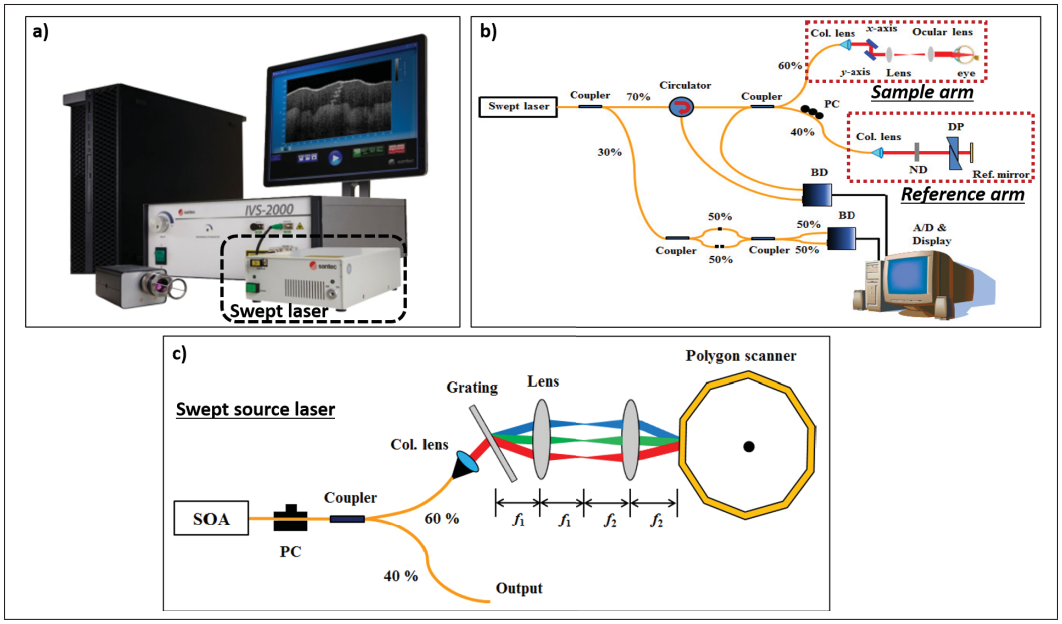

Figure 0.1 a) A table-top swept-source OCT system taken from SANTEC (2020), b) Schematic showing OCT system with swept source laser configuration taken from Lee, Song, Jung & Kim (2011), c) Schematic of swept source laser with polygon mirror for wavelength tuning taken from Lee, Song, Jung & Kim (2011)

The high cost of OCT systems is attributed to its various expensive electronic, mechanical and optical components. The user-base of this micro-imaging technique can be widened by developing a chip-scale solution for system miniaturization, especially the down-sizing of the optical scanning system that includes of a high-speed motorized polygon scanner. A miniaturized OCT system amenable to batch fabrication used as a point-of-care diagnostic device could be highly beneficial for clinical endoscopic applications and wider spread in cost-sensitive markets. A micro-optical bench having a micro-rotary polygon scanner can be implemented using MEMS for OCT scaling.

Likewise, in recent years, the micro-ranging techniques using LIDAR sensors have become an enabling technology for spatial sensing applications that require real-time, high-density, and accurate three-dimensional point clouds of the surroundings, including fully autonomous vehicles and advanced driver assistance systems (ADAS). LIDAR technology is anticipated to have a double digit annual growth (12%-22%) along the next decade as fully autonomous vehicles become more prominent, making LIDAR a strong candidate to develop a high-volume market.

A conventional LIDAR system comprises of control circuitry, laser beam source, beam steering mirrors and photo-detectors, thus it has huge potential for system miniaturization. The most common type of commercially available LIDAR scanners are motorized optomechanical mirrors, producing a wide field-of-view, a long ranging distance and a fast scanning speed.

A typical commercial 3D-LIDAR sensor for object detection from (Pepperl-Fuschs, 2020b) is shown in figure 0.2. The laser source, polygon scanner, photo-detector and the associated electronics are assembled together to build the sensor. The polygon scanner is an important component of the LIDAR sensor and it consists of a polygon mirror mounted on a motor using an attachment to perform rotary motion as shown in figure 0.2. The dimension of the LIDAR sensor is in the order of 10's of centimeter's and it weighs about 270 g (Pepperl-Fuschs, 2020a).

The large footprint of the LIDAR sensor is attributed to the large size of its components. Hence, to make a light-weight and compact LIDAR sensor, it is necessary that its constituting parts should be miniaturized.

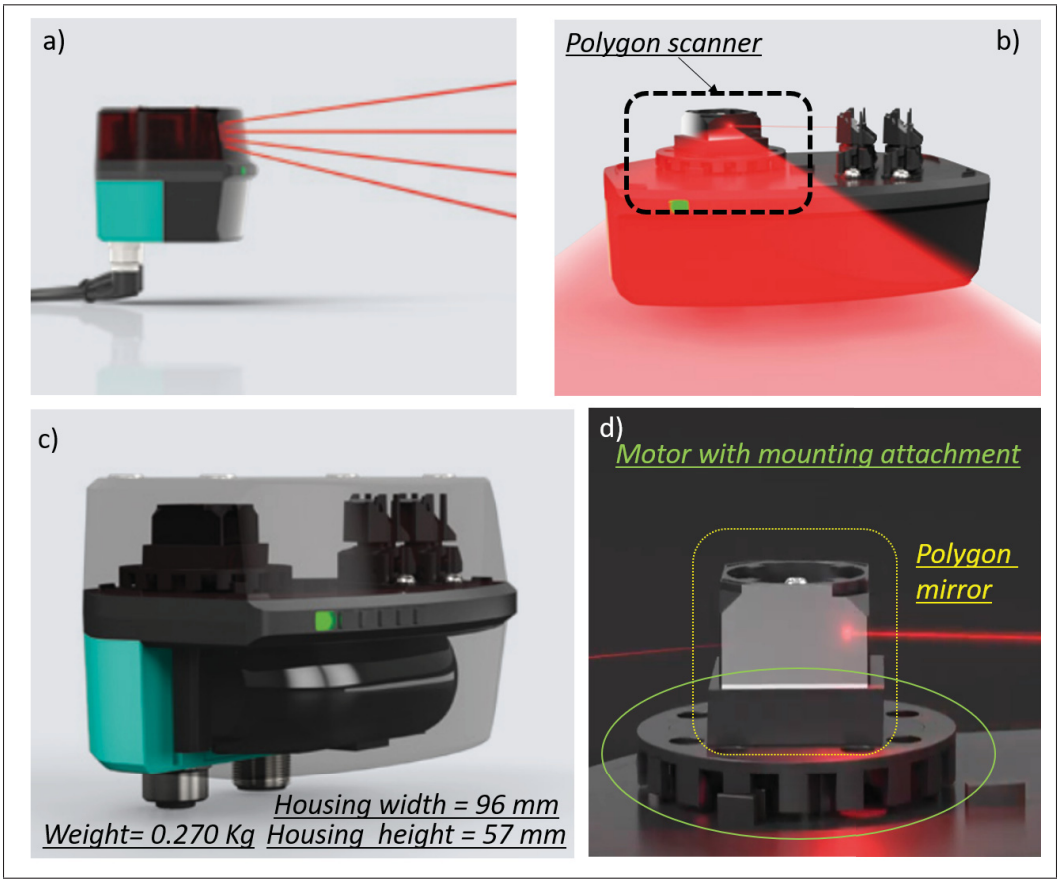

Figure 0.2 a) A LIDAR sensor scanning with a laser beam, b) Polygon scanner inside the LIDAR sensor, c) Weight and dimensions of the LIDAR sensor, d) Polygon scanner having a polygon mirror mounted on a motor.
Taken from Pepperl-Fuschs (2020b)

Many types of LIDAR sensor systems are available in the market, aimed at meeting the end application, but they are bulky, power-hungry and costly. For instance, automotive-grade LIDAR systems are sufficently expensive to have a significant cost impact on the car itself (Warren, 2019), prohibiting its use in consumer products. Accordingly, the cost of a LIDAR system could be reduced by adopting MEMS technologies to leverage the benefits of batch-fabrication

and integration techniques. Various components of the LIDAR could be miniaturized by using silicon as the baseline platform and optimizing the device fabrication and integration techniques to reduce the footprint of the overall system.

The rotational speed of the polygon scanner is an important parameter to determine the scan rate of the scanner. The specifications for the rotational speed of a polygon scanner are unique for each end-application (Oldenburg, Reynolds, Marks & Boppart, 2003; Royo & Ballesta-Garcia, 2019; Marshall, Rynkowski & Ketabchi, 1994) and is presented in table 0.1. Thanks to the linear and precise motion control of rotating motors and multi-facet mirrors, polygon scanners are capable of providing superior and desired performance in terms of scan speed and scan rate for various applications. A high speed motorized scanner can be replaced by a micro-scale polygon scanner that is light-weight, consumes low power and can be fitted within a small volume. Such a micro-scale scanner could greatly improve the performance of resource limited applications such as drones.

Table 0.1 Specifications of a polygon scanner for various applications.

Application	**Scan rate**	**Speed**
Swept source OCT	> 15 kHz	> 9000 rpm
Film recorder	1200 Hz	> 6000 rpm
Automotive LIDAR	1 Hz - 200 Hz	1000-8000 rpm
Laser-leveller	>50 Hz	> 1000 rpm
Airborne Laser scanning	10 Hz - 100 Hz	> 1000 rpm

Thus, the main motivation behind this work is to identify and address the challenges of developing a miniaturized rotary micro-scanner that is capable of providing high speeds and high scan rates. The primary focus of the work is to design and develop such new micro-devices using existing MEMS technologies and to develop a new integration technique for the micro-assembly of a 3D micro-scanner. The aim is to develop a low-cost and miniaturized polygon scanner that can attend the specification of a typical polygon scanner as mentioned in table 0.1. The

applications requiring a micro-rotating beam scanner can benefit from this work due to the attained performance metrics, form-factor and its implementation using a commercial batch fabrication process. Also, the developed integration technique is a general purpose process suitable for assembling other micro-components onto released MEMS structures.

Research Goals

Demand of high performance systems for MRMI application is increasing, requiring small form-factor and energy-efficient systems with a multitude of functionalities to enable their widespread applicability and deployment. The creation of a miniaturized micro-device for optical beam scanning applications utilizing a commercial fabrication process and novel MEMS compatible integration techniques was the overarching goal of this research work.

To ensure the successful implementation of the miniaturized scanner system and attain the research goal, several objectives were established. The objectives are listed below:

1. To identify the technical challenges that need to be addressed for the implementation of the miniaturized scanner system. Specifically, the envisaged system should be able to i) operate at low-power and provide continuous full-rotary motion, ii) address the optical requirements such as smooth and sufficiently large sidewall surface for beam deflection, iii) allow for the micro-components to be fabricated using reliable commercial MEMS processes, iv) require a feasible micro-component integration process without damaging the fabricated micro-rotating platform, and finally, v) ensure that the micro-rotating platform operates at high speed even after the integration of the micro-mirror.
2. To identify the common techniques which have been developed to achieve the goal.
3. To define the concept behind each of the techniques including the advantages and drawbacks related to them.
4. To illustrate the operational principles for the adopted methods, how they will be implemented and any benefits or drawbacks they may impose.

Original Contributions

This research project has led to the following original contributions that are presented in this thesis.

- New architectures of electrostatic side drive micromotors for performance improvement are developed and are reported in chapter 3.
- Several new techniques are developed to reduce friction and increase the speed of the micromotor and are presented in chapter 3.
- High speed rotary electrostatic side drive micromotor using the PolyMUMPS process are implemented, leading to a 60% improvement in speed from the state-of-the-art. The description of the implementation is available in chapter 3.
- A new versatile and simple method of micro-assembly using SU-8 is developed to integrate components onto released MEMS devices. The specifics of the methodology is described in chapter 4.
- The first operational demonstration of a micro-assembled polygonal micro-component onto a working micromotor is reported in chapter 4.
- The design and implementation of the first miniaturized chip-scale rotary micro-scanner. Chapter 5 presents the description of the micro-scanner.

These contributions led to three journal articles (2 published and 1 under review) and one conference paper (Gour, Ménard & Nabki, 2020a; Gour, Nabki & Ménard, 2020b; Gour, Ménard & Nabki, 2021). The journal articles are the basis for chapters 3 to chpater 5 and the conference paper is reported in Appendix III.

Thesis Organization

The thesis is organised as follows. Chapter 1 gives an overview of the competing MEMS scanning technologies relevant to this work. It includes the operating principle of various MEMS

scanner and their fabrication techniques. The state-of-the-art rotary micro-scanners and their applications are also discussed.

Chapter 2 describes the challenges involved in this project along with the solutions developed to address them.

In chapter 3, a description of the high speed micro-motor that will act as a micro-rotary platform is given. It includes the design, optimization, layout, fabrication and experimental verification of the micromotors.

Chapter 4 explains the micro-assembly technique developed to attach a micro-component such as a micro-polygon onto a micro-rotary platform.

Chapter 5 details the design, fabrication and integration of a chip-scale micro-scanner and presents experimental results of the electrical and optical performance of the device.

Finally, chapter 6 concludes the thesis, presenting a summary of the work, outlook of the research project and possible improvements and potential future developments.

CHAPTER 1

OVERVIEW OF POLYGON SCANNERS AND MEMS SCANNERS

1.1 Introduction

Over the past decades, MEMS technology has established itself as a key enabling technology for developing micro-scale devices and systems, and has greatly influenced various fields including motion sensors, MEMS microphones, pressure sensors, magnetometers, and MEMS print heads (Judy, 2001a; Kovacs, Maluf & Petersen, 1998; Bustillo, Howe & Muller, 1998). Hence, it is a compelling choice for implementing miniaturized optical scanning mechanism and systems. In contrast with conventional polygon scanning technology, scanners based on MEMS mirrors offer multi-fold advantages such as small footprint, high scanning frequencies, superior reliability, less wobbling and high volume fabrication at low-cost. However, MEMS scanners do not exhibit a constant scan rate and have a limited scanning angular range, whereas polygon scanners have none of these issues. Thus, the core aim of this thesis is to focus on the implementation of a miniaturized scanner that implements the polygon scanner concept using MEMS technology.

A micromirror capable of translation or rotary motion is the main component of a MEMS scanner, responsible for scanning an optical beam. MEMS micromirrors can be classified into two application groups: analog micromirrors, and on/off or binary micromirrors. Binary micromirrors (i.e. they feature two different positions) are by far the most common since they find applications in display devices and optical switches (Hornbeck, 1993). The digital light processor (DLP) chip from Texas Instrument (Hornbeck, 1993; Monk & Gale, 1995) is an outstanding example of a mature MEMS device.

On the other hand, analog micromirrors can steer light beams in a continuous angular range, and thus are more versatile than digital micromirrors. Consequently, analog micromirrors have received great attention and have been successfully commercialized for barcode reading and mobile projection applications (Microvision, 1998). When functioning as optical scanners, MEMS micromirrors must have one or two dimensional in-plane angular rotations, in order

to redirect light in different directions over a continuous range. However, there are trade-offs between the scan angle range, complexity of the structure and challenges in design and fabrication (Holmström, Baran & Urey, 2014; Zhang, Koppal, Zhang, Zhou, Butler & Xie, 2016).

The implementation of MEMS scanners can be divided into different categories based on three parameters: i) beam steering mechanism, ii) fabrication technology, and iii) actuation principle. Reflective mirrors, refractive lenses, diffraction gratings and phased array mirrors are key beam steering techniques employed in MEMS scanners (Mellette & Ford, 2015; Wang, Zhou, Zhang, Kwon, Blanche, Triesault, sik Yu & Wu, 2019). This work focuses on a MEMS scanner based on optical reflection for beam steering. Actuators based on electrostatic, electromagnetic, piezoelectric, and electrothermal bimorphs are commonly used in MEMS scanners and are fabricated using micromachining processes (Huang, Sai Sarathi Vasan, Doraiswami, Osterman & Pecht, 2012).

Large amounts of literature are available on this subject and hence this review outlines the approaches relevant to the research work presented in this thesis. In this chapter, first, a discussion on macro-scale polygon scanners is presented to introduce this scanner concept. Then, the applications of rotary MEMS scanners are reviewed. The chapter also discusses the different types of MEMS scanner fabrication techniques. Finally, the state-of-art of rotary MEMS scanners is discussed. An explanation of the various operating/actuating principles of MEMS scanners is provided in Appendix I.

1.2 Macroscopic Polygon Scanner

A typical polygon scanner module is shown in figure 1.1 with a polygon mirror having six sides and four sides, respectively. It comprises of a polygon mirror mounted on a driving mechanism with the help of a support bearing. The polygon mirror is made of a polished material such as aluminium or beryllium and lower-cost ones are made using plastic (Kim, Jang, Lee & Lim, 2008a). These mirrors can be of prismatic or pyramidal type with any desirable number of

sides and have footprints on the order of a few centimeters (Kim *et al.*, 2008a). The driving mechanism can either be a brush-less DC motor, a pneumatic drive, or a synchronous motor.

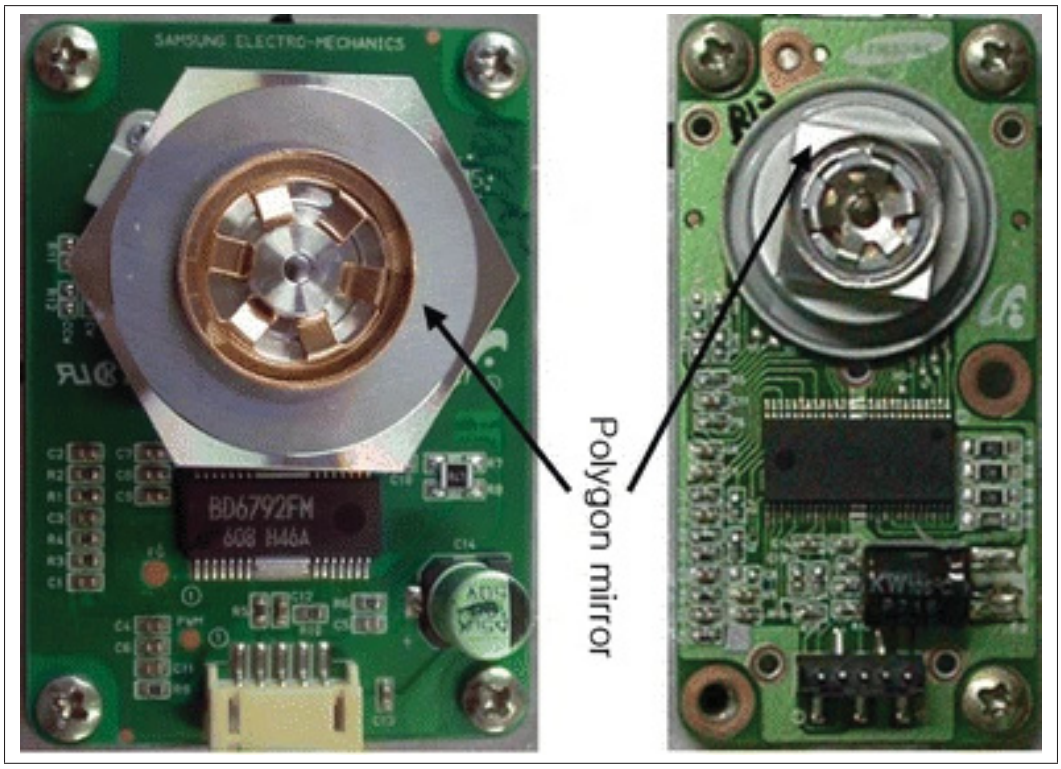

Figure 1.1 Polygon scanner with a mirror with six sides (left image) and a mirror with four sides (right image). Taken from Kim, Jang, Lee & Lim (2008a)

A pneumatic drive is suited only for ultra-high speed operation and is costly. In comparison, synchronous motors are relatively cheaper and have an efficient mode of operation. However, they suffer from phase jitter (also known as hunting) between the rotor and the excitation waveform (You & Yoon, 2019). They also need a specialty circuit such as a sync-detector to lower the drive current and a feedback loop to control the hunting-induced velocity variations. On the contrary, brush-less DC motors are widely used drive systems for polygon scanners since they are low-cost, have a wide range of operating speeds, and do not suffer from hunting issues (You & Yoon, 2019).

Polygon scanners also need a bearing support in addition to the drive system to rotate the polygon mirror. Ball bearings, aerodynamic bearings and aerostatic bearings are the three main bearing supports employed in polygon scanners. The aerodynamic bearing can support speeds up to 100,000 rpm but requires a complex structure and is not suitable for dirty environments (Kaposta & Duma, 2014). Aerostatic bearings are able to deliver superior performances but need a constant supply of pressurized air, which increase system complexity and cost. Ball bearings are the most used bearing support system in polygon scanners. Although these bearings can only support systems with rotational speeds of less than 20,000 rpm, they are much cheaper than the other types of bearings (Gerald F. Marshall, 2012).

Rotary micro-polygon scanners with limited angular rotation are common and used in various applications as discussed in the next section. This thesis addresses the challenge of implementing a miniaturized rotary polygon scanner that can perform high speed 360 degree rotations. For this purpose, all of the components of a typical polygon scanner need to be miniaturized to realize a microsystem that is functionally equivalent to the macro-scopic counterpart.

1.3 Rotary MEMS Scanners: Applications

Today, rotary MEMS scanners are a widely adopted in various fields, including pico-projectors, laser displays, laser scanners and wearable displays (Pengwang, Rabenorosoa, Rakotondrabe & Andreff, 2016; Holmström *et al.*, 2014). The size and shape of a scanning micromirror are important parameters for applications where small footprint, low mass and lower stiffness are required to increase the system performance. Notably, the dimensions of the micromirror should be larger than the laser spot size. For instance, compact rotary scanning micromirrors with typical dimensions in the range of 0.3 μm to 10 mm are required for non-invasive biomedical imaging applications (Pengwang *et al.*, 2016).

Reportedly, OCT systems based on scanning micromirrors offer high sensitivity, better resolution and high scan speed (Strathman, Liu, Keeler, Song, Baran, Xi, Sun, Wang, Li & Lin, 2015). Rotary MEMS mirrors offer the advantage of smaller size, superior performance, and integration

processes, making them attractive for endoscopy and OCT imaging applications (Zhou & Zhang, 2019; Ghazali, Hasan, Rehman, Nafea, Ali & Takahata, 2020). The side and forward imaging endoscopic resolution of OCT is about 2.4 μm and 10 μm respectively, for scanning micromirror systems (Pengwang *et al.*, 2016).

Rotary MEMS mirrors are also used with a variety of semiconductor lasers, such as external-cavity tunable lasers, to tune the wavelength (Pezeshki, Vail, Kubicky, Yoffe, Zou, Heanue, Epp, Rishton, Ton, Faraji, Emanuel, Hong, Sherback, Agrawal, Chipman & Razazan, 2002b; Álvaro Jiménez, Milde, Tatenguem, Honsberg, Carpintero, O'Gorman & Sacher, 2018). A wavelength tuning range of 24.38 nm to 28.38 nm is reported using a rotating a micromirror in dual-wavelength lasers (Cai, Liu, Zhang, Tamil, Tang, Wu & Zhang, 2008). A large mirror with electrostatic actuation provided an angular rotation of 5° for tuning an external cavity laser over a 38 nm wavelength range (Jerman & J., 2002). Tunable laser source operating in the range of 0.4 to 2 μm can be tuned over wide wavelength ranges using a displacement of only about half a wavelength (Liu & Zhang, 2006) and such short cavities are easily feasible using MEMS structures. However, the packaging and integration of MEMS is challenging and may cause optical alignment issues.

The specifications of MEMS scanners for LIDAR application bring both unique limitations and opportunities for rotary MEMS mirror design. A 1D MEMS mirror that is able to perform horizontal scanning can be used to construct a 3D LIDAR by using a large number of photo-detectors and a diffuser lens for vertical scanning (Zhang *et al.*, 2016). For such LIDARs, the horizontal resolution depends on the MEMS mirror scanning frequency and the sampling rate. These LIDAR are limited to short ranges due to the low power spectral density and poor signal-to-noise ratio of the detected signal. Another approach to build a 3D LIDAR using a 1D MEMS mirror is to use an array of laser sources for vertical scanning that can offer better laser power density and high signal-to-noise ratio of the detected signal, but these systems exhibit poor angular resolution (Maksymova, Greiner, Niedermueller & Druml, 2019; Yoo, Druml, Brunner, Schwarzl, Thurner, Hennecke & Schitter, 2018).

Resonant scanning 1D MEMS mirrors with large scanning angles and relatively simple structures are commonly used in MEMS based LIDARs. These scanning MEMS mirrors can offer high resonant frequency, large mirror size and wide angle using different actuation principles. An electrostatic fast scanning MEMS mirror operating at a resonant frequency of 38.5 kHz delivered an angular scanning range of 45° (Hofmann, Janes & Quenzer, 2012). A large MEMS mirror having a diameter of 12 mm used electromagnetic actuation and provided a scanning angle of 26° at a resonant frequency of 1.24 kHz with 250 mA of actuation current for LIDAR applications (Ye, Zhang & You, 2017a).

Resonant scanning MEMS mirrors are required to offer a constant scanning angular range with a fixed phase lag when operating at their resonant frequency (Khoury, Ramanathan, McCloskey, Smith & Campbell, 2016). A high resonance frequency can offer not only fast scanning but higher robustness. However, they are sensitive to their surrounding environment, wear and stress relaxation of the MEMS actuation structure. These factors may induce variations in the stiffness of the MEMS mirror causing a shift in the resonant frequency (Wang, Watkins & Xie, 2020b). Thus, they requires a feedback control and a real-time environment sensing system to adjust the resonant frequency to prevent scanning angle and phase delay variations. Consequently, it increases the dimensions and the cost of LIDAR systems. Moreover, these devices are limited to operate at resonance for optimal performance, which can complexify their use and packaging further.

The issue of scanning angle and phase lag variations due to the surrounding environment can be resolved using non-resonant scanning MEMS mirrors. These mirrors do not require feedback control and are more robust against changes in external conditions. A non-resonant electromagnetic MEMS mirror assembled using a complex mirror integration process delivered an angular scanning range of 20° (Xie, Myo, Chong, Ho, Wee, Premachandran, Wang, herer & Baram, 2010). Whereas, a slow speed non-resonant MEMS mirror based on electro-thermal actuation offered scanning angle of 180 ° (Wu & Xie, 2009).

Unfortunately, LIDAR systems based on MEMS mirrors, resonating or non-resonating, suffer from a limited scanning angle range at high speed, and do not have a constant scanning speed, unlike polygon scanner based LIDARs. Therefore, efforts are required to implement a micro-scanner that can approach the performance level of polygon scanners but have the size and cost advantage that can be achieved with MEMS technology. Thus, the choice of the MEMS technology is crucial for the implementation of the components of the rotary micro-polygon scanner.

1.4 MEMS Scanners: Fabrication Processes

The specifications of a MEMS scanner depend on the system-level design for the required application. These specifications are achieved by designing its various components, namely, a micromirror element, a supporting structure for the micromirror and actuators for moving the micromirror (Huang *et al.*, 2012). All these components are connected to each other and arranged so that a movable micromirror with the desired optical, mechanical and electrical characteristics is obtained. Hence, the characteristics of MEMS micromirrors are highly dependent on the actuation mechanism and the fabrication process. When designing a MEMS scanner, the key issues to consider are the driving voltage, power efficiency, compactness, simplicity of fabrication, robustness and reliability (Urey, Wine & Osborn, 2000).

Different types of MEMS micromirrors can be realized using a combination of surface or bulk micromachining techniques, with dimensions ranging from several micrometers to millimeters (Holmström *et al.*, 2014). The micromirror movement is controlled by the actuator and its design and size depend on the strength of the actuator. It is crucial to understand various actuation mechanisms and fabrication processes to develop a sophisticated scanner. Therefore, in the next sections, the fabrication techniques to build MEMS scanners are presented and a detailled description of the actuation principles of MEMS scanners is provided in Appendix I.

Generally, MEMS fabrication processes can be classified into two broad technologies: surface micromachining and bulk micromachining. Additionally, hybrid fabrication techniques are also

employed to fabricate complex three-dimensional micro-devices. Several commercial fabrication processes such as PolyMUMPs, SOI-MUMPS, SUMMiT-V, Optical iMEMS and IntelliSense technologies were developed to realize different types of MEMS devices (Liu, Zhang, Li & Tan, 2018).

1.4.1 Surface Micromachining and Bulk Micromachining

Surface micromachining involves the addition or removal of thin layers only at the surface of the substrate without processing or penetrating into its surface. On the other hand, material is removed from the substrate itself in the case of bulk micromachining (Judy, 2001b). The ability to add and remove layers of different materials makes surface micromachining easier to integrated with complementary metal–oxide–semiconductor (CMOS) processes, while challenges still remain, and allows a wide range of applications (Qu, 2016).

Figure 1.2 shows various types of micromirrors fabricated using surface-micromachining processes. In figure 1.2(a) a large gap between the mirror plate and the bottom electrode is obtained by releasing the structure after the fabrication process (Toshiyoshi, Piyawattanametha, Cheng-Ta Chan & Wu, 2001b). The micromirror shown in figure 1.2(b) and (c) are fabricated using the commercial PolyMUMPs process, in which multiple layers of polysilicon and silicon dioxide are deposited and patterned (He, Mrad & Chong, 2011; Toshiyoshi *et al.*, 2001b). Also, etch holes are created on each layer to obtain a free-standing structure after the final release process.

Devices with large surface area can be easily fabricated using surface-micromachining processes. However, their thickness is limited to a few microns, resulting in mirror plates having large curvature and small scanning angle (Cao, Liu & Talghader, 2001; Min & Kim, 1999). Moreover, the etch holes on each layer (including the mirror plate) are required to facilitate the release process which degrades the optical performance of the mirror (Tien & Lee, 2006; Jun Zou, Balberg, Byrne, Chang Liu & Brady, 1999).

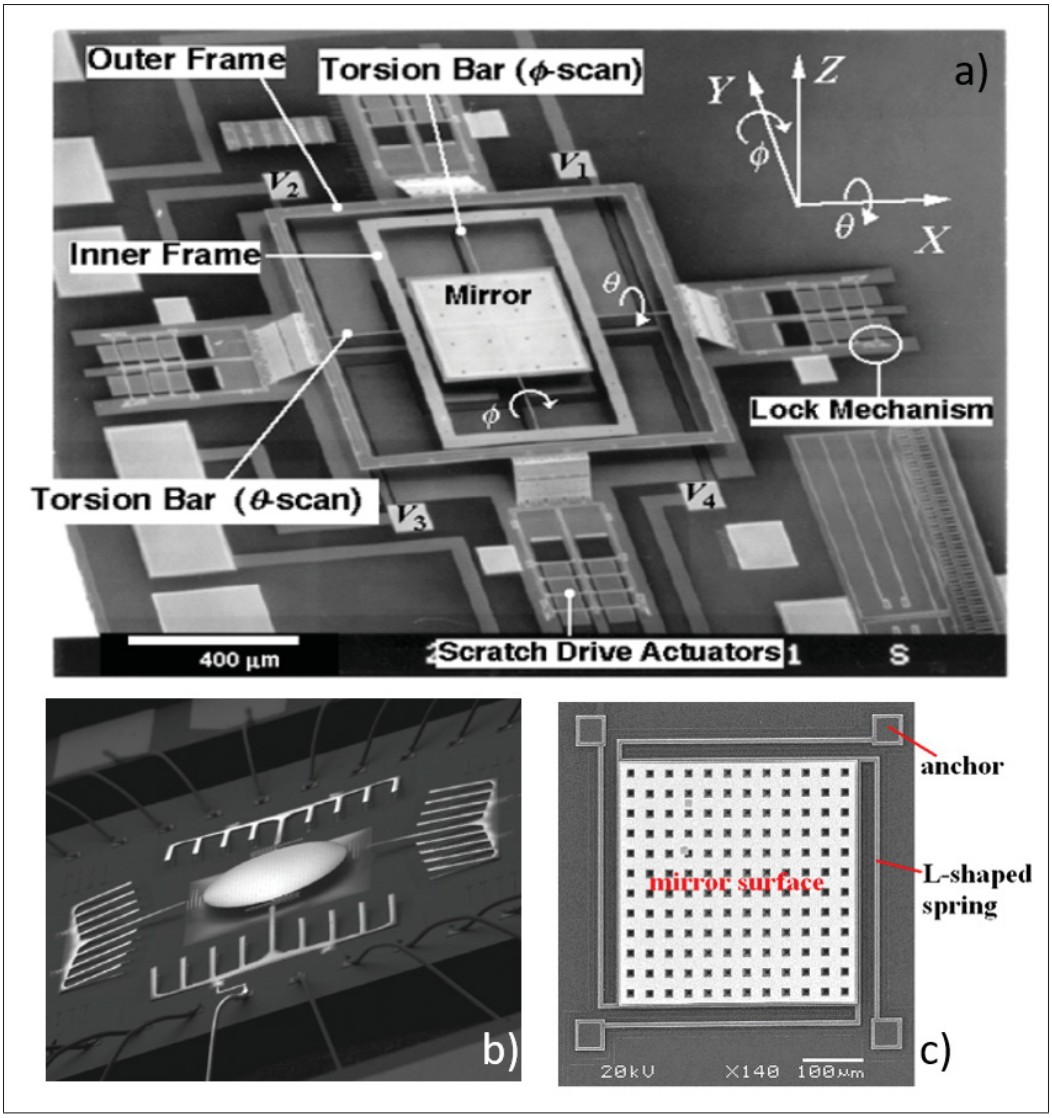

Figure 1.2 MEMS mirror fabricated using surface-micromachining,
a) A 2D-scanner, Taken from Toshiyoshi, Piyawattanametha, Cheng-Ta Chan & Wu (2001b),
b) A circular 2-D micromirror, Adapted from He, Mrad & Chong (2011),
c) Micromirror with L-spring,
Taken from Hu, Yao, Qiu & Ren (2010)

Bulk micromachining employs selective removal of the substrate to obtain a large cavity on the substrate and a thick structure. Figure 1.3 shows a MEMS scanner fabricated using bulk micromachining. In figure 1.3(a) the MEMS scanner is fabricated using bulk-micromachining of a silicon-on-insulator (SOI) wafer and it is actuated using electrostatic comb-drives (Piyawat-

tanametha & Wang, 2010). Similarly, bulk-micromachining of a silicon wafer is performed to fabricate a scanner with an electrostatic torsion micromirror, as shown in figure 1.3(b). This process is well-suited for fabricating structures with large area or mass, that are rugged and can withstand vibration and shock (Zhili Hao, Wingfield, Whitley, Brooks & Hammer, 2003). However, the fabrication technique is not compatible with CMOS processes and can produce only limited geometries.

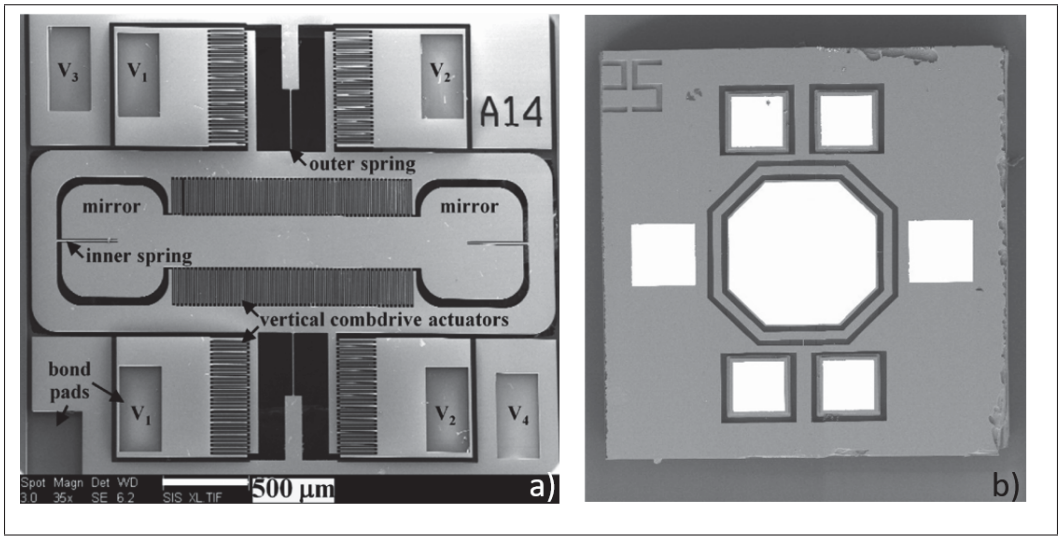

Figure 1.3 MEMS mirror fabricated using bulk-micromachining, a) A 2D-gimbal MEMS scanner Taken from Piyawattanametha & Wang (2010), b) A 2-D micromirror electrostatic torsion micromirror Adapted from Zhili Hao, Wingfield, Whitley, Brooks & Hammer (2003)

1.4.2 Hybrid Fabrication Techniques

Hybrid fabrication techniques consist of a combination of different technologies including bulk/-surface micromachining and are widely adopted to fabricate micromirrors (Yang, Gaines & Nelson, 2003; Koh & Lee, 2012b; Brown, Li, Bauer, Liu & Uttamchandani, 2010). Complex micromirror structures with a high aspect ratio can be realized using bulk micromachining with SOI technology (Bai, Yeow & Wilson, 2010). Various physical parameters of the scanner can be customized using hybrid fabrication techniques to modify the optical properties and actuation force in order to improve its performance. For example, the effective optical area of the scanner

can be increased using a large mirror plate fabricated with a deep reactive ion etching (DRIE) process and assembling it with the actuating element that can be fabricated with a different process (Su, Toshiyoshi & Wu, 2001).

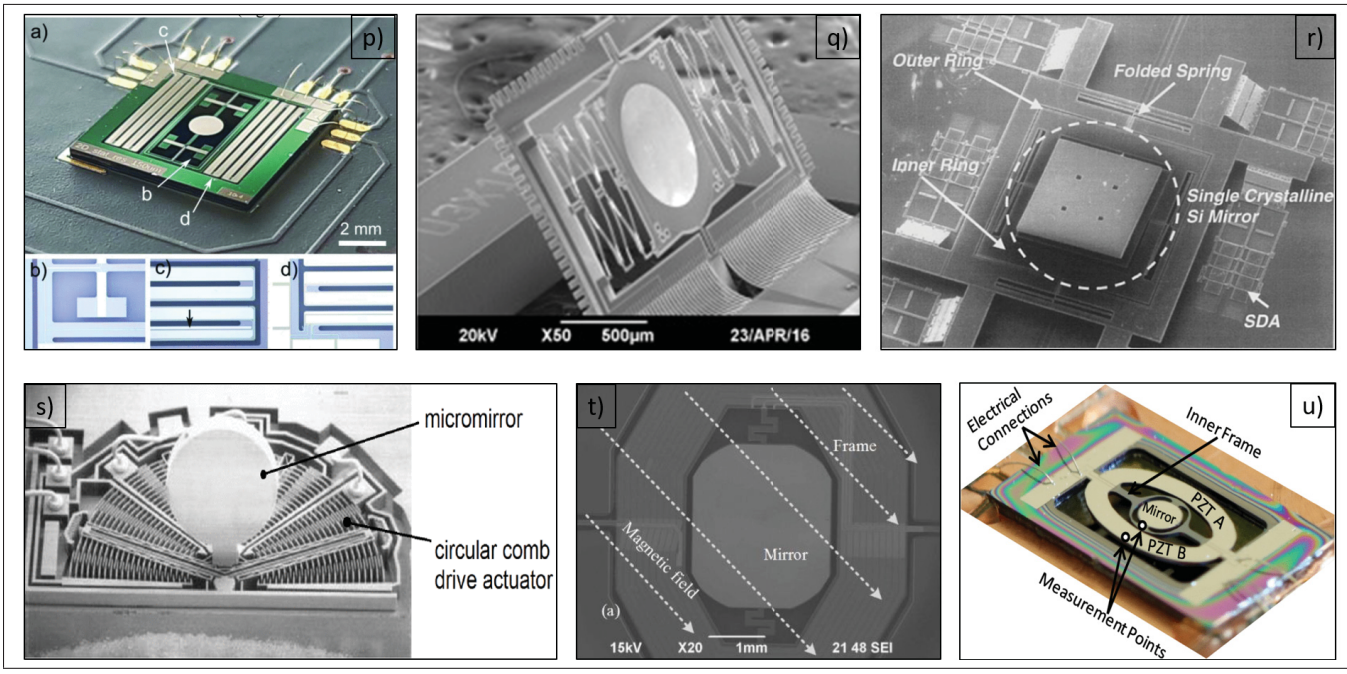

Figure 1.4 MEMS mirror fabricated using hybrid techniques, p) A PCB with a PZT micromirror attached to it Taken from Piot, Pribošek & Moridi (2021), (p)(a) PZT micromirror wire-bonded to the PCB: details marked by white arrows (p)(b) dog-bone structure, (p)(c) meander structure for flexure design. Black arrow pointing the sensing electrode. (p)(d) connection to the wire pads, q) An electro-thermal actuated micromirror fabricated using SOI and bulk micromachining Adapted from Su, Toshiyoshi & Wu (2001), r) A 2D MEMS scanner assembled by bonding a single crystalline mirror to a chip Adapted from Zhili Hao, Wingfield, Whitley, Brooks & Hammer (2003), s) A comb drive micromirror using DRIE process Adapted from Grade & Jerman (2001), t) A electromagnetic micromirror using custom fabrication process Adapted from Jiang, Peng, Liu, Zhou & Su (2019), u) A resonant PZT micromirror wire-bonded to a PCB
Adapted from Baran, Brown, Holmstrom, Balma, Davis, Muralt & Urey (2012)

Figure 1.4, shows various types of MEMS scanners fabricated using hybrid methods. A lead zirconate titanate (PZT) based dual-axis micromirror was fabricated using DRIE on a SOI wafer. The MEMS scanner is wire-bonded to a custom-made printed circuit board (PCB), as presented in figure 1.4(p) (Piot *et al.*, 2021) and figure 1.4(u) (Piot *et al.*, 2021). The PZT material was doped with barium using pulse laser deposition in (Piot *et al.*, 2021), whereas a

mechanical amplification scheme with the PZT actuator is introduced in (Baran *et al.*, 2012). In figure 1.4(s) a comb-drive actuator is fabricated using a DRIE process to rotate a micromirror (Grade & Jerman, 2001). An electrostatic scanner having a single crystalline silicon mirror is shown in figure 1.4(r) and was fabricated using a custom bonding process to minimize the curvature of the micromirror. Similarly, an eletro-thermal actuated micro-mirror (Su *et al.*, 2001) and an electro-magnetic actuated micro-mirror (Baran *et al.*, 2012) are presented in figure 1.4(q) and 1.4(t) respectively. These were fabricated using a custom process involving bulk micromachining and surface micromachining.

1.5 MEMS Scanners: the State-of-the-art

The design of a suitable rotary MEMS scanner depends on the target application and its requirements. Metrics include ease of miniaturization, low power operation and type of motion (Xie, 2018; Lara-Castro, Herrera-Amaya, Escarola-Rosas, Vázquez-Toledo, López-Huerta, Aguilera-Cortés & Herrera-May, 2017).

The MEMS scanner can offer both angular scanning range and linear scanning range according to the type of motion offered by the scanning micromirror. For PZT based scanning micromirrors, the average performance for angular motion and out-of-plane motion are at 12° and 34μm, respectively in (Pengwang *et al.*, 2016). These actuators can perform motion in two axes with the piston motion of the actuator up to 180μm at an operating voltage of 20 V (Smits, Fujimoto & Kleptsyn, 2005). On the other hand, rotary scanning micromirrors based on magnetic actuators offer an average angular motion and out-of-plane motion of about 15° and 80μm respectively in (Pengwang *et al.*, 2016; Werber & Zappe, 2006). In the case of electrostatic actuators, vertical comb actuators can deliver higher angular and transverse motion than linear comb-drive and rotary comb-drive, whereas, magnetic actuators can deliver out-of-plane motion with large forces but with a limited angular range (Bell, Lu, Fleck & Spearing, 2005; Ghazali *et al.*, 2020).

Linear comb electrostatic actuators achieved a maximum rotation range of up to 20° and provided a maximum translation distance of up to 60μm in (Laszczyk, Bargiel, Gorecki, Krężel, Dziuban, Kujawińska, Callet & Frank, 2010; Milanovic, Matus & McCormick, 2004a). The maximum amount of rotational range is about 46° and a maximum piston motion of 500μm was achieved by vertical comb-drives electrostatic actuators in (Wu, Chen, Yan, Yin, Chen, Hao, Xu & Wang, 2007; Sandner, Drabe, Schenk & Kenda, 2009). These actuators have natural frequencies in the range of 150–34,000 Hz and operate at a voltage of 250 V (Pengwang *et al.*, 2016).

Many types of MEMS scanners can be implemented using rotary MEMS mirrors such as resonant and non-resonant scanners. Electromagnetic, electrostatic and piezoelectric are the most common type of actuation principle adopted for realizing each type of MEMS scanner and are discussed in the following section.

1.5.1 Resonant MEMS Scanners

Resonant scanners have demonstrated high performance in terms of scanning speed, compactness and operational power (Urey, 2002; Yalcinkaya, Urey, Brown, Montague & Sprague, 2006; Raboud, Barras, Lo Conte, Fabre, Kilcher, Kechana, Abelé & Kayal, 2010; Baran, Brown, Holmstrom, Balma, Davis, Muralt & Urey, 2012). Most of the cutting-edge resonant scanners operate above 15 kHz (Holmström *et al.*, 2014). Resonant scanners that are capable of 2D scans offer an additional key benefit for various applications such as signal sensing, communication, automotive and aerospace technology (Asada, Matsuki, Minami & Esashi, 1994; Milanovic, Matus & McCormick, 2004c; Koh & Lee, 2012a).

1.5.1.1 Electrostatic Resonant Scanners

A large portion of state-of-the-art resonant scanners use electrostatic actuation due to low power consumption, small size, high actuation speed and relatively simple fabrication (Arslan, Brown, Davis, Holmstrom, Gokce & Urey, 2010; Yoda, Isamoto, Chong, Ito, Murata, Kamisuki, Atobe & Toshiyoshi, 2005). These scanners are frequently used in endoscopy and confocal

microscopy imaging systems. In these scanners, comb-drives are connected to mirror plates capable of providing extreme optical flatness of $\lambda \backslash 10$, high resonant frequency $30.84 - 42kHz$ and wide scanning angles (Cho, Park, Ko, Lee, Kang, Chung, kyoung Choi, Cho, Chang, Lee & Sunu, 2007; Ko, Cho, Mun, Jeong, Choi, Lee, Kim, Yoo & Lee, 2005; Hsu, Klose, Drabe & Schenk, 2008).

Dynamic deformation of the mirror and the stiffness of the structure are key concerns in these scanners. Additionally, they suffer from high voltage requirements as compared to the other MEMS actuated scanners, which limits their applications. To overcome this constraint, Liu and his group in 2010 implemented unstable Lissajous scanning where they achieved a lower frame rate of 2 Hz by exciting the fast axis with 20 V (Liu, Mandella, Loewke, Haeberle, Ra, Piyawattanametha, Solgaard, Kino & Contag, 2010).

1.5.1.2 Electromagnetic Resonant Scanners

Resonant scanners based on electro-magnetic actuation are slow but they can support mirrors with large dimensions operating at relatively low voltages (Raboud *et al.*, 2010; Yalcinkaya *et al.*, 2006). A fast resonant scanner using a moving magnet was reported to operate at 20 kHz with a mirror of 2 X 4 mm^2 and an angular scan range of up to 5° (Reyne, 2002).

A custom-made high-frequency electrocoil along with a NiFe layer deposited on the movable part produced 88° of scan angle along the fast axis and 1.8 ° of scan angle for the slow axis, consuming current in excess of 100 mA (Yalcinkaya, Urey & Holmstrom, 2007). Electro-magnetic actuated scanners are less popular as compared to electro-static scanners for resonant scanning. However, the literature illustrates that implementation of both the techniques depends on the final applications (Holmström *et al.*, 2014).

1.5.1.3 Piezoelelectric Resonant Scanners

The first successful piezoelectric scanners were demonstrated by Smith and his group in 2005, with a reported operating frequency of 17.4 KHz (Milanovic, Matus & McCormick, 2004b).

Researchers continue to progress in this field and make these scanners suitable for use in high frequency devices where electrostatic and electromagnetic resonant scanners cannot be used due to the requirement for operational frequencies over 30 KHz. (Gokce, Holmstrom, Brown, Davis & Urey, 2011; Urey, Holmstrom, Baran, Aksit, Hedili & Eides, 2013; Gu-Stoppel, Janes, Kaden, Quenzer, Hofmann & Benecke, 2013).

Lot of work is done to tackle the issue of limited stroke length in these scanners. In (Baran *et al.*, 2012), the PZT material for actuation is deposited on the moving structure to increase the mechanical coupling and thus enhance the stroke length of the actuator. The PZT actuating electrodes are tailored to enhance the static deflection profile to achieve 54.45° of angular range at 40 kHz (Urey *et al.*, 2013). Another issue with high speed resonant scanners is the dynamic deformation of the mirror and it is one of the most challenging problem in PZT scanners.

1.5.2 Non-Resonant MEMS Scanners

A non-resonant scanner must have a fast retrace time and constant operating speed as found in polygon scanners and galvanometric scanners (Holmström *et al.*, 2014). A typical MEMS scanner consists of torsional flexures, which connect the suspended mirrors to the frame, making it a spring, mass, and a damped system for dynamic characterization. Thus, by default they show a resonant behaviour due to damping while operating under ambient conditions.

MEMS based non-resonant scanners are often required to operate close to the frequency of incoming video rate which is about 60 Hz (Holmström *et al.*, 2014). However, it is challenging to obtain a constant operational frequency. Generally, these scanners are employed for raster scanning in which a low frequency vertical scan, also known as quasi-static scan, is coupled with an orthogonal high frequency horizontal scan.

1.5.2.1 Electrostatic Non-Resonant Scanners

Electrostatic non-resonant scanners require an offset between the static and the moving electrodes to offer quasi-static scanning. Staggered vertical combs (SVC) and angular vertical combs

(AVC) are the two main approaches used in comb drive actuators to facilitate quasi-static scan (Selvakumar, Najafi, Juan & Pang, 1995; Piyawattanametha, Patterson, Hah, Toshiyoshi & Wu, 2005). A mirror of 4 mm in diameter used SVC actuators and enabled 15° of angular scanning at 112 V(Jung, Sandner, Kallweit & Schenk, 2012).

The SVC fabrication process imposes major challenges since the static and the moving electrodes need two different masks, which makes their alignment very strict, and further complicates the overall fabrication process as well (Milanovic, 2004; Conant, Nee, Lau & Muller, 2000). On the other hand, the fabrication complexity is removed in AVC by using a single mask for the definition of static and moving fingers on one layer (Piyawattanametha *et al.*, 2005).

1.5.2.2 Electromagnetic Non-resonant Scanners

Electromagnetic scanners are successfully used in non-resonant MEMS devices. These scanners can provide large rotation of up to ±59° by consuming 250 mA of current (Makishi, Kawai & Esashi, 2009). Electro-magnetic scanners using large mirror have delivered 98% linearity for quasi-static operation up to ±15° at 120 Hz (Jeong, Park, Cho, Hwang, Chang, Kang, Jeong, Kim & Lee, 2008a). However, due to the bulky electromagnetic components, it is difficult to use them in miniaturized devices.

1.5.2.3 Piezoelectric Non-resonant Scanners

Only a few reports are available on non-resonant MEMS scanners based on piezoelectric actuation due to their limited displacements (Holmström *et al.*, 2014). Typically, piezoelectric cantilevers with meandering structures are used to improve the deflection range. An optical scan up to ±15° is reported for a quasi-static scan at 20 V (Tani, Akamatsu, Yasuda & Toshiyoshi, 2007). Linear scanning operation is a challenge in these scanners because cantilevers with meandering type structures have dominant parasitic modes at the low frequencies (Lee, Itoh, Ohashi, Maeda & Suga, 1997).

It can be concluded from the above discussion that rotary MEMS mirrors are capable of enabling compact and low-cost optical systems, but obtaining the wide scanning range along with constant and high scanning speed is a challenge. MEMS scanners that can offer high scanning speeds, large angular ranges and compact size are required for applications such as OCT systems and LIDARs, where polygon scanners are dominant. Thus, the implementation of a MEMS based micro-rotary scanner that can reap all the benefits of MEMS technology along-with the performance characteristics of the polygon scanner is a worthwhile goal.

1.6 Conclusion

In this chapter, an overview of different rotary MEMS scanners leveraging micromirrors is presented. The fabrication techniques involved in realizing MEMS scanners are discussed. State-of-art rotary MEMS scanners along with their applications were presented. From the review, it is concluded that different types of micro-scale rotary devices with limited scanning angle have been implemented using various MEMS technologies. Thus the MEMS technology that consumes less power, provide actuation mechanisms for 360 degree rotation of the micromirror, have a fast response, and a simple fabrication process is a well-suited choice for the implementation of the micro-rotary scanner targeted in this work.

CHAPTER 2

ROTARY 3D MICRO-SCANNER: DESIGN GUIDELINES

2.1 Introduction

In this chapter, the process developed to design a rotary micro-scanner is presented. The design requirements of rotary micro-scanners are discussed. Also, this chapter describes how the rotary platform is realized, how the micro-polyhedron mirror is designed, and how the complete system is assembled. The aim is to shed light on the relationships between the operating mechanism, implementation technology and the design choices.

The design options available for each component of the micro-scanner are strongly coupled with the micro-fabrication technology in which they are implemented. In this work, existing commercial multi-user-multi-project surface micromachining and bulk micromachining technologies are used to implement each component for fast prototyping. The rotary platform is fabricated using the PolyMUMPS surface micromachining process and the micro-polyhedron mirror is fabricated using the PizeoMUMPS bulk micromachining process.

2.2 Chip-scale 3D Rotary Micro-scanner: Architecture

A schematic diagram of the proposed chip-scale rotary scanner is shown in figure 2.1. The scanner comprises two main components: a micromotor to provide a rotary platform, and a multi-sided micro-polyhedron mirror for optical beam steering. The micromotor is fabricated onto a silicon substrate, and the micro-polyhedron mirror is fabricated in a silicon on insulator wafer and transferred to the micromotor die such that it can continuously revolve around the micromotor's axis. The micromotor is able to continuously rotate the 3D micro-polyhedron mirror element by a full 360 degrees. The sidewalls of the micro-polyhedron act as micromirrors and are normal to the substrate in order to deflect the incoming optical beam. The proposed scanner architecture is scalable and a variety of scanning configurations can be implemented.

2.3 Chip-scale 3D Rotary Micro-scanner: Operation

The operation of the micro-scanner is as follows: the input laser beam is incident on the sidewalls of the micro-polyhedron mirror and is then reflected from it, traveling parallel to the substrate away from the micro-chip. The micromirror is rotated from its rest position to repeatedly change the direction of the reflected laser beam to generate a scan line pattern. The function of the micromotor is to continuously rotate the micro-polyhedron mirror at a desired speed to achieve the required scan rate. The electrostatic operation of the micromotor makes it easy to adjust the scan speed of the micro-scanner by changing the excitation frequency of the actuating signal. Changing the number of sides of the micro-polyhedron mirror can modify the angular scanning range and scan-rate of the micro-scanner and it can be achieved by micro-assembling the desired micro-polyhedron with the required number of sides. The extra mass of the assembled micro-polyhedron structure increases the friction between the rotor bushing and the ground plane of the micromotor. Thus, the micromotor should be designed to deliver not only high speed, but sufficient torque to overcome this friction.

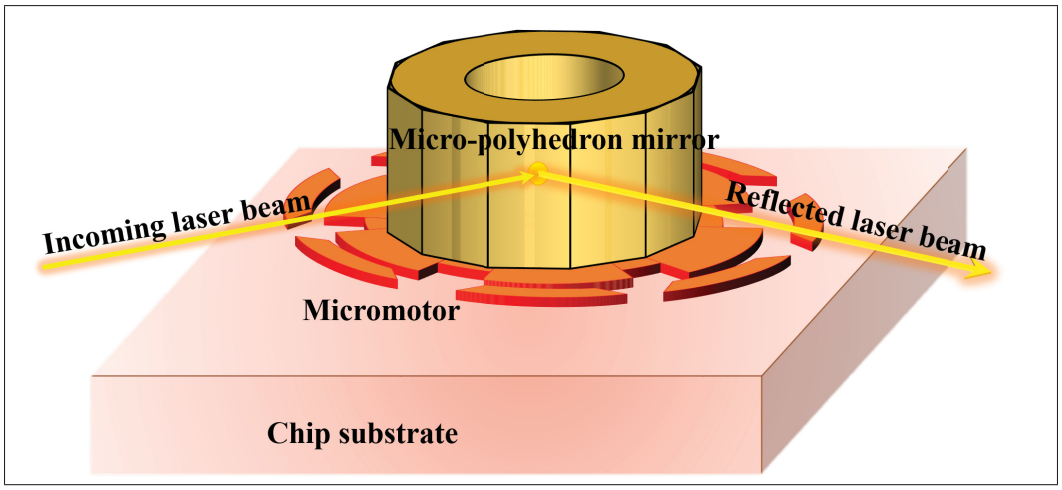

Figure 2.1 Architecture of the chip-scale rotary micro-scanner

2.4 Chip-scale 3D Rotary Micro-scanner: Design

The micro-scanner architecture shown in figure 2.1 should be designed to satisfy the following requirements: i) the micromirror should be free to continuously rotate 360 degrees around its axis at high speed (i.e., >1000 rpm); ii) the rotating speed of the micromirror should be programmable as needed via the control electronics; iii) the surface of the micromirror must have high reflectively and flatness to minimize optical losses; iv) the micromirror plane should be perpendicular to the substrate; iv) the micromirror structure should be rigid and have a high aspect ratio to allow for sufficient surface area to reflect a laser beam; v) the constituting micro-structures should be readily and precisely assembled without hampering the micro-scanner operation; and, vi) the footprint of the micro-scanner components should be sufficiently small to implement a micro-scale device.

The first step towards the miniaturization of the micro-scanner is the creation of a chip-scale rotary platform. Fabrication methods allowing a single-chip solution are desirable. However, monolithic surface micromachining processes are unable to create high aspect ratio 3-D micromirror with a rotary platform. Thus, the method envisioned to realize the 3-D micro-scanner is to employ a hybrid fabrication approach using heterogeneous micro-fabrication processes with a final assembly step. To reduce cost and be suitable to large-scale fabrication, in this work the various components of the micro-scanner are fabricated using commercial micro-machining processes with the exception of the micro-assembly and bonding process, which has been developed as part of this work. Notably, the assembly technique should not induce any damage to the micromotors which are already released from the foundry, and should be accurate enough to integrated the micro-polyhedron onto the micromotor.

The design of the micro-scanner is presented through the implementation of its constituting components, the spatial and functional relationship between them and the post-fabrication assembly technique. In the following sections, a discussion about each of these micro-scanner design challenges is presented.

2.5 Rotary Platform Design

In macro-scale polygon scanners, a DC motor acts as a rotary platform to continuously rotate the mirror for beam scanning. Similarly, for the micro-scanner implementation proposed here, a micro-device is required that can act as a rotary platform to rotate the micro-polyhedron mirror. The micro-device must rotate the micro-polyhedron mirror to perform a complete revolution at high angular speed. A variable capacitance micromotor (VCM) can meet these requirements and is chosen to implement the rotary platform of the micro-scanner.

The VCM is a three-phase device, requires side drive and can be fabricated using the PolyMUMPS process, which is a well-established surface micromachining process. Electrostatic micromotors require high driving voltages, on the order of several tens of volts, but they can potentially reach hundreds of volts. However, these micromotors consume very little power compared to other MEMS actuators, which makes them favorable candidates for low-power applications. Notably, the time constants related to electrostatic actuation are very short, allowing for 3-phase driving of the VCM at relatively high frequencies to operate the structure at elevated rotational speeds reaching a few thousand rotations per minute.

2.5.1 State of-the-art Variable Capacitance Micromotor

Various types of VCM have been designed and fabricated using surface and bulk micromachining (Long-Sheng Fan *et al.*, 1988; Mehregany & Tai, 1991; Mohr *et al.*, 1992; Basha *et al.*, 2007). Depending upon the rotor and stator configuration, the VCM can be of side-drive and top-drive and are shown in figure 2.2. The top-drive VCM suffered from the issue of rotor clamping to the stator due to the presence of non-zero electric field between the top stator and the rotor (Mehregany & Tai, 1991). This issue is resolved in side-drive micromotors by grounding the rotor using bushing (Mohr *et al.*, 1992). The tangential force between the rotor and the stator is the acting force in the ordinary side-drive VCM, whereas in harmonic side-drive VCM the acting force is the normal force. The harmonic side-drive VCM are also known as wobble micromotors due to the wobbling motion of the rotor and has the advantage of obtaining higher

torque by increasing the motor gear ratio (Mehregany, Bart, Tavrow, Lang & Senturia, 1990; Mehregany, Senturia & Lang, 1992). However the wobbling motion of the rotor is drawback for many application.

The VCM with large dimensions having poles with height of 200 μm and the gap of 17 μm between the poles are fabricated using deep reactive ion etching and offered maximum speed upto 300 rpm (Yasseen, Mitchell, Smith & Mehregany, 1999c; Azzam Yasseen, Mitchell, Klemic, Smith & Mehregany, 1999). Side-drive micromotors that can be used in harsh environment are

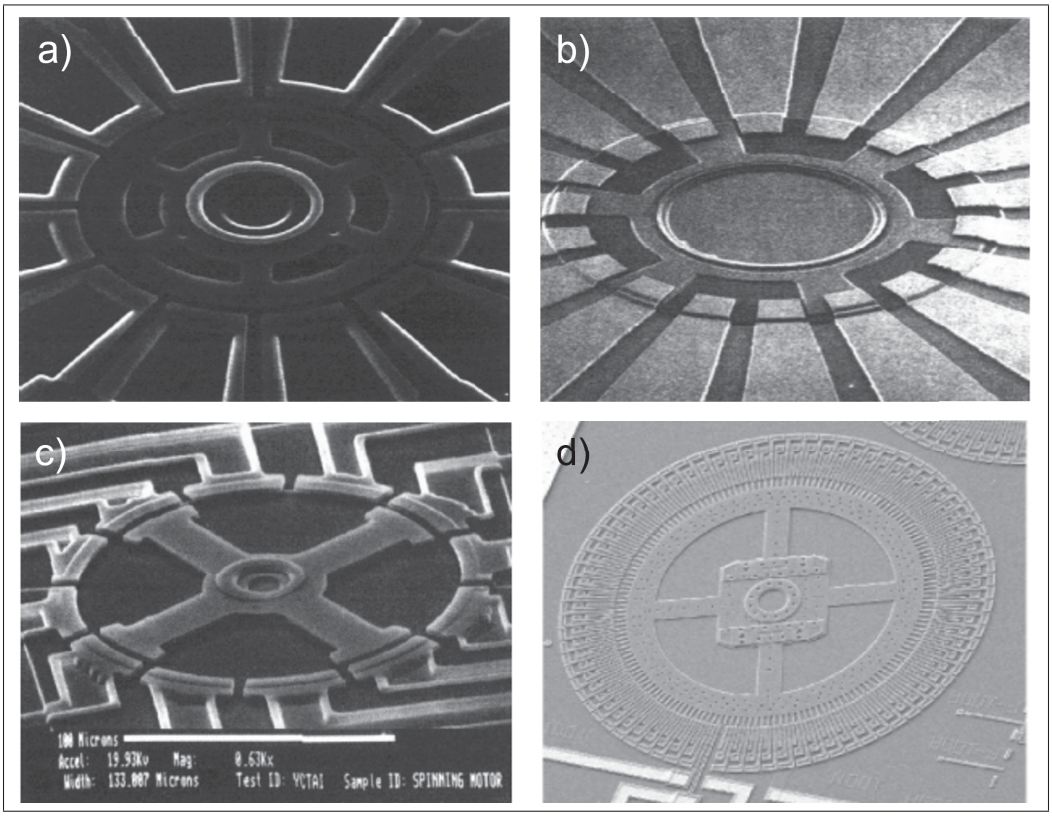

Figure 2.2 SEM images of various types of VCM,
a) A harmonic side-drive type VCM, Taken from Long-Sheng Fan, Yu-Chong Tai & Muller (1988),
b) A top-drive type VCM, Adapted from Mehregany & Tai (1991),
c) A side-drive type VCM,
Taken from Mohr, Bley, Stohrmann & Wallrabe (1992)
d) A side-drive type VCM fabricated using PolyMUMPS process,
Taken from Basha, Safavi-Naeini & Chaudhuri (2007)

fabricated using surface micromachining with silicon carbide as structural material but were able to operate at the speed of 37-317 rpm (Yasseen, Wu, Zorman & Mehregany, 1999a, 2000).

The PolyMUMPS process offers a three-layer polysilicon surface micromachining to fabricate various components of a VCM and allows to produce a gap of upto 2 μm between the rotor and stator poles (Cowen, Hardy, Mahadevan & Wilcenski, 2011). A VCM with large number of rotor and stator poles is fabricated using PolyMUMPS process as shown in figure 2.2(d). The VCM is able to operate at 16 V and rotated at the speed of 1.25 rpm (Basha, Safavi-Naeini & Chaudhuri, 2007b). The low voltage operation is beneficial for integrating it with a CMOS driving circuit but the slow speed of the micromotor is a major drawback for various applications. New VCM architecture can be explored to improve speed and can be easily realized using PolyMUMPS process for reliable and stable device fabrication.

2.5.2 Micromotor Architecture

A schematic showing different parts of the VCM is presented in figure 2.3. It consists of a rotor, stator poles and a central pin bearing (CPB). The stator poles are stationary, arranged in a circular manner around the rotor and a 3-phase excitation signal is applied to them. The rotor, supported by dimples, is the moving part, placed at a distance (or gap) from the stator to perform the free rotation. There is also a gap between the rotor and the support post or the CPB, so that the rotor can freely revolve around the CPB. The extended arcs at regular intervals on the rotor circumference are the rotor poles and are connected to the ground through the CPB or the dimples during the operation of the VCM. The micromotor has a complex device architecture due to the presence of many geometrical parameters. Therefore, the design parameters for the micromotor are the physical dimensions of its various parts as illustrated in figure 2.3. The definition of each parameter is given in table 2.1. The performance of the micromotor is strongly coupled to the optimization of these parameters to obtain maximum generated torque and high speed operation. Different VCM architectures can be obtained by changing the rotor-stator configuration and a detailed description is available in chapter 3.

2.5.3 Micromotor Operation

The geometry of the micromotor is such that the stator poles and the rotor poles are never perfectly aligned and a capacitance exists between the rotor poles and stator poles. The variation in this capacitance is responsible for the operation of the micromotor, through the electrostatic force stemming from the 3-phase electrical excitation. When the rotor is grounded and a 3-phase electric potential is applied to the stator poles, an electrostatic field is generated in the gap between the rotor poles and the stator poles. This produces electrostatic forces that produce torque and move the rotor. Accordingly, the initial alignment between the the rotor pole and the stator pole gets altered and the capacitance between the rotor pole and the stator pole varies due to the change in the overlap area between the poles. The generated motive torque (T) is proportional to the rate of change of this capacitance and is given by the following equation (Ghalichechian, Modafe, Beyaz & Ghodssi, 2008b):

$$T(V,\phi) = \frac{N_s V^2}{2q}\left(\frac{\partial C(\phi)}{\partial(\phi)}\right) \tag{2.1}$$

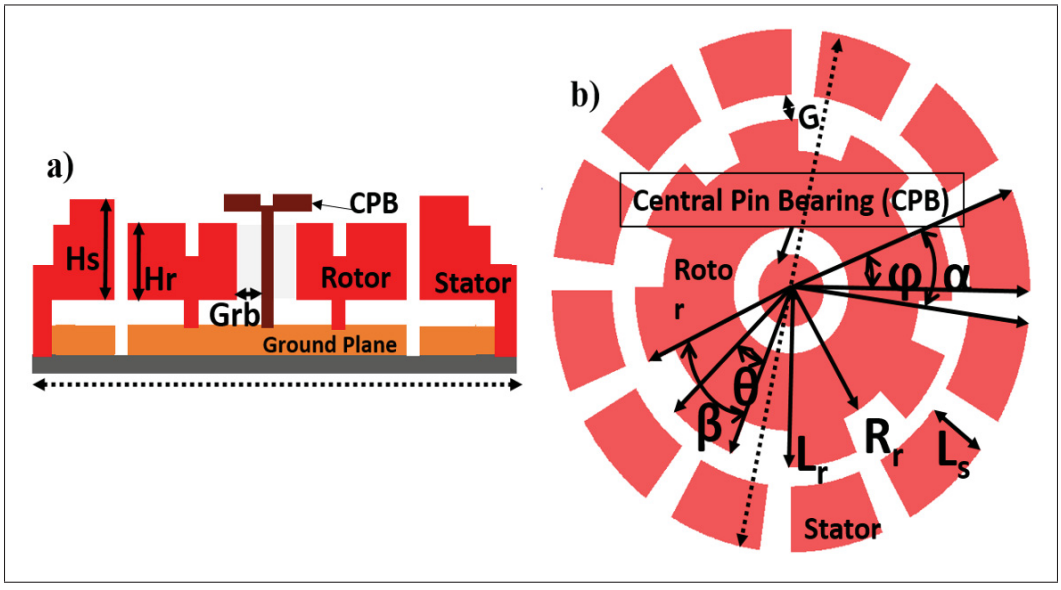

Figure 2.3 Different parts of a variable capacitance micromotor, a) side view, and b) top view

Table 2.1 Key Geometrical Parameters of the Variable Capacitance Micromotor

Micromotor geometrical parameter	**Notation**
Gap between rotor and stator	G
Radius of the micromotor rotor	R_r
Number of phase	q
Number of stators	N_s
Number of rotors	N_r
Rotor teeth angle/width	θ
Stator teeth angle/width	α
Rotor pitch	β
Stator pitch	ϕ
Gap between rotor and central pin bearing	G_{rb}
Thickness of the rotor	H_r
Thickness of the stator	H_s
Length of the rotor tooth	L_r
Length of the stator tooth	L_s

where C (ϕ) is the capacitance of a single rotor-stator pair, V is applied voltage to the stator pole, q is the number of phase, and N_s is the number of electrodes on the stator.

2.5.4 Micro-motor Design

The purpose of the micromotor is to provide a rotary base on which the micromirror could be placed and rotated at high speed. The micromotor parameters should be optimized to meet the following design requirements to enable a success-full scanning operation: i) the size of the rotary platform (that is the rotor of the micromotor) should be large enough to facilitate assembly on the reflecting element above it; ii) the micromotor should be designed to generate sufficient torque so that the rotor with assembled micromirror can start its rotation easily, overcoming

the associated friction and initial inertia; iii) the micromotor should be able to operate at high excitation frequencies in order to provide high rotational speed (i.e., >1000 rpm); iv) the excitation voltage for the operation of the should lie within the limits of dielectric breakdown of the air between the stator-rotor gap; and, v) the micromotor should be fabricated using a commercial micromachining fabrication process to reduce its implementation cost and allow for batch fabrication.

An improved micromotor design for generating high driving torques requires the optimization of various geometrical parameters. It is essential to generate a maximum average torque with minimum torque ripples, and this can be achieved by carefully choosing the ratio of total number of rotor poles to the total number of stator poles (Endemaño, Fourniols, Camon, Marchese, Muratet, Bony, Dunnigan, Desmulliez & Overton, 2003). In this work, this ratio is fixed to 2:3 due to its superior performance and, further design improvements are chosen accordingly, as described in chapter 3. Moreover, the choice of the design parameters are also affected by the micro-fabrication process, in this case the PolyMUMPS process.

The driving torque requirement of the micromotor increases when an extra micro-structure in the form of a micromirror is added on the top of the rotor. This is due to the increase in friction between the rotor bushing and the substrate. Consequently, the driving voltage required to rotate the micromotor also increases, pushing it to the limits of the breakdown voltage in the air gap between the rotor and the stator. Accordingly, several methods to increase the generated torque are investigated in this work, in order to decrease the required driving voltage to start the micro-scanner rotation with the load of the micro-polyhedron on the VCM. A thorough detail on the micromotor design to improve the speed and the torque is presented in Chapter 3. Note that as outlined in chapter 5, a reduction in mass of the micro-polyhedron mirror also helps reducing the required actuation voltage to start the motor.

2.6 Design and Fabrication of the Micro-polyhedron Mirror

The operation of the micro-scanner depends on the design of the micro-polyhedron mirror that has to meet the requirements of the proposed architecture. Investigation of several micromirror designs must be performed to achieve this goal. The micromirror for optical scanning requires a thick structure and high flatness. Accordingly in this work, it is fabricated using bulk micromachining of a silicon on insulator (SOI) wafer.

Moreover, the structure of the micromirror should be as rigid as possible to avoid bending and therefore should have thick sidewalls. However, the mass of such a rigid micromirror would be large. Since a VCM can provide only a finite amount of torque, a micromirror with a higher mass will adversely affect the operation of the micro-scanner. As such, with a massive micromirror, the system's switching time will increase or it will not be able to start its rotation. Thus, it is desired to investigate the driving capabilities of the micromotor in order to decide the sustainable dimensions and mass of the micromirror structure. This is detailed in chapter 3.

2.7 Assembly Process Requirements

The process of assembling the micro-scanner requires the integration of the VCM and the micro-polyhedron mirror. First, a bonding mechanism needs to be developed to bond the micromirror onto the rotor of the VCM. The bonding process should be convenient so that it can be easily applied on the fabricated and released VCM without introducing any anomalies that can compromise the micro-scanner operation. In addition, a method to place and align the micromirror accurately onto the rotor must be explored such that the rotor can freely move after attaching the micromirror. The small size of the micromirror makes it challenging to perform the assembly process. The bulk micromachining-fabricated micromirror goes through the following micro-assembly steps to integrate with the VCM:

1. The micromirror is detached from the substrate.
2. The micromirror is grasped with a microgripper.
3. The micromirror is translated and rotated to a specific position.

4. The bonding material is applied to the micromirror.
5. The micromirror with the adhesive layer is aligned at the desired location over the rotor.
6. The micromirror with the adhesive layer is placed onto the VCM's rotor.
7. The micromirror is released and bonded to the rotor.

The alignment and bonding procedure must be highly accurate and precise as the fabricated VCM is released and can rotate freely during assembly. A detailed description of the integration method is given in Chapter 4 and is used to assemble a micro-polyhedron mirror on to the VCM. The realized rotary micro-polygon scanner is presented in Chapter 5.

2.8 Conclusion

The challenges face by the proposed micro-scanner design and the requirement for its implementation were discussed in this chapter. The micro-scanner is a highly miniaturized version of a macro-scale polygon scanner, and it is operationally required to mimic the behaviour of such a scanner. These specifications require a micromotor as the rotary base that can support a micro-polyhedron mirror. The design requirements of the rotary platform using a VCM were introduced such that it can rotate at high speed after bonding the micromirror. In addition, the challenge of bonding and aligning the micromirror onto the released VCM for the micro-scanner assembly were introduced. The solutions to mitigate the challenges presented in this chapter are addressed in the next three chapters.

CHAPTER 3

LOW-FRICTION, HIGH-SPEED ROTARY 3-PHASE MICROMOTOR USING THE POLYMUMPS PROCESS

Amit Gour[1] , Michael Ménard[2] , Frederic Nabki[1]

[1] Departement of Electrical Engineering, École de Technologie Supérieure,
1100 Notre-Dame Ouest, Montréal, Québec, Canada H3C 1K3

[2] Department of Computer Science, Universite du Quebec a Montreal,
201 President-Kennedy Avenue, Montréal, Québec, Canada H2L 2C4

Paper published in IEEE Journal of Micro-electro-mechanical Systems, May 2020.

Preface

In the following chapter, a brief literature review of different types of rotary micromotors is presented. Each reviewed work is then investigated to determine the advantages and drawbacks in respect of size, speed and ease of fabrication. A variable capacitance micromotor (VCM) that offers micro-scale footprint, high speed operation and reliable fabrication process is presented. A literature review for the different types of VCM along with fabrication techniques and design challenges is introduced.

Finally, new architectures of VCM are proposed to improve the driving torque, reduce friction and increase the rotational speed. The variants of the VCM are fabricated using PolyMUMPS process and are characterized using a three-phase square wave excitation. The experimental results are discussed and the fastest VCM is able to rotate at the speed of 7875 rpm.

The envisioned micro-polygon scanner requires a rotary platform that can hold a micro-polyhedron mirror and operate at high speed. The VCMs presented in this chapter have very low footprint, high speed, high torque and are easy to fabricate, meeting the criteria of the required rotary platform.

3.1 Abstract

We present the design and fabrication of an electrostatic side-drive micromotor that achieves the fastest operating speed reported for a device fabricated using the PolyMUMPS process. High-speed is obtained by optimizing the geometric parameters of the rotor and the stator electrodes, employing techniques to reduce friction in various regions of the micromotor and adopting multiple approaches to enhance the driving torque of the micromotor. The key geometrical parameters of the micromotor are determined through analytical modelling, bypassing intensive computational methods. The rotor diameter of the micromotor is 600 μm and has only 12 circular bearing supports each having radius of 3 μm. The rotary micromotor exhibits a speed of up to 7,875 rpm.

Keywords—Electrostatic micromotor, micro-electromechanical- systems, PolyMUMPS, variable capacitance micromotor

3.2 Introduction

MICROELECTROMECHANICAL systems (MEMS) are enabling the development of miniaturized sensors and actuators for a wide range of applications such as microfluidics, micro-optics, and microsensors. MEMS are realized using batch microfabrication, or micromachining, which rely on techniques like those used to fabricate integrated circuits, allowing the co-integration of electronic and micromechanical devices on chips. MEMS rotary electrical machines, such as micromotors, micro-turbomachinery and micro-generators, are capable of energy conversion between the electrical and mechanical domains. High speed rotary micromotors can be used as a robust platform for developing microsystems required for drug-delivery (Laser & Santiago, 2004), fuel-delivery (Ahn & Allen, 1995) and vacuum applications (Laser & Santiago, 2004; Barbic, Mock, Gray & Schultz, 2001). Micromotors are also employed in optical switches (Alladi, Nagy & Gaverick, 1999)), scanners (Azzam Yasseen, Smith, Merat & Mehregany, 1999; Yasseen, Smith, Mehregany & Merat, 1995) endoscopes (Wang Xinli, Cui Shumei & Cheng Shukang, 2002), microsurgery (Polla, Erdman, Peichel, Rizq, Gao & Markus, 2000), MEMS

gyroscopes (Han, Liu, Wang & Ma, 2012; Kraft & Damrongsak, 2010), and micro-assembly (Fatikow, Falzullin & Seyfried, 2000), thanks to their precise and fast step movement.

Presently, various kinds of micromotors, such as electromagnetic (Büttgenbach, 2014), electrostatic (Bollée, 1969), resonant (Pisano, 1989), and ultrasonic (Moroney, White & Howe, 1989) have been demonstrated. Electromagnetic micromotors have a low operating voltage, large forces and are resistant to harsh conditions. High speed operation up-to 7,000 rpm (Büttgenbach, 2014) can be readily attained with these micromotors, but the high current density needed causes significant heat dissipation and thus appropriate cooling measures are required. Ultrasonic micromotors also operate at low voltages and have simple bearing-less designs. They can operate at speeds exceeding 9,000 rpm (Shilton, Langelier, Friend & Yeo, 2012) but their fabrication is complex. Moreover, these micromotors have a significant footprint due to their large stator and rotor (with diameters between 1.0 mm - 1.5 mm). Alternatively, the electrostatic variable capacitance micromotor (VCM) offers excellent scalability and higher speed (Zhang, Meng & Li, 2005) in comparison to the other types of micromotors. VCMs are well suited for applications such as microsensors and data storage. Additionally, heat dissipation is not an issue in VCMs, and they do not require thermal management since they operate with very low current density. Conventional surface micromachining techniques with polysilicon acting as the structural layer can be used to implement a VCM, enabling a micro-scale footprint. Thus, VCMs can be easily integrated within a chip, and enable a high degree of miniaturization.

Attempts have been made to improve the performance of VCMs in order to reap the benefits of scalability and batch fabrication. The first operational electrostatic VCM was demonstrated in (Long-Sheng Fan *et al.*, 1988; Tai, Fan & Muller, 1989) and had a driving voltage of more than 100 V and a rotor diameter of 60 μm. The micromotor was fabricated using an in-house process and exhibited a maximum rotational speed of 500 rpm in ambient atmospheric conditions with an actuation voltage of 350 V. Later work in (Megregany, Nagarkar, Senturia & Lang, 1990) reported rotational speeds for small micromotors of up to 15,000 rpm at 150 V with a 1 kHz excitation signal in a nitrogen environment. Large VCMs with rotors of 1,200 μm in diameter were reported in (Megregany *et al.*, 1990) with a rotational speed of more than 7,000

rpm at an operating voltage in the range of 35 V to 100 V in ambient conditions. Custom in-house polysilicon surface micromachining processes were used for the fabrication of these micromotors. Repeatability and reliability can be limited for these specially developed processes. These issues can be minimized by using a mature and reliable commercial fabrication process such as the PolyMUMPS process from MEMSCAP. For instance, the VCM reported in (Basha *et al.*, 2007) operated at 16 V with a low rotation speed of 42 rpm. It was fabricated using the PolyMUMPS process and had the following physical dimensions: the rotor diameter was 800 μm and the rotor-stator gap was 2.25 μm with a 70 μm bearing diameter. The highest reported rotational speed of the micromotor was 1,250 rpm at 70 V, but achieving this rotational speed required the assembly of additional micro-parts. From a commercialization standpoint, a VCM fabricated using only the PolyMUMPS process would result in higher level of integration with other MEMS, as the process has been widely used by academia, industry and government institutions worldwide for various applications. However, the slow rotation speed operation of VCMs previously proposed in PolyMUMPS limits their scope of application. This limitation is addressed here.

A typical VCM consists of a rotor, stators, a central pin bearing (CPB) or hub acting as the rotational axis and a bushing support for the rotor. The frictional forces between the CPB and the rotor, and between the bushings and the substrate, result in wear, fracture, and stiction. Efforts were made to minimize friction by using electromagnetic levitation (Shearwood, Ho, Williams & Gong, 2000), electric bearing (Han, Wang, Wu & Liu, 2011), gas-lubricated bearings (Chee Wei Wong, Xin Zhang, Jacobson & Epstein, 2004; Frechette, Jacobson, Breuer, Ehrich, Ghodssi, Khanna, Chee Wei Wong, Xin Zhang, Schmidt & Epstein, 2005) and microball-bearing technology (Ta-Wei Lin, Modafe, Shapiro & Ghodssi, 2004; Ghalichechian *et al.*, 2008b). The gas-lubricated bearing micromotor requires complex control schemes for stable operation and uses a stack of bonded wafers for fabrication. Moreover, fabrication of a micromotor with microball bearing requires the use of a separate silicon wafer for the rotor and stator with engraved grooves to support the micro-balls. The rotor diameter of these micromotors lies in the range of 4.2 mm to 7.0 mm, creating a large footprint compared to the VCMs fabricated using

surface micromachined processes. The fabrication process is complex and far from monolithic integration, requiring assembly of different micro-parts. Additionally, the drawback of such large footprint designs is the limited miniaturization they enabled and their increased production cost, minimizing the benefits of MEMS batch fabrication.

The PolyMUMPS process is a mature surface micromachining process that was introduced in 1993 and is adopted to fabricate the CPB based VCM presented in this work. Hall-effect sensors, RF switches, microwave MEMS devices, thermal actuators are only a few examples of devices fabricated using the PolyMUMPS process (Cai, Chan & Garmire, 2011; Mansour, Bakri-Kassem, Daneshmand & Messiha, 2003; Dec & Suyama, 2000; Varona, Tecpoyotl-Torres & Hamoui, 2009). It is an attractive low-cost alternative to in-house processes and is a standard MEMS device fabrication process offering high throughput, low-cost, fast prototyping and high reliability. Currently, to the best knowledge of the authors, the fastest VCM fabricated using the unaltered PolyMUMPS process achieved a maximal rotational speed of 42 rpm in atmospheric condition and has a low operating voltage of 16 V (Basha *et al.*, 2007). The low driving voltage makes it possible to integrate the micromotor with the CMOS driving circuit but because of its low speed it can be used only for limited applications.

In this work, the fastest micromotor fabricated using the PolyMUMPS process reported to date is demonstrated by implementing new micromotor architectures and by mitigating the friction causing elements of the micromotor. Various parameters of the micromotor are engineered to reduce friction and enhance motive torque to maximize speed. The various parameters of the micromotor were optimized analytically rather than using intensive computational techniques. CPB and bearing supports have been tailored to reduce friction and to achieve a speed of 7,875 rpm.

The article is structured as follows. Section 3.3 describes the design of the micromotor, section 3.4 presents the experimental results, and section 3.5 concludes the work.

3.3 Micromotor Design

The geometry of a VCM has a significant impact on its operation (Bollée, 1969; Trimmer & Gabriel, 1987a). The rotor-stator gap is one of the key parameters that controls the amount of driving torque generated during the operation of the micromotor and it should be as small as possible (Zhang *et al.*, 2005). The rotor-stator thickness, rotor diameter, rotor teeth angle, stator teeth angle, ratio between the number of rotors and the number of stators also affect the torque generated by the motor. Moreover, the bearing radius and the bearing clearance play important roles in the operation of the micromotor (Zhang *et al.*, 2005). The electro-mechanical coupling in the micromotor, along with its complex architecture, make it challenging to optimize the design. Computational tools providing multi-physics solution can be used for maximizing the driving torque but are not capable of optimizing the complete micromotor architecture. Additionally, micromotor optimization using finite element analysis (FEA) is computationally intensive due to the presence of many variables (Trimmer & Gabriel, 1987b; Maseeh, Harris & Senturia, 1990; Crary & Zhang, 1990; Beerschwinger, Milne, Yang, Reuben, Sangster & Ziad, 1994; Wiak, Di Barba & Savini, 1995; Milne, Yang, Sangster, Ziad & Spirkovitch, 1993; Sangster & Samper, 1997).

Generally, a stator-rotor pair of the micromotor is modelled as a parallel plate capacitor to approximate the electrostatic force responsible for generating torque with specific geometrical parameters (Bollée, 1969; Trimmer & Gabriel, 1987a; Endemaño *et al.*, 2003). A single stator-rotor pair of the micromotor and its associated geometrical parameters are optimized using FEA (Wiak *et al.*, 1995; Milne *et al.*, 1993; Sangster & Samper, 1997), (Dufour, Sarraute & Abbas, 1996b). The optimization of the micromotor using FEA does not present a complete picture of the micromotor performance but it gives an approximate solution (Dufour *et al.*, 1996b). Therefore, a mixture of FEA analysis and analytical models are required in order to achieve a valid design prior to fabrication.

3.3.1 Design Methodology

The micromotor reported in this work is a three-phase side-drive rotary variable-capacitance machine with in-built rotor bearing support. The operation of a VCM is based on the electrostatic torque generated by applying a voltage between the stator pole and the rotor pole. The driving torque is generated when the rotor pole aligns with the activated stator poles to minimize the field energy (Fan, Tai & Muller, 1989). A continuous motion of the rotor is obtained by sequential excitation of the stator electrodes with positive square pulses in a three phase configuration (e.g., P, Q, and R) where each phase is 120◦ apart. The detailed operation of VCMs is reported elsewhere (Megregany *et al.*, 1990). The torque of the micromotor as a function of applied voltage (V) and the angular position (ϕ) of the rotor is given by (Ghalichechian *et al.*, 2008b):

$$T(V,\phi) = \frac{N_e V^2}{12}\left(\frac{\partial C_1(\phi)}{\partial(\phi)} + \frac{\partial C_2(\phi)}{\partial(\phi)} + \frac{\partial C_3(\phi)}{\partial(\phi)}\right) \tag{3.1}$$

where C (ϕ) is the capacitance of a single rotor-stator pair and N_e is the number of electrodes on the rotor.

The generated torque is proportional to the rate of change of the capacitance with respect to the angle. Since the capacitance is in effect modulated as the angle is changing, its nominal value has a significant impact on the torque of the micromotor. Thus, increasing or decreasing the capacitance value (C (ϕ)) of the rotor-stator will effectively increase or decrease the constant coefficient present in the capacitance rate of change in equation 3.1. This will in turn increase or decrease the generated torque. As such, ultimately, the rate of change of the capacitance is proportional to the nominal capacitance value.

The typical layout of a micromotor is shown in Figure 3.1, along with its key parameters. The mechanical contact of the rotor with the CPB or the bushing supports provides the electrical contact between the rotor and the ground plane positioned beneath it (Behjat & Vahedi, 2006). The rotor teeth angle/rotor width ratio (θ), stator teeth angle/stator width ratio (φ), rotor pitch (β), stator pitch (α), radius of the rotor (R_r), gap between the rotor and stator (G), length of the

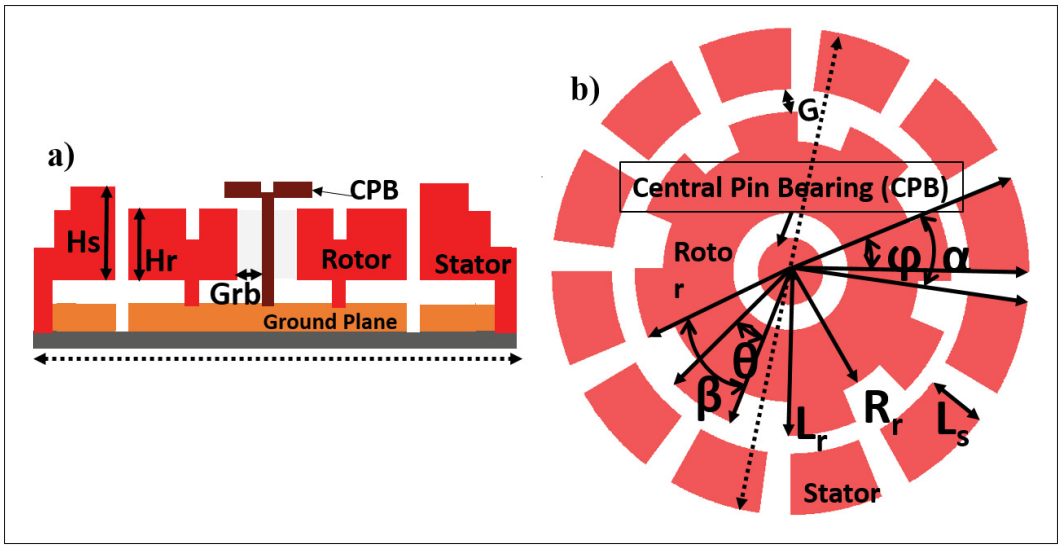

Figure 3.1 (a) Side-view of the micromotor, (b) Micromotor layout showing the key design parameters

rotor teeth (L_r), height of the stator (H_s), height of the rotor (H_r), bearing radius (R_b), clearance between rotor and bearing (G_{rb}), and the radius of the CPB (R_{cpb}) are key parameters for the design of a micromotor and are shown in Figure 3.1.

In this work, the analytical model developed in (Dufour *et al.*, 1996b) is adopted to extract the key physical parameters of the micromotor. They evaluated the validity of the analytical model using FEA simulations, whereas in this work the design is experimentally verified by fabricating it using the Poly-MUMPS process. The model is used to determine the optimal dimensions of the various micromotor parameters including the rotor width, stator width, rotor pitch, length of rotor teeth and stator pitch for a specific fabrication process. The designed micromotor has 12 rotors poles and 8 stators poles. The generated torque is maximum if the ratio of rotor poles (N_r) to stator poles (N_s) is 2:3 (Endemaño *et al.*, 2003). Assuming the capacitance between the rotor and the stator is similar to the one of an equivalent parallel plate capacitor and neglecting fringing effects, the maximum average torque for the operation of the micromotor can be obtained if the rotor width, stator width, rotor pitch and stator pitch satisfy the following relations as given in (Dufour *et al.*, 1996b):

$$\frac{\beta}{q} \leq \theta \leq \beta\left(1-\frac{1}{q}\right) \tag{3.2}$$

$$\frac{\beta}{q} \leq \varphi \leq min(\alpha, \beta(1-\theta)) \tag{3.3}$$

where q is the total number of phases of the driving signal.

The generated torque (T) and rotor angular position (φ) exhibits a nonlinear behavior, leading to torque ripples that can be minimized if the rotor and stator width meet the following condition:

$$\theta = \varphi = \frac{\beta}{2} \qquad if \ \frac{N_s}{N_r} \leq 2 \tag{3.4}$$

Table 3.1 Optimal Geomatrical Parameter of the Micromotor Based on Analytical Modelling

Micromotor geometrical parameters	**Optimization**	**Designed value**
Gap between rotor and stator(G)	Lower limit of fabrication	2 μm
Radius of the micromotor rotor(R_r)	Upper limit of available space/user defined	300 μm
Number of phase(q)	3	3
Multiplying factor (p)	p<R_r π/20G	4
Number of stators (N_s)	pq	12
Number of rotors N_r	$2N_s/3$	8
Rotor teeth angle/width(θ)	$\frac{\pi}{N_r}$	22.5°
Stator teeth angle/width(α)	$\frac{\pi}{N_r}$	22.5°
Length of the rotor tooth (L_r)	$L_r \leq R_r min(\theta, \beta)$	417.75 μm
Length of the stator tooth (L_s)	Lower limit of the fabrication process/user defined	140 μm

Table 3.1 presents the micromotor parameters and the condition for optimal operation based on analytical modelling for each parameter, in order to generate the maximum average torque with

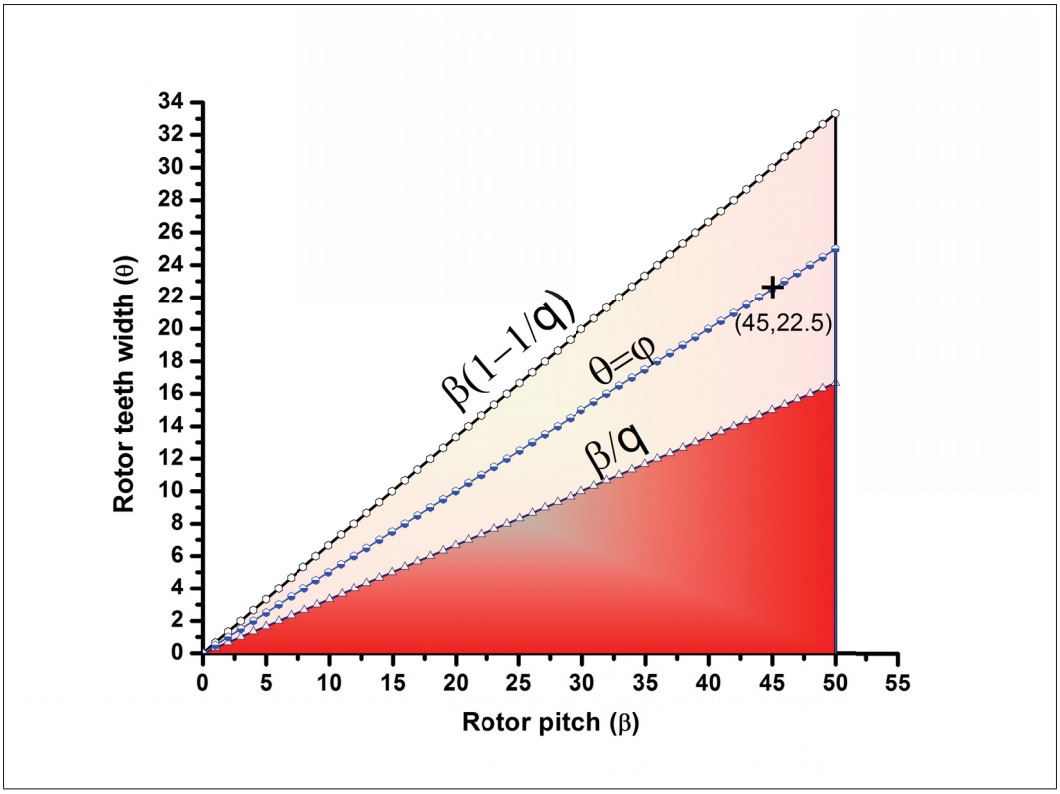

Figure 3.2 Graph showing the design space for optimum average torque and minimum torque ripples as a function of the rotor and stator parameters. Enough driving torque for rotation is obtained if the stator and rotor parameters lie above the red region. Rotor and stator teeth width should be equal as shown by blue line and are equal to 22.5° for this design.

minimum ripples. Figure 3.2 illustrates the relation between the rotor teeth width and rotor pitch based on equation 3.3 and equation 3.4.

As shown in Figure 3.2, the micromotor dimensions should lie in the area above the shaded region (red color) to obtain enough torque to move the rotor. The middle line (blue color) represents the design parameters of the proposed micromotor obtained using analytical modelling. For a specific rotor pitch and number of phases, the lower black line indicates the minimum possible rotor teeth width and the upper black line sets the maximum allowed value for the rotor teeth width.

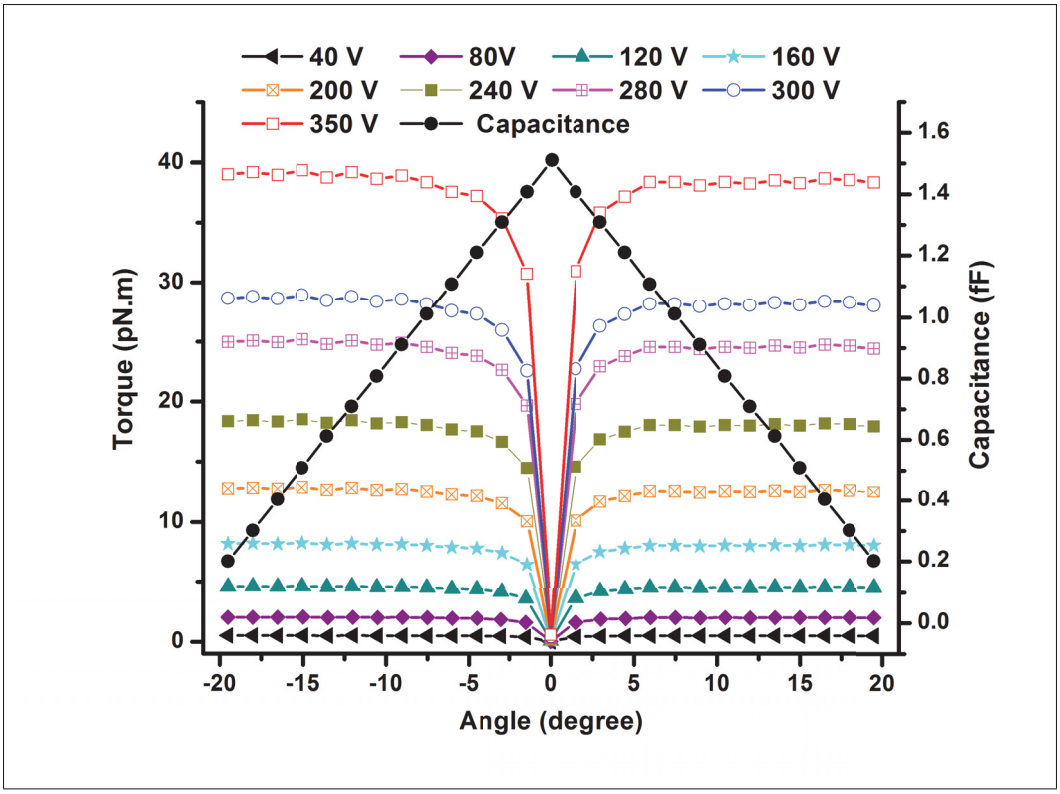

Figure 3.3 Torque vs angle and capacitance vs angle graph for single/rotor-stator pair at different voltage.

As explained above, a VCM starts operating when torque is generated by the electrostatic forces that result from a potential difference between the rotor and the stator. Consequently, continuous motion of the rotor is observed and the movement of the rotor changes the capacitance between the stator-rotor pole. This capacitance variation is periodic due to the symmetric arrangement of the poles. FEA for a single rotor-stator pair with the optimal parameters is performed to calculate the generated torque for different voltages applied to the stator electrode. Simulation results are shown in Figure 3.3. The angular position of the rotor is varied in steps of 2.5° covering the entire stator angular width and the applied potential is varied from 40 V to 350 V at each position. The torque at each position increases with the applied voltage. When the stator and the rotor are fully aligned, capacitance is maximum, and the torque is zero due to the balancing of the electrostatic forces. The capacitance decreases as the misalignment between the rotor and the stator increases but the torque is non-zero and increases. The curve is symmetric

about the angular position where the stator and rotor are aligned and in good agreement with the results presented in the literature (Dufour *et al.*, 1996b).

Increasing the generated torque can improve the micromotor speed. Micromotors with more stator and rotor poles produce high torque but are very slow (Dufour *et al.*, 1996b) due to the bulky size of the rotor. Small micromotors with a lower number of rotor-stator poles can achieve higher speeds but such configuration generates a small motive torque. Rotor size scaling as well as the maximization of generated torque can be obtained by keeping the ratio of stator poles to rotors to 1.5 (Dufour *et al.*, 1996b). In the proposed design, the ratio is maintained by keeping 12 stator poles and 8 rotor poles. Also, the motive torque can be increased by using a long lever arm by increasing the rotor radius (Megregany *et al.*, 1990; Basha *et al.*, 2007; Fan *et al.*, 1989; Tavrow, Bart & Lang, 1991; Wallrabe, Bley, Krevet, Menz & Mohr, 1994). In this work, the rotor radius is 300 μm, yielding a rotor teeth length of 417.75 μm based on the analytical model and acts as relatively long lever arm capable of generating a high motive torque.

High-speed operation can also be obtained by reducing the friction and wear in the micromotor. The rotor bearing supports, also referred to as dimples in the PolyMUMPS process terminology, can be either of the ring or bushing type. The contact between the dimples and the ground plane causes friction and wear that can be minimized by adopting a proper dimple design. A bushing type design is used for the dimples, offering a 20% smaller coefficient of friction compared to a ring-shaped (i.e. annular) design (Beerschwinger, Reuben & Yang, 1997). The dimples are placed away from the CPB post to improve the vibrational stability of the rotor (Beerschwinger *et al.*, 1994). The CPB post acts as a lever arm for the frictional torque. The constant contact between the CPB post and the rotor due to the rotor side-pull causes friction and wear. The effect of the rotor side-pull on the drive torque can be reduced by maintaining the ratio of stator width (φ) to stator pitch (α) greater than 0.6 (Beerschwinger *et al.*, 1997) and is set to 0.75. Moreover, the friction between the rotor and CPB axis can be reduced by using a small bearing size (Beerschwinger *et al.*, 1997), making the lever arm for the frictional torque smaller. The bearing is 12 μm in diameter, which is the smallest amongst the reported work until now (Kraus, Baltzer & Obermeier, 1997; Basha *et al.*, 2007; Fan *et al.*, 1989). The bearing clearance should

also be as small as possible (Zhang *et al.*, 2005) to reduce the wear and is fixed to 750 nm, which is the limit imposed by the PolyMUMPS process. Lastly, a bearing cap of 60 μm in diameter is used to prevent the rotor to overturn. This can happen because axial forces may cause the rotor to spin-out of the bearing axis.

Potential micromotor design improvements to increase the speed operation are investigated in this work by varying specific parameters. Design variants of the micromotor are fabricated by engineering the following parameters: i) varying the gap between the rotor and stator, ii) reducing the contact area between the rotor and the substrate, and iii) modifying the area of the capacitor formed between the rotor and the stator.

3.3.2 Device Fabrication and Variants

A micromotor layout based on the design rules of the PolyMUMPS process is shown in Figure 3.4(a). The gap between the rotor and the stator inversely affects the electrostatic force and is varied from 2 μm to 5 μm. As shown in Figure 3.4(b), teethed rotor edges were considered, alternatively to planar edges, to increase the effective length of the rotor edges, thereby increasing the overall capacitance.

The PolyMUMPS process is a three-layer polysilicon surface-micromaching process: POLY-0 is 0.5 μm thick, POLY-1 is 2 μm thick and POLY-2 is 1.5 μm thick. The thickness variation and the conformal deposition of the layers produces surface topography in the fabricated micromotors. The capacitance between the rotor and the stator can be modified by designing the film stack in the micromotor. First, the POLY-0 layer is deposited on the substrate and acts as a ground plane; then the POLY-1 layer is deposited to pattern the rotor and stator; and finally the POLY-2 layer is deposited to pattern the CPB and axis cap. Selectively removing or adding the POLY-0 layer under the POLY-1 layer can create a vertical offset between the two layers and this is used in this work to modify the rotor-stator capacitance. This is shown in 3.4(c) and 3.4(d). Inherently, for making dimples, the fabrication process introduces 0.75 μm of misalignment between the rotor and stator. The vertical offset is set to 0.75 μm by using the 0.5 μm POLY-0 layer under the

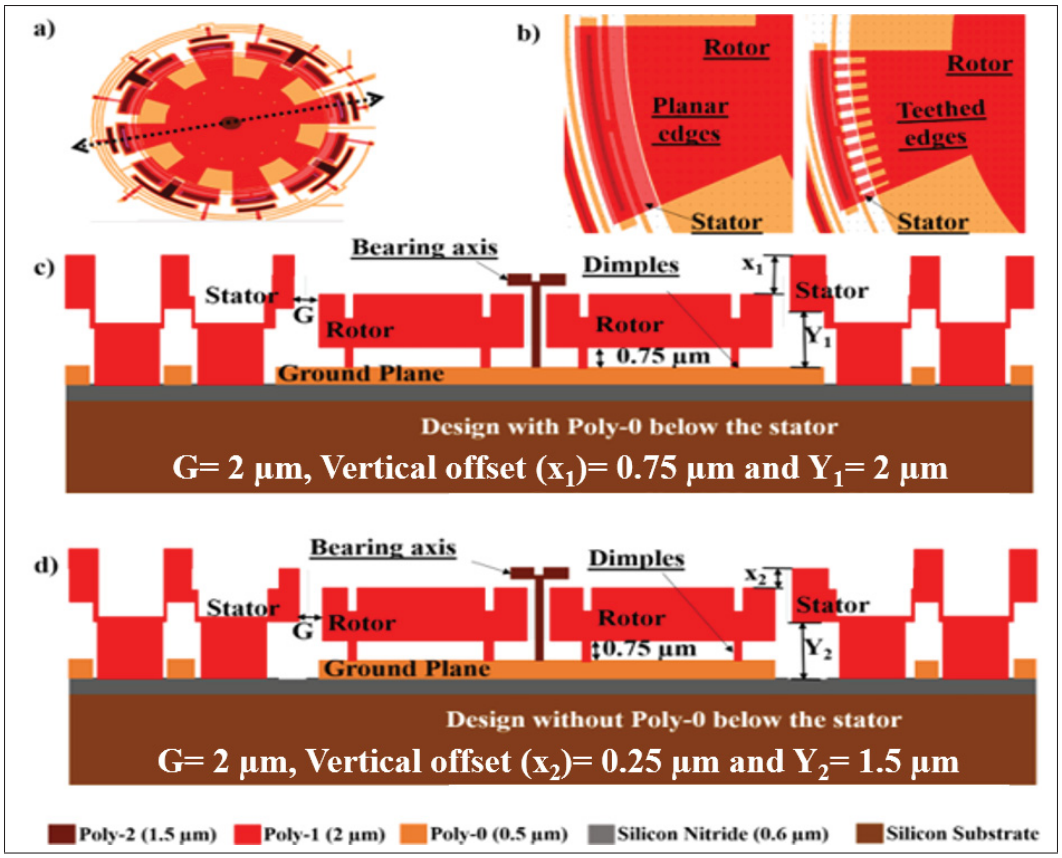

Figure 3.4 (a) Top view of the micromotor layout, (b) Top-view of a single rotor-stator pair showing planar edges and teethed edges design, (c) Cross-section of the micromotor design with Poly-0 below the stator (x1 = 0.75 μm, Y1 = 2 μm), (d) Cross-section of the micromotor design without Poly-0 below the stator (x2 = 0.25 μm Y2 = 1.5 μm)

POLY-1 layer in the stator design shown in Figure 3.4(c) (x1). Alternatively, the vertical offset can be decreased to 0.25 μm if the POLY-0 layer is not used under the POLY-1 layer for the stator design, as indicated in Figure 3.4(d) (x2). Accordingly, an increase of the rotor-stator capacitance can be obtained by modifying the vertical alignment of the layers in this fashion.

The micromotor layout was prepared using the L-EDIT layout editor following the design rules of the Poly-MUMPS process. The optimized geometrical parameters listed in Table I are used for implementing the micromotor layout. The steps involved in the fabrication are summarized in Figure 3.6.

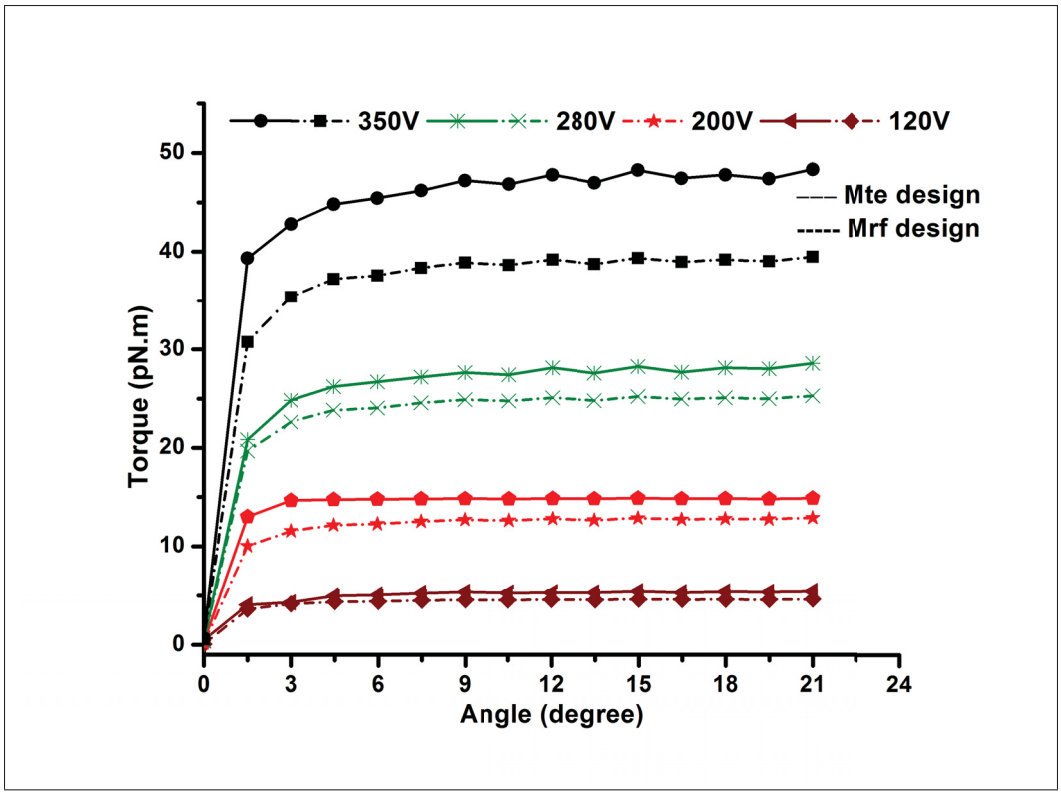

Figure 3.5 Calculated drive torque vs overlap angle at different voltages for the M_{te} and M_{rf} design micromotor variants using the modelling as indicated by (1) for a single rotor-stator pair.

A detailed description of the PolyMUMPS fabrication process can be found in (Cowen *et al.*, 2011). The first polysilicon layer (POLY-0) is used for making the electrical interconnections, stator-base, and the ground plane under the rotor. The rotor touches the ground plane via the dimples. The rotor and stator are created using the second polysilicon layer (POLY-1) layer. The bearing mask is drawn on the third polysilicon layer (POLY-2) over a hole in the POLY-1 layer to connect the bearing-axis to the ground plane. The diameter of the bearing is 12 μm. The dimple and hole layers are also used accordingly as suggested by the literature (Cowen *et al.*, 2011). Bushing type dimples with a 3 μm radius are used and spread across the rotor. All of the polysilicon layers are used to make a connection between the various stators by using electrical crossovers to avoid short circuits and to reduce the number of input pads. The electrical crossovers are realized in the form of released suspended micro-bridges.

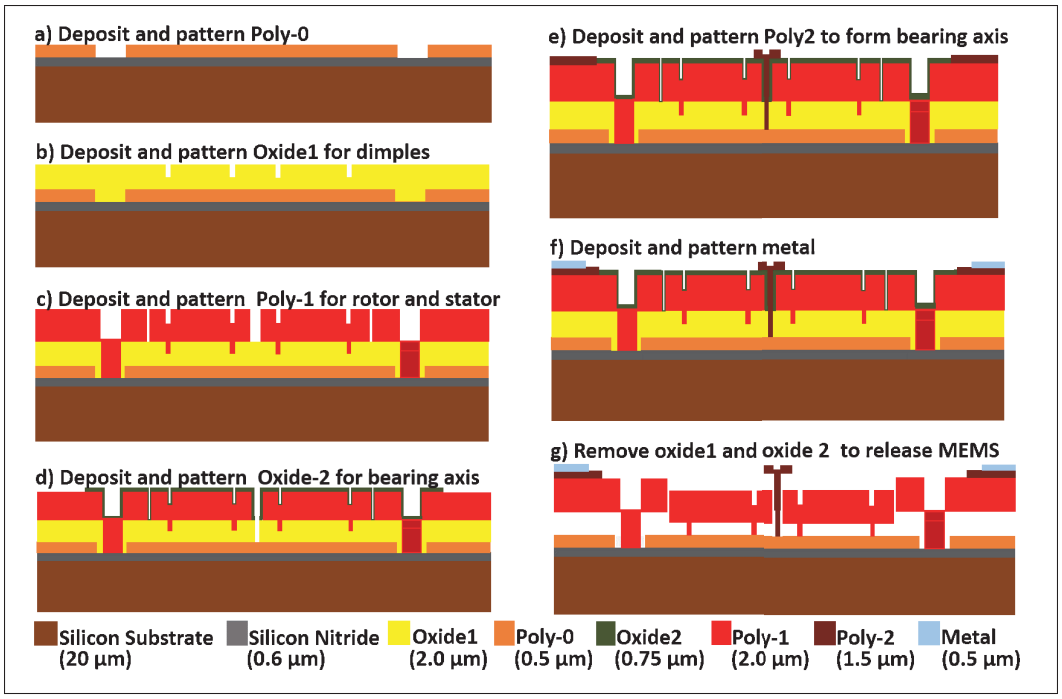

Figure 3.6 PolyMUMPS process flow for micromotor fabrication. The thicknesses of each layer are also indicated.

Table 3.2 Design variants of the fabricated micromotor

Design version	**Gap**	**Edge**	**Dimple**	**Stator/rotor vertical offset(μm)**
M_{gap}	2-5 μm	Planar	48	0.75
M_{dim}	2 μm	Planar	48 to 12	0.75
M_{vf}	2 μm	Planar	12	0.25
M_{te}	2 μm	Teethed edges	12	0.25

Different variants of the micromotor were fabricated and tested and are listed in Table 3.2. The M_{gap} and M_{dim} micromotors have gap variations and number of dimple variations, respectively. The M_{gap} micromotor variants are fabricated and tested to validate that the gap should be as small as possible for the micromotor operation. These designs have planar edges for the stator and the rotor electrodes with a 0.75 μm vertical offset and 48 dimples distributed across the rotor.

Friction at the micro-scale is dominated by Vander wall and capillary forces and dependent on the contact area between the bodies in motion. As such, the M_{dim} micromotor features a variation in the total number of dimples that are reduced by 75% while keeping the 0.75 μm vertical offset and a 2 μm gap between the planar edges of the rotor and the stator. The reduced number of dimples is expected to reduce friction.

The M_{vf} and M_{te} micromotors have overlap area variations and rotor/stator edge shape variations, respectively. These designs also have a vertical offset that is reduced to 0.25 μm by removing the POLY-0 layer under the POLY-1 layer in the stator as previously discussed. The M_{te} micromotor has teethed edges as illustrated in Figure 3.4b. The geometry of the rotor and stator is changed by including 12 grooves on the edges forming teethed edges. Each tooth is 10 μm long and 7 μm wide with a 7 μm gap between adjacent teeth. Both the M_{vf} and M_{te} variants are expected to have enhanced electric fields and thus more torque, yielding higher rotational speed. The generated torque vs. overlap angle for the M_{te} and M_{rf} design variants calculated using (1) is compared in Figure 3.5 for a single rotor-stator pair at different voltages. This indicates that the M_{te} variant generates higher torque than the reference design for a given voltage and overlap.

The modification of the shape of the rotor and the stator poles in the M_{te} micromotor does not affect the operating principle of the VCM as the electrical connectivity between the poles is still in a three-phase configuration. In this design, each arm of the rotor represents a single pole and grooves are made at the edge to form teethed rotor arms and increase the fringing electric fields. Each group of four stators is connected to a common phase and all the teeth of a rotor arm face the same stator pole, thus the 12 stators form a three phase configuration. The characterization of the fabricated micromotors is presented in the next section.

3.4 Experimental Results

The micromotors are fabricated in the same batch and are part of different dies. The fabrication process variability and its impact on the different micromotors can be seen by comparing their performance. Figure 3.7 shows the M_{gap} micromotor layout and scanning electron microscopy

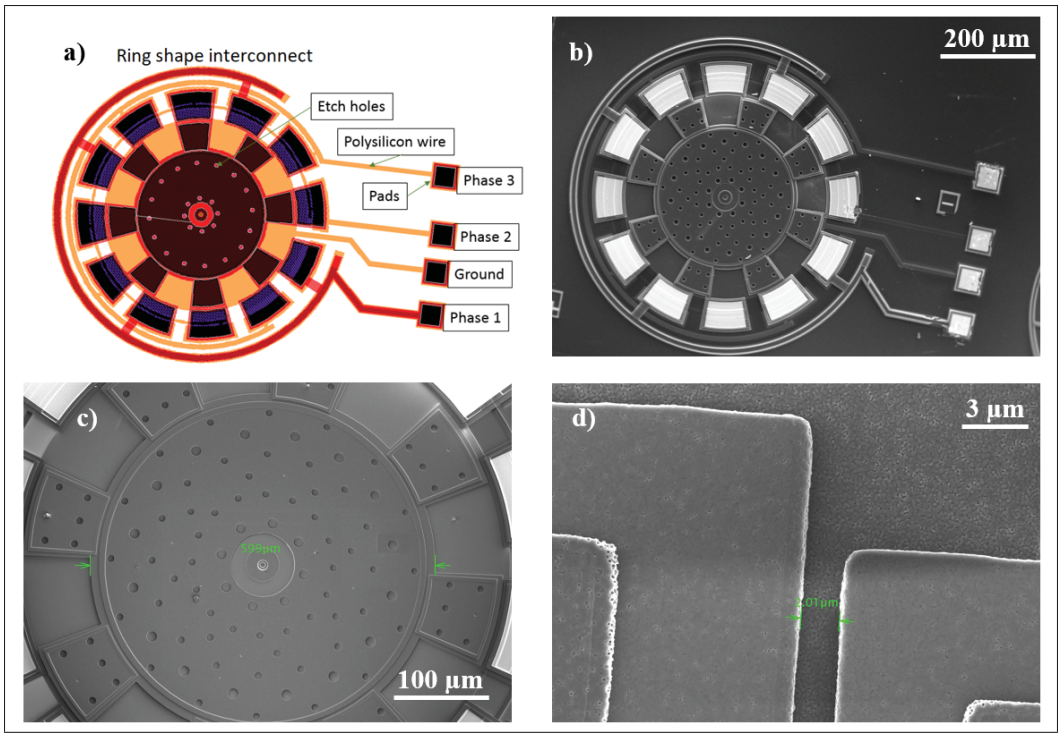

Figure 3.7 (a) Layout of the Mgap micromotor, (b) SEM micrograph showing the top view of the micromotor, (c) SEM micrograph showing the diameter of the rotor, (d) SEM micrograph of the gap between the stator and the rotor

(SEM) micrographs of its overall structure, gap and rotor. The layout of the micromotor and the corresponding SEM image are shown Figure 3.7(a) and Figure 3.7(b), respectively. Figure 3.7(c) is a SEM image of the rotor having a 600 μm diameter, CPB axis cap and release holes over the rotor. The minimum feature size fabricated by the PolyMUMPS process is 2 μm, which is the minimum gap between the rotor and the stator for the M_{gap} design, shown in Figure 3.7(d). In Figure 3.8, the interconnects and the M_{vf} and M_{te} variants are outlined. The circular layout and micro-bridges shown in Figure 3.8(a) are used for signal routing to connect the various electrodes of the micromotor. SEM micrographs of the M_{te} design and the corresponding teeth on the edge of the rotor and the stator are presented in Figure 3.8(b) and Figure 3.8(c), respectively. A perspective view of the M_{vf} design is shown in Figure 3.8(d).

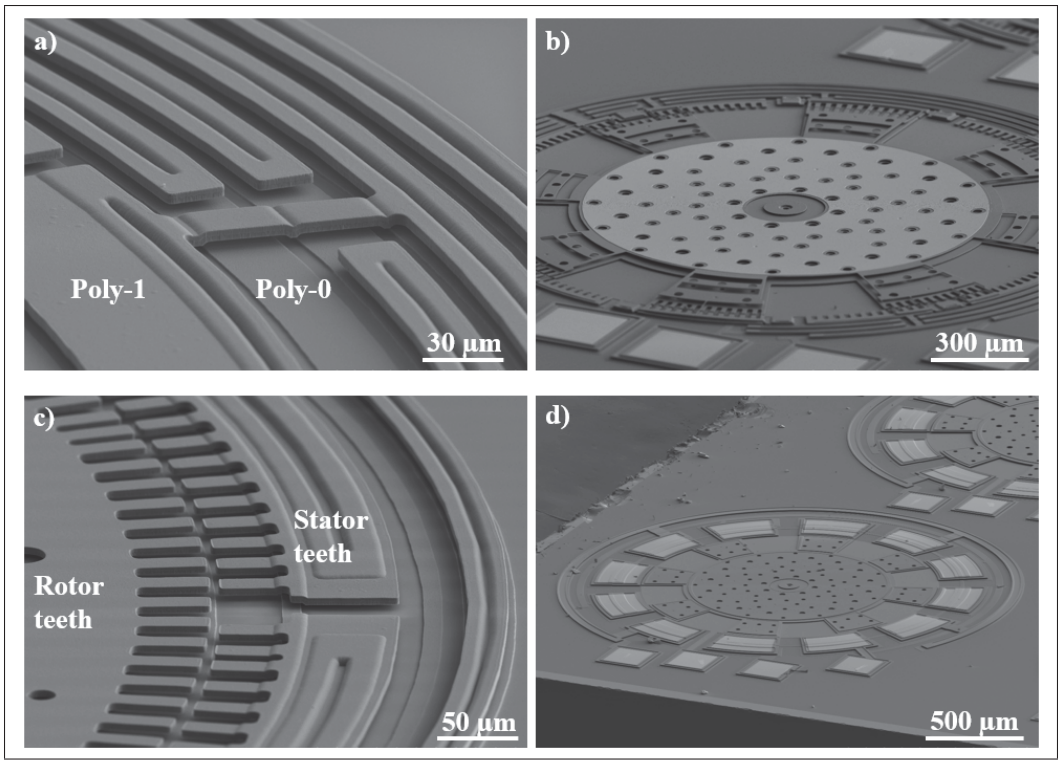

Figure 3.8 (a) SEM micrograph of the ring shape interconnects with micro-bridge used for electrical crossover on Poly-1 layer, (b) SEM micrograph of the M_{te} micromotor design, (c) SEM micrograph showing the perspective view of the M_{vf} micromotor design, (d) SEM micrograph of the rotor teeth and the stator

The 12 stators poles of the micromotor are divided into groups of 3 poles and each group consists of 4 stator poles that are electrically connected to a common input signal or a single phase. The micromotor has four input pads, each connected separately to a single stator from each group and the ground plane via polysilicon wires. The three input pads supply the excitation sequence to each stator group. The fourth input pad connects the ground plane and CPB axis to 0 V, avoiding the building of non-zero rotor potential. The electrical test setup used for the characterization of the micromotors is illustrated in Figure 3.9. The rotor is connected to the ground and the stator electrodes are connected to the excitation phases. The micromotor is actuated using a unipolar three-phase square wave sequence to generate maximum output power and to provide maximum torque coverage (Ghalichechian *et al.*, 2008b). The high unipolar voltage is obtained by cascading a DC supply and a DC amplifier that provides a voltage denoted VDC in this work,

and which represents the amplitude of the three-phase square waves. The output of the DC amplifier is fed to the signal generator that produces a three-phase square waveform using a custom printed circuit board. The current per phase consumed by the micromotor is measured by connecting an ammeter in series with a single input phase driving four stator electrodes. Initially, a low voltage excitation sequence is applied to avoid any damage due to dielectric breakdown, then voltage is increased in small steps. Note that the micromotors do not rotate as soon as the excitation is applied since the native oxide between the rotor and the bearing-axis, and between the dimples and the ground plane may cause the friction torque to be larger than the motive torque (Endemaño *et al.*, 2003).

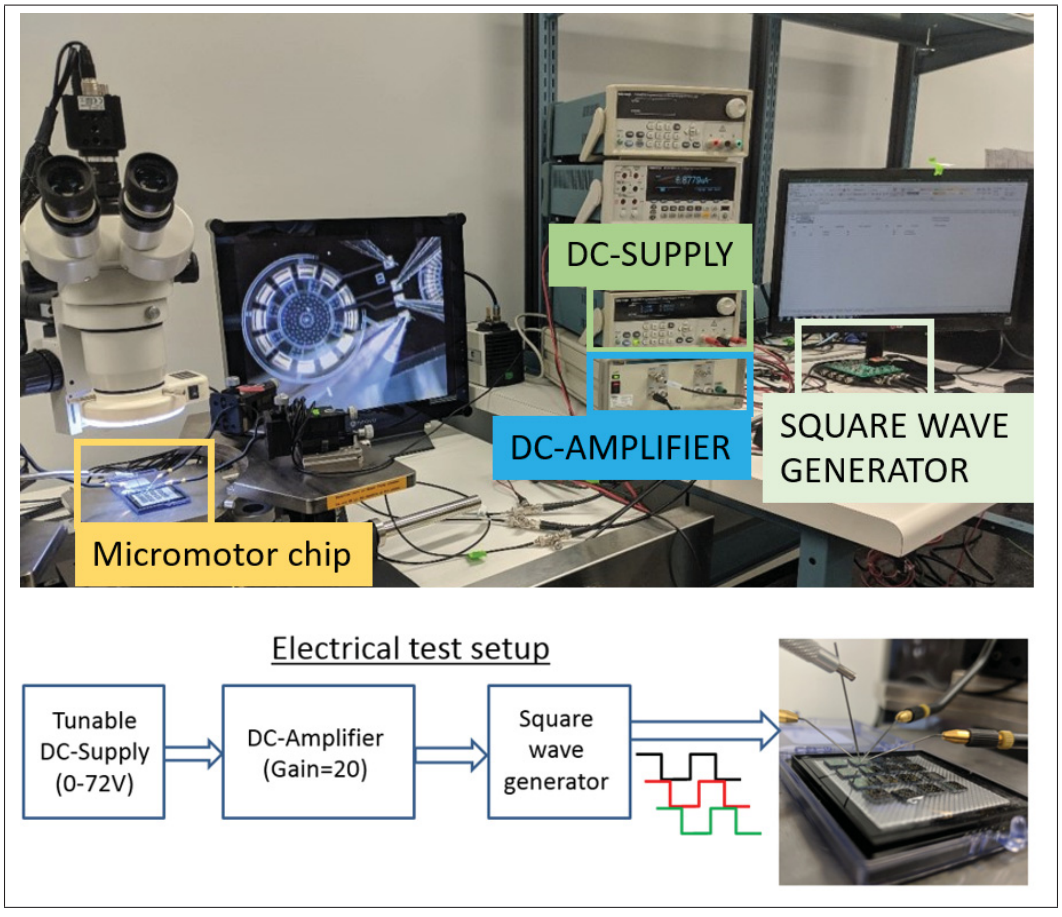

Figure 3.9 Electrical test setup for micromotor testing with block diagram.

In order to ensure that the correct minimal DC voltage that enables rotation is extracted, the native oxide is eroded by slightly moving the rotor manually using micro-probes to make better contact between the rotor and the ground plane. Furthermore, the manual micro-probing verifies that the rotor can freely rotate without stiction caused by fabrication process variations. The resistance between the rotor-stator, pad-stator, and rotor-pad is measured to confirm the presence of open or short circuits created by over etching or under etching of the polysilicon and silicon dioxide during fabrication.Then, the micromotor testing is performed through the following steps. First, the sequence voltage is set to VDC = 0 V followed by fixing the frequency. Next, VDC is incremented in step of 2 V until a regular rotation of the rotor is observed. Finally, the VDC value is measured and labelled VON and decreased down to zero. A similar approach is followed for different excitation frequencies. These measurements are carried out at atmospheric condition to record VON for different excitation frequencies. Another set of measurements is performed to measure the maximum operating frequency at a fixed driving voltage. First, the input excitation is set to VDC = 0 V and the excitation frequency is set to 10 Hz. Next VDC is incremented in steps of 2 V until a regular rotation of the rotor is observed. The value of VDC is kept fixed and the excitation frequency is increased in steps of 5 Hz, until the rotor is moving. The rotor speed increases with the excitation frequency and the rotor movement halts after a certain maximum operating frequency due to insufficient power as the voltage is fixed. VDC is then increased to continue the rotor motion and then frequency is again increased until the rotor is halted. In this way, the maximum excitation frequency at which an increase in voltage does not allow for continued rotor motion is identified.

The method used to calculate the speed of three-phase micromotor is explained in (Ghalichechian *et al.*, 2008b; Han, Wu & Wang, 2010b). It was used to determine the speed of each micromotor variant presented here. Assuming synchronization between the electrical excitation and the rotation of the rotor, the rotational speed of the micromotor (ω_r) and the excitation frequency are related by:

$$\omega_r = 60\frac{f_{ele}}{N_{rp}}\, rpm \tag{3.5}$$

where f_{ele} is the frequency of the applied electrical excitation and N_{rp} is the total number of rotor electrodes.

Figure 3.10 shows the experimental voltage-speed curves for the micromotors with different gaps between the rotor and the stator. The gap is 2 μm, 2.5 μm and 3 μm for the micromotors labelled $M1_{gap}$, $M2_{gap}$ and $M3_{gap}$, respectively. All the micromotors have 48 dimples, planar rotor-stator edges and a 0.75 μm vertical offset. As the spacing between the stator and the rotor decreases, the corresponding electrical force increases, leading to a higher motive torque that increases the speed of the motor. The highest speed is achieved by the $M1_{gap}$ micromotor whereas the $M3_{gap}$ micromotor is significantly slower. The $M2_{gap}$ and the $M3_{gap}$ designs are not able to sustain a rotational speed beyond 1,500 rpm, whereas the $M1_{gap}$ can reach a rotational speed of 6,000 rpm. The micromotors with stator-rotor gap greater than 3.5 μm do not rotate, due to insufficient electrostatic forces. It is observed that most of the micromotors rotate smoothly at low frequencies and eventually start vibrating as the frequency is increased. The starting voltage, VON, also increases with the excitation frequency. Also, it can be seen from Figure 3.10 that the $M1_{gap}$ micromotor is exhibiting a higher VON as compared to the other designs despite having a higher driving torque. This could be explained by considering that the presence of native oxide between the rotor bushing and the ground shield below disrupts the electrical contact and leads to space charge polarization. The polarization causes the clamping of the rotor to the ground shield. In the case of micromotors with a smaller gap the electric forces (and charge) acting on the rotor are larger, resulting in stronger clamping forces. Accordingly, a larger VON is required to overcome these clamping forces and initiate rotary motion of the rotor. Thus, micromotors with a high drive torque exhibits large VON as compared to the other micromotors. Nonetheless, the higher driving torque yields higher rotational speed once the micromotor has started.

The average power consumed by the micromotors vs rotational speed for the different gaps is presented in Figure 3.11. The average current consumed by a micromotor moving at a given rotational speed is measured, and the average power is calculated for each design by using the average drive voltage. The electrostatic force is directly proportional to the applied voltage and inversely proportional to the gap of the micromotor, thus the micromotor with the smaller

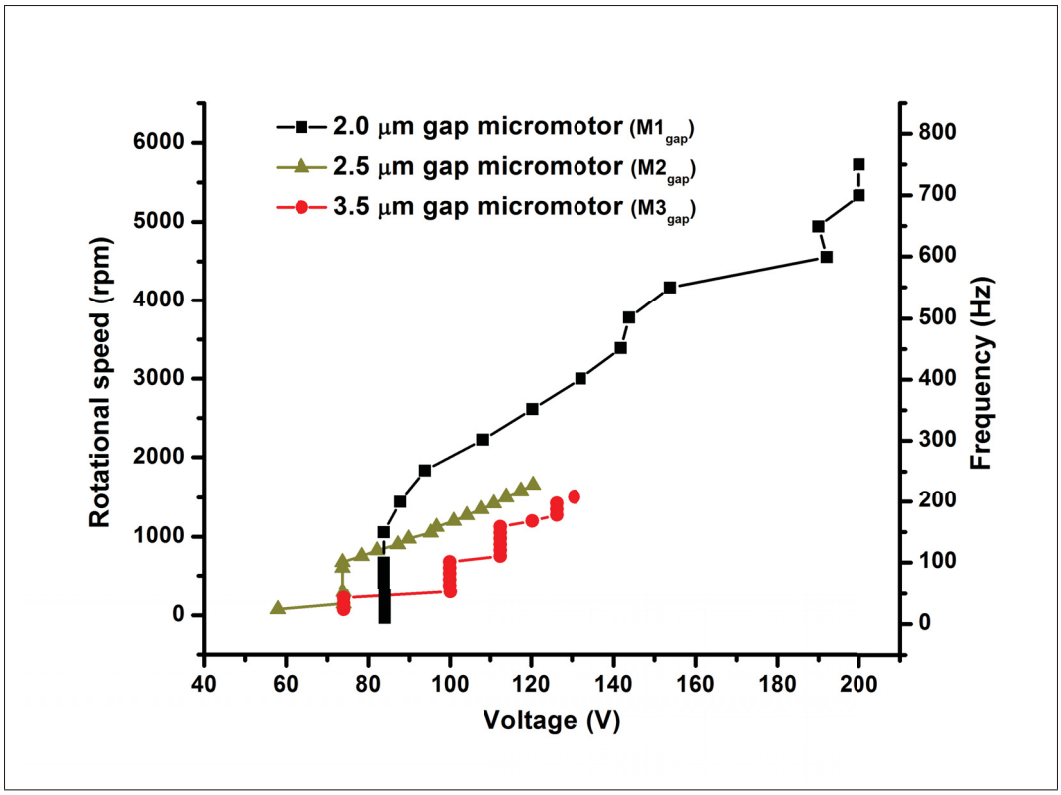

Figure 3.10 Rotational speed vs voltage plot for M_{gap} micromotors designs.

gap will exhibit more torque and will support higher rotational speed for a given drive voltage. Hence, the micromotor with the larger gap would need a higher drive voltage in order to attain the same rotational speed as a smaller gap micromotor. Consequently, for the same power consumption, a micromotor with a large gap will yield less rotational speed than the micromotor having a smaller gap.

The frictional torque in the micromotor can be described by observing its moving parts. Works in (Bart, Mehregany, Tavrow, Lang & Senturia, 1992; Yu-Chong & Muller, 1990; Tavrow, Bart & Lang, 1992) studied a few aspects of friction in micromotors. Frictional torque is present at the contact points of the dimples and the ground plane and at the contact points of the bearing axis and the rotor. The dimples continuously slide over the ground plane causing friction and wear. When a micromotor is in operation, the rotor continuously touches the hub by translating

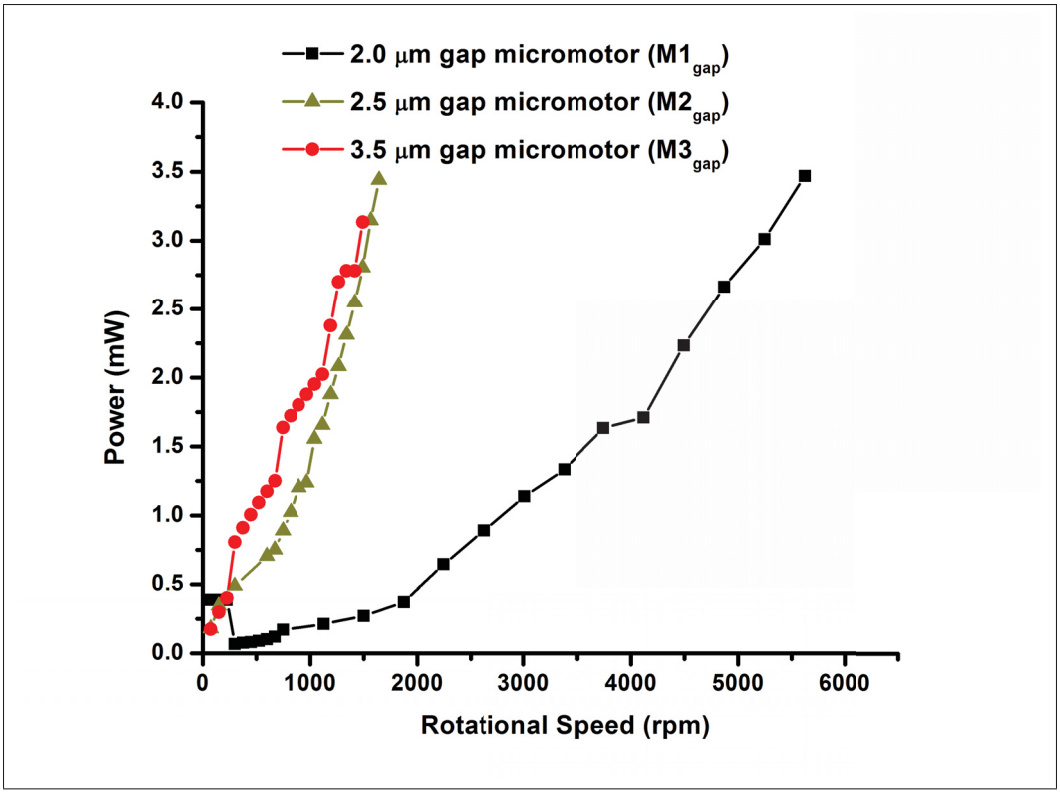

Figure 3.11 Average electrical power consumption vs rotational speed for the M_{gap} micromotors with different gap sizes.

in the bearing clearance leading to friction, which varies with the square of the drive voltage (Bart *et al.*, 1992). Also, friction due to the attractive forces between the rotor and the ground plane at the point of contact of the dimples depends on the square of the driving voltage (Bart *et al.*, 1992). Another cause of friction is viscous drag of the air resulting from different parts of the micromotor as mentioned in (Bart *et al.*, 1992; Omar, Mehregany & Mullen, 1992). The viscous friction drag between the rotor ground plane, bushing-ground plane, stator-rotor gap, bearing clearance, rotor-sidewalls and bushing-sidewalls is independent of rotational speed. The viscous friction drag due to the top surface of the rotor varies with the rotational speed. When the voltage applied to the micromotor is adjusted to achieve the desired rotational speed, consequently the associated friction at the various location of the micromotor also varies and is balanced by the driving torque to attain an equilibrium in rotational speed.

There are various factors that contribute to the halting of the rotor after reaching the maximum operating frequency. The speed of the micromotor increases with frequency as indicated by (3.5), resulting in high wear of the surface in contact with the rotor. The continuous movement of the dimples on the substrate causes wear that increase surface roughness and thus friction between them. Similarly, the friction and the wear between the rotor and the CPB axis also increases. Another factor could be the accumulation of charge on the scratched surface at higher voltage, leading to the formation of localized clamping forces as the contact between the dimple and the scratched area is tattered and not sufficient to remove the accumulated charge. The rotor motion is not only limited to the rotation about the CPB axis as it can also move in the vertical direction due to the axial component of the electrostatic force. The amplitude of vertical vibration causing a zigzag motion increases with the operating frequency as the rotor speeds-up. The turbulent motion of the micromotor was characterized by measuring the amplitude of the vertical vibration of the rotor using a Polytec vibrometer. The variation in the amplitude of vertical vibration for different operating frequencies of the $\mathrm{M1}_{gap}$ micromotor is shown in Figure 3.12. As can be seen, the amplitude of the rotor vertical vibration is lower at low frequencies than at high frequencies, indicating more turbulent vibration at higher rotational speeds, which is expected to ultimately limit the rotational speed and potentially further increase the voltage required to achieve the higher rotational speeds.

Ultimately, at low rotational speeds, the rotor motion is less turbulent due to low axial forces and slow movement, while at higher rotational speeds, the micromotor's motion is more turbulent, due to the higher operating voltage that results in large axial forces. At very high rotational speeds, the rotor may be hitting the bearing cap more frequently due to the increased vibration leading to wear and increased friction. A large bearing cap will cause high wear and may cause contamination in the bearing clearance or in other parts of the micromotor. The presence of debris in small spaces can increase friction and may lead to operational failure of the micromotor. This could be the reason that a few micromotors instances were observed to stop rotating after reaching the maximum speed and were functionally worn-out.

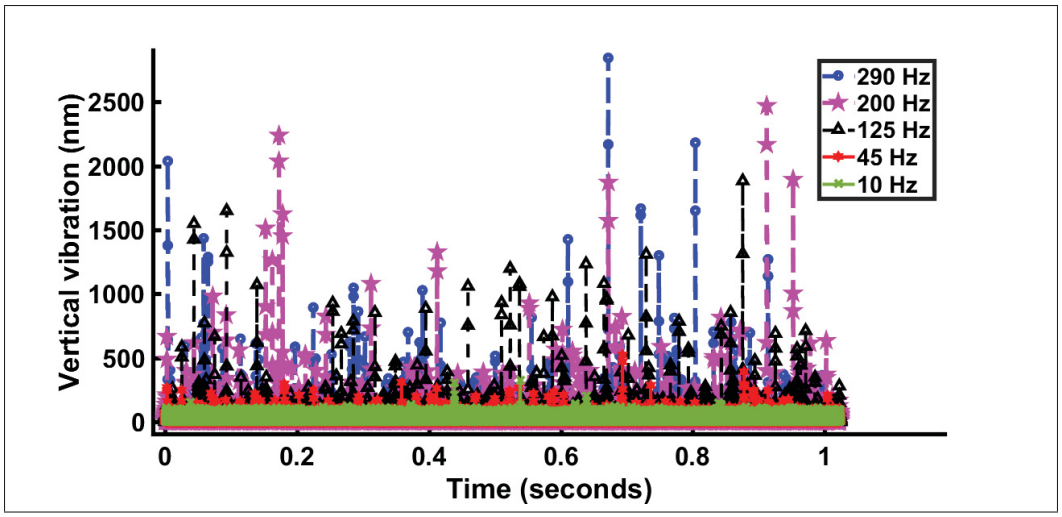

Figure 3.12 Amplitude of the vertical vibration of the rotor of the $M1_{gap}$ micromotor at different operating frequencies.

Moreover, the movement of the rotor affects the contact of the dimples with the underlying layer resulting in friction and wear. In order to mitigate this, the dimple contact area is reduced in the M_{dim} micromotor designs by using fewer dimples to support the rotor. Each dimple location provides a lever arm to frictional torque. The small size of the dimples and the smaller number of dimples reduces the number of asperities between the ground plane and the rotor. Hence, the resulting surface forces in the penumbral regions around the asperity contact become smaller and decrease the coefficient of friction (Beerschwinger *et al.*, 1997). The impact of the number of dimples on the micromotor performances can be seen in Figure 3.13. $M1_{dim}$, $M2_{dim}$, $M3_{dim}$, and $M4_{dim}$ are micromotors with 48 dimples, 28 dimples, 24 dimples and 12 dimples, respectively. A square wave excitation of 10 Hz is applied to all the devices to start the micromotors. The M1dim start rotating at peak voltage of 84 V while the $M4_{dim}$ rotated at a much lower peak voltage of 12 V. Thus, an 86% reduction in the starting voltage is obtained by reducing the dimple contact area by 75%. Once the $M1_{dim}$ and $M2_{dim}$ micromotors are set in motion, the peak voltage required for operation is constant for stable operation at different frequencies. On the other hand, for the $M3_{dim}$ and $M4_{dim}$ devices, the required peak voltage at different frequencies shows an upward trend and is constant only over a limited range of frequencies. This may be attributed to the decrease in stability of the rotor balance and the

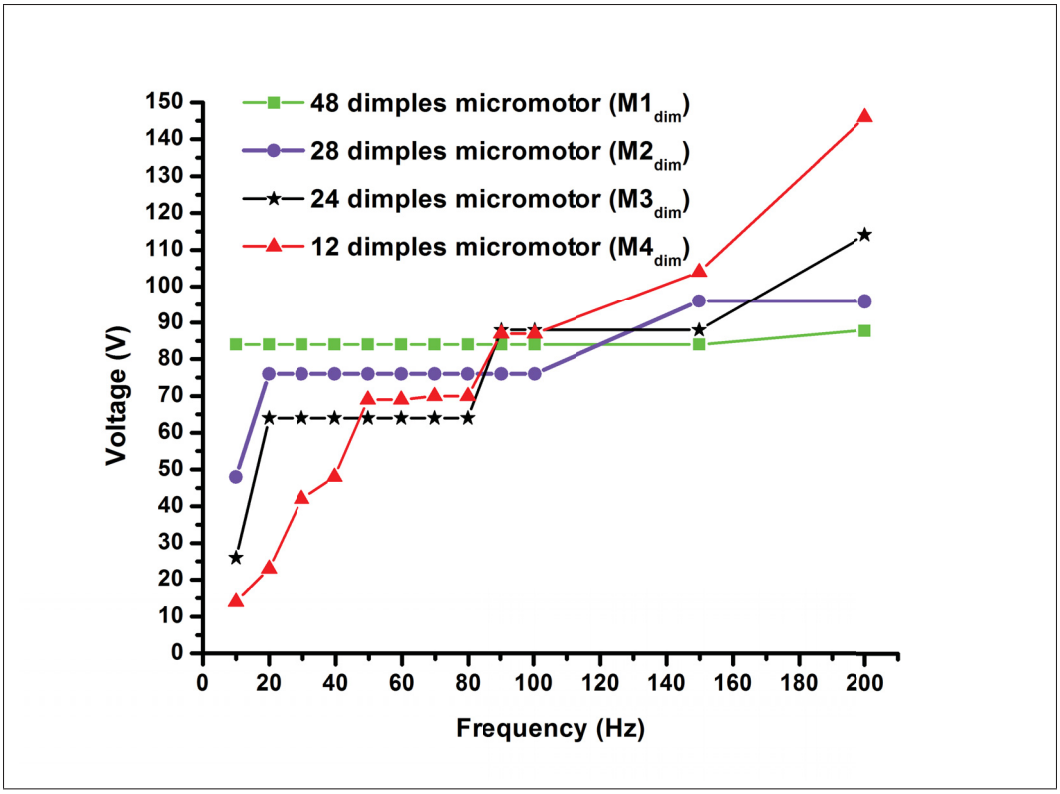

Figure 3.13 Driving voltage vs frequency for the M_{dim} micromotors with a different number of dimples.

turbulent motion of the rotor, as previously discussed. The rotor becomes less stable as the number of dimples supporting it decreases such that the micromotors with fewer dimples may exhibit higher wobbling motion with increasing frequency. Accordingly, they require a higher driving voltage than those with more dimples for stable operation at high frequencies. As such, an optimal number of dimples is expected to exist for a given micromotor geometry in order to achieve a balance between the excessive friction caused by too many dimples and the excessive wobbling caused by too few dimples.

The generated torque is directly proportional to the rotor-stator capacitance, as indicated by equation 3.1, and increasing the rotor-stator capacitance is expected to improve the micromotor performance. Accordingly, the capacitance is increased further by controlling the vertical offset between the rotor and the stator. For this, the vertical alignment between the rotor and the stator

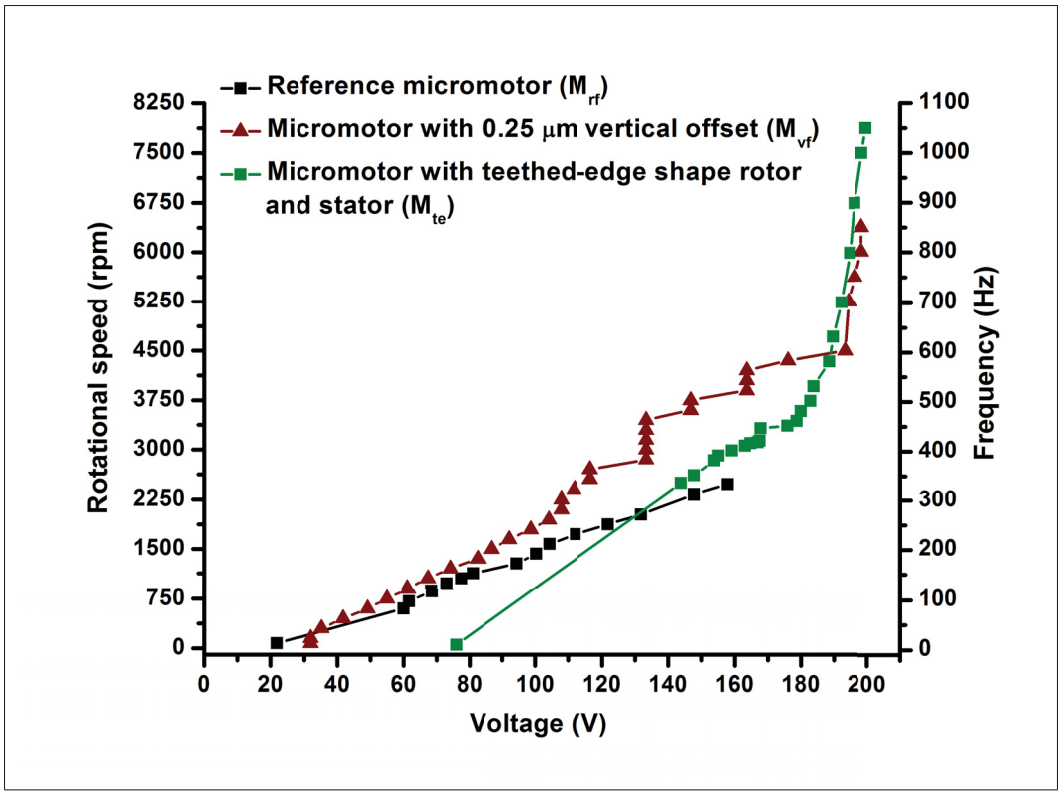

Figure 3.14 Rotational speed vs voltage for the M_{rf} (reference), M_{vf} (reduced vertical offset) and M_{te} (teethed rotor/stator edges).

pole is investigated by characterizing the M_{rf} and M_{vf} micromotor designs. These designs have vertical offsets of 0.75 μm or 0.25 μm, respectively, as discussed in section 3.3.2 (Figure 3.4(c) and Figure 3.4(d)).

In addition, the tangential component of the electrostatic force governs the rotor movement and is usually generated at the edges of the rotor (Basha *et al.*, 2007). Accordingly, changing the plane edges to teethed edges for the rotor and the stator as shown in Figure 3.4(b) improves the tangential force and this strategy is implemented in the M_{te} variant of the micromotor.

Figure 3.14 compares the rotational speed performance of the M_{rf}, M_{te} and M_{vf} micromotor variants. All these micromotor variants have 12 dimples supporting the rotor with a 2 μm gap between the stator and the rotor. The M_{rf} design has the plane edge shape rotor with a vertical offset of 0.75 μm. The M_{vf} design has a vertical offset of 0.25 μm but is otherwise identical to

the M_{rf} design. The M_{te} design also has a 0.25 μm vertical offset but has teethed edges for the rotor and the stator. As can be seen in Figure 3.14, the M_{vf} design achieved a speed of 6,375 rpm, which is a 168.42% improvement over the reference design (M_{rf}), indicating the importance of reducing the vertical offset between the rotor and the stator. Furthermore, the M_{te} devices can be operated at 7,875 rpm, which is the highest amongst all the designs, suggesting that the enhancement of tangential component of electrostatic force, provided by the teethed shape rotor and stator, is significant in increasing the rotational speed of the micromotor. Also, the starting voltage of the M_{te} and the M_{vf} devices is 72 V and 32 V, respectively, and is greater than the 22 V required by the M_{rf} design. The smaller vertical offset may reduce the upward force applied by the vertically offset stator, resulting in an increase in starting voltage in order to overcome the initial static friction. The effect becomes more prominent in case of the M_{te} design since it has a greater number of edges and more horizontally oriented forces. The electrostatic forces acting on the M_{vf} design are larger than the M_{rf} design due to the increased overlap between the rotor and the stator. This also implies that the clamping forces between the rotor bushing and the ground plane in the M_{vf} micromotor are greater than in the M_{rf} micromotor. Thus, the M_{vf} micromotor requires a higher VON than the M_{rf} micromotor in order to overcome the clamping forces and initiate rotary motion. A similar behavior is observed in the M_{te} design as well.

To characterize reproducibility, Table 3.3 presents the standard deviation that is normalized to the mean for the measured maximum drive frequency and the starting voltage, VON, of each tested micromotor variants. This indicates good repeatability between the copies of each variant.

Overall, the fast PolyMUMPS based micromotor can be obtained by adopting the design parameters provided in Table 3.1 and applying the guidelines presented in the Design Methodology section. Micromotors with rotational speeds of up to 2,500 rpm and with a VON as low as 22 V can be fabricated using the M_{rf} design. Micromotors providing speeds operation of up to 8,000 rpm can be fabricated using the M_{te}design but they will require a higher VON of 77 V. A middle ground can be achieved with the M_{vf} designs that offer VON as low as 32 V and speed of up to 6,500 rpm.

Table 3.3 Normalized standard deviation of the tested design variants parameters

Design variants	**Max. drive frequency norm. std. dev.(%)**	**V_{ON} norm. std. dev.(%)**	**Total no. of devices tested**
M_{gap}(3.5 μm)	8.5	5.2	7
M_{gap}(2.5 μm)	10.5	7.6	8
M_{gap}(2 μm)	8.4	14.3	7
M_{dim}(12 dimples)	7.8	10.4	6
M_{dim}(24 dimples)	6.7	9.9	6
M_{dim}(28 dimples)	9.1	14	7
M_{dim}(48 dimples)	8.4	14.3	7
M_{rf}	8.5	12.6	6
M_{vf}	8.5	10.8	7
M_{te}	9.2	3.2	6

3.5 Conclusion

In this work, different VCMs were presented. These micromotors were fabricated using the commercial PolyMUMPS surface micromachining process and were designed to optimize the rotational speed achievable with that process.

The wear and the friction at the contact of the CPB and the rotor was lowered by using a small size bearing with a radius of 6 μm, which is significantly smaller than in the previously reported work. The rotor-stator gap was studied, and it was found that the micromotor with rotor-stator gap of 2 μm had the higher rotational speed, and that gap sizes beyond 3.5 μm precluded rotation. Furthermore, small circular dimples were employed over big annular ring shape dimples to reduce the friction at the point of contact. It was determined that a small number of dimples minimized the static friction in various designs, resulting in a starting voltage of 12 V for the micromotor having 12 dimples. However, a trade-off between orderly micromotor rotational motion and friction caused by the dimples was also observed.

The vertical misalignment between the rotor and the stator was reduced in order to improve the rotor/stator capacitance of the micromotor, resulting in achieving a high rotational speed of 6,375 rpm due to the enhanced driving torque. Moreover, the planar edges of the rotor and the stator were modified to teethed edges, further improving the tangential component of the electrical force. Consequently, this design operated at 7,875 rpm in ambient conditions, which is to the authors' knowledge the highest reported speed for a VCM fabricated using the PolyMUMPS process.

Acknowledgement

The authors would like to thank CMC Microsystems for providing the CAD tools and microfabrication support.

CHAPTER 4

A RAPID TECHNIQUE TO INTEGRATE MICRO-COMPONENTS ON RELEASED MEMS DIES USING SU-8

Amit Gour[1] , Michael Ménard[2] , Frederic Nabki[1]

[1] Departement of Electrical Engineering, École de Technologie Supérieure,
1100 Notre-Dame Ouest, Montréal, Québec, Canada H3C 1K3

[2] Department of Computer Science, Universite du Quebec a Montreal,
201 President-Kennedy Avenue, Montréal, Québec, Canada H2L 2C4

Paper published in IOP JMM, September 2020.

Preface

In this chapter, a micro-assembly technique to bond and integrate a micro-structure with a MEMS device is presented. The post-processing of MEMS is required to implement 3D micro-devices that are difficult to realize using a surface micromachining process. Post-processing of fabricated and released MEMS dies is a challenging process. It requires diligent handling and precise alignment to avoid any damage to the released MEMS device.

A brief literature review of various post-processing techniques for MEMS devices is given in this chapter. The advantage and challenges of each techniques are evaluated for integration above released MEMS devices. A new post-processing technique to integrate a micro-polyhedron onto the rotor of a VCM using SU-8 is presented. The VCM with the assembled micro-polyhedron is able to rotate verifying that the post-processing technique is viable, clean and does not hamper the micromotor operation.

The post-processing technique is fast, relatively simple and does not require expensive sophisticated micro-manipulators. It can importantly be applied to released (or unreleased) rotary MEMS devices for the purposes of this thesis, which overarching objective is realizing a micro-polygon scanner.

4.1 Abstract

This technical note reports a rapid technique to post-process and assemble micro-components onto dies including released movable microstructures. The method is applied to microelectromechanical systems (MEMS) chips that were fabricated using a commercial process, PolyMUMPs from MEMSCAP. It allows the assembly of a micro-polyhedron over released micromotors and ensures that the micromotors remain fully functional. The micro-polyhedrons are fabricated using laser ablation and are spin coated with a thin layer of SU-8, acting as a bonding layer. Then, they are bonded to chips that are placed on a 3D integration platform with a navigating mask, which protects the released structure during the subsequent assembly steps. The resulting micro-polyhedron-integrated-micromotors were tested and found to rotate similarly to devices without micro-polyhedrons, demonstrating that the developed procedure can be applied for post-release 3D integration of MEMS without significantly affecting the mechanical performance of the devices.

Keywords: Microassembly, MEMS, PolyMUMPS, MOEM, Micromotor

4.2 Introduction

Microelectromechanical systems (MEMS) technology has been used to implement highly miniaturized devices that can integrate several functions, including mechanics, electronics, optics and fluidics, onto a single silicon chip. MEMS devices typically have a small footprint, low power consumption and low-cost owing to batch-fabrication. Multi-projectwafer (MPW) fabrication processes provide the most practical route for cost effective and fast prototyping of MEMS. Each MPW technology consists of specific materials and imposes lithographic constraints to device design. Also, many of these techniques prohibit complex three-dimensional fabrication. Therefore, manipulation and post-processing can be required on fabricated released dies to assemble a desired system.

Post-processing techniques and micro-assembly methods have been employed to manipulate surface micromachined 2D microstructures and assemble them into 3D, out-of-plane MEMS

devices. Out-of-plane rotation of a released hinged surface micromachined structures is widely adopted to assemble 3D microstructures (Pister, Judy, Burgett & Fearing, 1992). Quasi-3D-features can be fabricated using surface micromaching and the out-ofplane rotation can be obtained by using a variety of actuation mechanisms such as thermal shrinkage, surface tension force, magnetic force, strain mismatch force and solid-contact force (Wang, Maleki & Ziaie, 2008b). Hinged structure assembly suffers from mechanical slack in the hinges after the release of the flaps. Moreover, the degree of 3D assembly offered by these techniques is limited to the amount of out-of-plane rotation of the hinged structure. Assembly of 3D microsystems is also performed by joining micro-parts one-by-one sequentially using a pick-and-place strategy to manipulate the micro-components. This method offers six degrees of freedom for manipulating the micro-components but requires a passive microgripper which increases the procedure's complexity (Dechev, Cleghorn & Mills, 2004; Sin, Lee, Popa & Stephanou, 2006). Microassembly using flip chip bonding is also used to integrate hybrid systems such as microfluidics with CMOS (Welch & Christen, 2013). However, the bonding pressure required for the flip chip interconnection between the hybrid components may damage released MEMS. Thus, using flip chip bonding for the assembly of micro-structures onto released MEMS is challenging. Another approach is a pushing-based strategy. that may allow higher position accuracy with limited manipulation flexibility (Zesch & Fearing, 1998). Hybrid manipulation techniques simultaneously employing a pick-and-place strategy and a pushing-based strategy can also be used to assemble the 3D microsystem (Wang, Mills & Cleghorn, 2008a), but such techniques require micro-components with a snap-lock mechanism, thereby increasing design complexity.

Post-processing of MEMS fabricated dies, especially those with released movable structures, is challenging. Processing steps including spin-coating, wet-processing and thin film deposition may cause stiction or failure of the movable MEMS structure. For example, microoptoelectromechanical systems (MOEMS), which are used in a wide range of applications such as telecommunication, optical imaging, displays, optical switches (Briere, Elsayed, Saidani, Berard, Beaulieu, Rabbani-Haghighi, Nabki & Menard, 2017) and laser printers (Holmstrom,

Baran & Urey, 2014), have been fabricated by post-processing MEMS dies. In (Elsayed, Beaulieu, Briere, Menard & Nabki, 2016), post-processing steps of dry/wet etching were performed on a MEMS die with a released movable structure in order to create smooth facets for efficient optical coupling. A thin coating of S1813 photoresist protected the movable structure and was dry stripped using oxygen plasma after post-processing. A MEMS rotating polygon micromirror with six facets based on an outerrotor wobble micromotor was fabricated and assembled using an silicon-on-insulator wafer with a deep reactive ion etching technique (Yasseen *et al.*, 1999c). The rotor of the assembled 3D device got damaged, while rotating at high speed, thereby limiting the maximum operational speed to 58 rpm. An optical switch based on a 3D rotating polygon scanner was constructed by assembling a micromirror on top of a variable capacitance micromotor (VCM) using a robotic micromanipulator (Basha, 2012b). The micromirror and VCM have a complex architecture and are fabricated using the PolyMUMPS commercial process, to facilitate the assembly process. Unfortunately, the operation of the assembled scanner was not reported. Thus, it is crucial that the post-processing and assembly technique should not hamper the functionality of the assembled 3D device. Here, we present a micro-assembly technique that allows the integration of a micro-polyhedron onto a released movable MEMS micromotor at the die-level. The technique does not require any wet processing of the released MEMS, avoiding stiction due to the liquid surface tension. Additionally, the last step in the MEMS fabrication process such as Poly-MUMPs, is the release of the MEMS using a wet etchant, and it requires the presence of etch holes in all the layers to facilitate the complete removal of the sacrificial oxide. Thereby, if the micro-components are attached to the MEMS device prior to release, they may block the etch holes, resulting in a partial release of the MEMS. Also, if hydrofluoric acid is the primary etchant used for releasing the MEMS, as in PolyMUMPs, then it could damage the attached micro-component prior to the release process. Thus, for such cases, the technique mentioned in this work enables micro-assembly without the risk of device damage. The method was applied on MEMS dies fabricated using a commercial process, PolyMUMPS from MEMSCAP, and allows to integrate a micro-component without stiction or failure of the released structures. The micro-polyhedron integrated micromotors (μPIM) were tested and found to rotate similarly to micromotors without the micro-polyhedron,

demonstrating that the micro-assembly procedure does not affect significantly the mechanical performance of the device. The main objective of the technique is to provide a low-cost and rapid prototyping method of micro-assembly with dies from commercial multi-user MEMS fabrication runs. Specifically, this technical note aims at demonstrating the applicability of the technique with rotatory MEMS. In the next section, the fabrication and assembly of the rotary micro-polyhedron is discussed. Experimental results showing the rotation of the μPIM are presented in section 3. The integration protocol adopted in this work is fast, low-cost and allows dielevel micro-assembly of micro-components to released rotatory MEMS.

4.3 Fabrication and assembly methodology

In this section, the integration process required to assemble a rotary micro-polyhedron is presented. First, the design and fabrication of a micro-polyhedron of size that can fit on the rotor is introduced, then the deposition of a bonding layer is discussed and finally the micro-assembly protocol is presented.

4.3.1 Design and fabrication of micro-polyhedrons

The 3D rotating μPIM consists of a surface machined micromotor on which a square shape micro-polyhedron is glued. The rotor of the micromotor is used as a rotary platform that supports the micro-polyhedron. A schematic of the micromotor along with images of the micro-polyhedron and motor are shown in figure 4.1. A rotatory three-phase VMC is used in this work. More details on its design and operation can be found in (Gour, Ménard & Nabki, 2020b). The rotor diameter is 600 μm and the micro-polyhedron will be attached to it as illustrated in figure 4.1(b). The square shape of the micro-polyhedron is chosen for simplicity and the micro-assembly protocol can be applied to assemble microstructures of any shape on released or unreleased MEMS. The layout of the micro-polyhedrons is designed to fit the size of the rotor and they are fabricated using laser ablation machining of 90 μm thin steel sheets.

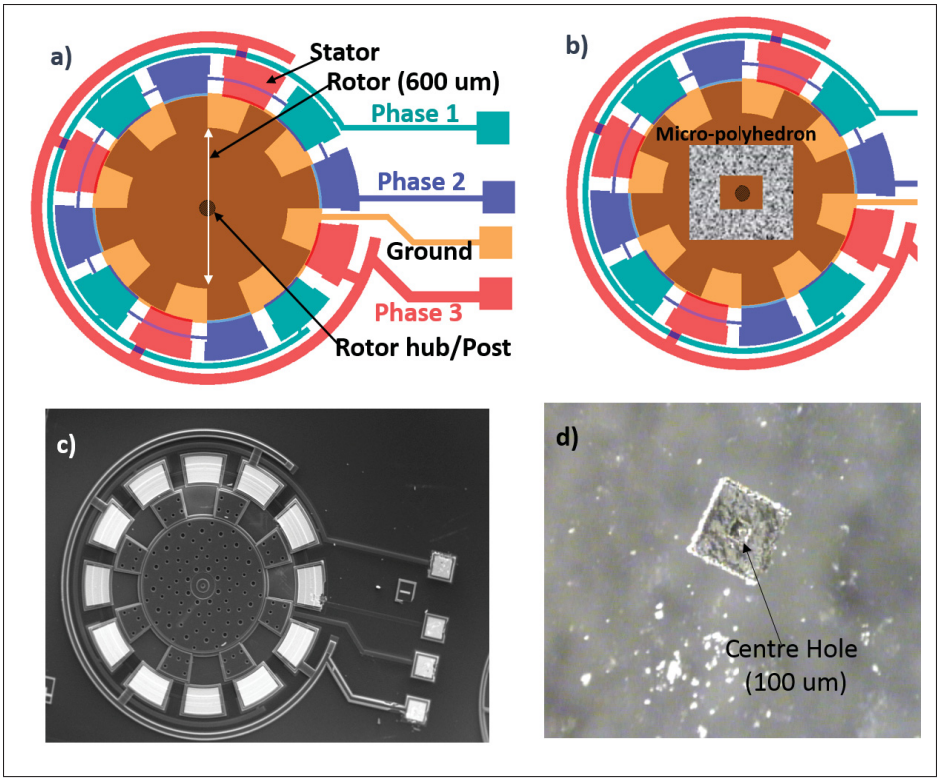

Figure 4.1 (a)Layout of the micromotor showing its different parts, (b) Top view showing the location of the micro-polyhedron on the rotor, (c) SEM image of the fabricated micromotor, (d) Microscope image of the polygon fabricated using laser ablation

All the steps of the micro-assembly process are illustrated in figure 4.2. Laser ablation is performed using an LPKF ProtoLaser U3 instrument using the following process parameters: 6 W of laser power and a 40 kHz laser pulse repetition rate. The wavelength of the laser is 355 nm and the feedrate is about 3.54 mil per minute to fabricate a single micro-polyhedron. Different sizes of micro-polyhedrons having edge lengths ranging from 380 μm to 200 μm were fabricated with enough margin to lie within the rotor boundaries. Each square shape micro-polyhedron has a square hole of 100 μm on a side at the centre acting as clearance to avoid damage to the micromotor hub/post. The laser ablation machining left micro-polyhedron size cavities on the steel sheet that can act as a slot to insert the micro-polyhedrons for processing. This slotted sheet, also referred as the navigating mask, is used to align the micro-polyhedron to the micromotor during microassembly. The navigating mask is attached over the micromotor using

a micro-positioning stage, such that the slot is aligned with the rotor and then the fabricated micro-polyhedron is placed onto the navigating mask and pushed into the slot using microprobes. It is important to note that the micro-polyhedrons fabricated using laser ablation, have rough sidewalls and need to be polished to create a reflecting surface for optical applications. In this work, unpolished micro-polyhedrons are used to illustrate the micro-assembly process. After fabrication, the micro-polyhedrons were cleaned using sonication with IPA and acetone for 10 min to remove the black residues formed during ablation. Manual pick and place with tweezers and microprobes is used to perform the global manipulation of the micro-size polyhedrons.

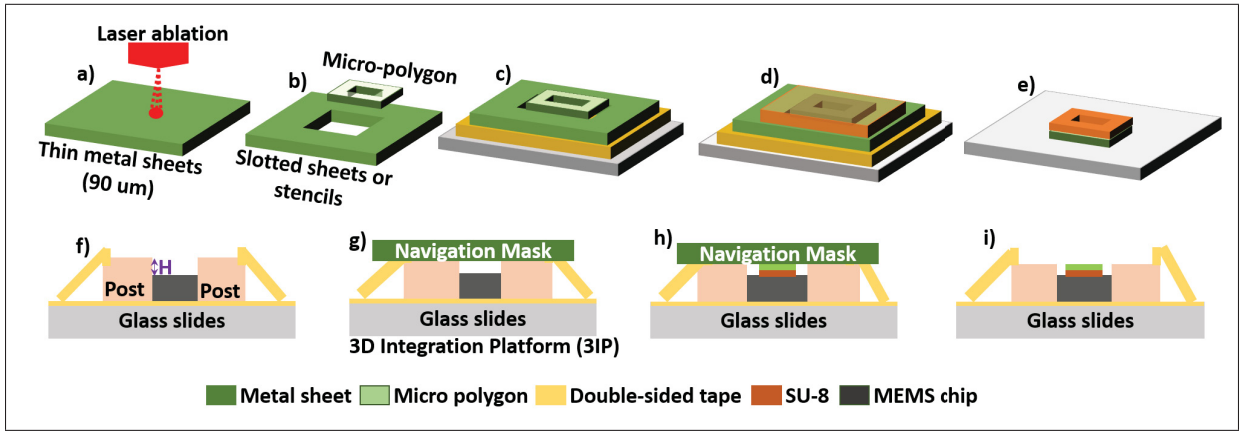

Figure 4.2 Steps involved in the micro-polygon assembly, (a) Laser ablation machining of the thin metal sheet, (b) Fabricated micropolygon and the corresponding stencil with cavities or slots, (c) Micro-polygon attached to the glass-slides using tape and stencil, (d) Spin coating of a thin layer of SU-8, (e) Formation of a dry film of SU-8 on the micro-polygon after heating, (f) The MEMS die and support posts are arranged and attached to the glass slide creating a height difference (H), (g) Configured 3IP with navigation mask aligned and placed over the MEMS die, (h) Micro-polygon accurately positioned on the rotor using the navigation mask, (i) Micro-polygon attached to the MEMS die after heating the assembled structure

4.3.2 Deposition of SU-8 on the micro-polyhedron

SU-8 is widely used in lithographic processes and MEMS structures because it has a low Young's modulus and excellent resistance to various chemicals. Furthermore, the literature clearly shows that crosslinked SU-8 is an excellent adhesive layer for wafer bonding. Wafer-level SU-8 bonding was used to fabricate devices such as thermal flow sensors (Vilares, Hunter,

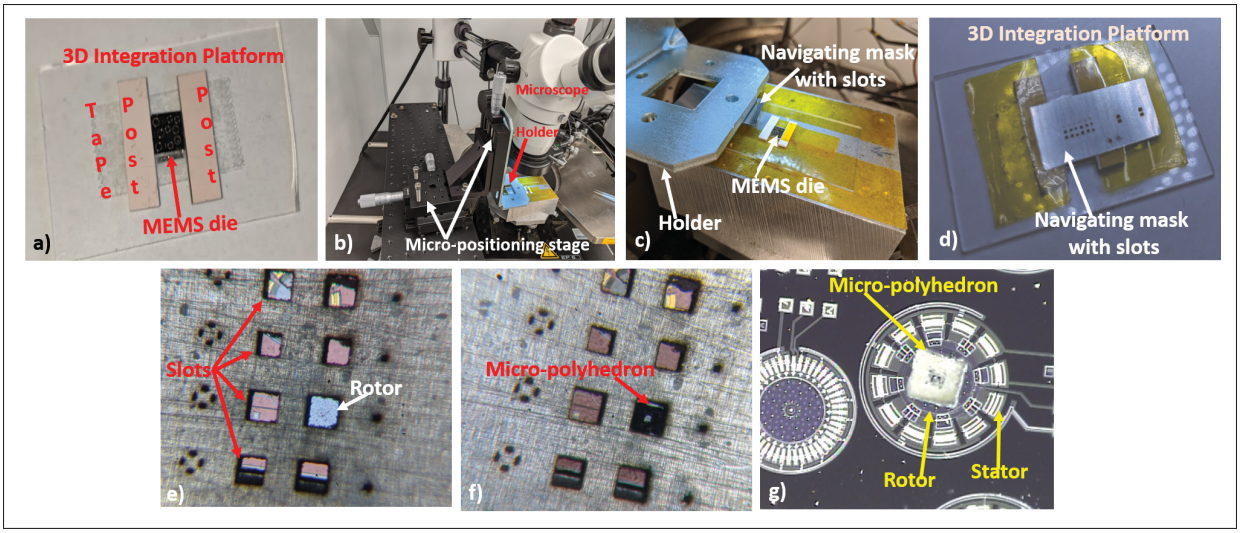

Figure 4.3 Images showing the system at various steps of the assembly protocol, (a) The 3IP with the MEMS die and support posts, (b) Image showing micro-assembly setup with micro-positioning stage, (c) The navigating mask before attaching it over the MEMS die, (d) The 3IP with the navigation mask attached to the support posts, (e) The micro-polygon placement site on the rotor and various slots on the navigation mask, (f) Image showing the micro-polygon placed over the rotor, (g) Micro-polygon attached to the MEMS die after heating the assembled structure, (h) Microscopic image showing the micro-polygon assembled over the micromotor

Ugarte, Aranburu, Berganzo, Elizalde & Fernandez, 2010), microfluidic devices (Svasek, Svasek, Lendl & Vellekoop, 2004a), ultrasonic transducers (Zhang, Adelegan, Yamaner & Oralkan, 2017), pressure sensors (Pang, Zhao, Du & Fang, 2008), GaAs Schottky diodes (Xie, Nadri, Alijabbari, Cyberey, Bauwens, Lichtenberger, Barker & Weikle, 2017), and was also used for MEMS packaging (Murillo, Davis, Keller, Abadal, Agusti, Cagliani, Noeth, Boisen & Barniol, 2010). Furthermore, uncross-linked SU-8 has several interesting properties, specifically as a planarizing sacrificial layer since it can provide a flat and stable surface. It can also be used as a glue for wafer bonding at low temperatures to fabricate microfluidic channels (Yu, Tay, Xu, Chen, Avram & Iliescu, 2006), micronozzles and microcavities (Abgrall, Conedera, Camon, Gue & Nguyen, 2007). This wafer bonding technique requires simple equipment such as a hotplate and a UV aligner (Yu *et al.*, 2006).

However, here we have used uncross-linked SU-8 to perform die-level bonding of a micro-polyhedron to a released MEMS structure. The proposed technique is simple and fast for fabricating 3D microdevices, allowing the integration of heterogenous components. Furthermore, it is a suitable and applicable solution in those cases where the substrate cannot withstand the SU-8 spin-coating procedure. A thin film of SU-8 is spin-coated onto the micro-polyhedron except at the outer sidewalls by placing it in the slots created during the laserablation machining, as shown in figure 4.2. The slotted sheet (navigating mask) is attached to a glass slide using double-sided tape. The micro-polyhedron is placed into the slots and pressed, so that it is glued to the tape and will not fly away during the spin-coating step. The following parameters are used to spin coat SU8-2002 of thickness ranging from 1.8 μm to 2 μm: (1) 100 rpm for 30 s; then (2) 1000 rpm for 30 s; and finally, (3) 500 rpm for 30 s. After spin coating of the sample with SU8, the navigation mask is pulled off from the tape, leaving the micro-polyhedron attached to the tape. The micro-polyhedron is then grabbed from the sides using tweezers and placed on a glass slide, heated at 100 $^{\circ}$C for 2 min to reflow the SU-8. The structure is then left to cool for 90 min at room temperature. A dry film of uncross-linked SU-8 that can act as glue when subjected to heat is obtained over the micro-polyhedron. Alternatively, the uncross-linked SU-8 can also be subjected to UV exposure for solidification, but that will add an extra step to the current protocol. Having a solid adhesive film onto the micro-polyhedron makes it easier to manipulate and handle it during assembly as compared to fluid adhesive films that may spill or cause stiction during the integration process.

4.3.3 Assembly of the micro-polyhedron onto the micromotor

The simplest method to fix the micro-polyhedron onto the micromotor would be to manualy pick-and-place it. This would require to grasp the micro-polyhedron with a microgripper or tweezer, position and then release it on the motor before heating the assembled system to bond the micro-polyhedron. Such manual manipulations are simple and cost-effective since they do not require sophisticated micro-assembly equipment but may lead to positional inaccuracy. However, unpredictable forces such as vibration, electrostatic forces, van der Wall forces, and

surface tensions, may deviate the released microstructure from its ideal position during assembly. Furthermore, these forces can destroy the devices present in the vicinity of the device being operated, due to mishandling of the released microstructure.

In order to increase the assembly accuracy and minimize the chance of damaging the micromotors, a 3D integration platform (3IP) is employed to adjust the orientation and ease the movement of the micro-polyhedron, as shown in figure 4.2. The 3IP has a simple architecture which consist of a navigating mask and two support posts that are arranged and placed to ease the assembly process. The support posts are made of a hard material such as glass and act as rigid supports. The MEMS die is attached to a glass slide using double-sided scotch tape and the two posts with same height are placed on opposite sides of the chip, as shown in figures 4.2(f) and 4.3(a). The height of the post is greater than the height of the MEMS die such that the posts are at the same level, but the chip is at a lower level creating a height difference H, as shown in figure 4.2(f). Thin stencils between the MEMS die and the glass slides can be placed to adjust the height difference H. The navigating mask is fixed to a holder using scotch tape and the holder is screwed to a custom micro-positioning stage as shown in figures 4.3(b) and (c). The 3-axis micro-positioner stage consist of a linear x-y translation stage from Thorlabs and a vertical translation stage, also from Thorlabs, for height adjustment.

Using the custom micro-positioner, the navigating mask is aligned and attached over the support posts using double-sided tape, resulting in a gap between the chip and the navigation mask. Only the micro-polyhedron placement site on the rotor is visible and can be easily accessed, as shown in figure 4.3(e). Then, the micro-polyhedron is placed over the navigation mask, moved, and pushed to the placement site. Thus, this enables precise obstruction-free movement of the microstructure across the chip while protecting the nearby devices from mishandling during the assembly. Moreover, the positional accuracy of the micro-assembly is improved and lies within the precision of the ablation process. The clearance between the polyhedron and the slot is approximately 5 μm. Thus, in this case the maximum translation positional error is 5 μm. The slots are designed such that only the part of the rotor required for assembly is exposed, blocking any lateral movement during assembly. If the clearance is too small, then the micro-polyhedron

may stick in the slot and will be difficult to release onto the MEMS. Conversely, if the clearance is too large, then the micro-polyhedron can exhibit large translational and rotational positioning errors and may result in misplacement and damage the MEMS device. Also, the centre hole in the micro-polyhedron is large enough to ensure that it does not touch the centre pin/post holding the rotor in place. The diameter of centre pin bearing is 60 μm, whereas the hole diameter at the centre of the micro-polyhedron is 100 μm, providing enough margin (i.e. 40 μm) to avoid damage to the centre pin/post.

Figure 4.3(h) shows the micro-polyhedron placed on the rotor after the assembly is subjected to thermal curing on a hot plate for bonding. The heating is done in steps as follows: (1) 100 ∘C for 1 min; (2) 110°C for 2 min; (3) 120°C for 2 min; and finally, the assembled structure is left to cool for 1.5 h at room temperature. The micro-polyhedron is firmly bonded to the micromotor and SEM images of the assembled structure are shown in figures 4.4 and 4.5.

The accuracy with which the microstructure can be placed over the released MEMS depends upon many factors. These include: (i) the clearance between the holes/slots of the navigation mask and the microstructure; (ii) the navigation mask sidewall roughness; (iii) the precision of the alignment equipment; and (iv) induced motion during the thermal curing step. The clearance around the micro-polyhedron in the navigation mask or stencil depends upon the process used for fabricating the holes/slots. Chemical processes such as wet etching can create holes/slots with smooth sidewalls, but their isotropic nature makes it challenging to control the shape of the slots. On the other hand, holes/slots fabricated using a physical process such as laser ablation or deep reactive ion etching (DRIE) have precise geometry with rough sidewalls. For cases where the clearance is small, rough sidewalls may tilt the micro-polyhedron during transfer from the slots causing offset placement. The precision of the alignment setup used for positioning the navigation mask over the placement site also contributes to the accuracy of the assembly method. For instances, fine alignment in the order of sub-micron can be achieved by using motorized mask aligners. In our case, manual standard translational micro-positioners (MP25 from MPI cooperation) with 5 μm resolution are used for simplicity. Also, the micro-polyhedron may displace from the placed site during the thermal curing of the SU8 to bond it to the MEMS. This

can be minimized by using a heating protocol with a slow thermal ramp, as suggested in this work. The demonstrated manual micro-assembly process is compatible with pick-and place techniques and could be scaled up for production by adopting industrial scale equipment to fabricate the navigation mask and microstructures, and by using automated robotic assembly lines for the micro-component integration. In this work, the immediate application of the technique lies in fabricating lab-scale 3D microdevices, providing rapid low-cost prototyping.

4.4 Experimental results

The rotatory motion of the assembled micro-polyhedron is characterized by applying a three-phase square wave signal to the VCM and observing the motion. The micromotor is a three-phase VCM with 12 stator poles and 8 rotor poles. Each group of four stators is connected to a common phase and the rotor is connected to ground. More details on the design of the micromotor are presented in (Gour *et al.*, 2020b). The rotational speed of the micromotor as a function of the frequency of the driving signal is determined by using the following equation (Gour *et al.*, 2020b):

$$\omega_r = 60\frac{f_{ele}}{N_{rp}}\, rpm, \tag{4.1}$$

where ω_r is the rotational speed of the micromotor, f_{ele} is the frequency of the applied excitation, and N_{rp} is the total number of rotor poles of the micromotor.

The testing procedure requires varying the peak voltage of the input excitation at a constant frequency until the rotation of the micromotor is seen. Under a microscope, the rotary motion of the micromotor is observed and recorded using a camera. Images of the rotating micro-polyhedron at different positions are shown in figure 4.6 where the edges of the micro-polyhedron are highlighted with coloured lines to indicate the motion. The assembled polyhedron rotated at a speed of 300 rpm by applying a three-phase square wave signal of 90 V at 40 Hz. The operational voltage is specific to this micromotor and could vary based on the device used as the

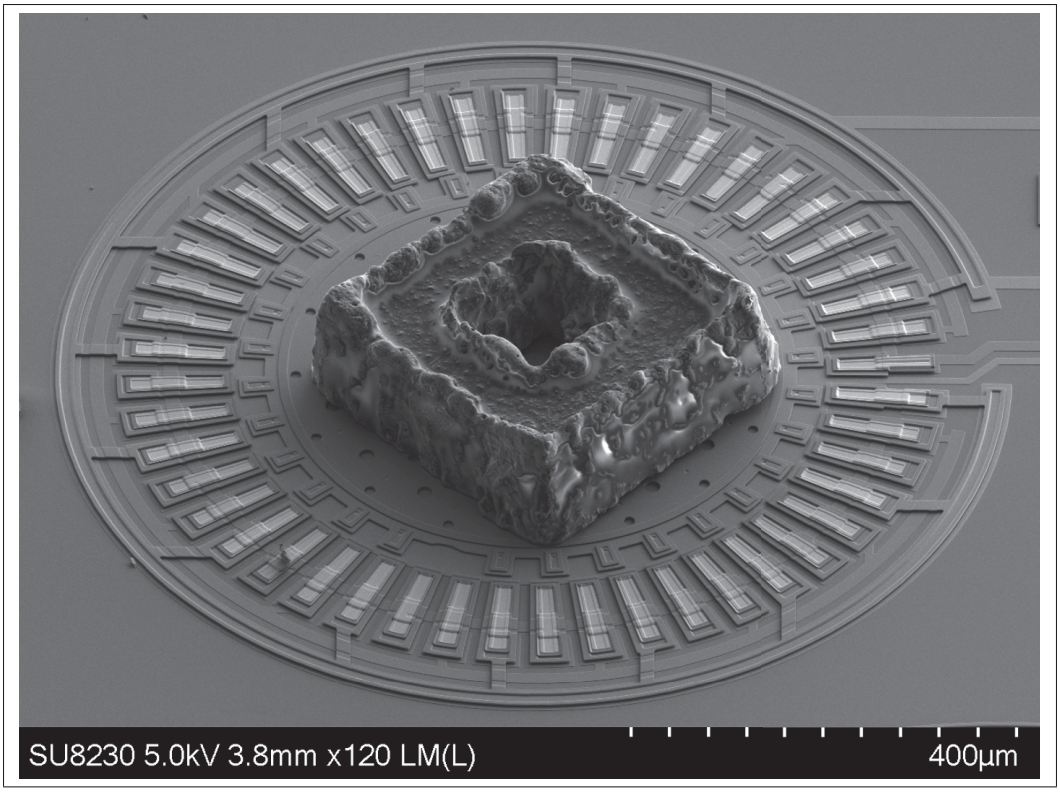

Figure 4.4 SEM image showing an isometric view of the VCM with the assembled rotary micro-polygon with rough sidewalls.

rotating platform. It also depends on the impact of the micropolyhedron on the rotation after assembly. Nonetheless, the higher driving voltage requirement post-assembly is expected to be a recurring trend. In comparison, a similar micromotor without a polyhedron can achieve the same speed at a peak voltage of 50 V. This can be explained by considering the increase in friction and load due to the addition of the micropolyhedron weight on the micromotor. The mass of the polysilicon rotor is 1.32×10^{-9} kg while the mass of the steel polyhedron is 1.08×10^{-7}kg, making the assembled structure approximately 100 times heavier than the rotor, requiring more torque to initiate motion. Moreover, the mechanical bearings of the rotor are in contact with the ground plane and are constantly rubbing the underlying layer during rotation. Thus, the friction between the mechanical bearings and the ground plane will increase due to the weight of the micro-polyhedron. Finally, while unlikely due to the support dimples beneath the rotor, it is possible that some deformation of the rotor could result from the mass of the micro-polyhedron

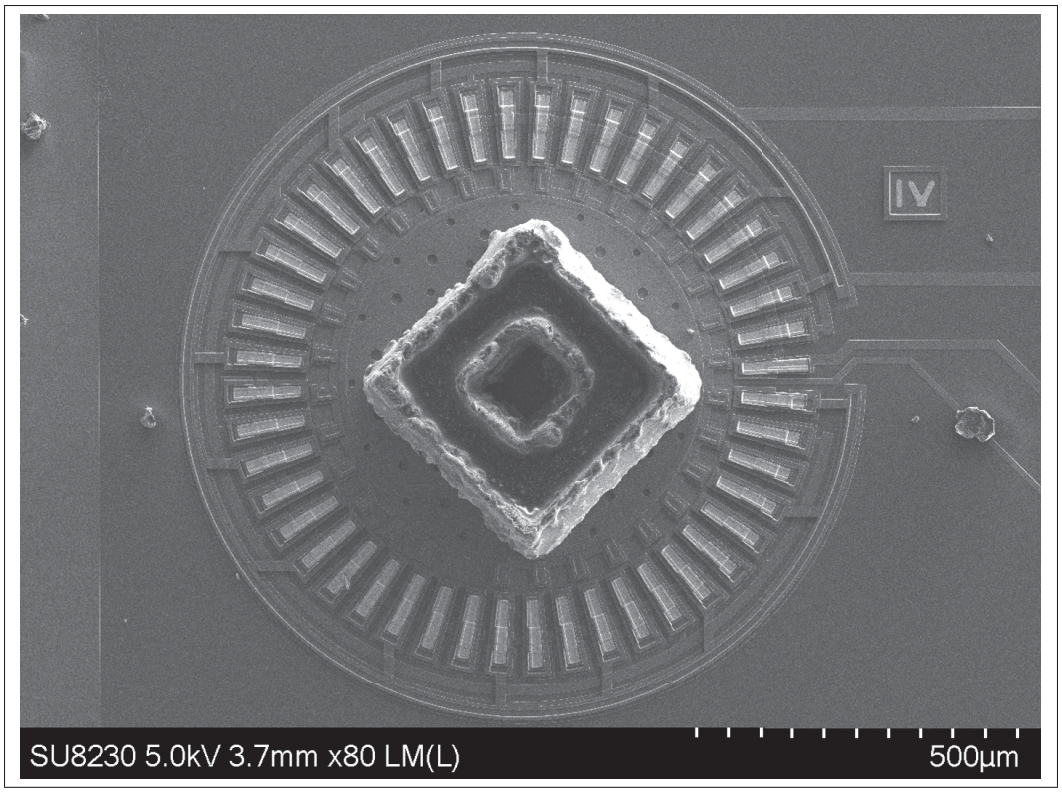

Figure 4.5 SEM image showing a top view of the assembled rotary micro-polygon onto the MEMS VCM rotor

and cause vertical misalignment of the capacitive overlap between the rotor and the stator. Therefore, due to one or more of these effects,the higher voltage that was required to induce motion of the micromotor is not unexpected, as sufficient rotational torque is required to rotate the assembled structure at the same frequency to that of the micromotor operated without the micropolyhedron.While rotating, the polyhedron remained firmly attached to the rotor and did not fly away, confirming that a strong joint was formed by the SU-8. The bonding protocol was successfully applied on seven released MEMS micromotors to confirm the repeatability of the process sequence before being performed on the final prototype. As discussed in section 4.3.3, the positional accuracy of the assembly process depends upon the clearance between the slot and the attaching microstructure, which is about 5 μm in this case. Along with the other alignment accuracy factors described in section 4.3.3, the overall accuracy achieved here is of about 20 μm. A MOEMS device consisting of a polished micro-polyhedron attached to the micromotor

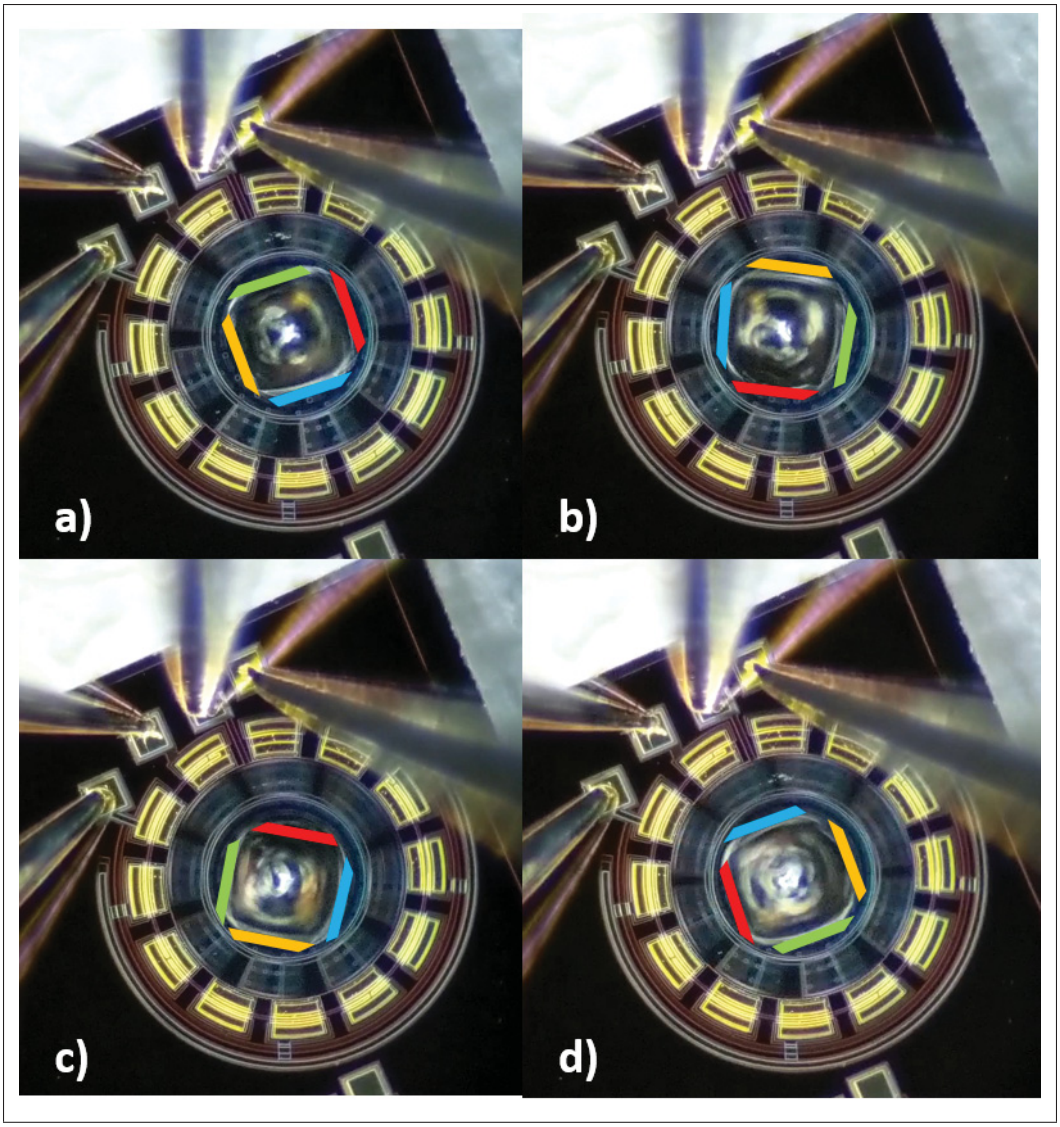

Figure 4.6 Microscope images showing different angular position of the rotating micro-polygon. The sides are accentuated in different colours to highlight the motion

could be fabricated by employing the aforementioned technique for applications such as optical switching and optical scanning. Note that the micro-polyhedron is placed away from the edges of the rotor arm, such that the impact on the rotor-stator alignment due to post-deposition stress is not significant. Also, the rotor is supported by dimples such that bending in the rotor film is reduced as compared to cases where the microstructure can bend in the vertical direction after the micro-polyhedron deposition like a cantilever. For case, in which the released structure

can bend up and down during the micro-component deposition, the current method could still be applied by using an appropriate navigation mask. In that case, even though the cantilever structure bends up or down, the attaching structure will not slip away and still be held at the placement site by the navigation mask.

4.5 Conclusion

A novel post-processing and micro-assembly technique to join microparts to dies having released movable structures was presented. The protocol was applied to MEMS dies fabricated with a commercial process, i.e. PolyMUMPs from MEMSCAP. The technique allows to bond a microstructure onto diced and released MEMS dies enabling a fast and low cost assembly of microdevices. A micro-polyhedron was bonded to a pre-released micromotor using uncross-linked SU-8. The micro-polyhedron is fabricated using laser-ablation; aligned and placed using a 3IP; and bonded to the micromotor by thermal curing. The 3IP is a versatile, reconfigurable and cost-effective system for positioning discrete microstructures onto released or unreleased MEMS dies. The assembled rotary μPIM was tested and rotated as expected, but it expectedly required a higher actuation voltage than that required for the micromotor without a micro-polyhedron. Nonetheless, the post-processing protocol proposed still allowed the micromotor to operate unhindered with a relatively small impact on its operation. Thus, the protocol can be applied to implement complex MEMS devices, where heterogonous microassembly of discrete component is required.

Acknowledgments

The authors would like to acknowledge the financial support of the Natural Sciences and Engineering Research Council of Canada (NSERC) and the Fonds de recherche du Québec Nature et technologies (FRQNT), and foundry support provided by CMC Microsystems.

CHAPTER 5

A HIGH-SPEED CHIP-SCALE ROTARY POLYGON OPTICAL SCANNER BASED ON A MICROMOTOR INTEGRATED WITH A MICRO-POLYHEDRON MIRROR

Amit Gour[1] , Michael Ménard[2] , Frederic Nabki[1]

[1] Departement of Electrical Engineering, École de Technologie Supérieure,
1100 Notre-Dame Ouest, Montréal, Québec, Canada H3C 1K3

[2] Department of Computer Science, Universite du Quebec a Montreal,
201 President-Kennedy Avenue, Montréal, Québec, Canada H2L 2C4

Paper submitted to Nature Microsystem & Nanoengineering, August 2021.

Preface

In this chapter, a brief literature review of different types of MEMS scanners is presented. Each reviewed work is then investigated to determine the advantages and drawbacks it offers, for applications such as LIDAR, where high scan speed and wide angular scanning range is required. A literature review for the different types of MEMS rotary scanners with fabrication method used and design challenges is introduced.

A new architecture of micro-polygon scanner for chip-level implementation is introduced. The chip-level micro-polygon scanner consists of a high speed variable capacitance micromotor (VCM) and a micro-polyhedron mirror. The design and implementation of the micro-polyhedron mirror are discussed whereas the details of the VCM is presented in chapter 3. The micro-assembly process discussed in chapter 4 is used to integrate the micro-polyhedron mirror with the VCM.

The envisioned micro-polygon scanner is implemented and its electrical and optical characterization results are presented and discussed. The device offers the advantages of small footprint, low power consumption and constant scan rate that are crucial in various applications such as biomedical imaging, LIDAR and so on. Fundamentally, it brings to the micro-scale the advantages of the polygon scanner concept.

5.1 Abstract

Biomedical imaging, light detection and ranging (LIDAR), optical communications and barcode reading are examples of areas where optical beam steering systems are needed. Micro-opto-electro-mechanical system (MOEMS) based mirrors with a suitable actuation range are often used for optical beam scanning applications. While several MOEMS scanners have been reported, they often have limitations with respect to their range of motion, field of view, mass, size and fabrication cost. In this work, we present a rotary micro-polygon scanner based on an electrostatic variable capacitance micromotor for laser beam steering applications. The miniaturized scanner consists of a hollow micro-polyhedron mirror with a base radius of 200 μm and a height of 400 μm. It is mounted on the rotor of a variable capacitance micromotor using an epoxy-based adhesive. The rotor has a diameter of 600 μm and is 2.5 μm thick. The micromotor was fabricated using a commercial three-layer polysilicon surface micro-machining process (PolyMUMPs) and the micro-polyhedrons were fabricated using a commercial bulk micro-machining process (PiezeoMUMPs). A variety of micro-polyhedrons were designed and fabricated, including devices with four, eight, and twelve facets. After fabrication of the components, the micro-scanner was assembled and operated under atmospheric conditions using a three-phase square wave excitation ranging from 0 V to 200 V and achieved rotational speeds up of to 2100 rpm. An optical laser beam with a wavelength of 632 nm was reflected off the sidewall of the rotating micro-polyhedron, achieving a scanning angular range of 57.88°, an angular scan rate of 220 radians per second and a scan speed of 25,200 lines per minute or 420 lines per second with a 12 sided micro-mirror. This rotary micro-scanner can provide high scanning speeds and a wide scanning field of view with a footprint of about 1 mm^2, which is suitable to implement chip-level high-performance micro-beam steering systems for various applications, including LIDAR scanners and optical switches.

5.2 Introduction

Optical scanning is used in a wide range of applications including telecommunications, barcode readers, light detection and ranging (LIDAR) systems, optical imaging systems, optical displays,

optical switches and laser printers (Holmström, Baran & Urey, 2014). Optical scanners with compact size, fast beam scanning and high resolution are required to push the boundaries of such applications. Polygon scanners(Li, Huang, Burgio, Heath & Lee, 2017), acousto-optic scanners(Wang, Zhang, Aleksov, Salama & Kar, 2016), Risley-prism scanners(Li, Sun, Yi & Zuo, 2016) and galvanometric scanners(Yoo, Ito & Schitter, 2016) are common techniques for laser beam scanning. Recently, LIDAR has gained popularity due to its application in autonomous cars and other unmanned vehicles where it acts as a core technology for remote sensing and environment monitoring(Harrison & Newman, 2008; Thakur, 2016; Hecht, 2018; Moosmann & Stiller, 2011; Gong, Li, Luo, Wen, Wang & Zelek, 2019). Advanced driver assistance systems (Thakur, 2016) based on LIDAR are required to cover a wide range of specifications, including wide or narrow fields of view (FoV), high scan rate, and long or short operating range. Typically, commercial LIDARs use a rotating mirror or a polygon scanner (NIDEC-COPAL-ELECTRONICS, 2020; Miradatechnologies, 2018; PLL, 2019; Weber, 2018; Moosmann & Stiller, 2011) actuated by an electric motor for beam scanning, resulting in a large system. Nevertheless, these devices provide a wide FoV with straight and parallel scan lines having a uniform speed, making them highly popular scanning solutions for LIDAR sensors. The scanning mechanism used in a LIDAR system is a key parameter to determine its overall size, mass and power consumption. LIDARs with a rotating scanner configuration can achieve the performance required but are bulky and expensive. Moreover, when these scanning systems are installed on a vehicle, they often disrupt the vehicle design, which is a major drawback for commercialization. Thus, a compact, i.e. match-box sized, affordable and reliable scanning unit for large-scale applications is needed and its development presents a significant challenge.

Scanners based on non-mechanical structures such as acousto-optic scanners employ refraction or diffraction to redirect the laser beam. They offer high scanning speeds but a small angular range compared to mirror scanners. They also suffer from high optical power losses. For instance, miniaturized and monolithic scanners using an optical phase array (OPA) can be implemented using silicon photonics that can deliver wide scanning angle at low operating voltage (Chung, Abediasl & Hashemi, 2018). However, the technology readiness level of OPA-based LIDAR

scanners is low due to several design trade-offs such as light source integration, grating coupler design, integration with driving electronics and thermal management (Hsu, Li, Solano-Rivas, Gohil, Chan, Moore & Donzella, 2021). Galvanometric scanners are widely used in laser displays and confocal microscopy due to their high speed, accurate movement, and good scanning resolution. However, to operate along two axes, they need two separate scanners mounted perpendicularly, resulting in a device that is too bulky for portable systems (Hafez, Sidler, Salathé, Jansen & Compter, 2000). Also, galvanometric scanners are unable to provide a linear scan rate due to the use of two resonating mirrors, limiting their applications to high-speed raster scanning systems (Ji, So & Kim, 2019). High-speed optical scanners are also realized by using rotating mirrors based on motors (Holmström *et al.*, 2014). These scanners consists of a polygon shaped mirror mounted on a motor to deflect the incoming laser beam and hence generating a line scan. The rotational motion of the polygon scanner provides a constant angular scan rate and fast scanning speed making it a key element in many applications such as digital scanners, laser printers, barcode readers and swept-source lasers (Chiang, Khanna, Mikkilineni, Ortiz Segovia, Suh, Allebach, Chiu & Delp, 2009; De Loor, Penning & Slagle, 2014; Yun, Boudoux, Tearney & Bouma, 2003; Oh, Yun, Tearney & Bouma, 2005). A high scanning frequency can be obtained at the expense of the scan angle with polygon scanners by increasing the number of facets of the polygon mirror, resulting in record-breaking image acquisition rates for optical coherence tomography and confocal microscopy (Duma & Podoleanu, 2013). Rotating mirror scanners are also used in LIDAR systems due to their ability to provide a wide FoV, but these polygon scanners suffer from high power consumption and have a large footprint (Luo, He, Lu & Ni, 1994). However, they are widely used in commercial laser scanners since they have shown the largest maximum deflection angles and the fastest angular speeds to date.

With the advent of applications requiring environment monitoring, such as surveillance drones, self-driving cars, and autonomous underwater vehicles, there are tremendous efforts to realize miniaturized scanning systems. Large-scale deployment of these systems requires scanner modules that are smaller and more efficient than macro-optical systems. Accordingly, LIDAR scaling can be achieved by using a scanning mechanism based on micro-electromechanical

systems (MEMS) technology. Scanning or switching mirrors based on MEMS actuators can reduce the size and cost of scanning systems (Wang, Watkins & Xie, 2020c). There are a variety of MEMS scanners that have built-in electrostatic actuation, external magnetic actuation or external galvanic actuation (Cho, Han, Ju, Jeong, Park, Kim, Bu & Ji, 2015). The latter provides large scan angles by using two single-axis mirrors for 2D scanning but makes the system rather large. Moreover, galvanometric MEMS mirrors are resonant devices, and thus are operated at their resonant frequency, providing non-uniform speed and non-linear resolution. On the other hand, polygon scanners operate at a constant speed offering a uniform scan rate, have a wide scanning range and better resolution than galvanometric mirrors. Thus, a MEMS based rotary polygon scanner offers a great alternative to exploit the fabrication benefits of MEMS technology and the scanning performance of polygon scanners.

A small footprint, light weight, low power consumption and low-cost due to batch-fabrication are a few of the benefits of MEMS-based optical scanners. Nonetheless, the implementation of a rotary polygon scanner using MEMS technology that is capable of full revolutions is challenging. The choice of the actuation mechanism, the development of the fabrication process and of the micro-assembly procedures are the key challenges for making a MEMS optical scanner. Several micro-assembly mechanisms and post-processing techniques have been developed to manipulate surface micro-machined 2-D micro-structures to construct 3-D, out-of-plane MEMS devices. In (Brière, Beaulieu, Saidani, Nabki & Menard, 2015), a MEMS scanner for optical switching applications was designed and fabricated to achieve a large angular displacement. The scanner was fabricated using the SOIMUMPS process and was able to rotate by ±8.5° in the X-Y plane at 290 V. A MEMS rotating polygon micromirror with six facets based on a outer-rotor wobble micromotor was fabricated using a silicon-on-insulator (SOI) wafer (Yasseen, Mitchell, Smith & Mehregany, 1999b). The rotor diameter was 1.4 mm and flew away when rotating at high speeds, thereby limiting the maximum operational speed to only 58 rpm. In (Tu, Fanchiang & Liu, 2005), deflecting flexible structures employing analog controls are reported to rotate micro-mirrors but the rotation angle of the micro-mirrors was limited to 1.5 °. In (Basha, 2012a) a 3D rotating polygon scanner was constructed by assembling a micromirror

on top of a variable capacitance micromotor using robotic micro-manipulators. A specially designed micromirror compatible with a variable capacitance micromotor was used to facilitate the assembly and was fabricated using the PolyMUMPS process. However, no rotation of the assembled scanner was reported. Therefore, developing a rotary micro-scanner based on MEMS technology remains challenging and requires solutions to a multitude of technical difficulties.

Accordingly, in this work, a rotary micro-polygon scanner with a 12 sided micromirror is designed, fabricated, assembled and tested. The size of the micro-scanner is 1 mm × 1 mm × 1 mm and it is capable of 25,200 line-scans per minute while covering an angular range of 57.88°. This integrated beam steering system consists of a reflecting movable high-aspect ratio element that interacts with a laser beam propagating parallel to the surface of the substrate. Traditional surface-micromachining technology produces planar films with thickness on the order of a few microns, which is very small compared to the diameter of a collimated laser beam. Thus, extra processing steps are required to make a three-dimensional structure with a height suitable to steer a laser beam. Therefore, additional components and space are required for precise alignment, increasing the challenges and complexity of scanner miniaturization. The assembled 3D micro-polygon scanner presented here is suitable for scanning applications requiring a wide FoV, small footprint, and low power consumption. Also, we estimated the output power of the reflected beam for potential optical switching or attenuation applications.

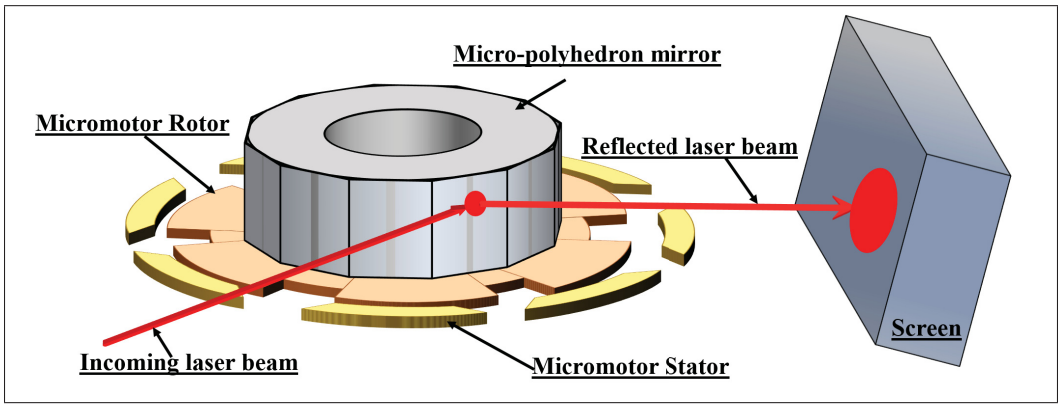

Figure 5.1 Diagram illustrating the design of the micro-rotary scanner.

The various parts of the micro-scanner (μRS) are shown in figure 5.1 and consist of a micro-polyhedron mirror (μPM) attached to the rotor of a micromotor. The μPM can rotate at a constant speed and perform optical line scanning. The μPM is attached to the micromotor using micro-assembly. The angular scan range and the scan line rate can be tuned by using a μPM with a suitable number of sides for the target application. The μPM has smooth sidewalls resulting in specular reflection of the incident laser beam and the reflected beam is imaged on a screen for demonstration purposes in this work. A three-phase variable capacitance micromotor (VCM) based on electrostatic actuation is used as the rotary platform and is capable of rotating at high speed with low power consumption. When the μPM starts rotating, a line scan of the reflected laser beam is observable on the screen. The frequency of the actuation signal of the micromotor determines the rotational speed of the μPM. Accordingly, the rate of the generated scan lines varies with the frequency of the excitation signal. The size of a single μRS is approximately 1 mm $\times$ 1 mm $\times$ 1 mm, making it a highly miniaturized and light-weight polygon scanner that can be integrated in chip-scale microsystems. The chip-scale implementation of the μRS demonstrated here involves : i) the design and fabrication of a chip-scale rotary platform; ii) the design and fabrication of a μPM that can be attached to the rotary platform; and iii) a micro-assembly technique to integrate the μPM with the rotary platform (i.e. the micromotor).

The implementation of the various components of the μRS and its characterization results are discussed in the next section. The design of the VCM, the design of the μPM, and the micro-assembly of the μRS are presented in the materials and methods section.

Results

Commercial multi-project wafer processes are used for the fabrication of the various components of the μRS. The VCM is fabricated using a surface-micromachining process and a bulk micro-machining process is used for the fabrication of the μPM. A micro-assembly technique is employed to integrate all of the components, resulting in a 3D chip-scale micro-scanner. The assembled μRS is experimentally tested and the results are discussed in this section.

Device fabrication results

Micromotor

The VCM was fabricated using the PolyMUMPs process (Cowen, Hardy, Mahadevan & S.) and a scanning electron microscope (SEM) micrograph of the device is shown in figure 5.2. Optical imaging is used to verify that there are no joints or contacts between the rotor and stator poles. In addition, the microwires connecting the input pads to the micromotor poles are electrically tested to identify short or open connections. The rotor acts as the rotary platform, and its free movement is verified by pushing it using micro-probes without any excitation. This ensures that the rotor is fully released and capable of motion without adhering to the substrate or the bearing axis. Various designs of VCMs were tested without micro-polyhedron mirrors, as reported in (Gour, Ménard & Nabki, 2020a), and most of the designs were readily able to achieve rotational speeds greater than 2000 rpm. Also, a specific VCM design with a stator to rotor gap of 2 μm can provide maximum speeds of up to 7,875 rpm. It was observed that a few devices having stator to rotor gaps of 2 μm suffered from incomplete etching of the gap making a connection between the rotor poles and the stator poles, precluding from correct operation. Consequently to avoid this issue, in this work, a VCM with a stator to rotor gap of 2.5 μm was used.

Micro-polyhedron mirror

Micro-polyhedrons with 4, 8 and 12 sides were fabricated using the PiezoMUMPs process (Cowen, Hames, Glukh & Hardy, 2013), and a μPM with 12 sides was selected to implement the μRS presented in this work. Images of the top and bottom of the μPMs are shown in figure 5.3. The μPMs are obtained from the deep reactive ion etching (DRIE) of the backside of the silicon wafer, creating high aspect ratio sidewalls suitable to act as mirrors to deflect a laser beam. Also, the DRIE process produces etched surfaces with low roughness, allowing for a reflective μPM. Moreover, the μPMs are firmly attached to the die with thin anchors or teethers in the silicon device layer, as shown in figure 5.3a. These can be easily broken with a micro-probe to release

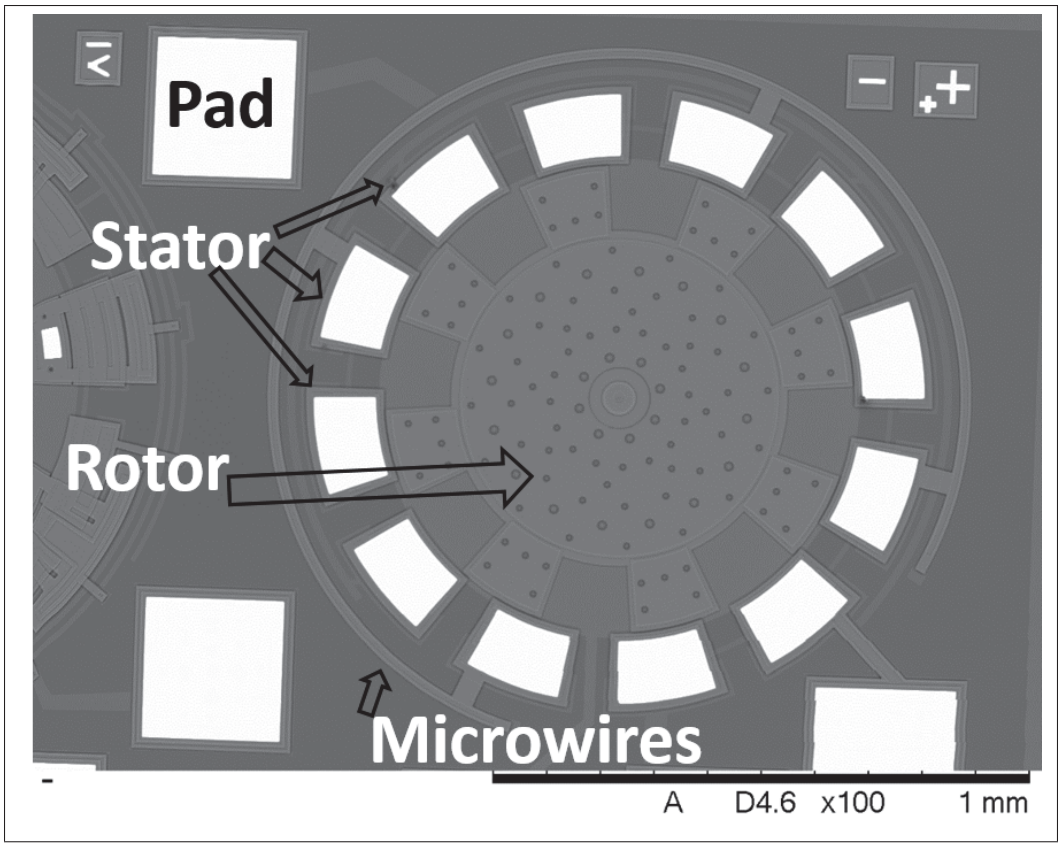

Figure 5.2 SEM micrograph of the micromotor fabricated using the PolyMUMPs process.

the μPM. This significantly facilitates the handling and manipulation of the μPMs during the micro-assembly operation. The DRIE step of the PizeoMUMPs process allows the formation of large trenches on the backside of the substrate but it is impossible to make a small recess inside the μPM from the back. A small recess is required to ensure that the μPM never touches the bearing post/axis of the VCM. Thus, a central recess in the μPM is created by etching the device layer, as illustrated in figure 5.3b. The diameter of the circular recess is 100 μm, which is sufficiently large to keep the edges of the μPM away from the bearing post/axis of the VCM after the micro-assembly process. Moreover, the depth of the recess is 10 μm, which is greater than the height of the VCM bearing post/axis to avoid any vertical contact. As apparent in figure 5.3c and figure 5.3d, the μPM is relatively thick. It has a thickness of 400 μm, base width of 200 μm,

and each of the 12 sides of the polyhedron are 100 μm long. The resulting silicon μPM has a mass of approximately 123 μg.

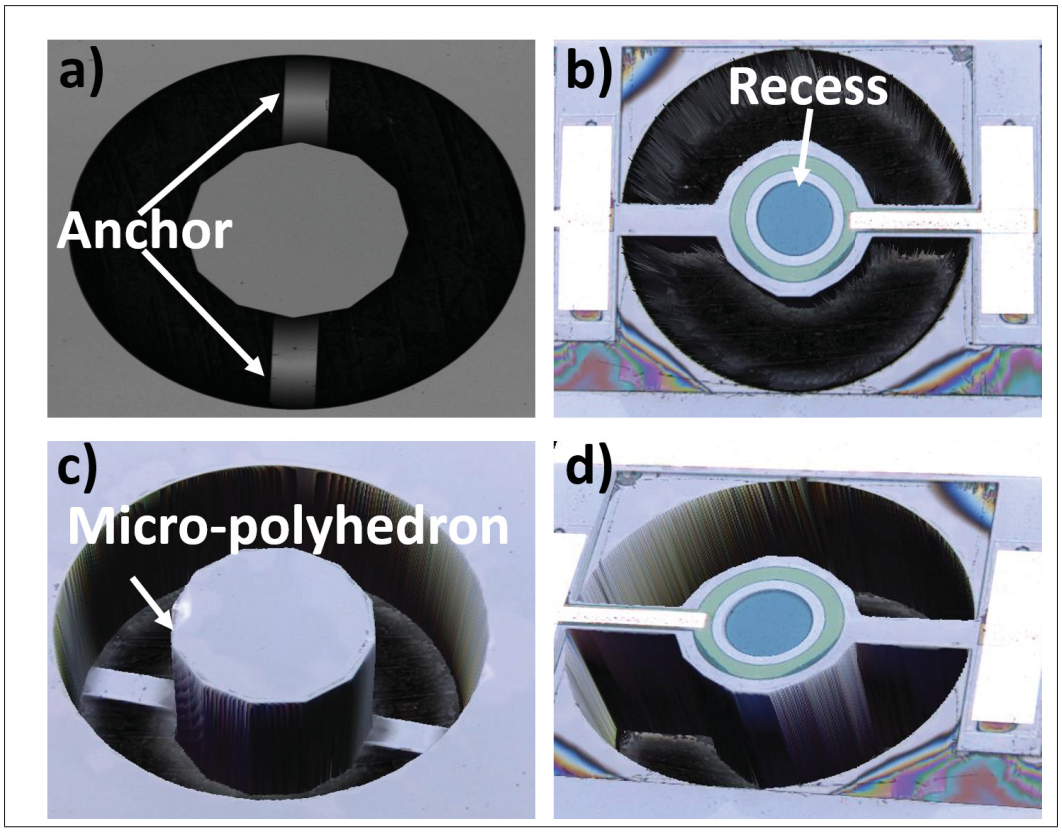

Figure 5.3 Images of the micro-polyhedron fabricated using the PizeoMUMPs process: a) top view of the bottom side of the micro-polyhedron; b) top view of the top-side; c) isometric view from the bottom; and d) isometric view from the top.

Experimental characterization of the scanner

A μPM was mounted on a VCM to build a μRS with the process described in the Materials and Methods section below. The characterization of the μRS is carried-out by activating the micromotor and focusing a laser beam onto the sidewalls of the rotating μPM. A block diagram of the experimental setup is shown in figure 5.4a. A DC-signal is amplified and supplied to a three-phase square wave generator to actuate the micromotor. The light from a 632 nm HeNe

laser (OFV-534 from Polytec) is focused onto the sidewall of the μPM. The laser power is less than 1 mW and the laser head optics can focus the beam down to a spot size of 1.5 μm using a 20X objective or 5 μm using a 5X objective. The collimator on the laser head can be adjusted to modify the spot size and a screen is placed near the edge of the chip to visualize the reflected signal. The maximum three-phase input voltage to the micromotor is limited to 200 V peak-to-peak in order to avoid dielectric breakdown in the gap between the rotor and the stator. After the optical alignment of the laser beam, the actuating three-phase signal is applied, and a CCD mounted onto the microscope captures the scanner motion and the beam position on the screen. The laser head also has a camera that captures a side-view of the polyhedron mirror as shown in figure 5.4c. A simplified top-view of the system, including the chip housing the μRS, is shown in figure 5.4b.

The voltages at which the μPM rotates and the maximum frequency that can be applied at those voltages was characterized to determine the mechanical performance of the μRS.

However, initially, the μPM remained motionless irrespective of the applied excitation in the initial testing. It was expected that the mirror would move at a high input voltage since the VCM torque is proportional to the applied voltage. Nevertheless, it was noticed that the increase in the inertial mass of the rotor due to the loading of the μPM had significantly increased the static friction of the rotor, precluding the startup of the VCM. The 0.5 μg rotor is a 2 μm thick layer supported by four dimples having a diameter of 6 μm and a height of 750 nm. These were included to minimize friction of the rotor during the rotation. Therefore, the mass of the loaded rotor (i.e., with a micro-polyhedron having mass of 123 μg) considerably increases the inertia, and as a result, it is impossible to start rotating when a voltage is applied.

Consequently, modifications to lighten the μPM were required to enable the rotary motion of the μRS. The dimensions of the μPM were chosen to ensure that it is sufficiently high and wide to reflect the laser beam entirely in order to minimize optical losses. When reducing its mass, the dimensions of the side-walls should not be modified to avoid compromising its optical characteristics. Accordingly, this issue was resolved by drilling a hole through the center of the

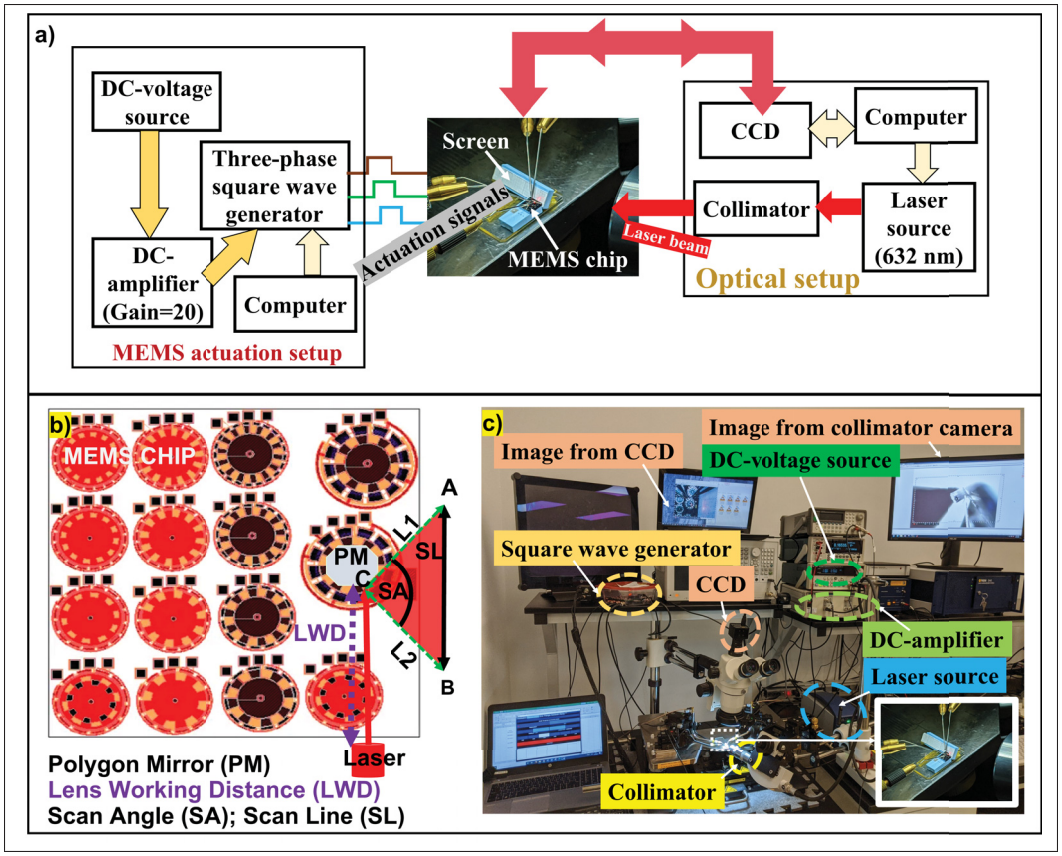

Figure 5.4 a) Block diagram showing the experimental setup required for micromotor actuation and optical characterization; b) diagram depicting the chip housing the μRS, which also includes different VCM designs, along with the incident laser beam and reflected beam; and c) image showing all of the instruments used in the characterization.

μPM using laser ablation to reduce its mass, while maintaining the optical requirements. The laser ablation technique is simple, fast, and capable of precisely removing the unnecessary mass from the desired location on the μPM structure. A SEM micrograph of the laser ablated μPM is shown in figure 5.5a. As can be seen, a cylinder having a diameter of 250 μm and centered within the μPM was removed by laser ablation. The ablated μPM has a mass of 75 μg, which is 39.1% less than the original structure. This method allowed to remove a significant portion of the mass without compromising the functionality of the μPM . The ablated μPM is attached to the micromotor using the same micro-assembly technique presented in the Materials and Methods section. SEM micrographs of the assembled system are shown in figures 5.5b-d. With

the aforementioned modification to the μPM, the device was able to operate as a results of the reduced mass.

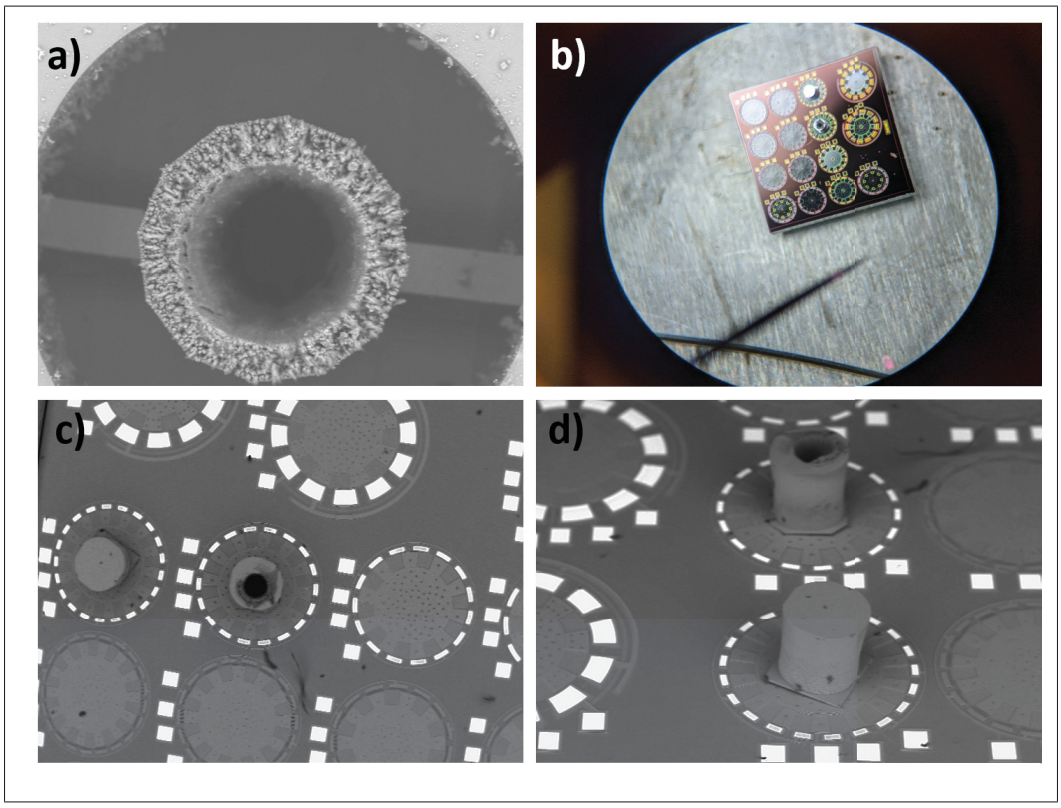

Figure 5.5 a) SEM micrograph of the laser ablated μPM; b) microscopic image of the assembled micro-scanner; c) SEM micrograph showing the top-view of the micro-scanner; and d) SEM micrograph showing isometric view of the micro-scanner.

Electrical characterization

The electrical characterization of the μRS was performed to measure its power consumption, rotational speed, and actuation voltage. This was done by applying the excitation voltage to the VCM loaded with an ablated μPM having 12 sides. The μPM rotates at the same speed as the VCM since it is attached directly to the rotor. Moreover, the rotational speed (ω_r) of the VCM is directly proportional to the frequency of the excitation signal (f_{ele}) and inversely proportional to the number of rotor poles ($N_r = 8$ in the tested device). It is given by the following equation

(Han, Wu & Wang, 2010a; Ghalichechian, Modafe, Beyaz & Ghodssi, 2008a):

$$\omega_r = 60\frac{f_{ele}}{N_r} \quad rpm \tag{5.1}$$

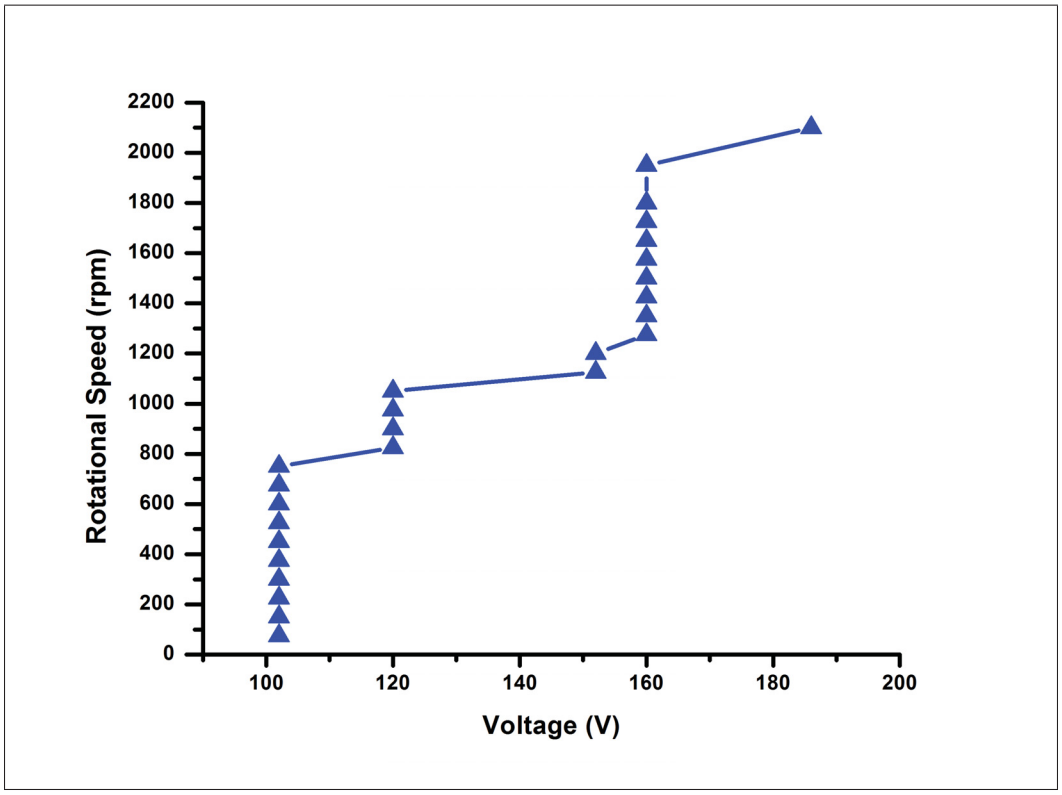

Figure 5.6 Measured rotational speed of the rotary micro-scanner vs the amplitude of the applied three-phase driving voltage.

The rotational speed of the μRS at various driving voltage amplitudes was calculated and plotted in figure 5.6. The maximum speed of the VCM is 2,100 rpm at a peak voltage of 186 V, with the 12-sided laser ablated μPM load. At a particular drive voltage, the μRS can provide a range of rotational speeds by changing the excitation frequency, but the input voltage needs to be increased to attain rotational speeds above that range. This behavior can be explained by considering the fact that, beyond a certain excitation frequency, the available electrical power has to be increased to match the required mechanical power that is increasing with the rotational

speed of the motor. The VCM stop operating when the required mechanical power is greater than the supplied electrical power. The electrical power consumed by the μRS and the unloaded VCM (i.e., without an ablated μPM) at different speeds is shown in figure 5.7. As expected, at a given rotational speed, the power consumed by the μRS is higher than the power consumed by the unloaded VCM. This is due to the extra load on the rotor. The unloaded VCM can operate at up to 3,300 rpm and consumes a maximal electrical power of 8.6 mW. The maximum power consumed by the μRS is 6.8 mW when operating at a speed of 2,100 rpm.

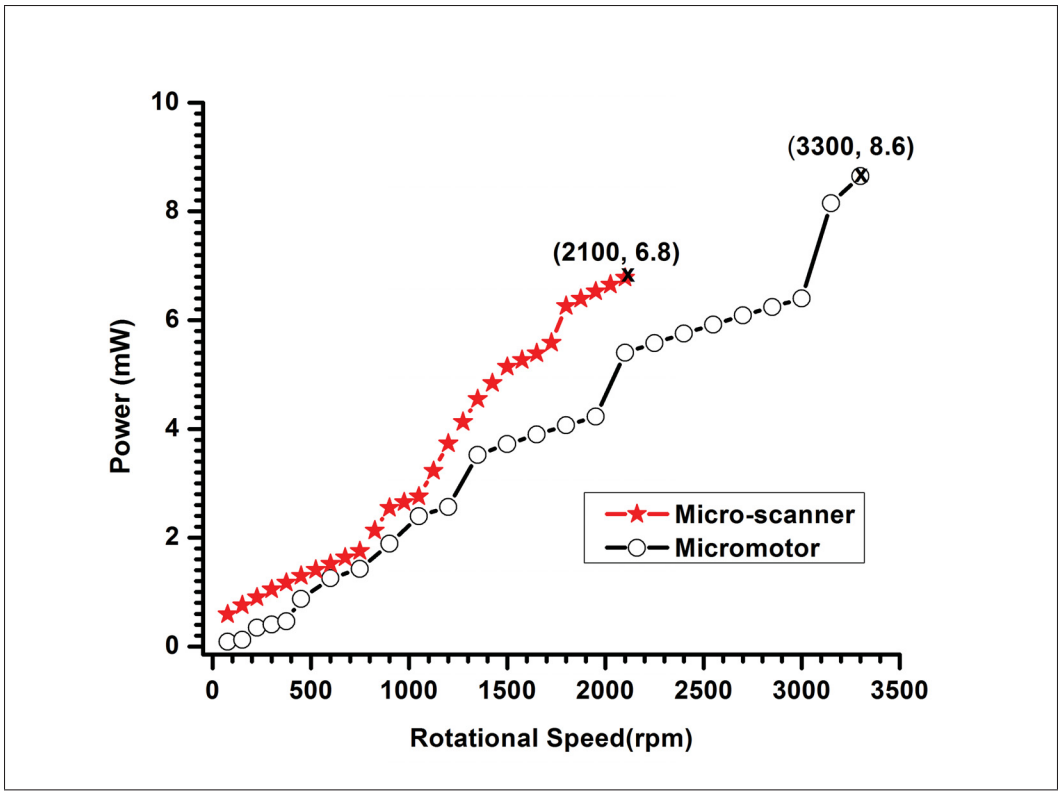

Figure 5.7 Measured electrical power consumption vs rotational speed for the rotary micro-scanner and the unloaded VCM.

Optical characterization

The optical characterization of the μRS was carried-out to measure the scan angle (SA) of the reflected beam, the line scan rate and the scanning frequency. When the μPM rotates, it generates

a scan line (SL) of the reflected beam between points A and B on the screen corresponding to the SA, as shown in figure 5.8a (also labeled in figure 5.4b). At low excitation frequencies, the μPM rotates slowly and the scan speed is low, thus the laser spot can be traced and captured on the screen. The rotor of the VCM exhibits a small wobbling motion because the electrostatic force continuously pulls it towards the stator poles. However, the rotor sliding motion is halted by the central bearing axis making the rotor trajectory circular. Also, the unbalanced vertical electrostatic forces between the rotor and the stator contribute to the wobbling motion of the rotor. These forces are generated due to the vertical misalignment between the rotor poles and stator poles. The misalignment is approximately 750 nm and it is a fabrication constraint of the PolyMUMPs process. The impact of the wobbling motion on the scanning is that the reflected beam follows a zigzag pattern on the screen, which is clearly visible at low speed (i.e., «~200 rpm), as shown in figure 5.8b. At higher frequencies, the rotor is moving very fast (i.e., »~200 rpm), reducing the μRS wobble due to the high inertia of motion. Consequently, the scan pattern of the reflected beam becomes significantly smoother and more linear, as shown in figure 5.8c. Moreover, the zigzag motion of the μPM resulted in the vertical misalignment of the reflected beam by ~6.3°. The high speed and the low speed operation of the μRS and the corresponding scan pattern can be seen in the video file submitted with the manuscript.

The μRS demonstrated here could be used to implement a 1×N optical switch by placing an array of optical ports at the screen location. For such applications, the optical power transmitted by the μRS to the output ports needs to be determined, and is measured with the optical setup used in the experiment. The 632-nm laser can provide a spot size of 5 μm using a 5X objective with depth of field of 14 μm. The power of the reflected beam was measured using a photo-diode sensor (S120VC from Thorlabs) placed at a distance of 6 cm from the μRS. The area of the photo-detector is a circle of 9.7 mm in diameter and it cannot cover the entire angular scanning range of the reflected beam. Consequently, the output optical power (P_{out}) is measured only across a section of the SL. The ratio of the output power over the input optical power (P_{in}) is plotted in figure 5.9. The optical power of the incident 632 nm laser beam is 856 μW (-0.68 dBm), and the beam is deflected by the rotating micro-polyhedron onto the photo-detector with

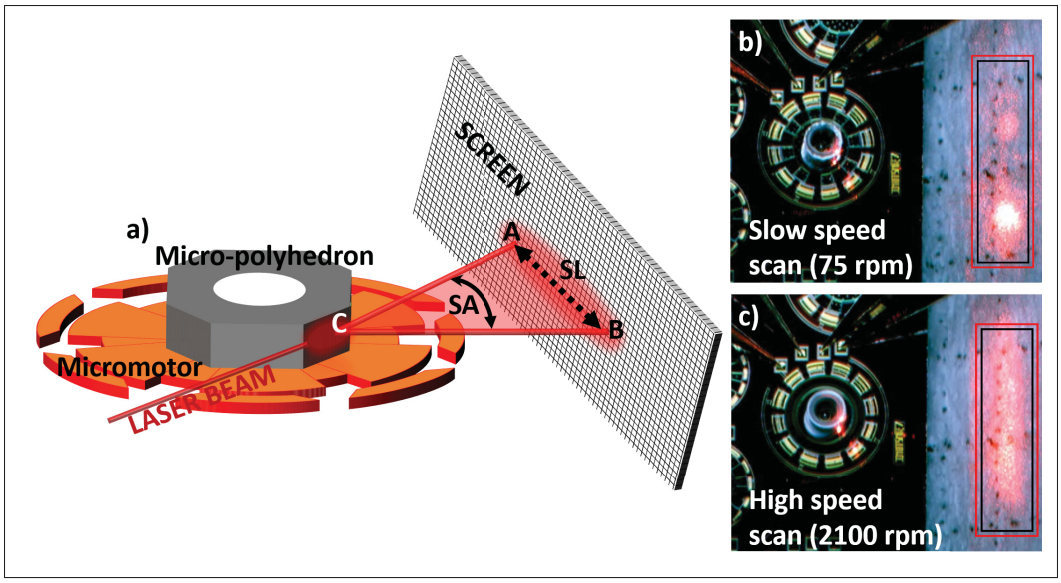

Figure 5.8 a) Schematic illustrating the scanning motion the rotary micro-scanner; b) image of the beam on the screen at slow rotational speed (~ 75 rpm); and c) image of the beam on the screen at high rotational speed (~ 2100 rpm).

an optical output power in the range of 154.08 μW (-8.12 dBm) to 188.32 μW (-7.25 dBm). This yeilds a range for P_{out}/P_{in} from 0.18 to 0.22. No other optical component was used after the beam was reflected from the μRS for experimental simplicity. This is one of the reason for the relatively high optical losses. The collimation of the laser beam could be improved by designing micro-optical elements for the target application. Additionally, during the scanning of the laser beam, the edges at the two ends of the photo-detector truncate the incident beam leading to vignetting, causing a non-uniform optical power distribution along the SL captured by the photo-detector (Zhang & Chen, 1999).

The angular scanning range (ARS) in degree, the angular scan-rate (ASR) in rad per seconds and the line scan rate (LSR) in line scans per minute for a polygon scanner are given by following equations (Erdelyi & Rynkowski, 2013):

$$ARS = \frac{4\pi}{N} \tag{5.2}$$

$$ASR = \frac{4\pi\omega_r}{60} \tag{5.3}$$

$$LSR = \omega_r N \tag{5.4}$$

where ω_r is the rotational speed of the polygon and N is its number of sides. The μRS presented here covered an angular scanning range of 57.88 °. This yields an angular scan rate of 440 radians per second and a maximum scan speed of 25,200 line-scans per minute or 420 line-scans per second. There is a 2.12 % variation in the measured scan angle as compared to the scan angle given by the equation due to scattering at the edges of the μPM facet. The wide scanning range of the μRS enables efficient beam steering to distribute the incoming optical signal across a large array of optical ports in switching applications or to scan a wide FoV in ranging applications.

Discussion

To the best knowledge of the authors, this μRS has the smallest size and highest FoV compared to previous miniaturized MEMS scanners, as shown in table 5.1. The precise integration of the μPM on the VCM make it a well-aligned vertical scanning mirror without the need of additional steps for alignment and positioning. The single pixel of a commercial digital micromirror device (DMD) module offers a smaller footprint than this scanner but the FoV of the pixel is limited to 24°. Moreover, it requires multiple light sources, such as an array of laser diodes, to enhance its FoV in LIDAR type applications (Smith, Hellman, Gin, Espinoza & Takashima, 2017) . The footprint of the proposed μRS is at least two orders of magnitude smaller than other scanning modules. In addition, it operates at low power and weighs much less than other modules, making it a highly compact optical scanner.

The μRS is a non-resonant device, while other reported scanners presented in table 5.1 are resonant devices. Therefore, a comparison to other commercial rotational polygon scanners is

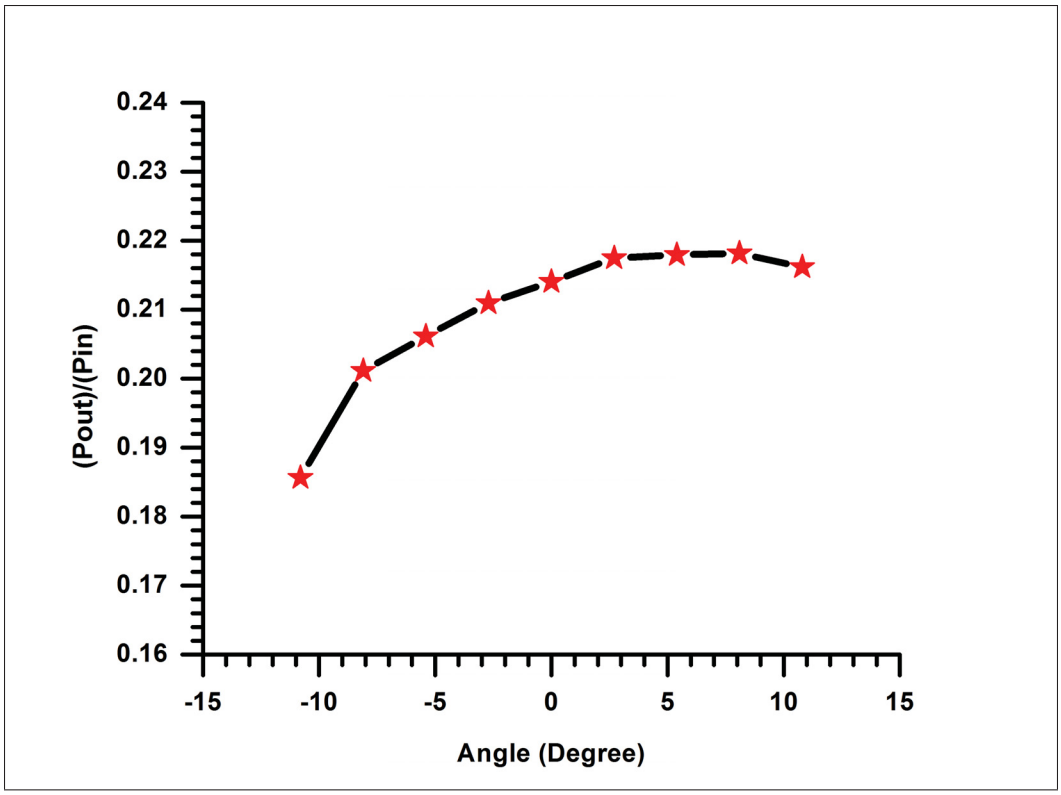

Figure 5.9 The output optical power (P_{out}) across the scan line captured by the photo-detector for a 632 nm laser beam reflected on the μPM and having an input optical power (P_{in}) of 856 μW (-0.68 dBm).

Table 5.1 Comparison of the proposed device to other MEMS scanners.

Device type	**FoV**	**Device Dimensions**
RBS	$28^{\circ} \times 31^{\circ}$	5.3×5.8×3.0 mm^3
DMD	48°	10.2×10.2 um^2
RBS	$45.3^{\circ} \times 42.6^{\circ}$	20×20×16 mm^3
UDS	30°	6.75×6.75×2 mm^3
This work	57.88°	**1×1×1 mm^3**

RBS stands for resonant bi-directional scanner; UDS stands for uni-directional scanner; DMD stands for digital micromirror device

presented in table 5.2, listing footprint, power, speed, and mass. The successful integration of the μPM onto the VCM makes the proposed device one of the smallest rotary polygon scanner reported to date. The dimensions of the μPM (height of 410 μm × base diameter of (400 μm) are

very small compared to commercial polygon mirrors, which have a height and a base diameter that are larger than 5 mm × 5 mm. Additionally, the mass of the assembled μRS is about 175 μg. The overall size of the μRS is about 1 mm × 1 mm × 1 mm, which is at-least five-fold smaller than other rotary polygon scanners (NANOPHORM, LLC, 2018; CAMBRIDGE TECHNOLOGY, 2020; NIDEC-COPAL-ELECTRONICS, 2020; Miradatechnologies, 2018; PLL, 2019). Also, the motors used in commercial polygon-scanners are bigger and heavier than the VCM presented in this work. Combined with the control electronics, a typical polygon-scanner typically goes beyond 5 mm × 5 mm × 5 mm in size and weighs in the order of hundreds of grams. In addition, the power consumed by the commercial polygon scanners is higher, as a considerable amount of energy is required to rotate the larger polygon mirrors. In contrast, the power required to operate the proposed μRS is a few milliwatts, due to the electrostatic operation of the VCM and the small size and mass of the μPM. Along with the supporting optics and electronics components, the commercial polygon scanners presented in table 5.2 are widely used in LIDAR modules (Rablau, 2019; Velodyne, 2019; Weber, 2018; SICK, 2019). Generally, an array of LIDAR modules is used to increase the scanning angle (Zeng, 2013) and are suitable for few applications despite their large size and high power consumption. However, these modules pose serious integration and cost challenges for compact systems such as small-scale robots like RoASCH, DASH, HARM, VelociRoACH (Kim, Kim, Kim & Jung, 2019) and micro air vehicles like the RoboBee (Clawson, Ferrari, Fuller & Wood, 2016). With a weight of only 175 μg, the compact scanner presented here is well-suited for chip-scale implementation of low-power LIDAR sensor modules for applications such as drones and miniaturized autonomous vehicles. It also has several other potential applications, including in variable optical attenuators, delay lines for biomedical imaging and chip-scale interferometers.

Table 5.2 Summary of the characteristics of the proposed device in comparison to commercially available polygon scanners.

Model(Polygon scanner)	**Size (Base × Diameter × Height)**	**Weight**	**Speed**	**Power**
PD40ERB (Nidac-Copal)	40 mm × 3 mm	200 g	3000-8000 rpm	>12 W
Gecko Four (PLL)	25 mm × 25 mm	190 g	1000-4000 rpm	>6 W
YA90 (Miradatechnology)	20 mm × 3 mm	250 g	1000-6000 rpm	NA
This work	**1 mm × 1 mm × 1 mm**	**175 μg**	**75-2100 rpm**	**<7 mW**

Conclusion

We presented an optical μRS with a 12 side μPM integrated onto a VCM. The μRS is implemented through the assembly of the μPM and VCM that are fabricated using low-cost commercial MEMS fabrication processes. The rotary platform consist of a high speed VCM built with the PolyMUMPs surface micromachining process, to enable a low power and compact rotational platform, while the μPM was fabricated using the PiezoMUMPs bulk micromachining process, to provide a large reflective surface for low optical power losses. The device demonstrated a high scan rate, large scan angle and low power consumption. This miniaturized polygon scanner has a small footprint and can be integrated in chip-scale subsystems. It is well-suited for applications where mass, compactness, power consumption and scanning speed are important. To the best of our knowledge, this work reports the first micro-scale high-speed rotary-scanner, and paves the way for the investigation of system applications that can take advantage of its unique properties. For instance, the micro-scanner could be well-suited to systems such as advanced driving assistance systems, LIDARs for robots and drones, endoscopic imagers, and optical switches, potentially enabling a significant miniaturization and cost reduction of these systems.

Materials and methods

Micromotor design

The requirements on the rotary platform for the implementation of the chip-scale μRS are: i) dimensions on the order of 100's of microns; ii) the ability to perform complete revolutions at high speed; and iii) a reliable fabrication process, preferably with commercial batch fabrication to minimize cost. VCMs are small, can rotate at high speeds and can be fabricated using surface micromachining processes, making them an ideal choice for implementing the rotary platform. Many types of electrostatic side drive micromotors were implemented in the past using surface micromachining processes. Often, the micromotor fabrication process is developed in-house

and this makes the reproducibility of the device challenging. Thus, it is preferable to adopt a standard commercial fabrication process. The PolyMUMPS process is a two-layer polysilicon micromachining process widely used in both the industry and academia to implement various MEMS devices. We implemented high-speed VCM architectures (Gour *et al.*, 2020a) using the PolyMUMPS process that can rotate at up to 8000 rpm without loading, i.e. without any component attached to the rotor, and we used them to implement the μRS. Figure 5.10 shows the various parts of a variable capacitance micromotor, and the key geometrical parameters optimized for torque enhancement based on analytical modelling (Dufour, Sarraute & Abbas, 1996a; Gour *et al.*, 2020a). The VCM used here consists of 8 rotor poles and 12 stator poles, the radius of the rotor is 300 μm, the bearing axis/post has a radius of 3 μm, and the dimples have a radius of 3 μm. The bearing post/axis is the axis of rotation of the rotor and it also prevents rotor-stator collisions. The dimples are part of the rotor and provide electrical contact to the underlying ground plane and stability while rotating. Important design parameters of the VCM are listed in table 5.3.

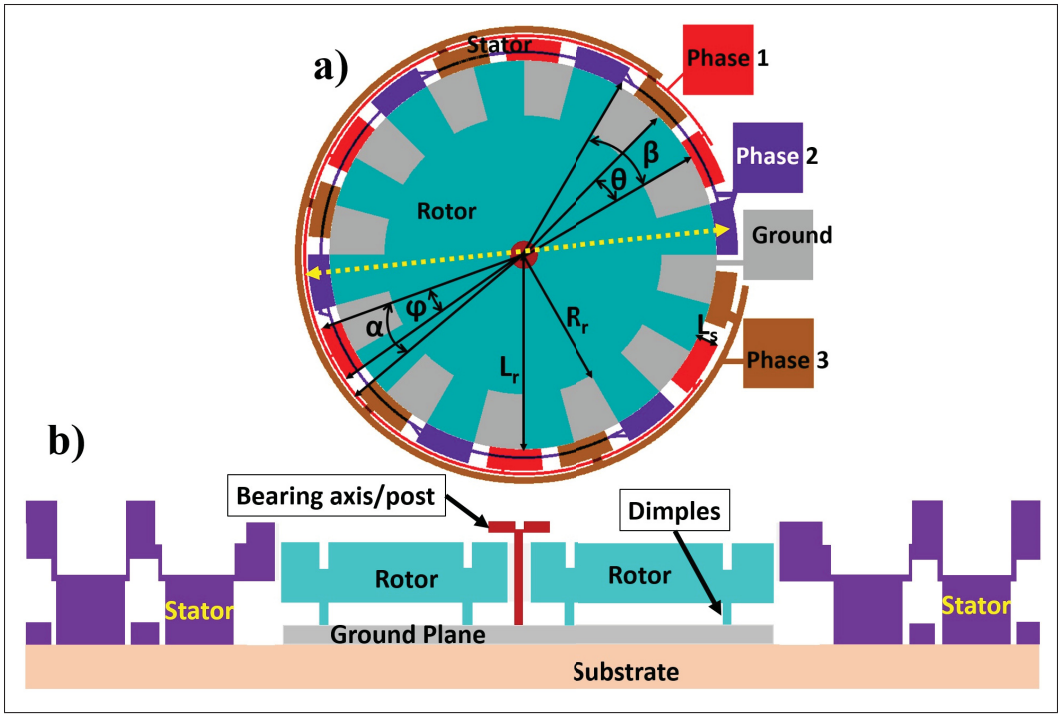

Figure 5.10 Diagram showing the various parts of the micromotor: a) top-view of the micromotor; and b) cross-section of the micromotor.

Table 5.3 VCM design parameters.

Geometrical parameters	Value
Number of phases (q)	3
Total number of stator poles (N_s)	12
Total number of rotor poles (N_r)	8
Radius of the micromotor rotor (R_r)	12
Gap between rotor and stator (G)	2.5 μm
Length of the stator tooth (L_s)	140 μm
Length of the rotor tooth (L_r)	417.75 μm
Number of dimples	4
Radius of the bearing axis	3 μm
Stator angular pitch (α) and angular width (ϕ)	22.5°, 30°
Rotor angular pitch (β) and angular width (θ)	22.5°, 45°

When the rotor is grounded and a voltage is applied to the stator poles, an electrostatic force is generated between the stator poles and the rotor poles. The tangential component of the electrostatic force moves the rotor and complete rotations are achieved by applying a three-phase varying voltage to the stator poles. The movement of the rotor changes the overlap area between the rotor poles and the stator poles, thereby modifying the capacitance between the rotor and the stator poles. The generated torque acting on the rotor is proportional to the change in the rotor-stator capacitance (C) with respect to the angular position of the rotor (Ω), applied voltage (V), total number of rotor poles (N_e) and the number of voltage phases (q). The derived motive torque per phase is given by (Ghalichechian *et al.*, 2008a; Gour *et al.*, 2020a):

$$T(\Omega) = \frac{N_e V^2}{2q} \left(\frac{dC(\Omega)}{d\Omega} \right) \tag{5.5}$$

Accordingly, a VCM with a large number of poles is slow and has high torque. In contrast, a VCM with a small number of poles is fast but unable to produce large torque. Here, the VCM is optimized to provide sufficient torque while providing rapid motion when loaded with the μPM element, resulting in a fast scanning chip-scale device.

Micro-polyhedron mirror design

The μPM used in the implementation of the μRS should be light weight and have smooth and sufficiently large facets to reflect the incident laser beam. The maximum possible size of the base of the μPM is determined by the diameter of the rotor, and in our case, it must be less than 600 μm. A contact between the μPM and stator poles can also lead to device failure by causing a short-circuit. Thus, it is important to ensure the proper placement of the μPM onto the rotor and prohibit any overhang outside of the rotor that may damage the stator poles. The bearing post/axis at the center of the VCM is the rotation axis of the rotor and it also prevents the rotor from touching the stators, as shown in figure 5.10. Thus, the geometry of the μPM must be designed to never touch the bearing post/axis. This design constraint is necessary to ensure proper operation of the rotor and requires a recess at the centre of the μPM. The dimension of the recess must be greater than the dimension of the bearing axis, which has a height of 1.5 μm and a diameter of 50 μm.

The facets of the μPM are acting as mirrors to reflect an incoming laser beam, and thus they must have a sufficiently large area to deflect the entire incoming beam. The number of sides of the μPM determines the angular range of the scanner and the scan line rate. More sides increases the line rate but decreases the angular range, therefore the shape of the μPM should be chosen according to the targeted application. Additionally, the maximum number of side-wall mirrors of the μPM are limited by its size, since as the number of sides increases, the area of each facet decreases, which could ultimately lead to significant optical losses. Here, we chose a μPM with 12 sides for demonstration purposes. Accordingly, the design constraints on the μPM includes a recess at the centre with a size greater than the dimensions of the bearing post/axis, and a μPM base size of less than 600 μm. Moreover, there is a trade-off between the angular range, line scan rate and facet size when choosing the number of sides of the μPM.

The final prototypes of the μPM were fabricated using the commercial PiezoMUMPs process. This process utilize deep reactive ion etching (DRIE) to create steep sidewalls and trenches in a silicon-on-insulator wafer, making it a suitable fabrication technique to implement the μPM

structure. Also, the process uses a silicon device layer with a thickness of 10 μm on top of the substrate that enables the creation of a recess with the required dimensions. The chip layout of various μPMs designed to meet these constraints are shown in figure 5.11a. A single μPM design consists of a trench region, a micro-polyhedron mirror, a recess region, and two anchors to support the mirror structure, as shown in figure 5.11b, and the corresponding cross-section is illustrated in figure 5.11c. Figure 5.11c also illustrates a circular region at the centre of the μPM, where the recess region must be present. The dimensions of the recess are chosen to allow easy placement of the μPM onto the rotor of the VCM, while avoiding any contact and damage to the bearing axis.

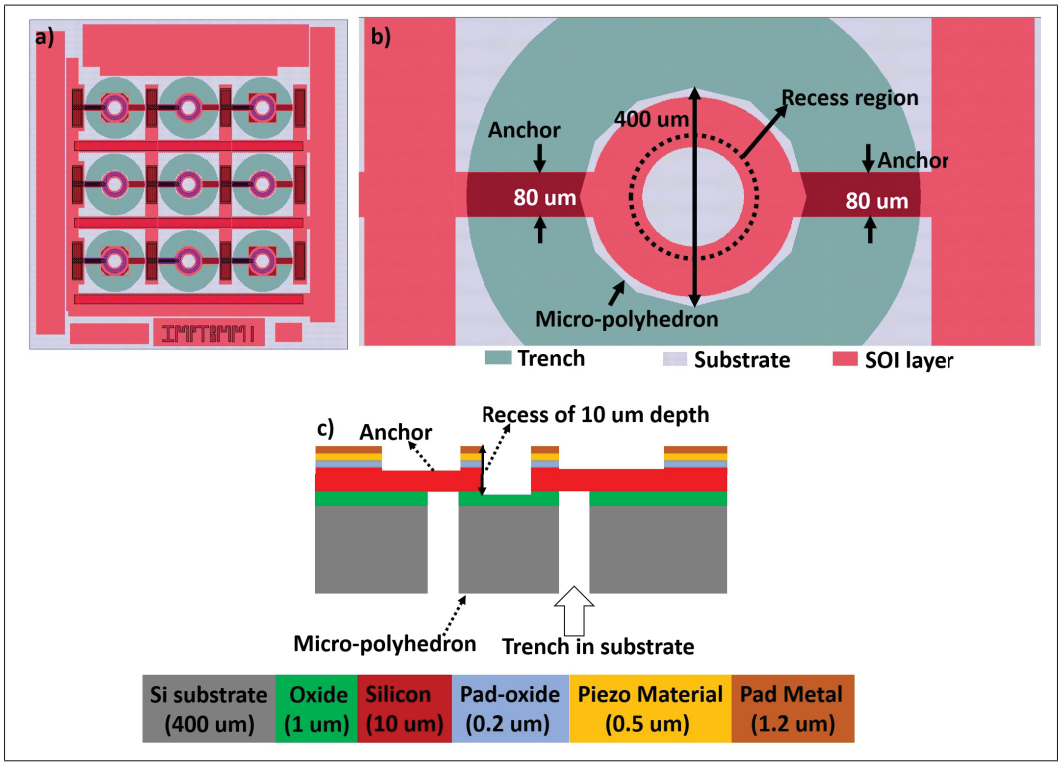

Figure 5.11 a) Image showing the layout of the micro-polyhedron chip; b) image of the layout showing the parts of a single μPM design; and c) cross-sectional view of the micro-polyhedron design implemented with the PizeoMUMPs process.

Assembly of the 3D micro-scanner

Serial micro-assembly was performed to integrate the μPM with the VCM. Often, specially designed structures need to be added to MEMS devices to perform 3D micro-assembly, which may add complexity to the integration operation. Here, a simple protocol was developed to integrate the μPM to the VCM rotor in order to simplify micro-assembly. The protocol involves the deposition of a bonding material on the μPM, placing the μPM on the rotary platform and finally bonding the μPM with the rotor using thermal curing. Figure 5.12 shows the various steps involved in the micro-assembly of the μPM on the rotor.

A SU-8 based adhesive is used to bond the μPM to the rotor. SU-8 is an epoxy based negative photo-resist that is commonly used for adhesive bonding with and without UV curing (Svasek, Svasek, Lendl & Vellekoop, 2004b). Here, bonding is performed by thermal curing of the SU-8. The advantage of using SU-8 is that it can rapidly change it physical state from a glue-like semi-solid phase to a solid phase and vice-versa at low temperature. The base of the μPM is not as wide as the diameter of the rotor of the VCM, but it is large enough to deposit droplets of adhesive. The following procedure is employed to deposit a solid SU-8 adhesive layer on the μPM. First, droplets of SU-8 are deposited onto the μPM by drop-casting and heated to 50°C for 2 minutes, 60°C for 2 minutes and 90°C for 2 minutes in order to vaporize the solvent. Then, the μPM with SU-8 drops is cooled down at room temperature for 30 minutes to solidify the adhesive drops.

A single MEMS chip consists of several VCMs, and to precisely place a μPM on a particular VCM without damaging or touching the other devices is challenging. Therefore, a pick and place technique using a placement mask was developed to position the μPM onto the rotor of the VCM. The placement mask was made from a 90 μm thick rigid steel composite sheet into which holes with a diameter equal to the one of the base of the μPM were drilled using laser ablation. The purpose of this mask is to allow an obstacle-free navigation of the μPM over the MEMS chip and to position them into a hole that is aligned to the rotor of the VCM. The MEMS chip was placed between two support posts such that the height of the support posts is slightly greater

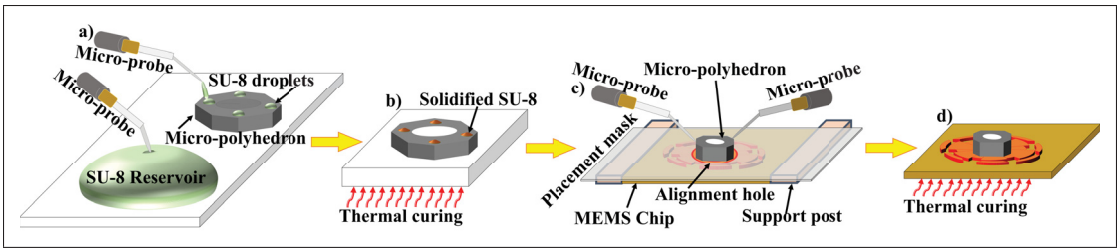

Figure 5.12 Diagram showing the steps involved in the micro-assembly technique to integrate the micro-polyhedron onto the micromotor: a) drop-casting of SU-8 droplets onto the micro-polyhedron; b) thermal curing of the micro-polyhedron to solidify the SU-8 droplets; c) alignment and placement of the micro-polyhedron with solidified SU-8 droplets on to the micromotor; and d) final thermal curing of the assembled micro-components to bond the micro-polyhedron with the micromotor.

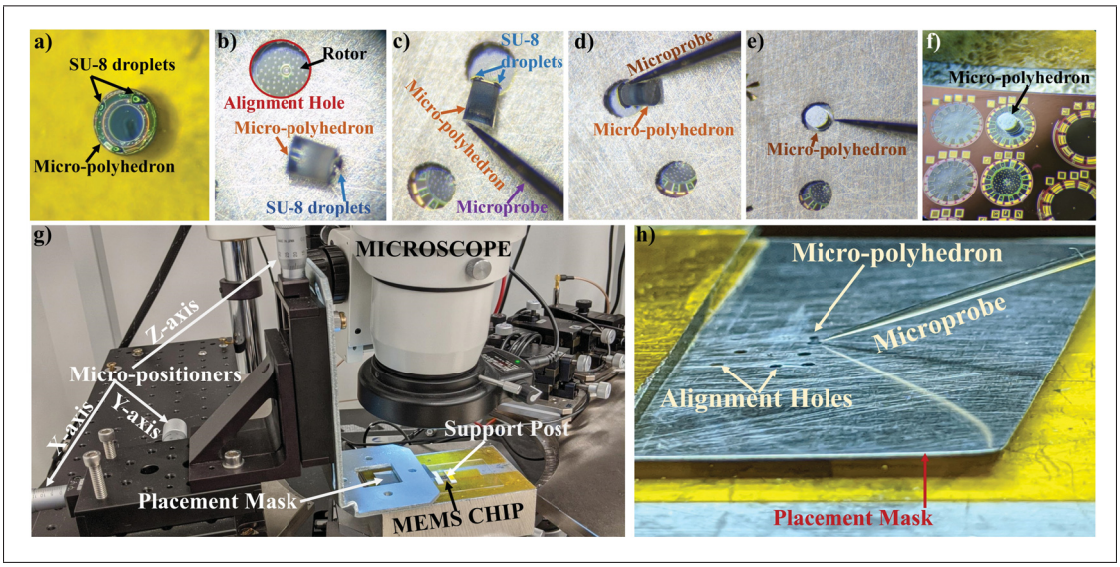

Figure 5.13 Images of different steps performed during the micro-assembly process: a) solidified SU-8 drop on the micro-polyhedron; b-e) images showing the placement of the micro-polyhedron onto the rotor via an alignment hole using micro-probes; f) assembled micro-scanner; g) setup used for the micro-assembly; and h) alignment holes on the placement mask and the placed micro-polyhedron.

than the MEMS chip by approximately 20-50 μm. Accordingly, when the placement mask is aligned with the rotor and placed onto the support posts, it does not touch the MEMS chip as the extra height of the support posts creates a gap between the chip and the placement mask, preventing damage to the devices during the micro-assembly. The micro-positioners can move the placement mask with 25 μm accuracy along each axis. The placement mask was aligned and placed over the rotor of the VCM using micro-positioners, as shown in figure 5.13. A μPM with solidified adhesive was picked and placed onto the placement mask using plastic tweezers and pushed into the alignment hole using micro-probes. The μPM cannot drop, fall or topple from the rotor after being inserted into the alignment hole since the thickness of the μPM is greater than that of the placement mask and gap combined.

After positioning the μPM onto the rotor of the VCM, the placement mask is removed and the assembled components are heated at 90°C for 2 minutes to reflow the SU-8. It is then cooled down to room temperature for 45 minutes to bond the μPM to the rotor. SEM micrographs of the assembled μRS are shown in figure 5.14.

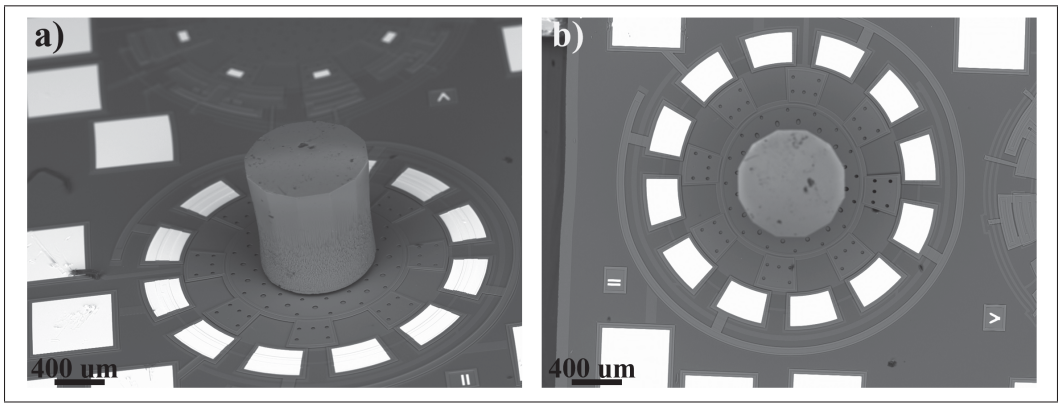

Figure 5.14 SEM micrographs of the assembled rotary micro-scanner: a) isometric view of the micro-polyhedron on the micromotor; and b) top view of the micro-polyhedron on the micromotor.

Electrical characterization

The following experimental procedure was used for the electrical characterization of the μRS, which started at an input voltage of 0 V: i) the input voltage was increased in steps of 2 V while keeping the three-phase signal frequency at 10 Hz until the VCM started rotating; ii) the input frequency was then increased in steps of 10 Hz while keeping the voltage obtained in the previous step constant until the VCM stopped rotating; iii) Steps i and ii were repeated until the input voltage reached 200 V.

Acknowledgements

The work was funded by the Natural Sciences and Engineering Research Council of Canada (NSERC), the Fonds de recherche du Québec - Natures et Technologie (FRQNT), and the Regroupement Stratégique en microsystème du Québec (ReSMiQ). We would like to thank CMC microsystems for providing access to the commercial fabrication processes used.

Author contributions statement

M.M. and F.N. supervised the project and edited the manuscript. A.G performed the simulations and experiments, analyzed the data, and wrote the manuscript.

Conflict of interest

The authors declare no competing interests.

CONCLUSION

Discussion

This thesis described a miniaturized three-dimensional micro-device for beam scanning applications, realized using commercial fabrication processes and MEMS compatible post-processing techniques. It can be used for applications that requires a compact polygon scanner such as LIDAR, OCT systems, and so on. The device is composed of a micromotor and a polygon micromirror that are micro-fabricated and assembled to create a rotating polygon beam scanner.

First, this thesis investigated the design and fabrication a rotary micromotor that can exhibit very high speed using the PolyMUMPS process. The rotary micromotor operated up to speed of 7875 rpm, which is a 60% enhancement compared to previous state-of-the-art devices fabricated using the same process. The performance of the micromotor is improved with different strategies. The friction and wear with the ground plane is minimized by employing a reduce number of small circular dimples instead of big annular ring shaped dimples. The high performance of the micromotor can be attributed to the new teethed edged architecture of the rotor/stator poles bypassing the planar edges to improve the tangential component of the electrical force. The implementation of the high speed micromotor fulfill the requirements of rotary platforms for micro-polygon scanners.

Second, this work presented a technique for post-processing and micro-assembling the micro-scanner. This technique allows for a rapid and cost-effective micro-device assembly by enabling the bonding of a micro-structure on a released MEMS device. A micro-polyhedron was fabricated using laser-ablation and precisely placed and bonded to the rotor of the micromotor using a specially designed 3-D integration platform. The assembled rotary structure was operational and required a higher actuation voltage as compared to the micromotors without a micro-polyhedron. This finding provided a very useful protocol to assemble complex MEMS devices where heterogeneous micro-assembly of discrete components is essential. This technique resolved the issue of the integration of the micromirror onto the rotary platform in order to assemble the micro-polygon scanner.

Finally, a compact micro-polygon scanner was realized by integrating a micro-polyhedron mirror onto a micromotor. The miniaturized scanner was comprised of a hollow micro-polyhedron mirror and an electrostatic variable capacitance micromotor. All the micro-components were fabricated using commercial MEMS fabrication processes and the custom micro-assembly technique developed was used for the integration. The presented micro-scanner exhibited a high scan rate with a large scanning angle while keeping the power consumption low.

The maximum speed of the micro-polygon scanner is 2100 rpm, hence it can be used in LIDAR for automotive applications, LIDAR for small unmanned aerial vehicle such as drones, terrestrial mapping scanners, measurement instruments such as laser-level devices. However, the micro-polygon needs further improvement for its use in application requiring high scanning speeds such as OCT system to provide optimal performance. Nonetheless the low-cost, low-power and small footprint of the micro-polygon is advantageous to many applications.

This miniaturized scanner can be used in various applications where mass, compactness and scanning speeds are crucial for enhancing the device performance. Moreover, as this field advances, better and improved MEMS devices starting from optical scanning and biomedical imaging to laser beam steering in LIDAR systems can be anticipated in the future.

This thesis presents a reliable methodology to implement a rotary MOEMS device with following key contributions:

- Improved design of variable capacitance micromotors for delivering high torque and high speed operation that can be fabricated using the commercial PolyMUMPS process.
- A simple and novel micro-assembly process to integrate micro-structures on released MEMS using SU-8 as bonding material to implement complex micro-devices.
- A method to design and fabricate micro-polyhedron mirrors using the commercial PiezoMUMPS process. Also, a fabrication process to reduce the mass of the micro-polyhedron mirrors using laser-ablation without diminishing their sidewall reflectivity.
- The first functional implementation of a chip-level rotary micro-polygon scanner that can provide large scan-rate and wide angular scanning range.

Outlook

Advancements in integration and micro-assembly of MEMS components will continue and lead to an increase in high-performance micro-devices for various applications. The presented high speed micromotor fabricated using the PolyMUMPS process can be used in micro-pumps, micro-gear systems, and micro-valves, to name a few. In light of the simple post-processing integration technique presented, it is believed that this rapid technique is convenient for implementing complex 3-D MEMS devices. The technique enable precise bonding of micro-components to released or unreleased MEMS structures that require heterogeneous micro assembly of discrete components. Therefore, these contributions provide powerful tools to push forward research in complex micro-systems and their applications.

The implementation of the first micro-polygon scanner presented here provides a breakthrough in realizing miniaturized systems by replacing bulky polygon-scanners, to provide cheap, compact and low-power solutions.

Future work

Based on this work, several avenues of exploration are possible for the development of chip-scale systems, including the following:

- Study and development a custom fabrication process using a combination of bulk and surface micromachining to allow monolithic fabrication of a micro-scanner with enhanced mechanical and optical performances.
- Study the dynamic behaviour of micromotors with different architectures in vacuum and atmospheric conditions. Experimental data should be collected and analyzed to accurately characterize the dynamic operation of the micromotors. This study could help in developing similar micro-devices for space applications where gravity is absent.
- Investigate a micro-assembly technique for the micro-scanner to further improve alignment accuracy of the integrated components with a goal for commercial implementation.
- Investigate an optical delay line based on micro-scanners for OCT application. The study could be performed to characterize the wavelength tuning filter for swept-source OCT system and to analyze the features of endoscopic OCT.

- Develop and optimize surface gratings that could be integrated on the rotor to make a chip-scale rotary diffraction grating filter for the selection of required diffracted beams that could be of interest in systems such as Fourier-domain OCT. This could lead to lower cost OCT systems.
- Investigate and study the implementation of LIDAR system based on the micro-polyhedron scanner. This study could be pivotal for realizing a micro-LIDAR system for drone applications.

APPENDIX I
MEMS SCANNERS ACTUATION METHODS

The actuation principles used with micromirrors include electrostatic, electromagnetic, electro thermal, electrowetting, and piezoelectric actuation. Each actuation mechanism has its own benefits and limitations, making the development process challenging. For instance, electrothermal bimorph devices have a long response time but operate at low voltages. Scanners based on this actuation technology are not suitable for most applications, but can be possibly used in combination with a fast scanner that uses a different actuation principle in order to actuate a slow scanner (Holmstrom *et al.*, 2014). Thus, the performance of MEMS scanners is highly dependent on the actuation mechanism and considerable effort is required in the implementation of the actuators in order to meet the specification. In the next section, a discussion on commonly used actuation mechanisms for MEMS scanning systems are presented along with their merits and demerits.

1. Electromagnetic Actuation

In electromagnetic actuators, a Lorentz force is utilized to move the micromirror element and these actuators can be of the moving coil type or the moving magnet type. In both the cases, the Lorentz force ($F=I\times B$) is generated by passing an electric current (I) through a coil in an external electromagnetic field with magnetic flux density (B). A moving magnet actuators based scanner is shown in figure I-1. These are simple to fabricate and have an external coil along with either a magnetic thin film or a bulk magnet for actuation (Ataman, Lani, Noell & de Rooij, 2012; Aoyagi, Shimaoka, Kato, Makishi, Kawai, Tanaka, Ono, Esashi & Hane, 2011). In contrast, in moving coil type actuators, a coil is fabricated on the moving portion of the device and the static magnetic field is produced using external magnets (Yan, Luanava & Casasanta, 2003). Usually, all the components of these actuators are fabricated individually and final assembly is performed to realize the scanner, leading to a large form factor compared to the other MEMS techniques (Holmstrom *et al.*, 2014).
Electromagnetic actuators can deliver high torque, move the mirror element through a large scan angle, and support a mirror element having a size on the order of millimeters (Yalcinkaya, Urey, Brown, Montague & Sprague, 2006). Compared to other actuation

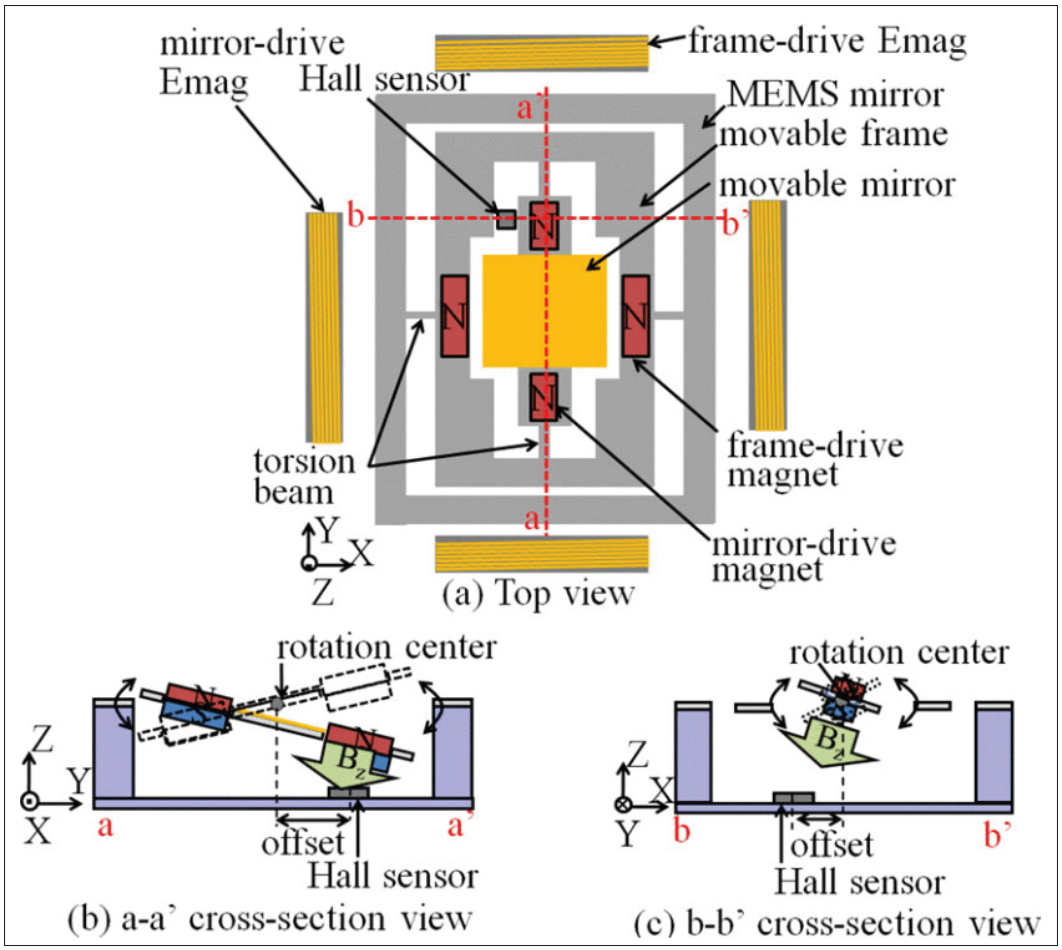

Figure-A I-1 Structure of an electromagnetic scanner
Adapted from Aoyagi, Shimaoka, Kato, Makishi, Kawai, Tanaka, Ono, Esashi & Hane (2011)

techniques, electromagnetic actuation has a more linear response, making it desirable for slow scanning applications. Most micromirrors can easily perform 1-D scan, but a 2-D scan is also possible (Jeong, Park, Jeong, Cho, Chang, Kim, Kang, Hwang & Lee, 2008b; Miyajima, 2004; Miyajima, Asaoka, Isokawa, Ogata, Aoki, Imai, Fujimori, Katashiro & Matsumoto, 2003; Bernstein, Lee, Rogomentich, Bancu, Kim, Maguluri, Bouma & DeBoer, 2007). In spite of the low driving voltage, the coil consumes high current and dissipates relatively large amounts of heat, thereby compromising the performance of the electromagnetic actuated MEMS scanners and making them unsuitable for low-power portable applications. Moreover,

the fabrication of such actuators requires magnetic materials that are typically less common in micro-fabrication facilities.

2. Piezoelectric Actuation

These actuators operate using the piezoelectric effect and depend on the amount of stress created within the piezoelectric thin film when an electric field is applied in the transverse direction. For instance in (Kawabata, Ikeda, Goto, Matsumoto & Yada, 1997; Sano, ichi Inoue, Kanda, Fujita & Maenaka, 2015), the mirror plate moves at each mode of the resonant vibration, when the applied excitation frequency matches the torsional mode frequency of the mirror supporting structure. A PZT micromirror with different material layers of the anchor for actuation is shown in figure I-2. These actuators have a sandwich design such that a metal/piezoelectric/metal structure is stacked on an insulating layer and has a very simple fabrication process but challenging piezoelectric film quality requirements (Lee, Hsiao, Kobayashi, Koh, Ramana, Xiang, Yang, Tan & Pinjala, 2009; Koh, Lee & Kobayashi, 2010; Liu, Zhu, Li, Virendrapal, Tang, Wang & Xie, 2010b).

PZT scanners are more compact than electromagnetic scanners as they do not require a magnet and shielding elements. PZT hysteresis and polarization fatigue need to be considered for the long-time reliability of these devices. Although PZT scanners require small voltages for operation, they suffer from high leakage current in the PZT capacitor. They can deliver large forces due to the high energy density in the PZT films but they have short stroke length, i.e. the displacement of the moving plates is small (Uchino, 2008). Finally, PZT is a material that is seeing challenges due to environmental concerns, and replacement films such as AlN pose transducer efficiency challenges.

3. Electro-thermal Bimorph Actuation

Electro-thermal bimorph actuators are based on the principle of thermal expansion to produce motion. The actuators consist of a beam that has materials with different coefficients of thermal expansion (CTE). When a current is passed through the beam, its temperature rises causing rotation and deformation due to the CTE difference between the materials and the residual stress. These actuators are able to produce large output forces and a large

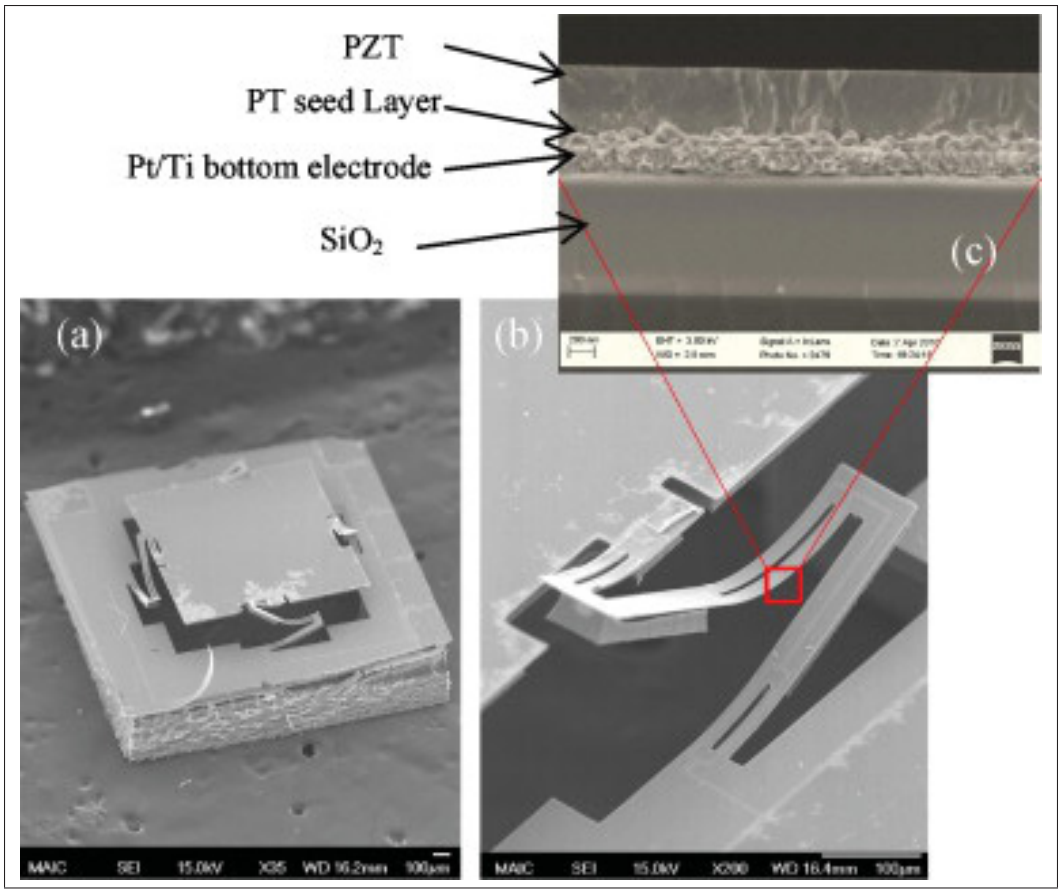

Figure-A I-2 SEM pictures of a fabricated PZT micromirror showing the structure of a PZT scanner,
(a) 2 mm × 2 mm chip, (b) Close-up view of a PZT actuator, (c) Cross-section view of the PZT unimorph
Taken from Kawabata, Ikeda, Goto, Matsumoto & Yada (1997)

displacement in one direction, thus they are primarily used to deflect MEMS mirrors in one direction (i.e., upward or downward) (Huang & Lee, 1999; Jia, Pal & Xie, 2009; Wu & Xie, 2007). Moreover, an appropriate heat management strategy is needed for designing a bimporph actuator.

The bimorph layers of the actuator are made of materials with different CTE such as metal/silicon nitride, aluminium/silicon-dioxide, gold/silicon-dioxide, or a heater element enclosed by aluminium and silicon-dioxide (Jia, Samuelson & Xie, 2011; Jain, Kopa, Yingtian Pan, Fedder & Huikai Xie, 2004; Guan & Zhu, 2010; Huang, Cheng, Chung & Hsu, 2009).

A micromirror based on bimorph actuation was fabricated using a SOI wafer and its SEM image is shown in figure I-3. The fabrication of monolithic micromirrors with bimorph actuators is possible using SOI wafers or silicon wafers, avoiding any assembly technique, thus making the fabrication process more easily compatible with standard CMOS technology (Gilgunn, Liu, Sarkar & Fedder, 2008; Singh, Teo, Xu, Premachandran, Chen, Kotlanka, Olivo & Sheppard, 2007).

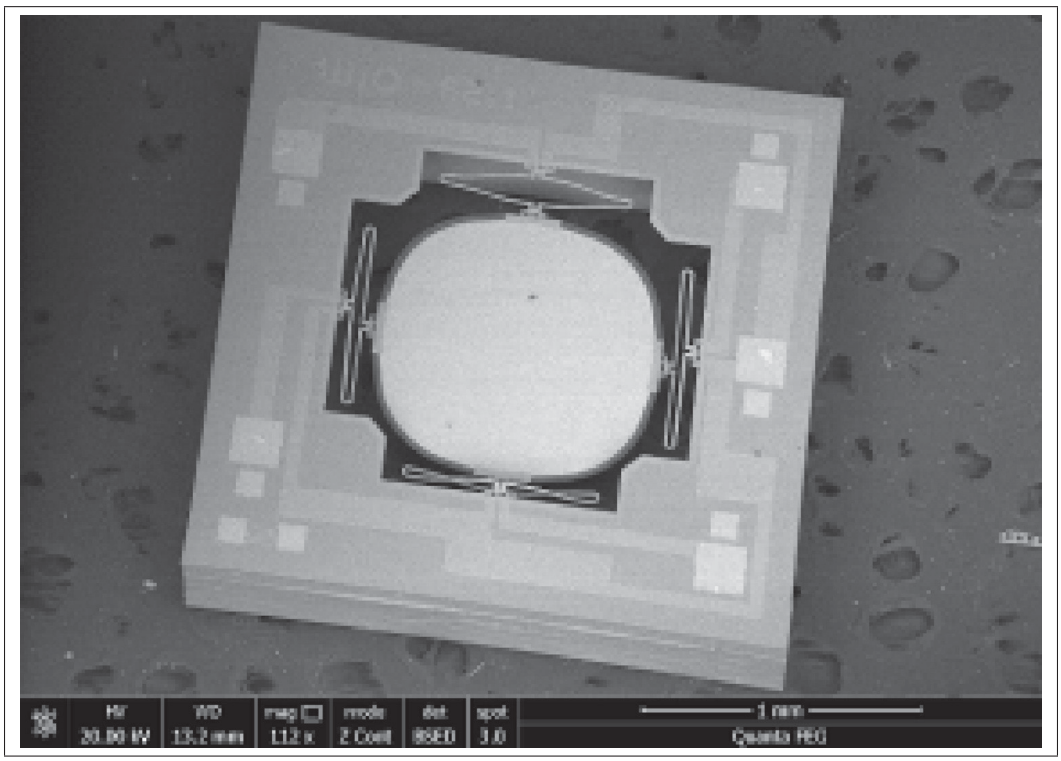

Figure-A I-3 SEM image of a bimorph scanner
Taken from Gilgunn, Liu, Sarkar & Fedder (2008)

These actuators are slow and consume relatively high power, making them suitable for applications in which high frequency operation is not required and the power consumption is not critical, such as endoscopic imaging applications (Jia *et al.*, 2009). Apart from the high power requirement and the slow speed operation, these actuators also suffer from out-of-plane curling of the structure, causing difficulties in controlling the curling angles of the mirror plate after it is released. Also, the compressive thermal stress induces material degradation and fatigue, resulting in potential structure buckling and failure.

4. Electrowetting Actuation

The shape of an electrolyte drop on an electrode can be controlled with an electric potential. This principle known as electrowetting. The resulting droplet shape deformation is utilized to move a micromirror in electrowetting scanners. A micromirror with electrowetting actuation with various device configuration is shown in figure I-4. The droplet acts as a pivot point around which the micromirror tilts continuously when the droplet-shape is modified with an applied voltage (Dhull, Fuller, Kao, Liao & Lu, 2011; Lee, Moon, Fowler, Schoellhammer & Kim, 2002; Wan, Zeng & Feinerman, 2006). Generally, water drops (Hyungmin Kang & Joonwon Kim, 2006), electrolyte drops (Dhull, Puchades, Fuller & Lu, 2009) and liquid metal drops (LMD) (Zeng, Wan & Feinerman, 2006) are used as electrowetting droplets (EWD) confined between the mirror plate and the wetting spot. Lower vapour pressure, better electrical/thermal contact with the surrounding layers and smaller electrolysis are desirable from the electrowetting droplets, and these properties are better found in LMD than other kinds of electrowetting drops (Liu, Sen & Kim, 2010a; Tang, Zhu, Sivan, Gol, Soffe, Zhang, Mitchell & Khoshmanesh, 2015). The LMD is sandwiched between a mirror plate at the top and a bottom substrate treated with a insulation layer in order to assemble a EWD scanner. It must have a small actuation gap between the mirror plate and the substrate to achieve high switching speeds. However, the uncertainty of obtaining a small actuation gap in EWD based devices is a problem because it is challenging to precisely control the deposited volume and position of the EWD in the device (Sen & Kim, 2009). Also, obtaining a small actuation gap becomes more difficult due to the errors associated with the assembly process. These scanners have small scanning range due to the limited tilt angle of the mirror plate.

5. Electrostatic Actuation

Electrostatic actuation is the very first and the most common actuation technique used in MEMS scanners. This is due to its ease of fabrication without the need of any special material and its suitability to any fabrication facility with MEMS capability. In comparison, the fabrication of other actuators is more challenging requiring the deposition of special materials such as piezoelectric materials or needing complex packaging and assembly methods such as

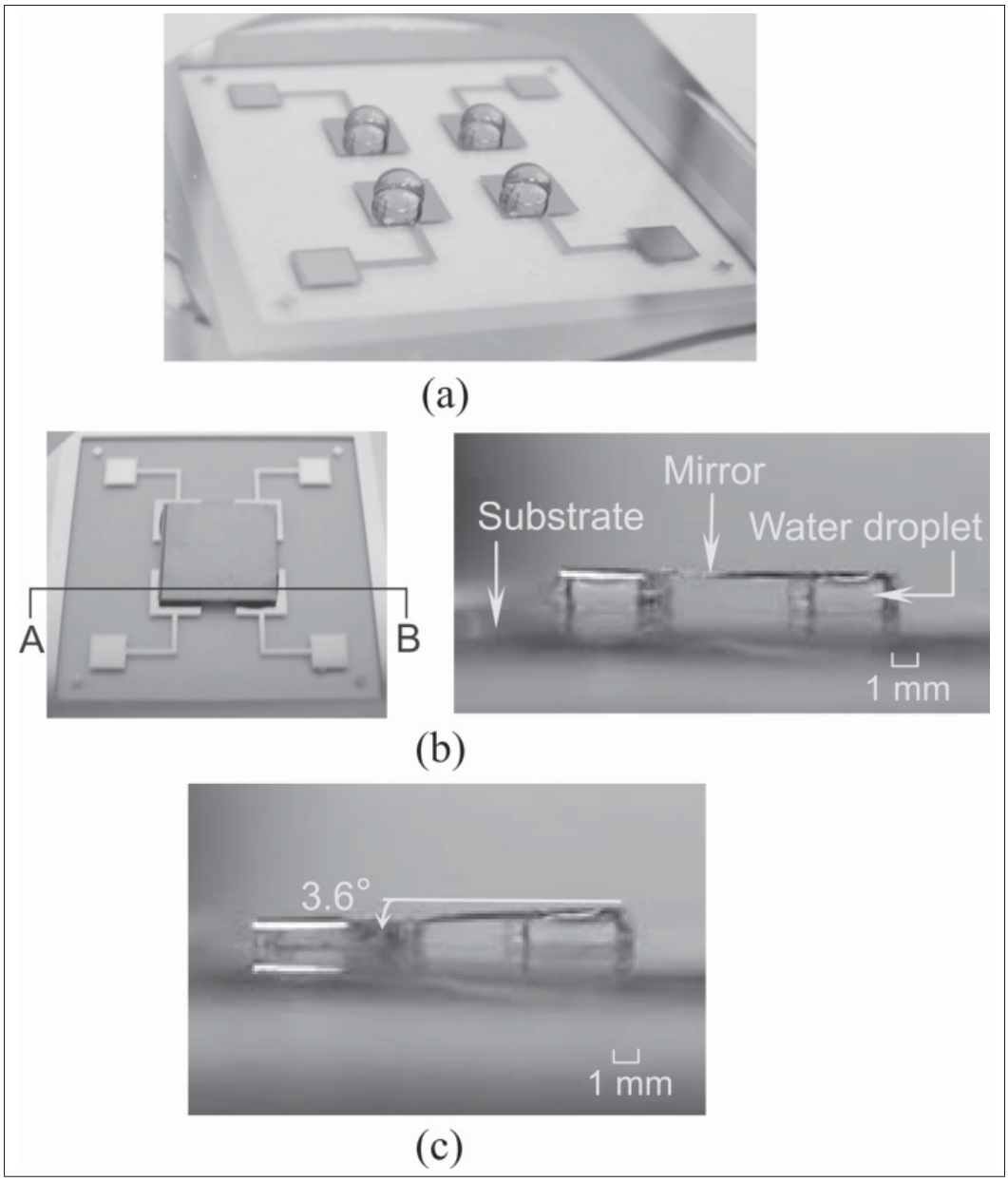

Figure-A I-4 Image showing eletrowetting actuation based scanner, (a) 4 water droplets on electrodes, (b) Self-aligned mirror and its AB cross section view, and, (c) Tilted micromirror
Taken from Hyungmin Kang & Joonwon Kim (2006)

including a magnet for electromagnetic actuators. The working principle of electrostatic actuators relies on the electrostatic force (F_{ele}) generated between the two oppositely charged electrodes with a potential difference V and is given by:

$$F_{ele} = \frac{A\epsilon V^2}{2g^2} \tag{A I-1}$$

where g is the distance between the electrodes, ϵ is the effective dielectric constant of the medium between the electrodes and A is the overlap area between the electrodes. Parallel plate actuation and the comb-drive actuation are the two main configurations of electrostatic actuators.

The parallel plate actuation scheme comprises of a ground electrode and a driving electrode facing each other such that one plate is suspended over the other plate. Also, one plate is anchored using a fixed beam while the other the plate is connected to a separate torsional beam. The grounded electrodes move toward the driving electrode when the electric potential is applied until an equilibrium is reached between the generated mechanical restoring torque of the torsional beam and the electrostatic attractive torque. Micromirrors capable of bi-axial scanning can be fabricated by adopting various configurations of the electrodes (Toshiyoshi, Piyawattanametha, Cheng-Ta Chan & Wu, 2001a; Yeow, Yang, Chahwan, Gordon, Qi, Vitkin, Wilson & Goldenberg, 2005). A bi-axial electrostatic scanner with its components is shown in figure I-5. However, the scanners based on parallel plate actuators have small tilt angles and require high voltages (Mathias *et al.*).

Comb-drive actuators are also used in various MEMS scanners and consist of a pair of rotor and stator comb drives with a vertical offset for torque generation. Upward or downward rotary motion can be generated by applying an actuation voltage between the rotor and stator. Scanners based on comb-drive actuation are fabricated using multiple SOI wafers and are assembled using wafer bonding. A large area on the device is required to accommodate the micromirror along with comb-drive actuators, which increase the overall footprint of the device.

An overview of the key characteristics of different actuators used in MEMS micromirrors are summarized in Table 1.1. Ease of fabrication, voltage requirement, angular scanning range, compactness, scan speed, and power efficiency are a few of the important parameters that are considers for selecting a MEMS scanner. Electrostatic, electromagnetic, piezoelectric, and electro-thermal are the main actuation principles used in MEMS scanners. Each actuation

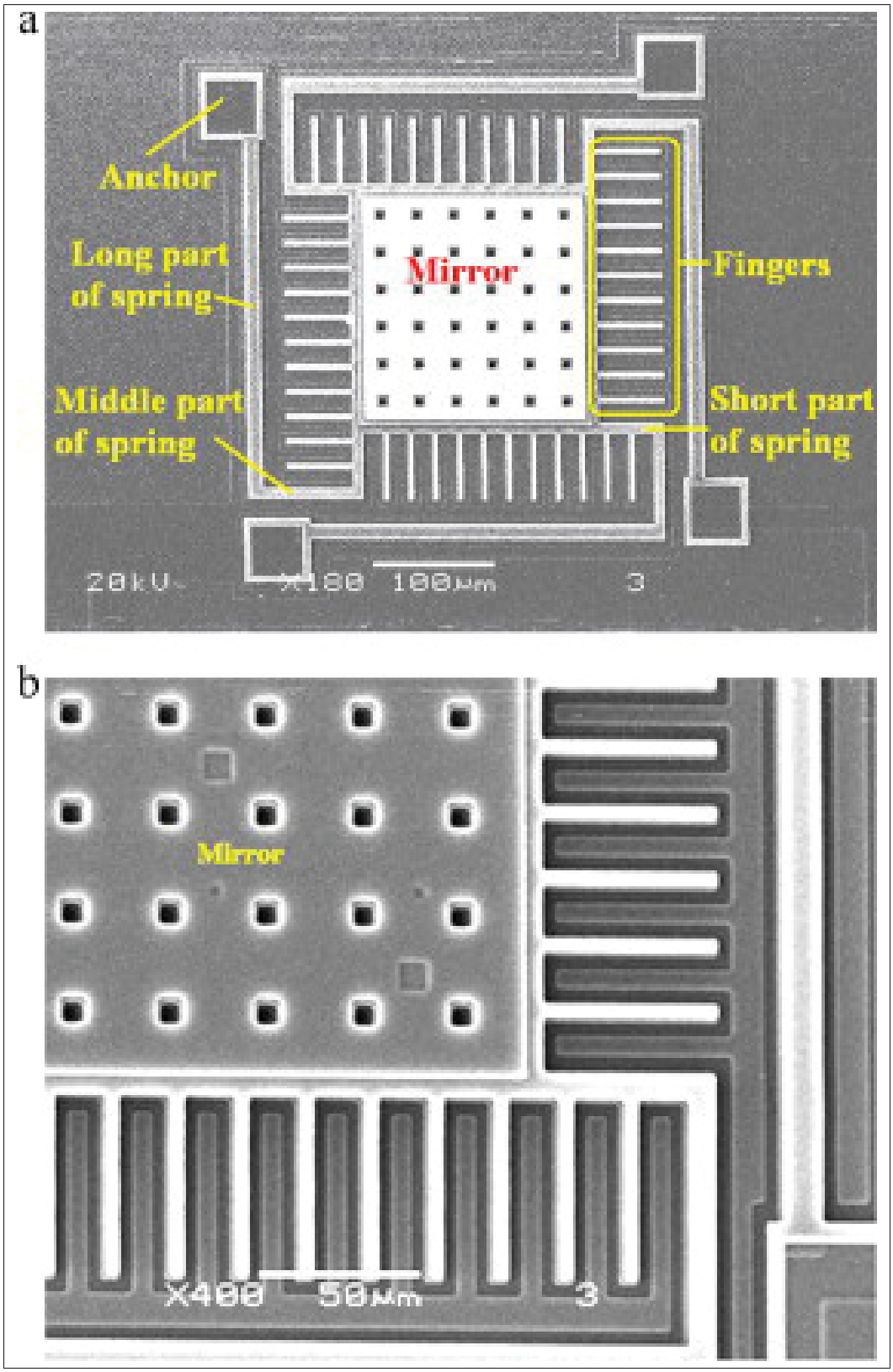

Figure-A I-5 SEM of the micromirror prototype based on electrostatic actuation, (a) micromirror device, (b) zoomed view
Adapted from Mathias, Fox, Temmen & Tuck

mechanism offers advantage in some aspects and have limitations in others. For instance, electromagnetic and electrostatic are simple to fabricate and have large mirror displacement. However, electromagnetic consumes high power and are large in size. Likewise, electrostatic requires high voltage, deliver very low force and suffer from non-linearity. On the other hand, piezoelectric are compact, deliver high force and operate at low-voltage but have small displacements.

Table-A I-1 Different types of actuation principle used in MEMS scanners

Characteristics of various actuation principle		
Actuation principle	**Benefits**	**Limitations**
Electro-magnetic	- Large scan angle - Low voltage operation - Linear and fast response	- Complex fabrication process - Needs high power and current - Bulky
Electro-thermal	- Compact and simple structure - Low voltage and linear operation - High scan angle and displacement	- Slow response and high power consumption - Bandwidth limited by thermal time constant - Complex fabrication process
Piezoelectric	- Low power and low voltage operation - Fast response time - Better for resonant systems	- Small displacement - Hysteresis and non-linear operation - Requires special materials
Eletrowetting	- Low power operation - Linear and fast response - Simple fabrication process	- Small displacement and scan range - Needs high voltage - Requires component assembly
Eletrostatic	- Easy to fabricate - Highly compact - Fast response and highly accurate	- Non-linear operation - Requires high voltage - Small scan range

APPENDIX II
FINITE ELEMENT ANALYSIS OF MICROMOTOR ARCHITECTURE

The optimization of the micromotor is performed by using finite element analysis (FEA). The distribution of the electric potential and electric field between in the gap between the rotor and the stator poles is determined. The FEA is performed using COMSOL multiphysics to model the micromotor and to obtain the generated torque. The micromotor has a complex structure due to the three-dimensional shape and size of its components. However the micromotor is a symmetric device with respect to the central pin bearing and is exploited to ease the modelling process.

1. Definition of the unit sector

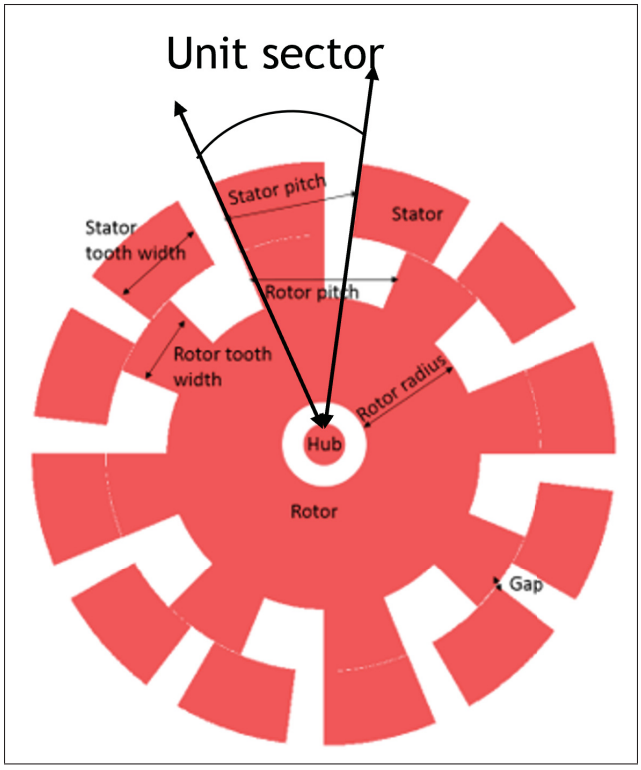

Figure-A II-1 Image showing the unit sector of the VCM

Consider the micrmotor with 12 stator poles and 8 rotor poles and dividing it in 12 identical sectors with angular width equal to stator pitch such that each sector has atleast single stator and rotor pole. This sector is called as unit sector as shown in the figure II-1. By repeating the unit sector, a complete micromotor can be constructed due to its angular symmetry. Thus the net generated torque per phase can be calculated by multiplying the generated torque of the unit sector by the total number of stator poles per phase. This approach can be extended to different architectures of the micromotor where the number of poles and the shape of the poles is modified.

2. Geometrical design of the unit sector

The size and shape of the various components of the unit sector i.e. the stator pitch β), the rotor pitch (α), the width of the rotor (θ), the width of the stator (φ), the gap between the stator pole and the rotor pole (G), the length of the rotor teeth (L_r) and the radius of the rotor (R_r) are calculated analytically using following relation given in (Dufour *et al.*, 1996b):

$$\frac{\beta}{q} \leq \theta \leq \beta\left(1 - \frac{1}{q}\right) \tag{A II-1}$$

$$\frac{\beta}{q} \leq \varphi \leq min(\alpha, \beta\,(1-\theta)) \tag{A II-2}$$

where q is the total number of phases of the driving signal. The ripples of the generated torque (T) can be minimized if the rotor and stator width meet the following condition:

$$\theta = \varphi = \frac{\beta}{2} \tag{A II-3}$$

During the operation of the micromotor the stators are stationary and the rotor moves around the central axis. This motion continuously modifies the rotor and stator pole alignment, thereby changing the stator-rotor pole capacitance and the generated torque. This behaviour can be simulated in COMSOL by incrementally adjusting the alignment of the rotor pole with the stator poles and calculating the capacitance and torque at each position for the applied voltage. The angular range starts from the point of no-overlap where the leading edge of the

rotor poles is aligned with the starting edge of the stator pole. The final value of the angular range is the point of no-overlap where the trailing edge of the rotor pole is aligned with the ending edge of the stator pole.

A three-dimensional model of the unit sector is developed using COMSOL layout editor. The rotor poles and the stator poles are realized using the POLY1 layer of the PolyMUMPS process. Thus, the thickness of the rotor and the stator is pole is 2 μm which is equal to the thickness of the POLY1 layer of the PolyMUMPS process. The fabricated rotor has etch holes evenly distributed on its surface to facilitate the release process and these holes are neglected in the rotor model. This is because the electric field is prominent near the edges of the rotor than any other location on the rotor, so the absence of etch holes have negligible effect on the generated torque.The steps of the PolyMUMPS process are such that the realized rotor is vertically misaligned with the stator due to the construction of the dimples on the rotor structure. Thus, the top edge of the stator pole is at higher position than the top edge of the rotor pole by an amount of 250 nm and is considered during the model definition.

3. Mesh for the unit sector

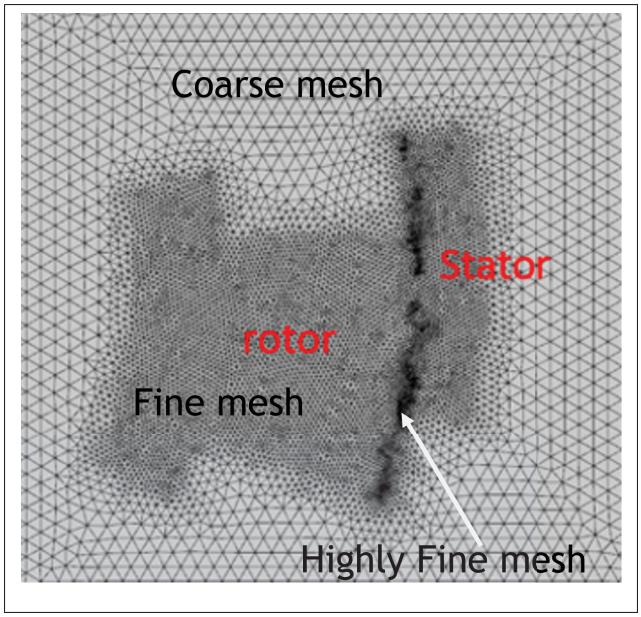

Figure-A II-2 Mesh of the unit sector for finite element analysis

The unit sector is placed inside a bounding box with air as the medium and the mesh for the FEA is defined. The tetrahedral mesh type is used to define the finite elements with variable size of the mesh element. The mesh elements are highly fine at the edges of the stator pole and the rotor pole in the gap region; the mesh elements are relatively are fine at the surface of the stator and the rotor and the mesh elements are coarse in the bounding box as shown in figure II-2. The choice of the non-uniform meshing is done to reduce the computation time and resources and also, to obtain accurate solutions in the regions of dominating electric field.

4. Simulated electric field distribution, capacitance and the generated torque

For the purpose of the FEA, the position of the rotor pole is fixed and it is electrically grounded. At the same time, the stator poles are supplied an electric potential starting from 0 V to 200 V and the distribution of the electric field is captured. In the next iteration, the position of the rotor pole is modified to change the overlap area between the stator pole and rotor pole and the FEA is performed by applying the excitation to the stator poles. This process is repeated such that the rotor pole moves along the periphery of the stator pole, mimicking a circular motion thereby changing the overlap area between the poles. The distribution of the electric field for a simple micromotor is shown in figure II-5 and and the teethed edge architecture is presented in figure II-6.

For each position of the rotor pole, the effective overlap area between the rotor pole and the stator pole is calculated from the model and is used to determine the capacitance between the poles. The fringe capacitance and parasitic capacitance between the poles is neglected and parallel plate capacitance is assumed for the simplicity of the calculation. Similarly the generated torque for each position of the rotor pole at various applied voltage is calculated and is shown in figure II-5 and II-6 for different architecture of the micromotor.

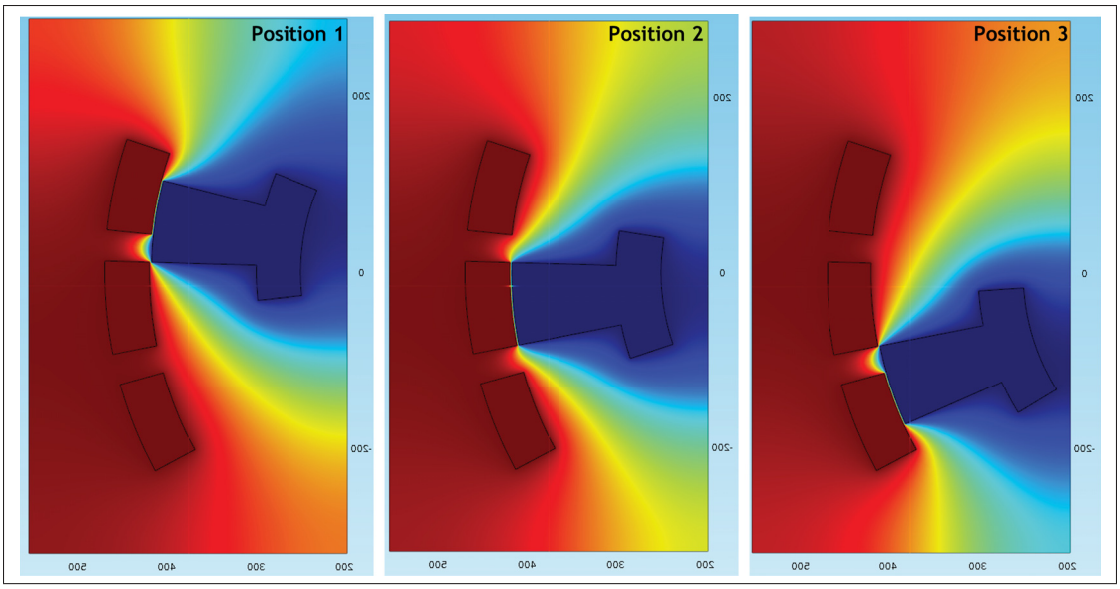

Figure-A II-3 Electric field distribution for simple architecture micromotor at various rotor positions

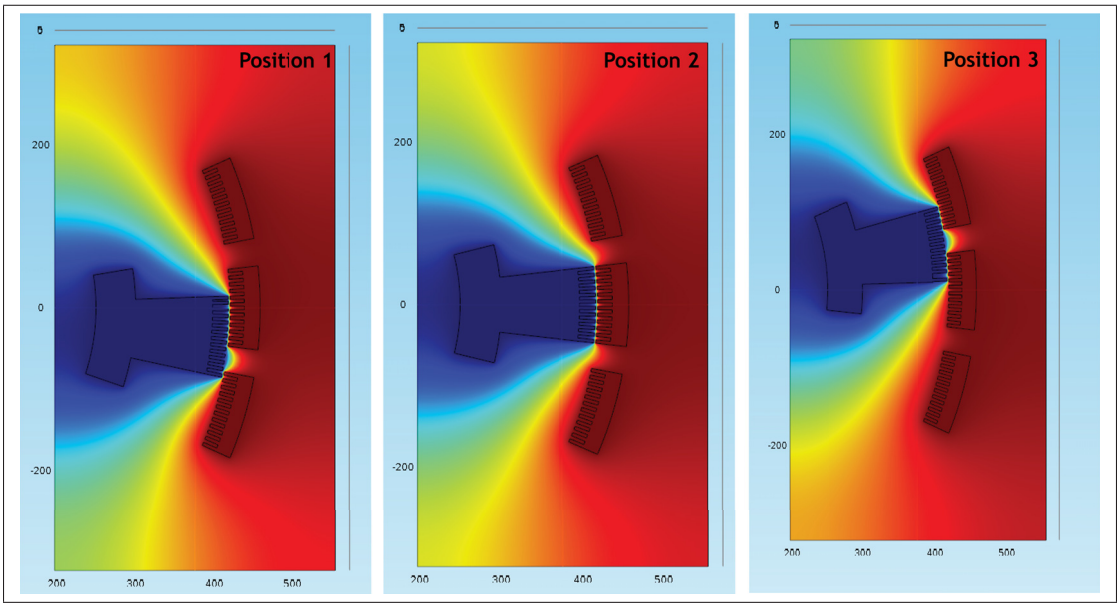

Figure-A II-4 Electric field distribution for teethed-edge architecture micromotor at various rotor positions

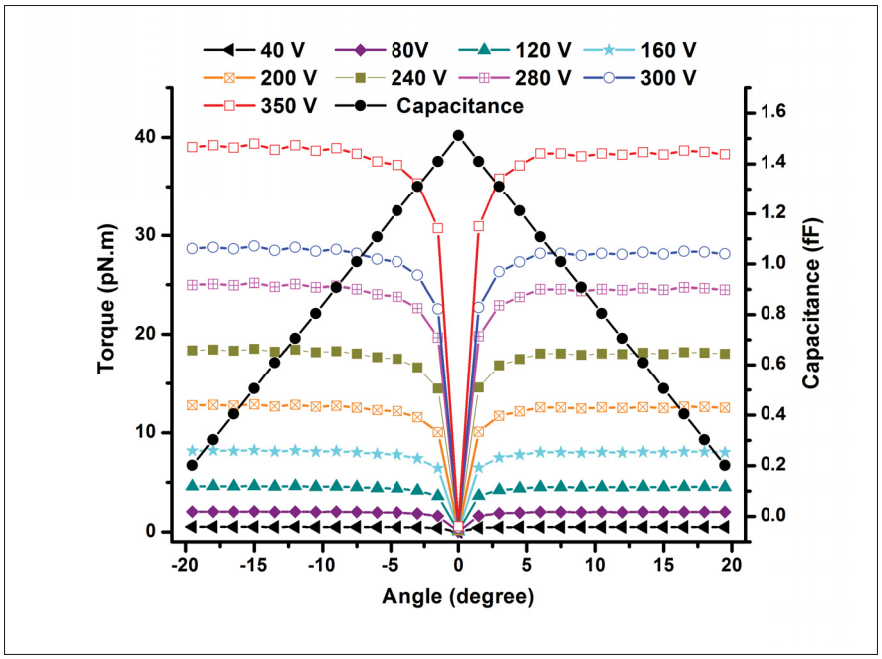

Figure-A II-5 Torque vs rotor position and capacitance vs rotor position at different voltage for simple micromotor

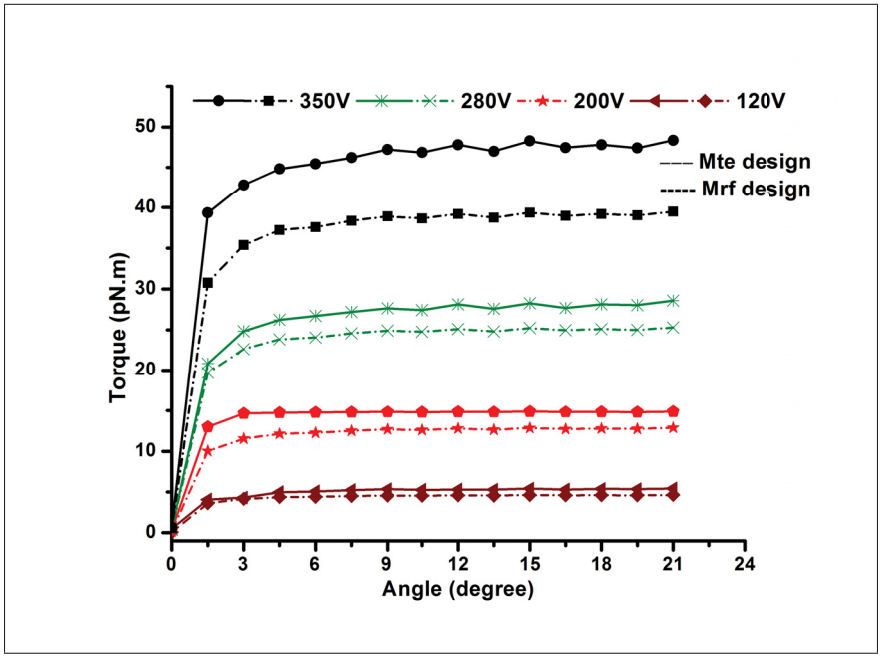

Figure-A II-6 Generated torque for teethed-edge architecture micromotor at various rotor positions

APPENDIX III
HIGH TORQUE ELECTROSTATIC MICROMOTOR FABRICATED USING POLYMUMPS FOR OPTICAL SCANNING APPLICATIONS

Abstract

We demonstrate high-performance rotary electrostatic side-drive variable capacitance micromotors with high speed and high driving torque. The micromotors are fabricated using the PolyMUMPS process and the fastest device can rotate at 8040 rpm. Micromotors with a varying number of rotor and stators poles were designed, fabricated and characterized. Multiple techniques were applied to enhance the motive torque and to reduce the friction presents in the micromotor. The diameter of the rotor is 600 m and it is supported by only four dimples/bearing of 3.5 m in radius. These electrostatic micromotors achieve record speed as well as torque for devices fabricated using the PolyMUMPS process. Micro-polyhedrons were integrated onto the micromotors to illustrate their capability to rotate them as part of an optical scanning system.

Keywords

Variable Capacitance Micromotors, PolyMUMPS process, Torque, Rotational speed, Electrostatic side drive.

Introduction

Micromotors are important micromechanical systems (MEMS) that can enable several applications. Various MEMS micromotors have been successfully fabricated and tested in the past. Amongst them, micromotors based on electrostatic actuation have demonstrated a high powervolume ratio. Electrostatic variable capacitance micromotors (VCMs) are electrostatic MEMS actuators that include a miniaturized rotating stage. They can be fabricated using commercial multi-layer polysilicon surface-micromachining such as the PolyMUMPS process. Low power consumption, very small size, high positioning resolution and high speed are key features of VCMs and they were employed to develop micro-pumps (Agrawal, Hasan, Ashraf, Sundaram, Chow, Kapat & Vaidya, 2002), microrobotics (Stark, Mehregany & Phillips, 1997), and optical systems (Basha, 2012b; Simard, Khalid & Kirk, 2006). Recently, light

detection and ranging (LIDAR) modules have received special attention for a use in unmanned aerial vehicles (UAVs) and autonomous vehicles (Wang, Koppal & Xie, 2020a). These modules require motorized scanners for optical scanning that are bulky and consumes lots of power. However, optical scanner based on MEMS mirrors have been demonstrated and have reduced the overall dimension of the scanning modules down to 20-50 mm (Wang *et al.*, 2020a). Nevertheless, these scanners can be scaled down further by using a high speed VCM to reduce the weight and size by orders of magnitude, and significantly decrease costs through batch fabrication. A VCM rotating at a speed of 5200 rpm was able to provide 347 scans per second (Azzam Yasseen *et al.*, 1999) but the micromotor was fabricated using an in-house micro-machining process. In (Basha, Dechev, Safavi-Naeini & Chaudhuri, 2007a) a slow speed VCM for rotary optical switch application was fabricated using the PolyMUMPs process. VCMs featuring high speed and high torque that are fabricated using commercial processes for optical scanner applications are thus desirable. Recently, 3-phase electrostatic VCMs with different architectures that are suitable for high speed operation (Gour *et al.*, 2020a) were devised. The micromotors were fabricated using the PolyMUMPS process and were among the fastest MEMS devices implemented with this process. Micromotors rotating at 7680 rpm at 200 V were demonstrated. However, all the micromotor design variants had 12 stators and 8 rotors, thus they could deliver only a relatively low driving torque. Here, we present 3-phase electrostatic VCMs with improved performance. These were fabricated to provide higher speed as well as higher torque as compared to the previously reported work so that they can be integrated with a micro-polyhedron and drive it in optical scanning applications. In the following sections, we describe the operating principle of the micromotor, provide an analytical model used in their design, and detail the different design variants. We then present experimental results and show the integration with a micro-polyhedron for optical scanning applications.

Rotary Micromotors

Fig. III-1 shows a schematic of the main elements of a VCM. A VCM operates by converting the electrical energy stored in the rotor-stator capacitor to mechanical energy. The rotor

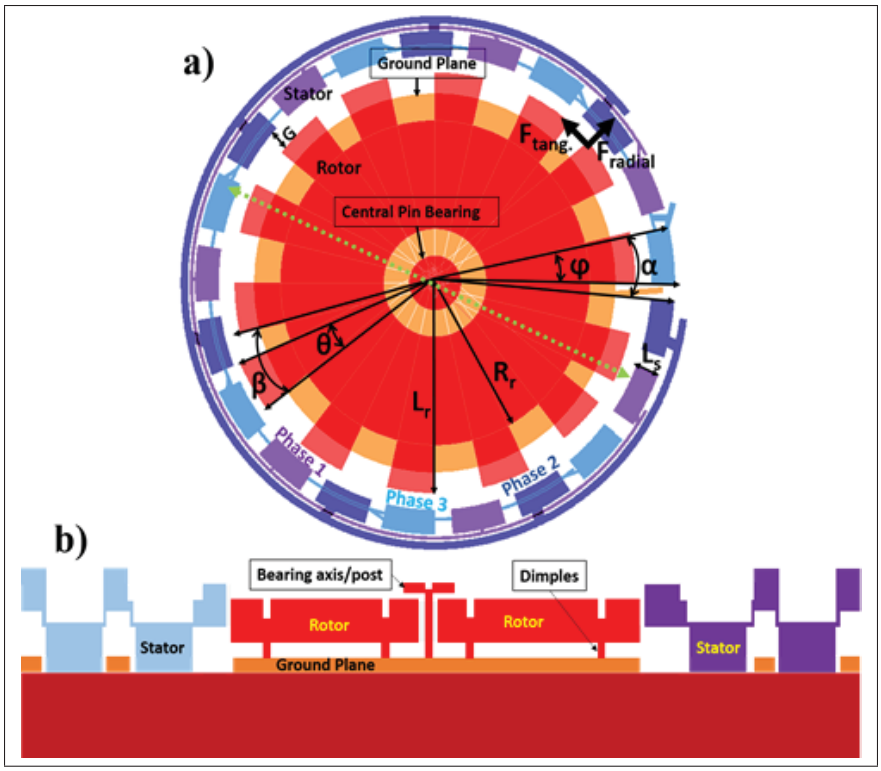

Figure-A III-1 Schematic of VCM showing a) top view b) cross-section view

stands freely on a ground plane and when a potential with varying phase is applied to the stator poles, an electric field is produced between the rotor pole and the stator pole. The tangential component of the electric force moves the rotor and starts the rotation of the rotor.

Modelling

The angular motion of the rotor changes the statorrotor capacitance. The output torque of the micromotor is proportional to the rate of change of this capacitance with respect to the angular position of the rotor ϕ. The torque generated by a group of rotor-stator electrodes belonging to a single phase excitation is given by (Ghalichechian, Modafe, Beyaz & Ghodssi, 2008b):

$$T(V,\phi) = \frac{N_s V^2}{2p}\left(\frac{\partial C(\phi)}{\partial(\phi)}\right) \qquad \text{(A III-1)}$$

where V is the applied potential, N_s is the number of stator poles, p is the number of phases of the driving signal and N_ϕ is the capacitance of a rotor-stator pair. The geometry of the micromotor significantly affects the stator-rotor capacitance and its operation, thus optimizing the key physical parameters is required to maximize the generated torque. This was done by using the analytical model presented in (Gour *et al.*, 2020a) to derive the key geometrical parameters, which are listed in Table 1.

Table-A III-1 Optimal geomatrical parameter obtained using analytical modelling

Micromotor geometrical parameters	**Designed value**
Gap between rotor and stator(G)	2.5 μm
Radius of the micromotor rotor(R_r)	300 μm
Number of phase(q)	3
Total number of stators poles (N_s)	12,15,18,21
Total number of rotors poles (N_r)	8,10,12,14
Length of the stator tooth (L_s)	140 μm
Length of the stator tooth (L_s)	417.75 μm
Rotor pitch (β) & width(θ) for N_r=10	36°,18°
Rotor pitch (β) & width(θ) for N_r=12	30°,15°
Rotor pitch (β) & width(θ) for N_r=14	25.7°,12.85°
Stator pitch (α) & width(ϕ) for N_s=15	24°,18°
Stator pitch (α) & width(ϕ) for N_s=18	20°,15°
Stator pitch (α) & width(ϕ) for N_s=21	17.14°,12.85°

The generated drive torque can be increased by applying a higher excitation voltage but this can lead to dielectric breakdown since the gap between the rotor pole and stator pole is only 2.5 m. However, VCMs with a large number of stator poles should deliver high driving torque as it is directly proportional to the number of stator poles. At the same time, the ratio of total number of stators to total number of rotors should be 1.5 to maximize torque

[10] and for rotor size scaling. However, the number of stator poles cannot be increased arbitrarily otherwise it will make the micromotor slow since the maximum speed of VCMs is inversely proportional to the number of rotor poles. Thus, we implemented VCMs with up to 21 stators. Also, the friction present in the VCM should be minimized to enhance its performance. The friction between the rotor and the ground plane can be minimized by reducing the contact area between the ground plane and the dimples supporting the rotor. Here, only four dimples are used in all the designs. This is a reduction of 75% as compared to the previously reported work (Gour *et al.*, 2020a). The friction between the rotor and the hub is minimized by using a small hub with a diameter of 12 μm.

Design Variants

Two VCM architectures, one with a simple pie-shape rotor-stator poles geometry, hereon referred to as s-arc, and another with teethed edges of the rotor-stator poles, referred to as t-arc, were investigated (see Fig. III-2). Each architecture was used to implement the variants listed in Table 2 based on the parameters in Table 1.

Table-A III-2 Design variants of the fabricated micromotors

Design version	N_s	N_r	**Type**
M_{1s}	15	10	s-arc
M_{2s}	18	12	s-arc
M_{3s}	21	14	s-arc
M_{1t}	15	10	t-arc
M_{2t}	18	12	t-arc
M_{3t}	21	14	t-arc

Finite element analysis (FEA) of the optimized micromotor was performed to obtain the generated torque shown in Fig. III-3. The torque is calculated at different excitation voltages and at a particular rotor-stator alignment for all the variants. The torque generated in the Mt-arc designs is higher than the Ms-arc designs. Also, among the same architecture group, VCMs with a higher number of stator poles provide more torque.

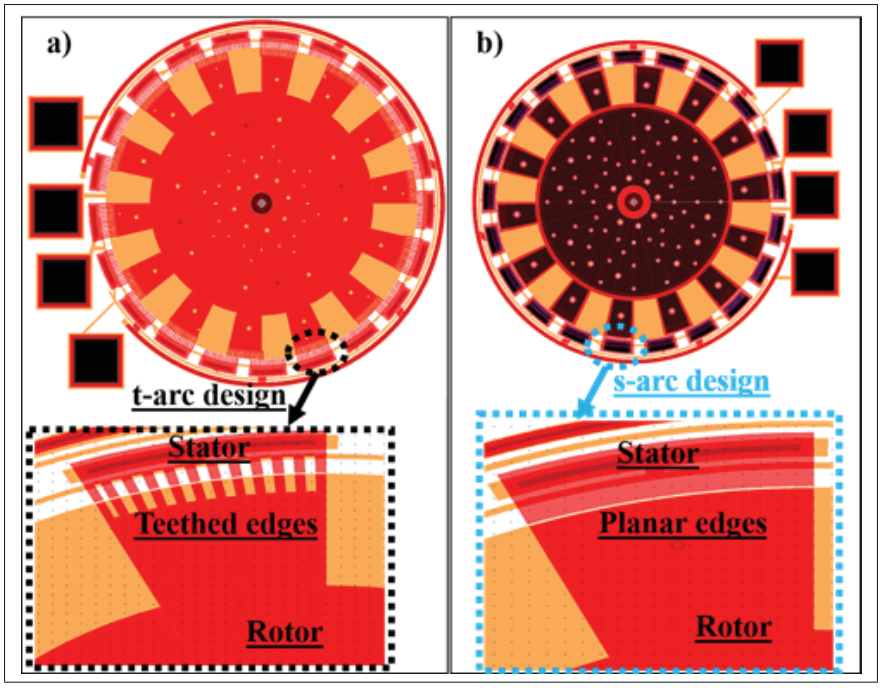

Figure-A III-2 Schematic of VCM showing a) t-arc VCM b) s-arc VCM

Fabrication and Testing Results

The micromotors were fabricated using the PolyMUMPs process and SEM images are shown in Fig. III-4. VCMs are 3-phase devices, thus the electrical characterization of the micromotors is performed by using a 3-phase square wave excitation. Each phase is connected to a group of stator poles such that the 3-phase signal is distributed equally among all the stator poles, making the micromotor a synchronous device. The rotor is always connected to ground via the dimples. The testing procedure is as follows: i) set the frequency of the excitation signal to 10 Hz; ii) increase the voltage of the excitation signal from 0 V in steps of 2 V until motion of the rotor is observed at a constant frequency; iii) keep the voltage at the same level obtained in the previous step and increase the frequency in steps of 10 Hz until the rotor stops; iv) keep the frequency the same as in the previous step and increase the voltage until motion of the rotor is observed again. The testing procedure is followed up to a maximum input voltage of 200 V, to operate the micromotor within the safe limits of electrical breakdown. The rotational speed of each design variant is calculated according

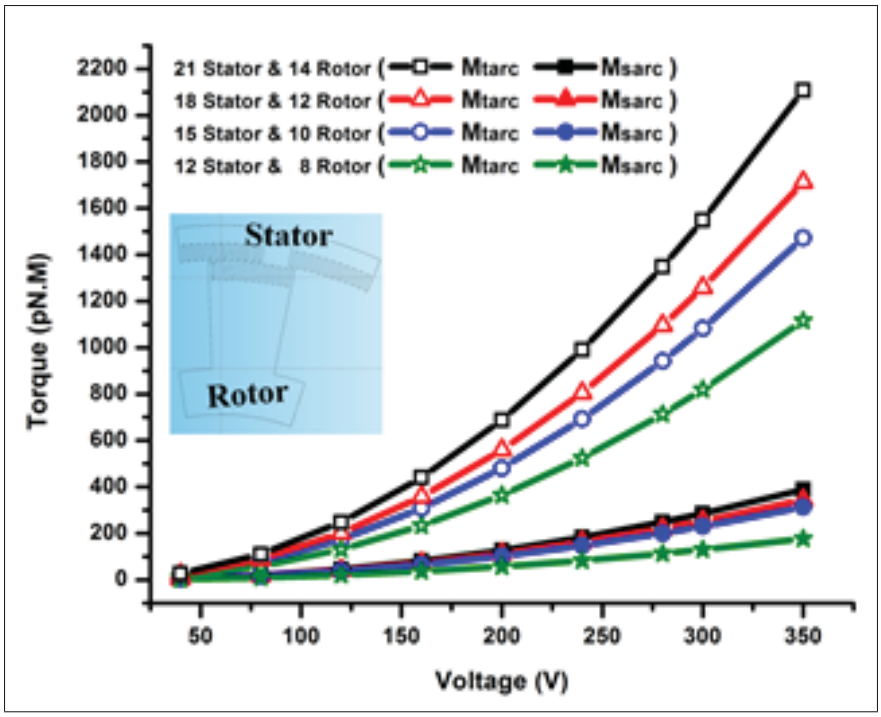

Figure-A III-3 Schematic of VCM showing a) t-arc VCM b) s-arc VCM

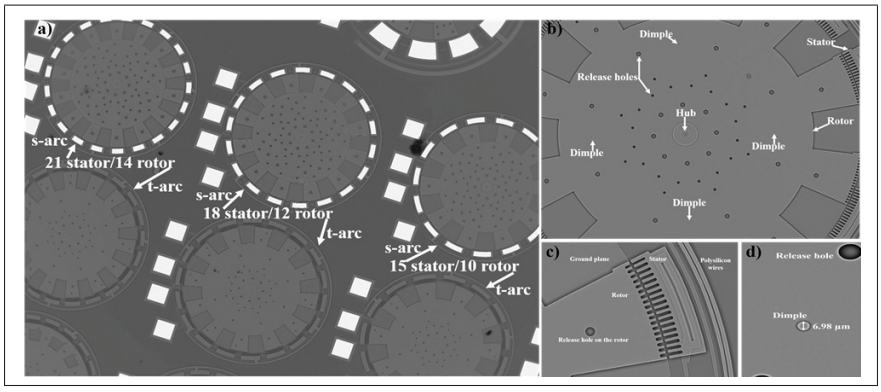

Figure-A III-4 Schematic of VCM showing a) t-arc VCM b) s-arc VCM

to the operating frequency and is shown in Fig. 5 and Fig. 6. The speed of a VCM with N_r number of rotor poles at a given excitation frequency (f_{ele}) is determined by using the following equation (Gour *et al.*, 2020a):

$$\omega_r = 60\frac{f_{ele}}{N_r}\, rpm \qquad \text{(A III-2)}$$

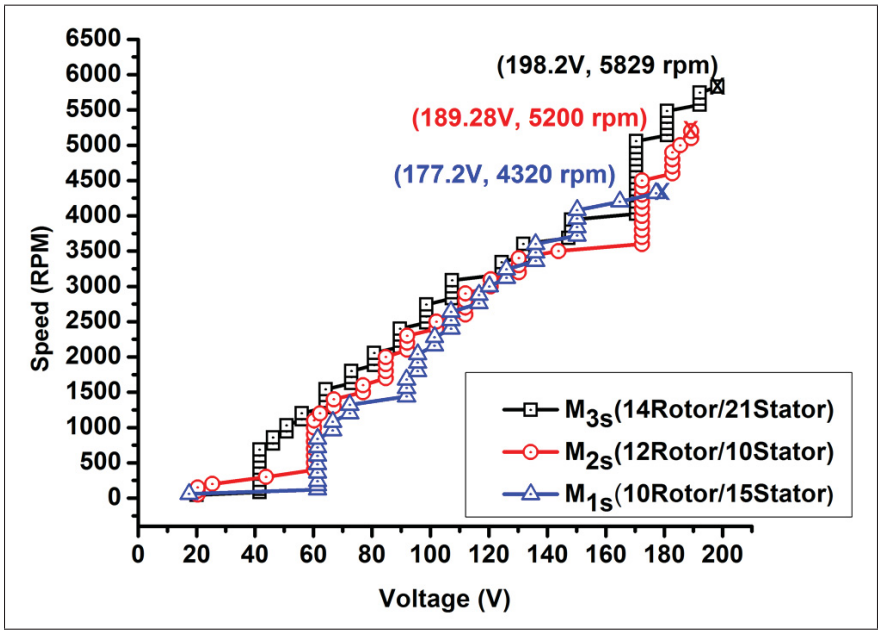

Figure-A III-5 Rotational speed vs voltage for s-arc VCMs

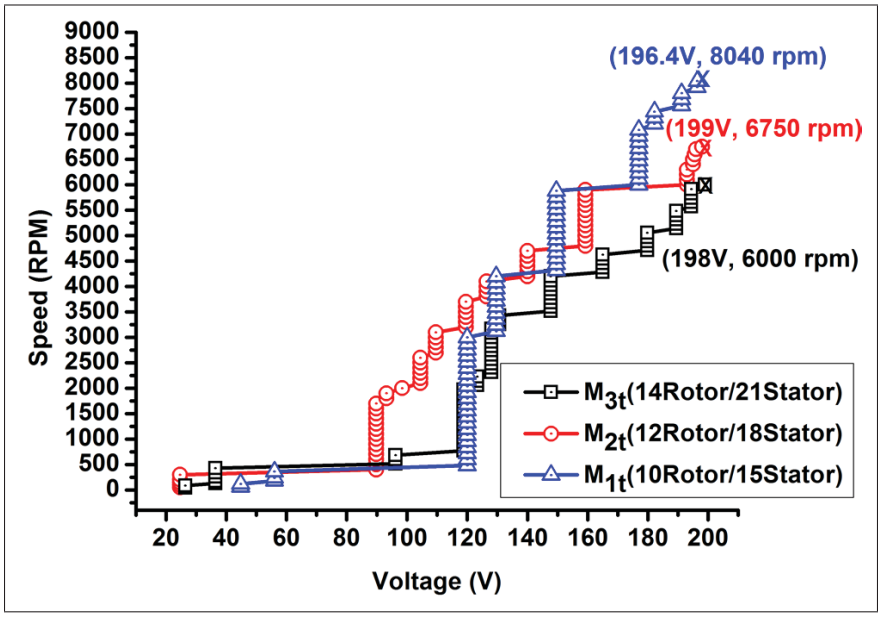

Figure-A III-6 Rotational speed vs voltage for t-arc VCMs

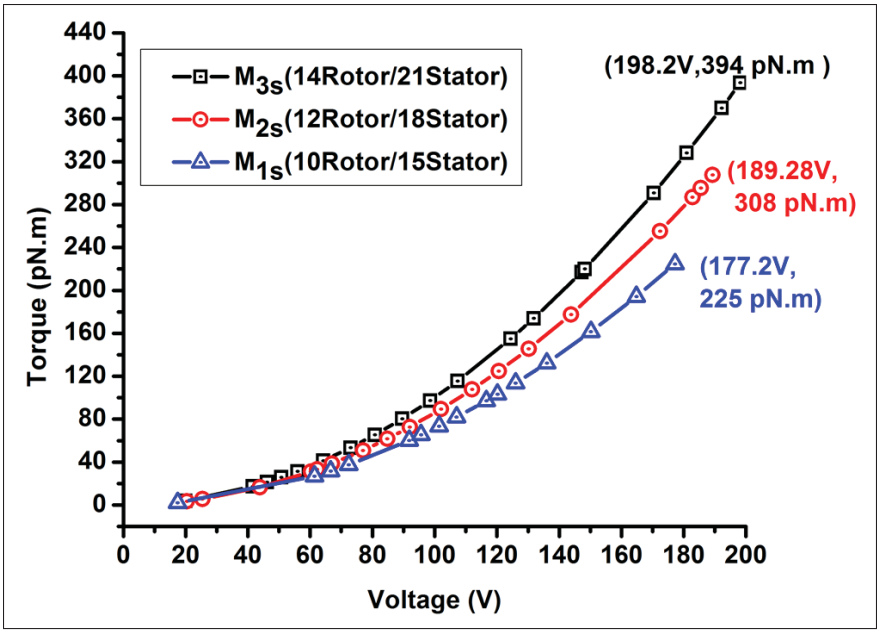

Figure-A III-7 Rotational speed vs voltage for t-arc VCMs

VCM M_{3s} reaches a speed of 5829 rpm operating at 1360 Hz and 198.2 V; M_{2s} rotates with a speed of 5200 rpm operating at 1040 Hz and 189.3 V; and M_{1s} attains a speed of 4320 rpm operating at 700 Hz and 177.2 V. When subjected to excitation at 10 Hz, the M_{3s}, M_{2s}, and M_{1s} VCMs rotate at a speed of 43 rpm, 50 rpm and 60 rpm, respectively, requiring voltages of 20 V; 20.4 V and 17.4 V. In s-arc variants, the M_{3s} VCM outperformed other designs since it can operate at higher frequency even with a higher number of rotor poles. Moreover, the s-arc designs are operating at higher speed than the previous work due to the reduced number of dimples in these designs.

Amongst t-arc variants, M1t achieved the fastest speed of 8040 rpm at 1340 Hz and 196.4 V; M2t attained a speed of 6750 rpm at 1350 Hz and 199 V; and M3t reached 6000 rpm at 1400 Hz and 198 V. All the t-arc variants are faster than the s-arc variants, showing a trend similar to the previously reported work. The speed of 8040 rpm achieved by M1t is a 2.1% improvement over the previous work and is the highest operating speed for this class of VCM. The driving torque of the VCM can be estimated by assuming that the rotor-stator pole capacitance is similar to a parallel plate capacitor and neglecting fringing fields. Thus, the

simplified analytical model to calculate the driving torque per phase is given by (Endemaño, Fourniols, Camon, Marchese, Muratet, Bony, Dunnigan, Desmulliez & Overton, 2003):

$$T(\phi) = \frac{N_{ps} V^2 h L_r \epsilon}{2g} \qquad \text{(A III-3)}$$

where N_{ps} is the total number of stators electrodes per phase, h is the thickness of the rotor-stator film, g is the gap between the rotor and stator pole and L_r is the length of the rotor pole.

The teethed edges of the t-arc designs may impact the electric field distribution near the rotor-stator poles, thus the analytical model for torque calculation is applied to the s-arc designs only. The driving torque of s-arc designs vs. applied voltage is shown in figure 7. The 21 stator VCM can provide a 40% greater driving torque than the VCM with 15 stators at 177 V.

VCM Applications

The teethed edges of the t-arc designs may impact the electric field distribution near the rotor-stator poles, thus the analytical model for torque calculation is applied to the s-arc designs only. The driving torque of s-arc designs vs. applied voltage is shown in figure 7. The 21 stator VCM can provide a 40% greater driving torque than the VCM with 15 stators at 177 V.

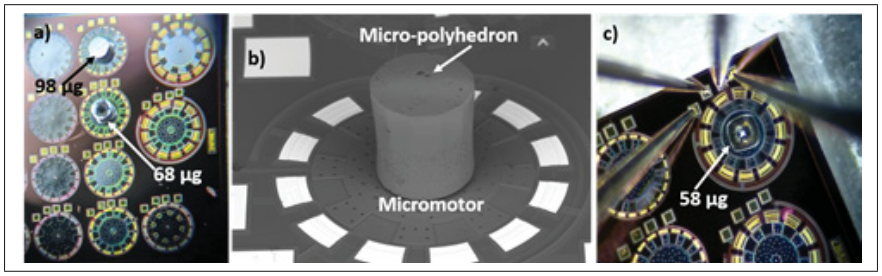

Figure-A III-8 a) Micro-polyhedrons weighing 98 μ and 68 μµg b) SEM micrograph of the assembled micro-system. c)Micro-polyhedron weighing 58 μg in motion.

Conclusion

In this work, high speed VCMs with high torque were successfully demonstrated. Compared to the previous work (Gour, Ménard & Nabki, 2020a), the two architectures can operate at higher speed with a greater number of rotor and stator poles. In addition, the new designs have only four dimples, which drastically decrease the contact area between the rotor and the underlying plane reducing friction and wear. The VCMs were optimized to achieve high performance with the PolyMUMPS process. With a maximum speed of 8040 rpm and torque in order of 100's of pN.m, these VCMs can implement a micro-rotary platform to develop compact high-speed scanning systems with a large field of view for UAVs, for instance. They also have potential applications in biomedical imaging and optical switching systems.

BIBLIOGRAPHY

Abgrall, P., Conedera, V., Camon, H., Gue, A.-M. & Nguyen, N.-T. (2007). SU-8 as a structural material for labs-on-chips and microelectromechanical systems. *ELECTROPHORESIS*, 28(24), 4539-4551.

Agrawal, R., Hasan, Q., Ashraf, N., Sundaram, K. B., Chow, L. C., Kapat, J. S. & Vaidya, J. (2002). Design and fabrication of meso-scale variable capacitance motor for miniature heat pumps. *Journal of Micromechanics and Microengineering*, 13(1), 1–7. doi: 10.1088/0960-1317/13/1/301.

Ahn, C. H. & Allen, M. G. (1995). Fluid micropumps based on rotary magnetic actuators. *Proceedings IEEE Micro Electro Mechanical Systems. 1995*, pp. 408-.

Alarousu, E. et al. (2005). Study on the use of optical coherence tomography in measurements of paper properties. *Measurement Science and Technology*, 16(5), 1131–1137. doi: 10.1088/0957-0233/16/5/012.

Alladi, D. J., Nagy, M. L. & Gaverick, S. L. (1999). An IC for closed-loop control of a micromotor with an electrostatically levitated rotor. *1999 IEEE International Symposium on Circuits and Systems (ISCAS)*, 6, 489-492.

Aoyagi, I., Shimaoka, K., Kato, S., Makishi, W., Kawai, Y., Tanaka, S., Ono, T., Esashi, M. & Hane, K. (2011). 2-axis MEMS scanner for a laser range finder. *16th International Conference on Optical MEMS and Nanophotonics*, pp. 39-40. doi: 10.1109/OMEMS.2011.6031035.

Arslan, A., Brown, D., Davis, W. O., Holmstrom, S., Gokce, S. K. & Urey, H. (2010). Comb-Actuated Resonant Torsional Microscanner With Mechanical Amplification. *Journal of Microelectromechanical Systems*, 19(4), 936-943. doi: 10.1109/JMEMS.2010.2048095.

Asada, N., Matsuki, H., Minami, K. & Esashi, M. (1994). Silicon micromachined two-dimensional galvano optical scanner. *IEEE Transactions on Magnetics*, 30(6), 4647-4649. doi: 10.1109/20.334177.

Ataman, Ç., Lani, S., Noell, W. & de Rooij, N. (2012). A dual-axis pointing mirror with moving-magnet actuation. *Journal of Micromechanics and Microengineering*, 23(2), 025002. doi: 10.1088/0960-1317/23/2/025002.

Ayerden, N. P., Aygun, U., Holmstrom, S. T. S., Olcer, S., Can, B., Stehle, J.-L. & Urey, H. (2014). High-speed broadband FTIR system using MEMS. *Appl. Opt.*, 53(31), 7267–7272. doi: 10.1364/AO.53.007267.

Azzam Yasseen, A., Mitchell, J., Klemic, J., Smith, D. & Mehregany, M. (1999). A rotary electrostatic micromotor 1/spl times/8 optical switch. *IEEE Journal of Selected Topics in Quantum Electronics*, 5(1), 26-32. doi: 10.1109/2944.748101.

Azzam Yasseen, A., Smith, S. W., Merat, F. L. & Mehregany, M. (1999). Diffraction grating scanners using polysilicon micromotors. *IEEE Journal of Selected Topics in Quantum Electronics*, 5(1), 75-82.

Bai, Y., Yeow, J. T. W. & Wilson, B. C. (2010). Design, Fabrication, and Characteristics of a MEMS Micromirror With Sidewall Electrodes. *Journal of Microelectromechanical Systems*, 19(3), 619-631. doi: 10.1109/JMEMS.2010.2044139.

Bao, J. et al. (2020). Integrated navigation for autonomous underwater vehicles in aquaculture: A review. *Information Processing in Agriculture*, 7(1), 139-151. doi: https://doi.org/10.1016/j.inpa.2019.04.003.

Baran, U., Brown, D., Holmstrom, S., Balma, D., Davis, W. O., Muralt, P. & Urey, H. (2012). Resonant PZT MEMS Scanner for High-Resolution Displays. *Journal of Microelectromechanical Systems*, 21(6), 1303-1310. doi: 10.1109/JMEMS.2012.2209405.

Baran, U., Brown, D., Holmstrom, S., Balma, D., Davis, W. O., Muralt, P. & Urey, H. (2012). Resonant PZT MEMS Scanner for High-Resolution Displays. *Journal of Microelectromechanical Systems*, 21(6), 1303-1310. doi: 10.1109/JMEMS.2012.2209405.

Barbedo, J. G. A. (2019). A Review on the Use of Unmanned Aerial Vehicles and Imaging Sensors for Monitoring and Assessing Plant Stresses. *Drones*, 3(2). doi: 10.3390/drones3020040.

Barbic, M., Mock, J. J., Gray, A. P. & Schultz, S. (2001). Electromagnetic micromotor for microfluidics applications. *Applied Physics Letters*, 79(9), 1399-1401.

Bart, S. F., Mehregany, M., Tavrow, L. S., Lang, J. H. & Senturia, S. D. (1992). Electric micromotor dynamics. *IEEE Transactions on Electron Devices*, 39(3), 566-575.

Bart, S. F., Lober, T. A., Howe, R. T., Lang, J. H. & Schlecht, M. F. (1988). Design considerations for micromachined electric actuators. *Sensors and Actuators*, 14(3), 269-292. doi: https://doi.org/10.1016/0250-6874(88)80074-X.

Basha, M. A., Safavi-Naeini, S. & Chaudhuri, S. K. (2007). Design and Fabrication of an Electrostatic Micromotor with a Low Operating Voltage. *TRANSDUCERS 2007 - 2007 International Solid-State Sensors, Actuators and Microsystems Conference*, pp. 1139-1142.

Basha, M. A. (2012a). 3D rotating octagonal micromirror optical scanner: design, fabrication, and assembly. *Micro-Optics 2012*, 8428, 275 – 282. doi: 10.1117/12.924282.

Basha, M. A. (2012b). 3D rotating octagonal micromirror optical scanner: design, fabrication, and assembly. *Micro-Optics 2012*, 8428, 275 – 282.

Basha, M. A., Dechev, N., Safavi-Naeini, S. & Chaudhuri, S. K. (2007a). A Scalable <formula formulatype="inline"><tex>1 × *N*</tex></formula> Optical MEMS Switch Architecture Utilizing a Microassembled Rotating Micromirror. *IEEE Journal of Selected Topics in Quantum Electronics*, 13(2), 336-347. doi: 10.1109/JSTQE.2007.894068.

Basha, M. A., Safavi-Naeini, S. & Chaudhuri, S. K. (2007b). Design and Fabrication of an Electrostatic Micromotor with a Low Operating Voltage. *TRANSDUCERS 2007 - 2007 International Solid-State Sensors, Actuators and Microsystems Conference*, pp. 1139-1142. doi: 10.1109/SENSOR.2007.4300336.

Beerschwinger, U., Milne, N. G., Yang, S. J., Reuben, R. L., Sangster, A. J. & Ziad, H. (1994). Coupled electrostatic and mechanical FEA of a micromotor. *Journal of Microelectromechanical Systems*, 3(4), 162-171.

Beerschwinger, U., Reuben, R. & Yang, S. (1997). Frictional study of micromotor bearings. *Sensors and Actuators A: Physical*, 63(3), 229 - 241.

Behjat, V. & Vahedi, A. (2006). Minimizing the torque ripple of variable capacitance electrostatic micromotors. *Journal of Electrostatics*, 64(6), 361 - 367.

Bell, D. J., Lu, T. J., Fleck, N. A. & Spearing, S. M. (2005). MEMS actuators and sensors: observations on their performance and selection for purpose. *Journal of Micromechanics and Microengineering*, 15(7), S153–S164. doi: 10.1088/0960-1317/15/7/022.

Bernstein, J. J., Lee, T. W., Rogomentich, F. J., Bancu, M. G., Kim, K. H., Maguluri, G., Bouma, B. E. & DeBoer, J. F. (2007). Scanning OCT endoscope with 2-axis magnetic micromirror. *Endoscopic Microscopy II*, 6432, 115 – 124. doi: 10.1117/12.701266.

Bollée, B. (1969). Electrostatic motors. *Philips Technical Review*, 30(6), 178-194.

Breguet et al. (2006). A review on actuation principls for few cubic millimeter sized mobile micro-robots. *Proceedings of the 10th International Conference on New Actuators (Actuator 2006)*, 374-381. Consulted at http://infoscience.epfl.ch/record/99664.

Briere, J., Elsayed, M., Saidani, M., Berard, M., Beaulieu, P.-O., Rabbani-Haghighi, H., Nabki, F. & Menard, M. (2017). Rotating Circular Micro-Platform with Integrated Waveguides and Latching Arm for Reconfigurable Integrated Optics. *Micromachines*,

8(12), 354.

Brière, J., Beaulieu, P.-O., Saidani, M., Nabki, F. & Menard, M. (2015). Rotational MEMS mirror with latching arm for silicon photonics. *MOEMS and Miniaturized Systems XIV*, 9375, 20 – 26. doi: 10.1117/12.2077033.

Brown, G., Li, L., Bauer, R., Liu, J. & Uttamchandani, D. (2010). A two-axis hybrid MEMS scanner incorporating electrothermal and electrostatic actuators. *2010 International Conference on Optical MEMS and Nanophotonics*, pp. 115-116. doi: 10.1109/OMEMS.2010.5672156.

Bustillo, J. M., Howe, R. T. & Muller, R. S. (1998). Surface micromachining for microelectromechanical systems. *Proceedings of the IEEE*, 86(8), 1552-1574. doi: 10.1109/5.704260.

Büttgenbach, S. (2014). Electromagnetic Micromotors—Design, Fabrication and Applications. *Micromachines*, 5(4), 929-942.

Cai, H., Liu, A. Q., Zhang, X. M., Tamil, J., Tang, D. Y., Wu, J. & Zhang, Q. X. (2008). Tunable dual-wavelength laser constructed by silicon micromachining. *Applied Physics Letters*, 92(5), 051113. doi: 10.1063/1.2840152.

Cai, W., Chan, J. & Garmire, D. (2011). 3-axes MEMS Hall-effect sensor. *2011 IEEE Sensors Applications Symposium*, pp. 141-144.

Cao, K., Liu, W. & Talghader, J. J. (2001). Curvature compensation in micromirrors with high-reflectivity optical coatings. *Journal of Microelectromechanical Systems*, 10(3), 409-417. doi: 10.1109/84.946795.

Chang-Hasnain, C. (2000). Tunable VCSEL. *IEEE Journal of Selected Topics in Quantum Electronics*, 6(6), 978-987. doi: 10.1109/2944.902146.

Chee Wei Wong, Xin Zhang, Jacobson, S. A. & Epstein, A. H. (2004). A self-acting gas thrust bearing for high-speed microrotors. *Journal of Microelectromechanical Systems*, 13(2), 158-164.

Chellappan, K. V., Erden, E. & Urey, H. (2010). Laser-based displays: a review. *Appl. Opt.*, 49(25), F79–F98. doi: 10.1364/AO.49.000F79.

Chiang, P., Khanna, N., Mikkilineni, A. K., Ortiz Segovia, M. V., Suh, S., Allebach, J. P., Chiu, G. T. . & Delp, E. J. (2009). Printer and scanner forensics. *IEEE Signal Processing Magazine*, 26(2), 72-83. doi: 10.1109/MSP.2008.931082.

Cho, A. R., Han, A., Ju, S., Jeong, H., Park, J.-H., Kim, I., Bu, J.-U. & Ji, C.-H. (2015). Electromagnetic biaxial microscanner with mechanical amplification at resonance. *Opt. Express*, 23(13), 16792–16802. doi: 10.1364/OE.23.016792.

Cho, J.-W., Park, Y.-H., Ko, Y.-C., Lee, B.-L., Kang, S.-J., Chung, S.-W., kyoung Choi, W., Cho, Y.-C., Chang, S.-M., Lee, J.-H. & Sunu, J. (2007). Electrostatic 1D microscanner with vertical combs for HD resolution display. *MOEMS and Miniaturized Systems VI*, 6466, 106 – 117. Consulted at https://doi.org/10.1117/12.702163.

Choi, J. et al. (2014). A three-degree-of-freedom thin-film PZT-actuated microactuator with large out-of-plane displacement. *Journal of Micromechanics and Microengineering*, 24(7), 075017. doi: 10.1088/0960-1317/24/7/075017.

Chung, S., Abediasl, H. & Hashemi, H. (2018). A Monolithically Integrated Large-Scale Optical Phased Array in Silicon-on-Insulator CMOS. *IEEE Journal of Solid-State Circuits*, 53(1), 275-296. doi: 10.1109/JSSC.2017.2757009.

Clawson, T. S., Ferrari, S., Fuller, S. B. & Wood, R. J. (2016). Spiking neural network (SNN) control of a flapping insect-scale robot. *2016 IEEE 55th Conference on Decision and Control (CDC)*, pp. 3381-3388. doi: 10.1109/CDC.2016.7798778.

Conant, R. A., Nee, J. T., Lau, K. Y. & Muller, R. S. (2000). A flat high-frequency scanning micromirror. *Hilton Head Solid-State Sensor and Actuator Workshop 2000, pp.6-9, Transducer Research Foundation*, pp. 6–9.

Cowen, A., Hardy, B., Mahadevan, R. & S. *Wilcenski PolyMUMPs Design Handbook MEMSCAP Inc 13 (2011*. Durham, NC: USA:MEMSCAP Inc.

Cowen, A., Hardy, B., Mahadevan, R. & Wilcenski, S. (2011). *PolyMUMPs Design Handbook* (ed. 13). Durham, NC, USA: MEMSCAP Inc.

Cowen, A., Hames, G., Glukh, K. & Hardy, B. (2013). PiezoMUMPs design handbook".

Crary, S. & Zhang, Y. (1990). CAEMEMS: an integrated computer-aided engineering workbench for micro-electro-mechanical systems. *IEEE Proceedings on Micro Electro Mechanical Systems, An Investigation of Micro Structures, Sensors, Actuators, Machines and Robots.*, pp. 113-114.

Czajkowski, J. et al. (2010). Optical coherence tomography as a method of quality inspection for printed electronics products. *Optical Review*, 17, 257-262. doi: https://doi.org/10.1007/s10043-010-0045-0.

De Loor, R., Penning, L. & Slagle, R. (2014). Polygon Laser Scanning. *Laser Technik Journal*, 11(3), 32-34. doi: https://doi.org/10.1002/latj.201400033.

Dec, A. & Suyama, K. (2000). Microwave MEMS-based voltage-controlled oscillators. *IEEE Transactions on Microwave Theory and Techniques*, 48(11), 1943-1949.

Dechev, N., Cleghorn, W. L. & Mills, J. K. (2004). Microassembly of 3-D microstructures using a compliant, passive microgripper. *Journal of Microelectromechanical Systems*, 13(2), 176-189.

Dhull, R. K., Puchades, I., Fuller, L. & Lu, Y. W. (2009). Optical Micromirror Actuation using Thermocapillary Effect in Microdroplets. *2009 IEEE 22nd International Conference on Micro Electro Mechanical Systems*, pp. 995-998. doi: 10.1109/MEMSYS.2009.4805553.

Dhull, R. K., Fuller, L., Kao, P.-C., Liao, Y.-C. & Lu, Y.-W. (2011). Two degree-of-freedom micromirror actuation using thermocapillary effect in liquid droplets. *Sensors and Actuators A: Physical*, 168(1), 162-167. doi: https://doi.org/10.1016/j.sna.2011.03.041.

Doe, J. (1999, October, 2). Web page title [Format]. Consulted at http://www.google.ca.

Dufour, I., Sarraute, E. & Abbas, A. (1996a). Optimization of the geometry of electrostatic micromotors using only analytical equations. *Journal of Micromechanics and Microengineering*, 6(1), 108–111. doi: 10.1088/0960-1317/6/1/026.

Dufour, I., Sarraute, E. & Abbas, A. (1996b). Optimization of the geometry of electrostatic micromotors using only analytical equations. *Journal of Micromechanics and Microengineering*, 6(1), 108–111.

Duma, V.-F. & Podoleanu, A. G. (2013). Polygon mirror scanners in biomedical imaging: a review. *Optical Components and Materials X*, 8621, 175 – 183. doi: 10.1117/12.2005065.

Elsayed, M. Y., Beaulieu, P.-O., Briere, J., Menard, M. & Nabki, F. (2016). A novel technique for die-level post-processing of released optical MEMS. *Journal of Micromechanics and Microengineering*, 26(5), 057001.

Endemaño, A., Fourniols, J. Y., Camon, H., Marchese, A., Muratet, S., Bony, F., Dunnigan, M., Desmulliez, M. P. Y. & Overton, G. (2003). VHDL-AMS modelling and simulation of a planar electrostatic micromotor. *Journal of Micromechanics and Microengineering*, 13(5), 580–590.

Erdelyi, E. & Rynkowski, G. A. (2013). Motors and Controllers (Drivers) for High-Performance Polygonal Scanners. *Handbook of Optical and Laser Scanning*, Second, 282 – 318.

Fan, L.-S., Tai, Y.-C. & Muller, R. S. (1989). IC-processed electrostatic micromotors. *Sensors and Actuators*, 20(1), 41 - 47. A Special Issue Devoted to Micromechanics.

Fatikow, S., Falzullin, A. & Seyfried, J. (2000). Planning of a microassembly task in a flexible microrobot cell. *Proceedings 2000 ICRA. Millennium Conference. IEEE International Conference on Robotics and Automation. Symposia Proceedings (Cat. No.00CH37065)*, 2, 1121-1126 vol.2.

Frechette, L. G., Jacobson, S. A., Breuer, K. S., Ehrich, F. F., Ghodssi, R., Khanna, R., Chee Wei Wong, Xin Zhang, Schmidt, M. A. & Epstein, A. H. (2005). High-speed microfabricated silicon turbomachinery and fluid film bearings. *Journal of Microelectromechanical Systems*, 14(1), 141-152.

Freeman, M., Champion, M. & Madhavan, S. (2009). Scanned Laser Pico-Projectors: Seeing the Big Picture (with a Small Device). *Opt. Photon. News*, 20(5), 28–34. doi: 10.1364/OPN.20.5.000028.

Gerald F. Marshall, G. E. S. (2012). *Handbook of Optical and Laser Scanning* (ed. 2). Boca Raton, FL, USA: CRC Press.

Ghalichechian, N., Modafe, A., Beyaz, M. I. & Ghodssi, R. (2008a). Design, Fabrication, and Characterization of a Rotary Micromotor Supported on Microball Bearings. *Journal of Microelectromechanical Systems*, 17(3), 632-642. doi: 10.1109/JMEMS.2008.916346.

Ghalichechian, N., Modafe, A., Beyaz, M. I. & Ghodssi, R. (2008b). Design, Fabrication, and Characterization of a Rotary Micromotor Supported on Microball Bearings. *Journal of Microelectromechanical Systems*, 17(3), 632-642.

Ghazali, F. A. M., Hasan, M. N., Rehman, T., Nafea, M., Ali, M. S. M. & Takahata, K. (2020). MEMS actuators for biomedical applications: a review. *Journal of Micromechanics and Microengineering*, 30(7), 073001. doi: 10.1088/1361-6439/ab8832.

Gilgunn, P. J., Liu, J., Sarkar, N. & Fedder, G. K. (2008). CMOS–MEMS Lateral Electrothermal Actuators. *Journal of Microelectromechanical Systems*, 17(1), 103-114. doi: 10.1109/JMEMS.2007.911373.

Gokce, S. K., Holmstrom, S., Brown, D., Davis, W. O. & Urey, H. (2011). A high-frequency comb-actuated resonant MEMS scanner for microdisplays. *16th International Conference on Optical MEMS and Nanophotonics*, pp. 35-36. doi: 10.1109/OMEMS.2011.6031064.

Gong, Z., Li, J., Luo, Z., Wen, C., Wang, C. & Zelek, J. (2019). Mapping and Semantic Modeling of Underground Parking Lots Using a Backpack LiDAR System. *IEEE Transactions on Intelligent Transportation Systems*, 1-13. doi: 10.1109/TITS.2019.2955734.

Gour, A., Ménard, M. & Nabki, F. (2020a). Low-Friction, High-Speed Rotary 3-Phase Micromotor Using the PolyMUMPS Process. *Journal of Microelectromechanical Systems*, 29(4), 532-543. doi: 10.1109/JMEMS.2020.2992179.

Gour, A., Ménard, M. & Nabki, F. (2020b). Low-Friction, High-Speed Rotary 3-Phase Micromotor Using the PolyMUMPS Process. *Journal of Microelectromechanical Systems*, 29(4), 532-543.

Gour, A., Ménard, M. & Nabki, F. (2020a). Low-Friction, High-Speed Rotary 3-Phase Micromotor Using the PolyMUMPS Process. *Journal of Microelectromechanical Systems*, 29(4), 532-543. doi: 10.1109/JMEMS.2020.2992179.

Gour, A., Nabki, F. & Ménard, M. (2020b). A rapid technique to integrate micro-components on released MEMS dies using SU-8. *Journal of Micromechanics and Microengineering*, 30(11), 117001. doi: 10.1088/1361-6439/abb52e.

Gour, A., Ménard, M. & Nabki, F. (2021). High Torque Electrostatic Micromotor Fabricated using Polymumps for Optical Scanning Applications. *2021 IEEE 34th International Conference on Micro Electro Mechanical Systems (MEMS)*, pp. 716-719. doi: 10.1109/MEMS51782.2021.9375343.

Grade, J. D. & Jerman, H. (2001). MEMS electrostatic actuators for optical switching applications. *OFC 2001. Optical Fiber Communication Conference and Exhibit. Technical Digest Postconference Edition (IEEE Cat. 01CH37171)*, 3, WX2-WX2. doi: 10.1109/OFC.2001.928421.

Gu-Stoppel, S., Janes, J., Kaden, D., Quenzer, H. J., Hofmann, U. & Benecke, W. (2013). Piezoelectric resonant micromirror with high frequency and large deflection applying mechanical leverage amplification. *Micromachining and Microfabrication Process Technology XVIII*, 8612, 122 – 129. Consulted at https://doi.org/10.1117/12.2001620.

Guan, C. & Zhu, Y. (2010). An electrothermal microactuator with Z-shaped beams. *Journal of Micromechanics and Microengineering*, 20(8), 085014. doi: 10.1088/0960-1317/20/8/085014.

Hafez, M., Sidler, T., Salathé, R., Jansen, G. & Compter, J. (2000). Design, simulations and experimental investigations of a compact single mirror tip/tilt laser scanner. *Mechatronics*, 10(7), 741 - 760. doi: https://doi.org/10.1016/S0957-4158(99)00093-8.

Han, F. T., Wu, Q. P. & Wang, L. (2010a). Experimental study of a variable-capacitance micromotor with electrostatic suspension. *Journal of Micromechanics and Microengineering*, 20(11), 115034. doi: 10.1088/0960-1317/20/11/115034.

Han, F. T., Wu, Q. P. & Wang, L. (2010b). Experimental study of a variable-capacitance micromotor with electrostatic suspension. *Journal of Micromechanics and Microengineering*, 20(11), 115034.

Han, F. T., Wang, L., Wu, Q. P. & Liu, Y. F. (2011). Performance of an active electric bearing for rotary micromotors. *Journal of Micromechanics and Microengineering*, 21(8), 085027.

Han, F. T., Liu, Y. F., Wang, L. & Ma, G. Y. (2012). Micromachined electrostatically suspended gyroscope with a spinning ring-shaped rotor. *Journal of Micromechanics and Microengineering*, 22(10), 105032.

Harrison, A. & Newman, P. (2008). High quality 3D laser ranging under general vehicle motion. *2008 IEEE International Conference on Robotics and Automation*, pp. 7-12. doi: 10.1109/ROBOT.2008.4543179.

He, S., Mrad, R. B. & Chong, J. (2011). Repulsive-force out-of-plane large stroke translation micro electrostatic actuator. *Journal of Micromechanics and Microengineering*, 21(7), 075002. doi: 10.1088/0960-1317/21/7/075002.

Hecht, J. (2018). Lidar for Self-Driving Cars. *Optics Photonics News*, 29(19), 26-33. Consulted at https://www.osa-opn.org/home/articles/volume_29/january_2018/features/lidar_for_self-driving_cars/.

Hedili, M. K., Freeman, M. O. & Urey, H. (2012). Microstructured head-up display screen for automotive applications. *Micro-Optics 2012*, 8428, 201 – 206. doi: 10.1117/12.923556.

Hofmann, U., Janes, J. & Quenzer, H.-J. (2012). High-Q MEMS Resonators for Laser Beam Scanning Displays. *Micromachines*, 3(2), 509–528. doi: 10.3390/mi3020509.

]rot$_c$*alHolmgren*, *D. E. & Robinett*, *W.* (1992.[*Online*]).*Scanned Laser Displays for Head Mounted* Chapel Hill, NC, USA. Consulted at http://www.cs.unc.edu/techreports/92-029.pdf.

Holmstrom, S. T. S., Baran, U. & Urey, H. (2014). MEMS Laser Scanners: A Review. *Journal of Microelectromechanical Systems*, 23(2), 259-275.

Holmström, S. T. S., Baran, U. & Urey, H. (2014). MEMS Laser Scanners: A Review. *Journal of Microelectromechanical Systems*, 23(2), 259-275. doi: 10.1109/JMEMS.2013.2295470.

Holmström, S. T. S., Baran, U. & Urey, H. (2014). MEMS Laser Scanners: A Review. *Journal of Microelectromechanical Systems*, 23(2), 259-275. doi: 10.1109/JMEMS.2013.2295470.

Hornbeck, L. J. (1993). Current status of the digital micromirror device (DMD) for projection television applications. *Proceedings of IEEE International Electron Devices Meeting*, pp. 381-384. doi: 10.1109/IEDM.1993.347329.

Hsu, C.-P., Li, B., Solano-Rivas, B., Gohil, A. R., Chan, P. H., Moore, A. D. & Donzella, V. (2021). A Review and Perspective on Optical Phased Array for Automotive LiDAR. *IEEE Journal of Selected Topics in Quantum Electronics*, 27(1), 1-16. doi: 10.1109/JSTQE.2020.3022948.

Hsu, S., Klose, T., Drabe, C. & Schenk, H. (2008). Fabrication and characterization of a dynamically flat high resolution micro-scanner. *Journal of Optics A: Pure and Applied Optics*, 10(4), 044005. doi: 10.1088/1464-4258/10/4/044005.

Hu, F., Yao, J., Qiu, C. & Ren, H. (2010). A MEMS micromirror driven by electrostatic force. *Journal of Electrostatics*, 68(3), 237-242. doi: https://doi.org/10.1016/j.elstat.2010.01.005.

Huang, C.-S., Cheng, Y.-T., Chung, J. & Hsu, W. (2009). Investigation of Ni-based thermal bimaterial structure for sensor and actuator application. *Sensors and Actuators A: Physical*, 149(2), 298-304. doi: https://doi.org/10.1016/j.sna.2008.11.019.

Huang, Q.-A. & Lee, N. K. S. (1999). Analysis and design of polysilicon thermal flexure actuator. *Journal of Micromechanics and Microengineering*, 9(1), 64–70. doi: 10.1088/0960-1317/9/1/308.

Huang, Y., Sai Sarathi Vasan, A., Doraiswami, R., Osterman, M. & Pecht, M. (2012). MEMS Reliability Review. *IEEE Transactions on Device and Materials Reliability*, 12(2), 482-493. doi: 10.1109/TDMR.2012.2191291.

Hyungmin Kang & Joonwon Kim. (2006). EWOD (Electrowetting-on-Dielectric) Actuated Optical Micromirror. *19th IEEE International Conference on Micro Electro Mechanical Systems*, pp. 742-745. doi: 10.1109/MEMSYS.2006.1627906.

Jain, A., Kopa, A., Yingtian Pan, Fedder, G. K. & Huikai Xie. (2004). A two-axis electrothermal micromirror for endoscopic optical coherence tomography. *IEEE Journal of Selected Topics in Quantum Electronics*, 10(3), 636-642. doi: 10.1109/JSTQE.2004.829194.

Jeong, H.-M., Park, Y.-H., Cho, Y.-C., Hwang, J.-S., Chang, S.-M., Kang, S.-J., Jeong, H.-K., Kim, J.-O. & Lee, J.-H. (2008a). Slow scanning electromagnetic scanner for laser display. *Journal of Micro/Nanolithography, MEMS, and MOEMS*, 7(4), 1 – 13. doi: 10.1117/1.3033210.

Jeong, H.-M., Park, Y.-H., Jeong, H.-K., Cho, Y.-C., Chang, S.-M., Kim, J.-O., Kang, S.-J., Hwang, J.-S. & Lee, J.-H. (2008b). Slow scanning electromagnetic MEMS scanner for laser

display. *MOEMS and Miniaturized Systems VII*, 6887, 41 – 52. doi: 10.1117/12.762549.

Jerman, H. & J., D. G. (2002). *A mechanically-balanced, drie rotary actuator for a high-power tunable laser*. Technical Digest 2002 Solid State Sensor and Actuator Workshop.

Jeught, S. V. D., Bradu, A. & Podoleanu, A. G. (2010). Real-time resampling in Fourier domain optical coherence tomography using a graphics processing unit. *Journal of Biomedical Optics*, 15(3), 1 – 3. doi: 10.1117/1.3437078.

Ji, Y.-Y., So, B. H. & Kim, D. Y. (2019). High-speed time-domain characterization method for polygon scanners. *Measurement*, 135, 278 - 286. doi: https://doi.org/10.1016/j.measurement.2018.11.039.

Jia, K., Pal, S. & Xie, H. (2009). An Electrothermal Tip–Tilt–Piston Micromirror Based on Folded Dual S-Shaped Bimorphs. *Journal of Microelectromechanical Systems*, 18(5), 1004-1015. doi: 10.1109/JMEMS.2009.2023838.

Jia, K., Samuelson, S. R. & Xie, H. (2011). High-Fill-Factor Micromirror Array With Hidden Bimorph Actuators and Tip–Tilt-Piston Capability. *Journal of Microelectromechanical Systems*, 20(3), 573-582. doi: 10.1109/JMEMS.2011.2127449.

Jiang, B., Peng, M., Liu, Y., Zhou, T. & Su, Y. (2019). The fabrication of 2D micromirror with large electromagnetic driving forces. *Sensors and Actuators A: Physical*, 286, 163-168. doi: https://doi.org/10.1016/j.sna.2018.12.038.

Judy, J. W. (2001a). Microelectromechanical systems (MEMS): fabrication, design and applications. *Smart Materials and Structures*, 10(6), 1115–1134. doi: 10.1088/0964-1726/10/6/301.

Judy, J. W. (2001b). Microelectromechanical systems (MEMS): fabrication, design and applications. *Smart Materials and Structures*, 10(6), 1115–1134. doi: 10.1088/0964-1726/10/6/301.

Jun Zou, Balberg, M., Byrne, C., Chang Liu & Brady, D. J. (1999). Optical properties of surface micromachined mirrors with etch holes. *Journal of Microelectromechanical Systems*, 8(4), 506-513. doi: 10.1109/84.809066.

Jung, D., Sandner, T., Kallweit, D. & Schenk, H. (2012). Vertical comb drive microscanners for beam steering, linear scanning, and laser projection applications. *MOEMS and Miniaturized Systems XI*, 8252, 232 – 241. Consulted at https://doi.org/10.1117/12.906690.

Kaposta, I. & Duma, V.-F. (2014). Driving solutions and optomechanical design of scanners with Risley prisms . *Fifth International Conference on Lasers in Medicine:*

Biotechnologies Integrated in Daily Medicine, 8925, 195 – 201. Consulted at https://doi.org/10.1117/12.2044053.

Kawabata, T., Ikeda, M., Goto, H., Matsumoto, M. & Yada, T. (1997). The 2-dimensional micro scanner integrated with PZT thin film actuator. *Proceedings of International Solid State Sensors and Actuators Conference (Transducers '97)*, 1, 339-342 vol.1. doi: 10.1109/SENSOR.1997.613653.

Khoury, J., Ramanathan, R., McCloskey, D., Smith, R. & Campbell, T. (2016). RadarMAC: Mitigating Radar Interference in Self-Driving Cars. *2016 13th Annual IEEE International Conference on Sensing, Communication, and Networking (SECON)*, pp. 1-9. doi: 10.1109/SAHCN.2016.7733011.

Kiang, M.-H. et al. (1996). Surface-micromachined electrostatic-comb driven scanning micromirrors for barcode scanners. *Proceedings of Ninth International Workshop on Micro Electromechanical Systems*, pp. 192-197. doi: 10.1109/MEMSYS.1996.493852.

Kim, J. et al. (2019). Unmanned Aerial Vehicles in Agriculture: A Review of Perspective of Platform, Control, and Applications. *IEEE Access*, 7, 105100-105115. doi: 10.1109/ACCESS.2019.2932119.

Kim, M. G., Jang, G. H., Lee, C. J. & Lim, D. O. (2008a). Experimental identification of abnormal noise and vibration in a high-speed polygon mirror scanner motor due to mechanical contact of plain journal bearing. *Microsystem Technologies*, 16(1), 3. doi: 10.1007/s00542-008-0729-6.

Kim, S.-J. et al. (2008b). Piezoelectrically pushed rotational micromirrors using detached PZT actuators for wide-angle optical switch applications. *Journal of Micromechanics and Microengineering*, 18(12), 125022. doi: 10.1088/0960-1317/18/12/125022.

Kim, T.-Y., Kim, C., Kim, S.-H. & Jung, G.-P. (2019). MutBug: A Lightweight and Compact Crawling Robot That Can Run on Both Sides. *IEEE Robotics and Automation Letters*, 4(2), 1409-1415. doi: 10.1109/LRA.2019.2895896.

Ko, Y.-C., Cho, J.-W., Mun, Y.-K., Jeong, H.-G., Choi, W.-K., Lee, J.-H., Kim, J.-W., Yoo, J.-B. & Lee, J.-H. (2005). Eye-type scanning mirror with dual vertical combs for laser display. *MOEMS Display and Imaging Systems III*, 5721, 14 – 22. Consulted at https://doi.org/10.1117/12.591276.

Koh, K. H., Lee, C. & Kobayashi, T. (2010). A Piezoelectric-Driven Three-Dimensional MEMS VOA Using Attenuation Mechanism With Combination of Rotational and Translational Effects. *Journal of Microelectromechanical Systems*, 19(6), 1370-1379. doi: 10.1109/JMEMS.2010.2076785.

Koh, K. H. & Lee, C. (2012a). A low power 2-D raster scanning MEMS mirror driven by hybrid electrothermal and electromagnetic actuation mechanisms. *2012 International Conference on Optical MEMS and Nanophotonics*, pp. 236-237. doi: 10.1109/OMEMS.2012.6318890.

Koh, K. H. & Lee, C. (2012b). A Two-Dimensional MEMS Scanning Mirror Using Hybrid Actuation Mechanisms With Low Operation Voltage. *Journal of Microelectromechanical Systems*, 21(5), 1124-1135. doi: 10.1109/JMEMS.2012.2196497.

Koller, D. et al. (2011). Non-destructive analysis of tablet coatings with optical coherence tomography. *European Journal of Pharmaceutical Sciences*, 44(1), 142-148. doi: https://doi.org/10.1016/j.ejps.2011.06.017.

Kovacs, G. T. A., Maluf, N. I. & Petersen, K. E. (1998). Bulk micromachining of silicon. *Proceedings of the IEEE*, 86(8), 1536-1551. doi: 10.1109/5.704259.

Kraft, M. & Damrongsak, B. (2010). Micromachined gyroscopes based on a rotating mechanically unconstrained proof mass. *SENSORS, 2010 IEEE*, pp. 23-28.

Kraus, T., Baltzer, M. & Obermeier, E. (1997). Design and fabrication of surface micromachined micromotors with large dimensions. *Journal of Micromechanics and Microengineering*, 7(3), 196–199.

Lara-Castro, M., Herrera-Amaya, A., Escarola-Rosas, M. A., Vázquez-Toledo, M., López-Huerta, F., Aguilera-Cortés, L. A. & Herrera-May, A. L. (2017). Design and Modeling of Polysilicon Electrothermal Actuators for a MEMS Mirror with Low Power Consumption. *Micromachines*, 8(7). doi: 10.3390/mi8070203.

Laser, D. J. & Santiago, J. G. (2004). A review of micropumps. *Journal of Micromechanics and Microengineering*, 14(6), R35–R64.

Laszczyk, K., Bargiel, S., Gorecki, C., Krężel, J., Dziuban, P., Kujawińska, M., Callet, D. & Frank, S. (2010). A two directional electrostatic comb-drive X–Y microstage for MOEMS applications. *Sensors and Actuators A: Physical*, 163(1), 255-265. doi: https://doi.org/10.1016/j.sna.2010.06.020.

Lee, C., Hsiao, F., Kobayashi, T., Koh, K. H., Ramana, P. V., Xiang, W., Yang, B., Tan, C. W. & Pinjala, D. (2009). A 1-V Operated MEMS Variable Optical Attenuator Using Piezoelectric PZT Thin-Film Actuators. *IEEE Journal of Selected Topics in Quantum Electronics*, 15(5), 1529-1536. doi: 10.1109/JSTQE.2009.2022959.

Lee, C. (2004). Design and fabrication of epitaxial silicon micromirror devices. *Sensors and Actuators A: Physical*, 115(2), 581-590. doi: https://doi.org/10.1016/j.sna.2004.03.045. The 17th European Conference on Solid-State Transducers.

Lee, C., Itoh, T., Ohashi, T., Maeda, R. & Suga, T. (1997). Development of a piezoelectric self-excitation and self-detection mechanism in PZT microcantilevers for dynamic scanning force microscopy in liquid. *Journal of Vacuum Science & Technology B: Microelectronics and Nanometer Structures Processing, Measurement, and Phenomena*, 15(4), 1559-1563. doi: 10.1116/1.589400.

Lee, J., Moon, H., Fowler, J., Schoellhammer, T. & Kim, C.-J. (2002). Electrowetting and electrowetting-on-dielectric for microscale liquid handling. *Sensors and Actuators A: Physical*, 95(2), 259-268. doi: https://doi.org/10.1016/S0924-4247(01)00734-8. Papers from the Proceedings of the 14th IEEE Internat. Conf. on MicroElectroMechanical Systems.

Lee, S.-W., Song, H.-W., Jung, M.-Y. & Kim, S.-H. (2011). Wide tuning range wavelength-swept laser with a single SOA at 1020 nm for ultrahigh resolution Fourier-domain optical coherence tomography. *Opt. Express*, 19(22), 21227–21237. doi: 10.1364/OE.19.021227.

Li, A., Sun, W., Yi, W. & Zuo, Q. (2016). Investigation of beam steering performances in rotation Risley-prism scanner. *Opt. Express*, 24(12), 12840–12850. doi: 10.1364/OE.24.012840.

Li, Y., Yuen, W., Li, G. & Chang-Hasnain, C. (1998). Top-emitting micromechanical VCSEL with a 31.6-nm tuning range. *IEEE Photonics Technology Letters*, 10(1), 18-20. doi: 10.1109/68.651087.

Li, Y., Huang, H. M., Burgio, G., Heath, W. & Lee, W. M. (2017). Dynamic control over field of view in polygon mirror-based laser scanning multiphoton microscope. *Optics in the Life Sciences Congress*, pp. BoTu3A.2. doi: 10.1364/BODA.2017.BoTu3A.2.

Liu, A. Q. & Zhang, X. M. (2006). A review of MEMS external-cavity tunable lasers. *Journal of Micromechanics and Microengineering*, 17(1), R1–R13. doi: 10.1088/0960-1317/17/1/r01.

Liu, H., Zhang, L., Li, K. H. H. & Tan, O. K. (2018). Microhotplates for Metal Oxide Semiconductor Gas Sensor Applications—Towards the CMOS-MEMS Monolithic Approach. *Micromachines*, 9(11). doi: 10.3390/mi9110557.

Liu, J. T., Mandella, M. J., Loewke, N. O., Haeberle, H., Ra, H., Piyawattanametha, W., Solgaard, O. D., Kino, G. S. & Contag, C. H. (2010). Micromirror-scanned dual-axis confocal microscope utilizing a gradient-index relay lens for image guidance during brain surgery. *Journal of Biomedical Optics*, 15(2), 1 – 5. doi: 10.1117/1.3386055.

Liu, T., Sen, P. & Kim, C. (2010a). Characterization of liquid-metal Galinstan® for droplet applications. *2010 IEEE 23rd International Conference on Micro Electro Mechanical*

Systems (MEMS), pp. 560-563. doi: 10.1109/MEMSYS.2010.5442440.

Liu, W., Zhu, Y., Li, J., Virendrapal, A. S., Tang, Y., Wang, B. & Xie, H. (2010b). Two-axis scanning micromirror based on a tilt-and-lateral shift-free piezoelectric actuator. *SENSORS, 2010 IEEE*, pp. 2189-2192. doi: 10.1109/ICSENS.2010.5690601.

Long-Sheng Fan, Yu-Chong Tai & Muller, R. S. (1988). IC-processed electrostatic micro-motors. *Technical Digest., International Electron Devices Meeting*, pp. 666-669.

Luo, B.-K., He, A., Lu, J. & Ni, X.-W. (1994). Studies on nonlinearity of rotating mirror scanning in laser imaging radar. *Industrial Applications of Laser Radar*, 2271, 109 – 114. doi: 10.1117/12.188144.

CAMBRIDGE TECHNOLOGY. (2020). Polygon Laser Scanner.

MINEBEAMITSUMI INC. (2020). Polygon Laser Scanner.

NANOPHORM, LLC. (2018). Polygon Scanners.

NIDEC-COPAL-ELECTRONICS. (2020). Polygon Laser Scanner.

PLL. (2019). GECKO FOUR LIDAR scanner with 25 mm aperture.

SICK. (2019). LMS-4000 Datasheet.

Makishi, W., Kawai, Y. & Esashi, M. (2009). Magnetic torque driving 2D micro scanner with a non-resonant large scan angle. *TRANSDUCERS 2009 - 2009 International Solid-State Sensors, Actuators and Microsystems Conference*, pp. 904-907. doi: 10.1109/SENSOR.2009.5285920.

Maksymova, I., Greiner, P., Niedermueller, L. C. & Druml, N. (2019). Detection and Compensation of Periodic Jitters of Oscillating MEMS Mirrors used in Automotive Driving Assistance Systems. *2019 IEEE Sensors Applications Symposium (SAS)*, pp. 1-5. doi: 10.1109/SAS.2019.8706008.

Mansour, R. R., Bakri-Kassem, M., Daneshmand, M. & Messiha, N. (2003). RF MEMS devices. *Proceedings International Conference on MEMS, NANO and Smart Systems*, pp. 103-107.

Marshall, G. F., Rynkowski, G. A. & Ketabchi, M. (1994). Polygonal scanners for television and high-definition television laser projectors: spatial and temporal tolerances versus resolution. *Journal of Electronic Imaging*, 3(3), 318 – 327. doi: 10.1117/12.180510.

Maseeh, F., Harris, R. M. & Senturia, S. D. (1990). A CAD architecture for microelectromechanical systems. *IEEE Proceedings on Micro Electro Mechanical Systems, An Investigation of Micro Structures, Sensors, Actuators, Machines and Robots.*, pp. 44-49.

Mathias, A., Fox, J., Temmen, M. & Tuck, E. A High Speed Electrostatically Actuated Al-MEMS Micromirror Array. In *Infotech@Aerospace 2011*. doi: 10.2514/6.2011-1578.

Megregany, M., Nagarkar, P., Senturia, S. D. & Lang, J. H. (1990). Operation of microfabricated harmonic and ordinary side-drive motors. *IEEE Proceedings on Micro Electro Mechanical Systems, An Investigation of Micro Structures, Sensors, Actuators, Machines and Robots.*, pp. 1-8.

Mehregany, M. & Tai, Y.-C. (1991). Surface micromachined mechanisms and micromotors. *Journal of Micromechanics and Microengineering*, 1(2), 73–85. doi: 10.1088/0960-1317/1/2/001.

Mehregany, M., Senturia, S. & Lang, J. (1992). Measurement of wear in polysilicon micromotors. *IEEE Transactions on Electron Devices*, 39(5), 1136-1143. doi: 10.1109/16.129094.

Mehregany, M., Bart, S. F., Tavrow, L. S., Lang, J. H. & Senturia, S. D. (1990). Principles in design and microfabrication of variable-capacitance side-drive motors. *Journal of Vacuum Science & Technology A*, 8(4), 3614-3624. doi: 10.1116/1.576515.

Mellette, W. M. & Ford, J. E. (2015). Scaling Limits of MEMS Beam-Steering Switches for Data Center Networks. *Journal of Lightwave Technology*, 33(15), 3308-3318. doi: 10.1109/JLT.2015.2431231.

Michel, D., Xiao, F. & Alameh, K. (2012). MEMS-Based Tunable Linear-Cavity Fiber Laser. *IEEE Photonics Journal*, 4(3), 895-902. doi: 10.1109/JPHOT.2012.2200037.

Microvision. (1998). Virtual retinal display technology. *17th DASC. AIAA/IEEE/SAE. Digital Avionics Systems Conference. Proceedings (Cat. No.98CH36267)*, 1, D35/1-D35/6 vol.1. doi: 10.1109/DASC.1998.741542.

Milanovic, V. (2004). Multilevel beam SOI-MEMS fabrication and applications. *Journal of Microelectromechanical Systems*, 13(1), 19-30. doi: 10.1109/JMEMS.2003.823226.

Milanovic, V., Matus, G. & McCormick, D. (2004a). Gimbal-less monolithic silicon actuators for tip-tilt-piston micromirror applications. *IEEE Journal of Selected Topics in Quantum Electronics*, 10(3), 462-471. doi: 10.1109/JSTQE.2004.829205.

Milanovic, V., Matus, G. & McCormick, D. (2004b). Gimbal-less monolithic silicon actuators for tip-tilt-piston micromirror applications. *IEEE Journal of Selected Topics in*

Quantum Electronics, 10(3), 462-471. doi: 10.1109/JSTQE.2004.829205.

Milanovic, V., Matus, G. & McCormick, D. (2004c). Gimbal-less monolithic silicon actuators for tip-tilt-piston micromirror applications. *IEEE Journal of Selected Topics in Quantum Electronics*, 10(3), 462-471. doi: 10.1109/JSTQE.2004.829205.

Milne, N. G., Yang, S. J. E., Sangster, A. J., Ziad, H. & Spirkovitch, S. (1993). Determination of the forces present in an electrostatic micromotor. *1993 Sixth International Conference on Electrical Machines and Drives (Conf. Publ. No. 376)*, pp. 9-14.

Min, Y.-H. & Kim, Y.-K. (1999). Modeling, design, fabrication and measurement of a single layer polysilicon micromirror with initial curvature compensation. *Sensors and Actuators A: Physical*, 78(1), 8-17. doi: https://doi.org/10.1016/S0924-4247(99)00198-3.

Miradatechnologies. (2018). Polygon Laser Scanner.

Miyajima, H., Asaoka, N., Isokawa, T., Ogata, M., Aoki, Y., Imai, M., Fujimori, O., Katashiro, M. & Matsumoto, K. (2003). A MEMS electromagnetic optical scanner for a commercial confocal laser scanning microscope. *Journal of Microelectromechanical Systems*, 12(3), 243-251. doi: 10.1109/JMEMS.2003.809961.

Miyajima, H. (2004). Development of a MEMS electromagnetic optical scanner for a commercial laser scanning microscope. *Journal of Micro/Nanolithography, MEMS, and MOEMS*, 3(2), 348 – 357. doi: 10.1117/1.1666879.

Mohr, J., Bley, P., Stohrmann, M. & Wallrabe, U. (1992). 2(4), 234–241. doi: 10.1088/0960-1317/2/4/003.

Monk, D. W. & Gale, R. O. (1995). The digital micromirror device for projection display. *Microelectronic Engineering*, 27(1), 489-493. doi: https://doi.org/10.1016/0167-9317(94)00151-J.

Moosmann, F. & Stiller, C. (2011). Velodyne SLAM. *2011 IEEE Intelligent Vehicles Symposium (IV)*, pp. 393-398. doi: 10.1109/IVS.2011.5940396.

Moroney, R. M., White, R. M. & Howe, R. T. (1989). Ultrasonic micromotors. *Proceedings., IEEE Ultrasonics Symposium,*, pp. 745-748 vol.2.

Motamedi, M. E., Wu, M. C. & Pister, K. S. J. (1997). Micro-opto-electro-mechanical devices and on-chip optical processing. *Optical Engineering*, 36(5), 1282 – 1297. doi: 10.1117/1.601356.

Murillo, G., Davis, Z. J., Keller, S., Abadal, G., Agusti, J., Cagliani, A., Noeth, N., Boisen, A. & Barniol, N. (2010). Novel SU-8 based vacuum wafer-level packaging for MEMS devices. *Microelectronic Engineering*, 87(5), 1173 - 1176. The 35th International Conference on Micro- and Nano-Engineering (MNE).

Nemeth, A. et al. (2013). *Optical Coherence Tomography – Applications in Non- Destructive Testing and Evaluation*. London: InTech Open Access Publisher.

Nemirovsky, Y. & Bochobza-Degani, O. (2001). A methodology and model for the pull-in parameters of electrostatic actuators. *Journal of Microelectromechanical Systems*, 10(4), 601-615. doi: 10.1109/84.967384.

Nielson, G. & Barbastathis, G. (2006). Dynamic pull-in of parallel-plate and torsional electrostatic MEMS actuators. *Journal of Microelectromechanical Systems*, 15(4), 811-821. doi: 10.1109/JMEMS.2006.879121.

Nikitenko et al. (2014). Multi-robot System for Vacuum Cleaning Domain. *Advances in Practical Applications of Heterogeneous Multi-Agent Systems. The PAAMS Collection*, pp. 363–366.

Oh, W. Y., Yun, S. H., Tearney, G. J. & Bouma, B. E. (2005). 115?kHz tuning repetition rate ultrahigh-speed wavelength-swept semiconductor laser. *Opt. Lett.*, 30(23), 3159–3161. doi: 10.1364/OL.30.003159.

Oldenburg, A. L., Reynolds, J. J., Marks, D. L. & Boppart, S. A. (2003). Fast-Fourier-domain delay line for in vivo optical coherence tomography with a polygonal scanner. *Appl. Opt.*, 42(22), 4606–4611. doi: 10.1364/AO.42.004606.

Omar, M. P., Mehregany, M. & Mullen, R. L. (1992). Electric and fluid field analysis of side-drive micromotors. *Journal of Microelectromechanical Systems*, 1(3), 130-140.

Pang, C., Zhao, Z., Du, L. & Fang, Z. (2008). Adhesive bonding with SU-8 in a vacuum for capacitive pressure sensors. *Sensors and Actuators A: Physical*, 147(2), 672 - 676.

Patterson, P. R., Hah, D., Fujino, M., Piyawattanametha, W. & Wu, M. C. (2004). Scanning micromirrors: an overview. *Optomechatronic Micro/Nano Components, Devices, and Systems*, 5604, 195 – 207. Consulted at https://doi.org/10.1117/12.582849.

Pengwang, E., Rabenorosoa, K., Rakotondrabe, M. & Andreff, N. (2016). Scanning Micromirror Platform Based on MEMS Technology for Medical Application. *Micromachines*, 7(2). doi: 10.3390/mi7020024.

Pensala, T., Kyynäräinen, J., Dekker, J., Gorelick, S., Pekko, P., Pernu, T., Ylivaara, O., Gao, F., Morits, D. & Kiihamäki, J. (2019). Wobbling Mode AlN-Piezo-MEMS Mirror Enabling 360-Degree Field of View LIDAR for Automotive Applications. *2019 IEEE International Ultrasonics Symposium (IUS)*, pp. 1977-1980. doi: 10.1109/ULTSYM.2019.8925660.

Pepperl-Fuschs. (2020a). 3-D LiDAR sensor OMD10M-R2300-B23-V1V1D-4s [Online datasheet]. Consulted at https://files.pepperl-fuchs.com/webcat/navi/productInfo/pds/322226_eng.pdf?v=20210426185211.

Pepperl-Fuschs. (2020b). LiDAR Sensors [Online Product Overview]. Consulted at https://files.pepperl-fuchs.com/webcat/navi/productInfo/doct/tdoct6563a_eng.pdf?v=20201214160328.

Petersen, K. E. (1980). Silicon Torsional Scanning Mirror. *IBM Journal of Research and Development*, 24(5), 631-637. doi: 10.1147/rd.245.0631.

Pezeshki, B., Vail, E., Kubicky, J., Yoffe, G., Zou, S., Heanue, J., Epp, P., Rishton, S., Ton, D., Faraji, B., Emanuel, M., Hong, X., Sherback, M., Agrawal, V., Chipman, C. & Razazan, T. (2002a). 20-mW widely tunable laser module using DFB array and MEMS selection. *IEEE Photonics Technology Letters*, 14(10), 1457-1459. doi: 10.1109/LPT.2002.802392.

Pezeshki, B., Vail, E., Kubicky, J., Yoffe, G., Zou, S., Heanue, J., Epp, P., Rishton, S., Ton, D., Faraji, B., Emanuel, M., Hong, X., Sherback, M., Agrawal, V., Chipman, C. & Razazan, T. (2002b). 20-mW widely tunable laser module using DFB array and MEMS selection. *IEEE Photonics Technology Letters*, 14(10), 1457-1459. doi: 10.1109/LPT.2002.802392.

Piot, A., Pribošek, J. & Moridi, M. (2021). Dual-Axis Resonant Scanning MEMS Mirror with Pulsed-Laser-Deposited Barium-Doped PZT. *2021 IEEE 34th International Conference on Micro Electro Mechanical Systems (MEMS)*, pp. 89-92. doi: 10.1109/MEMS51782.2021.9375326.

Pisano, A. P. (1989). Resonant-structure micromotors. *IEEE Micro Electro Mechanical Systems, , Proceedings, 'An Investigation of Micro Structures, Sensors, Actuators, Machines and Robots'*, pp. 44-48.

Pister, K., Judy, M., Burgett, S. & Fearing, R. (1992). Microfabricated hinges. *Sensors and Actuators A: Physical*, 33(3), 249 - 256.

Piyawattanametha, W. & Wang, T. D. (2010). MEMS-Based Dual-Axes Confocal Microendoscopy. *IEEE Journal of Selected Topics in Quantum Electronics*, 16(4), 804-814. doi: 10.1109/JSTQE.2009.2032785.

Piyawattanametha, W., Patterson, P., Hah, D., Toshiyoshi, H. & Wu, M. (2005). Surface- and bulk- micromachined two-dimensional scanner driven by angular vertical comb actuators. *Journal of Microelectromechanical Systems*, 14(6), 1329-1338. doi: 10.1109/JMEMS.2005.859073.

Polla, D., Erdman, A., Peichel, D., Rizq, R., Gao, Y. & Markus, D. (2000). Precision micromotor for surgery. *1st Annual International IEEE-EMBS Special Topic Conference on Microtechnologies in Medicine and Biology. Proceedings (Cat. No.00EX451)*, pp. 180-183.

Prasad, N. S. & Mylapore, A. R. (2020). Picosecond pulsewidth direct detection lidar for imaging applications. *Photonic Instrumentation Engineering VII*, 11287, 113 – 121. doi: 10.1117/12.2548003.

Qu, H. (2016). CMOS MEMS Fabrication Technologies and Devices. *Micromachines*, 7(1). doi: 10.3390/mi7010014.

Rablau, C. I. (2019). Lidar: a new self-driving vehicle for introducing optics to broader engineering and non-engineering audiences. *SPIE*, 5(3), 48-54. doi: 10.1117/12.2523863.

Raboud, D., Barras, T., Lo Conte, F., Fabre, L., Kilcher, L., Kechana, F., Abelé, N. & Kayal, M. (2010). MEMS based color-VGA micro-projector system. *Procedia Engineering*, 5, 260-263. doi: https://doi.org/10.1016/j.proeng.2010.09.097. Eurosensor XXIV Conference.

Reyne, G. (2002). Electromagnetic actuation for MOEMS, examples, advantages and drawbacks of MAGMAS. *Journal of Magnetism and Magnetic Materials*, 242-245, 1119-1125. doi: https://doi.org/10.1016/S0304-8853(01)00981-7. Proceedings of the Joint European Magnetic Symposia (JEMS'01).

Risteska Stojkoska, B. L. & Trivodaliev, K. V. (2017). A review of Internet of Things for smart home: Challenges and solutions. *Journal of Cleaner Production*, 140, 1454-1464. doi: https://doi.org/10.1016/j.jclepro.2016.10.006.

Roylance, L. & Angell, J. (1979). A batch-fabricated silicon accelerometer. *IEEE Transactions on Electron Devices*, 26(12), 1911-1917. doi: 10.1109/T-ED.1979.19795.

Royo, S. & Ballesta-Garcia, M. (2019). An Overview of Lidar Imaging Systems for Autonomous Vehicles. *Applied Sciences*, 9(19). doi: 10.3390/app9194093.

Sandner, T., Drabe, C., Schenk, H. & Kenda, A. (2009). Large stroke MOEMS actuators for optical path length modulation in miniaturized FTIR spectrometers. *Next-Generation Spectroscopic Technologies II*, 7319, 136 – 145. Consulted at https://doi.org/10.1117/12.818605.

Sangster, A. J. & Samper, V. D. (1997). Accuracy assessment of 2-D and 3-D finite-element models of a double-stator electrostatic wobble motor. *Journal of Microelectromechanical Systems*, 6(2), 142-150.

Sano, R., ichi Inoue, J., Kanda, K., Fujita, T. & Maenaka, K. (2015). Fabrication of multilayer Pb(Zr,Ti)O3thin film by sputtering deposition for MEMS actuator applications. *Japanese Journal of Applied Physics*, 54(10S), 10ND03. doi: 10.7567/jjap.54.10nd03.

SANTEC. (2020). SANTEC'S COLUTION FOR OCT [Online Product Overview]. Consulted at https://www.santec.com/dcms_media/other/oct_HSL-1-C-E.pdf.

Selvakumar, A., Najafi, K., Juan, W. & Pang, S. (1995). Vertical comb array microactuators. *Proceedings of the IEEE Micro Electro Mechanical Systems*, pp. 43–48.

Sen, P. & Kim, C. (2009). A Fast Liquid-Metal Droplet Microswitch Using EWOD-Driven Contact-Line Sliding. *Journal of Microelectromechanical Systems*, 18(1), 174-185. doi: 10.1109/JMEMS.2008.2008624.

Shearwood, C., Ho, K., Williams, C. & Gong, H. (2000). Development of a levitated micromotor for application as a gyroscope. *Sensors and Actuators A: Physical*, 83(1), 85 - 92.

Shilton, R. J., Langelier, S. M., Friend, J. R. & Yeo, L. Y. (2012). Surface acoustic wave solid-state rotational micromotor. *Applied Physics Letters*, 100(3), 033503.

Shin, S. C. et al. (2012). The Compact Systems Design Based on DMD and the Straight Line 2-Channel LED for a Mobile Embedded Pico Projector. *J. Display Technol.*, 8(4), 219–224. Consulted at http://jdt.osa.org/abstract.cfm?URI=jdt-8-4-219.

Simard, M., Khalid, Z. & Kirk, A. (2006). Digital optical space switch based on micromotor grating scanners. *IEEE Photonics Technology Letters*, 18(2), 313-315. doi: 10.1109/LPT.2005.860374.

Sin, J., Lee, W. H., Popa, D. & Stephanou, H. E. (2006). Assembled Fourier transform micro-spectrometer. *Micromachining and Microfabrication Process Technology XI*, 6109, 29 – 36.

Singh, J., Teo, J. H. S., Xu, Y., Premachandran, C. S., Chen, N., Kotlanka, R., Olivo, M. & Sheppard, C. J. R. (2007). A two axes scanning SOI MEMS micromirror for endoscopic bioimaging. *Journal of Micromechanics and Microengineering*, 18(2), 025001. doi: 10.1088/0960-1317/18/2/025001.

Smith, B., Hellman, B., Gin, A., Espinoza, A. & Takashima, Y. (2017). Single chip lidar with discrete beam steering by digital micromirror device. *Opt. Express*, 25(13), 14732–14745. doi: 10.1364/OE.25.014732.

Smits, J. G., Fujimoto, K. & Kleptsyn, V. F. (2005). Microelectromechanical flexure PZT actuated optical scanner: static and resonance behavior. *Journal of Micromechanics and Microengineering*, 15(6), 1285–1293. doi: 10.1088/0960-1317/15/6/021.

Stark, K., Mehregany, M. & Phillips, S. (1997). Mechanical coupling and direct torque measurement of outer-rotor polysilicon micromotors. *Proceedings of the IEEE Micro Electro Mechanical Systems (MEMS)*, pp. 221–226.

Stifter, D. et al. (2010). Dynamic optical studies in materials testing with spectral-domain polarization-sensitive optical coherence tomography. *Opt. Express*, 18(25), 25712–25725. doi: 10.1364/OE.18.025712.

Strathman, M., Liu, Y., Keeler, E. G., Song, M., Baran, U., Xi, J., Sun, M.-T., Wang, R., Li, X. & Lin, L. Y. (2015). MEMS scanning micromirror for optical coherence tomography. *Biomed. Opt. Express*, 6(1), 211–224. doi: 10.1364/BOE.6.000211.

Su, G. . J., Toshiyoshi, H. & Wu, M. C. (2001). Surface-micromachined 2-D optical scanners with high-performance single-crystalline silicon micromirrors. *IEEE Photonics Technology Letters*, 13(6), 606-608. doi: 10.1109/68.924038.

Svasek, P., Svasek, E., Lendl, B. & Vellekoop, M. (2004a). Fabrication of miniaturized fluidic devices using SU-8 based lithography and low temperature wafer bonding. *Sensors and Actuators A: Physical*, 115(2), 591 - 599. The 17th European Conference on Solid-State Transducers.

Svasek, P., Svasek, E., Lendl, B. & Vellekoop, M. (2004b). Fabrication of miniaturized fluidic devices using SU-8 based lithography and low temperature wafer bonding. *Sensors and Actuators A: Physical*, 115(2), 591-599. doi: https://doi.org/10.1016/j.sna.2004.03.055. The 17th European Conference on Solid-State Transducers.

Ta-Wei Lin, Modafe, A., Shapiro, B. & Ghodssi, R. (2004). Characterization of dynamic friction in MEMS-based microball bearings. *IEEE Transactions on Instrumentation and Measurement*, 53(3), 839-846.

Tai, Y. ., Fan, L. . & Muller, R. S. (1989). IC-processed micro-motors: design, technology, and testing. *IEEE Micro Electro Mechanical Systems, , Proceedings, 'An Investigation of Micro Structures, Sensors, Actuators, Machines and Robots'*, pp. 1-6.

Tang, S.-Y., Zhu, J., Sivan, V., Gol, B., Soffe, R., Zhang, W., Mitchell, A. & Khoshmanesh, K. (2015). Creation of Liquid Metal 3D Microstructures Using Dielectrophoresis. *Advanced Functional Materials*, 25(28), 4445-4452. doi: https://doi.org/10.1002/adfm.201501296.

Tanguy, Q. A. A., Bargiel, S., Xie, H., Passilly, N., Barthès, M., Gaiffe, O., Rutkowski, J., Lutz, P. & Gorecki, C. (2017). Design and Fabrication of a 2-Axis Electrothermal MEMS Micro-Scanner for Optical Coherence Tomography. *Micromachines*, 8(5). doi: 10.3390/mi8050146.

Tani, M., Akamatsu, M., Yasuda, Y. & Toshiyoshi, H. (2007). A two-axis piezoelectric tilting micromirror with a newly developed PZT-meandering actuator. *2007 IEEE 20th International Conference on Micro Electro Mechanical Systems (MEMS)*, pp. 699-702. doi: 10.1109/MEMSYS.2007.4432994.

Targowski, P. & Iwanicka, M. (2012). Optical Coherence Tomography: its role in the non-invasive structural examination and conservation of cultural heritage objects—a review. *Applied Physics A*, 106(2), 265-277. doi: 10.1007/s00339-011-6687-3.

Tavrow, L. S., Bart, S. F. & Lang, J. H. (1991). Operational characteristics of microfabricated electric motors. *TRANSDUCERS '91: 1991 International Conference on Solid-State Sensors and Actuators. Digest of Technical Papers*, pp. 877-881.

Tavrow, L. S., Bart, S. F. & Lang, J. H. (1992). Operational characteristics of microfabricated electric motors. *Sensors and Actuators A: Physical*, 35(1), 33 - 44.

Thakur, R. (2016). Scanning LIDAR in Advanced Driver Assistance Systems and Beyond: Building a road map for next-generation LIDAR technology. *IEEE Consumer Electronics Magazine*, 5(3), 48-54. doi: 10.1109/MCE.2016.2556878.

Thrane, L. et al. (2012). Application of optical coherence tomography (OCT) as a 3-dimensional imaging technique for roll-to-roll coated polymer solar cells. *Solar Energy Materials and Solar Cells*, 97, 181-185. doi: https://doi.org/10.1016/j.solmat.2011.10.004. Dedicated to the Global Organic Photovoltaics (GOPV) conference in Hangzhou, China.

Tien, C.-H. & Lee, C.-H. (2006). Optical Properties of Surface Micromachining with Randomly Distributed Etch Holes. *Japanese Journal of Applied Physics*, 45(2A), 1015–1017. doi: 10.1143/jjap.45.1015.

Todd, S. T., Jain, A., Qu, H. & Xie, H. (2006). A multi-degree-of-freedom micromirror utilizing inverted-series-connected bimorph actuators. *Journal of Optics A: Pure and Applied Optics*, 8(7), S352–S359. doi: 10.1088/1464-4258/8/7/s10.

Toshiyoshi, H., Piyawattanametha, W., Cheng-Ta Chan & Wu, M. C. (2001a). Linearization of electrostatically actuated surface micromachined 2-D optical scanner. *Journal of Microelectromechanical Systems*, 10(2), 205-214. doi: 10.1109/84.925744.

Toshiyoshi, H., Piyawattanametha, W., Cheng-Ta Chan & Wu, M. C. (2001b). Linearization of electrostatically actuated surface micromachined 2-D optical scanner. *Journal of Microelectromechanical Systems*, 10(2), 205-214. doi: 10.1109/84.925744.

Trimmer, W. & Gabriel, K. (1987a). Design considerations for a practical electrostatic micro-motor. *Sensors and Actuators*, 11(2), 189 - 206.

Trimmer, W. & Gabriel, K. (1987b). Design considerations for a practical electrostatic micro-motor. *Sensors and Actuators*, 11(2), 189 - 206.

Tu, C.-C., Fanchiang, K. & Liu, C.-H. (2005). 1xN rotary vertical micromirror for optical switching applications. *MOEMS and Miniaturized Systems V*, 5719, 14 – 22. doi: 10.1117/12.589810.

Uchino, K. (2008). Piezoelectric actuators 2006. *Journal of Electroceramics*, 20(3), 301-311. doi: 10.1007/s10832-007-9196-1.

Urey, H., Holmstrom, S., Baran, U., Aksit, K., Hedili, M. K. & Eides, O. (2013). MEMS scanners and emerging 3D and interactive Augmented Reality display applications. *2013 Transducers Eurosensors XXVII: The 17th International Conference on Solid-State Sensors, Actuators and Microsystems (TRANSDUCERS EUROSENSORS XXVII)*, pp. 2485-2488. doi: 10.1109/Transducers.2013.6627310.

Urey, H. (2002). Torsional MEMS scanner design for high-resolution scanning display systems. *Optical Scanning 2002*, 4773, 27 – 37. Consulted at https://doi.org/10.1117/12.469198.

Urey, H., Wine, D. W. & Osborn, T. D. (2000). Optical performance requirements for MEMS-scanner-based microdisplays. *MOEMS and Miniaturized Systems*, 4178, 176 – 185. Consulted at https://doi.org/10.1117/12.396486.

Varona, J., Tecpoyotl-Torres, M. & Hamoui, A. A. (2009). Design of MEMS vertical–horizontal chevron thermal actuators. *Sensors and Actuators A: Physical*, 153(1), 127 - 130.

Velodyne. (2019). VLP-16 Datasheet.

Vilares, R., Hunter, C., Ugarte, I., Aranburu, I., Berganzo, J., Elizalde, J. & Fernandez, L. (2010). Fabrication and testing of a SU-8 thermal flow sensor. *Sensors and Actuators B: Chemical*, 147(2), 411 - 417.

Wallrabe, U., Bley, P., Krevet, B., Menz, W. & Mohr, J. (1994). Design rules and test of electrostatic micromotors made by the LIGA process. *Journal of Micromechanics and Microengineering*, 4(1), 40–45.

Wan, Z., Zeng, H. & Feinerman, A. (2006). Area-tunable micromirror based on electrowetting actuation of liquid-metal droplets. *Applied Physics Letters*, 89(20), 201107. doi: 10.1063/1.2388943.

Wang, D., Koppal, S. J. & Xie, H. (2020a). A Monolithic Forward-View MEMS Laser Scanner With Decoupled Raster Scanning and Enlarged Scanning Angle for Micro LiDAR Applications. *Journal of Microelectromechanical Systems*, 29(5), 996-1001. doi: 10.1109/JMEMS.2020.3001921.

Wang, D., Watkins, C. & Xie, H. (2020b). MEMS Mirrors for LiDAR: A Review. *Micromachines*, 11(5). doi: 10.3390/mi11050456.

Wang, D., Watkins, C. & Xie, H. (2020c). MEMS Mirrors for LiDAR: A Review. *Micromachines*, 11(5). doi: 10.3390/mi11050456.

Wang, L., Mills, J. K. & Cleghorn, W. L. (2008a). Assembly of three-dimensional microsystems using a hybrid manipulation strategy. *2008 IEEE International Conference on Mechatronics and Automation*, pp. 545-550.

Wang, M., Maleki, T. & Ziaie, B. (2008b). Enhanced 3-D Folding of Silicon Microstructures via Thermal Shrinkage of a Composite Organic/Inorganic Bilayer. *Journal of Microelectromechanical Systems*, 17(4), 882-889.

Wang, T., Zhang, C., Aleksov, A., Salama, I. & Kar, A. (2016). Effect of large deflection angle on the laser intensity profile produced by acousto-optic deflector scanners in high precision manufacturing. *Journal of Laser Applications*, 28(1), 012012. doi: 10.2351/1.4937174.

Wang, Y., Zhou, G., Zhang, X., Kwon, K., Blanche, P.-A., Triesault, N., sik Yu, K. & Wu, M. C. (2019). 2D broadband beamsteering with large-scale MEMS optical phased array. *Optica*, 6(5), 557–562. doi: 10.1364/OPTICA.6.000557.

Wang Xinli, Cui Shumei & Cheng Shukang. (2002). Advantages of electrostatic micromotor and its application to medical instruments. *Conference Record of the 2002 IEEE Industry Applications Conference. 37th IAS Annual Meeting (Cat. No.02CH37344)*, 4, 2466-2468 vol.4.

Warren, M. E. (2019). Automotive LIDAR Technology. *2019 Symposium on VLSI Circuits*, pp. C254-C255. doi: 10.23919/VLSIC.2019.8777993.

Weber, H. (2018). SICK AG WHITE PAPER.

Webster, P. J. L. et al. (2010). In situ 24 kHz coherent imaging of morphology change in laser percussion drilling. *Opt. Lett.*, 35(5), 646–648. doi: 10.1364/OL.35.000646.

Welch, D. & Christen, J. B. (2013). Seamless integration of CMOS and microfluidics using flip chip bonding. *Journal of Micromechanics and Microengineering*, 23(3), 035009.

Werber, A. & Zappe, H. (2006). Thermo-pneumatically actuated, membrane-based micro-mirror devices. *Journal of Micromechanics and Microengineering*, 16(12), 2524–2531. doi: 10.1088/0960-1317/16/12/002.

Wiak, S., Di Barba, P. & Savini, A. (1995). 3-D computer aided analysis of the "Berkeley" electrostatic micromotor. *IEEE Transactions on Magnetics*, 31(3), 2108-2111.

Wu, L. & Xie, H. (2007). 124° Rotation Angle Electrothermal Micromirror With Integrated Platinum Heater. *IEEE Journal of Selected Topics in Quantum Electronics*, 13(2), 316-321. doi: 10.1109/JSTQE.2007.894066.

Wu, L. & Xie, H. (2009). A scanning micromirror with stationary rotation axis and dual reflective surfaces for 360° forward-view endoscopic imaging. *TRANSDUCERS 2009 - 2009 International Solid-State Sensors, Actuators and Microsystems Conference*, pp. 2222-2225. doi: 10.1109/SENSOR.2009.5285589.

Wu, W., Chen, Q., Yan, G., Yin, D., Chen, Z., Hao, Y., Xu, A. & Wang, Y. (2007). Micro torsion mirror actuated by compound electrostatic driving structure. *Sensors and Actuators A: Physical*, 135(2), 758-764. doi: https://doi.org/10.1016/j.sna.2006.08.007.

Xie, H., Lan, S., Wang, D., Wang, W., Sun, J., Liu, H., Cheng, J., Ding, J., Qin, Z., Chen, Q., Kang, H. & Tian, Z. (2015). Miniature fourier transform spectrometers based on electrothermal MEMS mirrors with large piston scan range. *2015 IEEE SENSORS*, pp. 1-4. doi: 10.1109/ICSENS.2015.7370315.

Xie, H. (2018). Editorial for the Special Issue on MEMS Mirrors. *Micromachines*, 9(3). doi: 10.3390/mi9030099.

Xie, H., Pan, Y. & Fedder, G. K. (2003). Endoscopic optical coherence tomographic imaging with a CMOS-MEMS micromirror. *Sensors and Actuators A: Physical*, 103(1), 237-241. doi: https://doi.org/10.1016/S0924-4247(02)00347-3. Micromechanics section of Sensors and Actuators, based on contributions revised from the Technical Digest of the 15th IEEE International conference on Micro Electro mechanical Systems (MEMS 2002).

Xie, L., Nadri, S., Alijabbari, N., Cyberey, M. E., Bauwens, M. F., Lichtenberger, A. W., Barker, N. S. & Weikle, R. M. (2017). An Epitaxy Transfer Process for Heterogeneous Integration of Submillimeter-Wave GaAs Schottky Diodes on Silicon Using SU-8. *IEEE Electron Device Letters*, 38(11), 1516-1519.

Xie, L., Myo, P., Chong, S. C., Ho, S. W., Wee, J., Premachandran, C. S., Wang, S., herer, I. & Baram, A. (2010). Packaging and testing of electro-magnetically actuated silicon micro mirror for Pico-projector applications. *2010 12th Electronics Packaging Technology Conference*, pp. 731-736. doi: 10.1109/EPTC.2010.5702734.

Yalcinkaya, A. D., Urey, H., Brown, D., Montague, T. & Sprague, R. (2006). Two-axis electromagnetic microscanner for high resolution displays. *Journal of Microelectromechanical Systems*, 15(4), 786-794. doi: 10.1109/JMEMS.2006.879380.

Yalcinkaya, A., Urey, H., Brown, D., Montague, T. & Sprague, R. (2006). Two-axis electromagnetic microscanner for high resolution displays. *Journal of Microelectromechanical Systems*, 15(4), 786-794. doi: 10.1109/JMEMS.2006.879380.

Yalcinkaya, A. D., Urey, H. & Holmstrom, S. (2007). NiFe Plated Biaxial MEMS Scanner for 2-D Imaging. *IEEE Photonics Technology Letters*, 19(5), 330-332. doi: 10.1109/LPT.2007.891592.

Yan, J., Luanava, S. & Casasanta, V. (2003). Magnetic actuation for MEMS scanners for retinal scanning displays. *MOEMS Display and Imaging Systems*, 4985, 115 – 120. doi: 10.1117/12.477808.

Yang, G., Gaines, J. A. & Nelson, B. J. (2003). A Supervisory Wafer-Level 3D Microassembly System for Hybrid MEMS Fabrication. *Journal of Intelligent and Robotic Systems*, 37(1), 43-68. doi: 10.1023/A:1023982907874.

Yasseen, A. A., Smith, S. W., Mehregany, M. & Merat, F. L. (1995). Diffraction grating scanners using polysilicon micromotors. *Proceedings IEEE Micro Electro Mechanical Systems. 1995*, pp. 175-.

Yasseen, A., Wu, C.-H., Zorman, C. & Mehregany, M. (1999a). Fabrication and testing of surface micromachined silicon carbide micromotors. *Technical Digest. IEEE International MEMS 99 Conference. Twelfth IEEE International Conference on Micro Electro Mechanical Systems (Cat. No.99CH36291)*, pp. 644-649. doi: 10.1109/MEMSYS.1999.746903.

Yasseen, A., Wu, C. H., Zorman, C. & Mehregany, M. (2000). Fabrication and testing of surface micromachined polycrystalline SiC micromotors. *IEEE Electron Device Letters*, 21(4), 164-166. doi: 10.1109/55.830969.

Yasseen, A., Mitchell, J. N., Smith, D. A. & Mehregany, M. (1999b). High-aspect-ratio rotary polygon micromotor scanners. *Sensors and Actuators A: Physical*, 77(1), 73 - 79. doi: https://doi.org/10.1016/S0924-4247(99)00187-9.

Yasseen, A., Mitchell, J. N., Smith, D. A. & Mehregany, M. (1999c). High-aspect-ratio rotary polygon micromotor scanners1Paper presented as part of the SSAW-98 Workshop.1. *Sensors and Actuators A: Physical*, 77(1), 73 - 79.

Ye, L., Zhang, G., You, Z. & Zhang, C. (2016). A 2D resonant MEMS scanner with an ultra-compact wedge-like multiplied angle amplification for miniature LIDAR application. *2016 IEEE SENSORS*, pp. 1-3. doi: 10.1109/ICSENS.2016.7808932.

Ye, L., Zhang, G. & You, Z. (2017a). Large-Aperture kHz Operating Frequency Ti-alloy Based Optical Micro Scanning Mirror for LiDAR Application. *Micromachines*, 8(4). doi: 10.3390/mi8040120.

Ye, L. et al. (2017b). Large-Aperture kHz Operating Frequency Ti-alloy Based Optical Micro Scanning Mirror for LiDAR Application. *Micromachines*, 8(4). doi: 10.3390/mi8040120.

Yeow, J., Yang, V., Chahwan, A., Gordon, M., Qi, B., Vitkin, I., Wilson, B. & Goldenberg, A. (2005). Micromachined 2-D scanner for 3-D optical coherence tomography. *Sensors and Actuators A: Physical*, 117(2), 331-340. doi: https://doi.org/10.1016/j.sna.2004.06.021.

Yoda, M., Isamoto, K., Chong, C., Ito, H., Murata, A., Kamisuki, S., Atobe, M. & Toshiyoshi, H. (2005). A MEMS 1D optical scanner for laser projection display using self-assembled vertical combs and scan-angle magnifying mechanism. *The 13th International Conference on Solid-State Sensors, Actuators and Microsystems, 2005. Digest of Technical Papers. TRANSDUCERS '05.*, 1, 968-971 Vol. 1. doi: 10.1109/SENSOR.2005.1496616.

Yoo, H. W., Ito, S. & Schitter, G. (2016). High speed laser scanning microscopy by iterative learning control of a galvanometer scanner. *Control Engineering Practice*, 50, 12 - 21. doi: https://doi.org/10.1016/j.conengprac.2016.02.007.

Yoo, H. W., Druml, N., Brunner, D., Schwarzl, C., Thurner, T., Hennecke, M. & Schitter, G. (2018). MEMS-based lidar for autonomous driving. *e & i Elektrotechnik und Informationstechnik*, 135(6), 408-415. doi: 10.1007/s00502-018-0635-2.

You, Y.-m. & Yoon, K.-y. (2019). A Study on Performance Improvement of Polygon Mirror Scanner Motor. *Journal of Electrical Engineering & Technology*, 14(2), 747-755. doi: 10.1007/s42835-018-00079-5.

Yu, L., Tay, F. E. H., Xu, G., Chen, B., Avram, M. & Iliescu, C. (2006). Adhesive bonding with SU-8 at wafer level for microfluidic devices. *Journal of Physics: Conference Series*,

34, 776–781.

Yu-Chong, T. & Muller, R. S. (1990). Frictional study of IC-processed micromotors. *Sensors and Actuators A: Physical*, 21(1), 180 - 183. Proceedings of the 5th International Conference on Solid-State Sensors and Actuators and Eurosensors III.

Yun, S. H., Boudoux, C., Tearney, G. J. & Bouma, B. E. (2003). High-speed wavelength-swept semiconductor laser with a polygon-scanner-based wavelength filter. *Opt. Lett.*, 28(20), 1981–1983. doi: 10.1364/OL.28.001981.

Zeng, H., Wan, Z. & Feinerman, A. D. (2006). Tilting Micromirror With a Liquid-Metal Pivot. *Journal of Microelectromechanical Systems*, 15(6), 1568-1575. doi: 10.1109/JMEMS.2006.883531.

Zeng, S. (2013). A Tracking System of Multiple LiDAR Sensors Using Scan Point Matching. *IEEE Transactions on Vehicular Technology*, 62(6), 2413-2420. doi: 10.1109/TVT.2013.2245694.

Zesch, W. & Fearing, R. S. (1998). Alignment of microparts using force-controlled pushing. *Microrobotics and Micromanipulation*, 3519, 148 – 156.

Zhang, W., Meng, G. & Li, H. (2005). Electrostatic micromotor and its reliability. *Microelectronics Reliability*, 45(7), 1230 - 1242.

Zhang, X., Adelegan, O., Yamaner, F. Y. & Oralkan, O. (2017). An optically transparent capacitive micromachined ultrasonic transducer (CMUT) fabricated using SU-8 or BCB adhesive wafer bonding. *2017 IEEE International Ultrasonics Symposium (IUS)*, pp. 1-4.

Zhang, X., Koppal, S. J., Zhang, R., Zhou, L., Butler, E. & Xie, H. (2016). Wide-angle structured light with a scanning MEMS mirror in liquid. *Opt. Express*, 24(4), 3479–3487. doi: 10.1364/OE.24.003479.

Zhang, Y. & Chen, L. (1999). Vignetting and the scan duty cycle of dual-beam scanning field by polygon scanners. *Color Imaging: Device-Independent Color, Color Hardcopy, and Graphic Arts V*, 3963, 544 – 550. Consulted at https://doi.org/10.1117/12.373436.

Zhili Hao, Wingfield, B., Whitley, M., Brooks, J. & Hammer, J. A. (2003). A design methodology for a bulk-micromachined two-dimensional electrostatic torsion micromirror. *Journal of Microelectromechanical Systems*, 12(5), 692-701. doi: 10.1109/JMEMS.2003.817888.

Zhou, Q. & Zhang, Y. (2019). Editorial for the Special Issue on MEMS Technology for Biomedical Imaging Applications. *Micromachines*, 10(9). doi: 10.3390/mi10090615.

Zhu, J. et al. (2020). Development Trends and Perspectives of Future Sensors and MEMS/NEMS. *Micromachines*, 11(1). Consulted at https://www.mdpi.com/2072-666X/11/1/7.

Álvaro Jiménez, Milde, T., Tatenguem, H., Honsberg, M., Carpintero, G., O'Gorman, J. & Sacher, J. R. (2018). MEMS-based widely tunable external cavity diode laser. *MOEMS and Miniaturized Systems XVII*, 10545, 127 – 132. Consulted at https://doi.org/10.1117/12.2287849.